



**HAL**  
open science

# Contributions à la simulation Monte-Carlo pour l'optimisation du traitement en radiothérapie

Julien Bert

► **To cite this version:**

Julien Bert. Contributions à la simulation Monte-Carlo pour l'optimisation du traitement en radiothérapie. Physique Médicale [physics.med-ph]. Université de Bretagne Occidentale (UBO), 2018. tel-01906265

**HAL Id: tel-01906265**

**<https://hal.science/tel-01906265v1>**

Submitted on 26 Oct 2018

**HAL** is a multi-disciplinary open access archive for the deposit and dissemination of scientific research documents, whether they are published or not. The documents may come from teaching and research institutions in France or abroad, or from public or private research centers.

L'archive ouverte pluridisciplinaire **HAL**, est destinée au dépôt et à la diffusion de documents scientifiques de niveau recherche, publiés ou non, émanant des établissements d'enseignement et de recherche français ou étrangers, des laboratoires publics ou privés.



Université de Bretagne Occidentale

FACULTÉ DE MÉDECINE DE BREST

HABILITATION À DIRIGER DES RECHERCHES

---

**Contributions à la simulation Monte-Carlo  
pour l'optimisation du traitement en radiothérapie**

---

**Julien Bert**

Soutenance le 25 octobre 2018

**Jury**

<b>M. David Brasse</b>	DR CNRS, IPHC Strasbourg	Rapporteur
<b>M. Sébastien Jan</b>	IR CEA, SHFJ Orsay	Rapporteur
<b>M. Christian Morel</b>	PU Aix Marseille Université, CPPM Marseille	Rapporteur
<b>M. Antoine Valeri</b>	PU-PH UBO, service urologie CHRU Brest	Examineur
<b>M. Dimitris Visvikis</b>	DR INSERM, LaTIM Brest	Examineur



FACULTÉ  
DE MÉDECINE &  
SCIENCES DE LA SANTÉ

UNIVERSITÉ  
BRETAGNE  
LOIRE



# Table des matières

<b>1</b>	<b>Curriculum vitae</b>	<b>1</b>
<b>2</b>	<b>Enseignements et encadrements</b>	<b>2</b>
<b>3</b>	<b>Activités de recherche</b>	<b>4</b>
<b>4</b>	<b>Revue, communications et ouvrages</b>	<b>6</b>
<b>5</b>	<b>Travaux de recherches</b>	<b>8</b>
5.1	Introduction . . . . .	8
5.2	Travaux de thèse et de postdoctorat . . . . .	9
5.2.1	Thèse (2004-2007) . . . . .	9
5.2.2	Post doctorat (2007-2010) . . . . .	10
5.3	Travaux au LaTIM (depuis 2010) . . . . .	11
5.3.1	Problématique générale . . . . .	12
5.3.2	Simulation Monte-Carlo sur architecture GPU . . . . .	14
5.3.3	Simulation Monte-Carlo pour les applications médicales . . . . .	19
5.3.4	Modélisation des systèmes de traitement . . . . .	23
5.3.5	Modélisation du patient . . . . .	25
5.4	Travaux en cours et futurs . . . . .	27
5.4.1	Curiethérapie de la prostate assistée par ordinateur . . . . .	28
5.4.2	Optimisation de la dose pour les procédures guidées par rayons X . . . . .	33
5.4.3	Radiothérapie externe . . . . .	35
<b>6</b>	<b>Conclusion</b>	<b>36</b>
	<b>Références bibliographiques</b>	<b>37</b>
	<b>ANNEXES</b>	<b>41</b>
A	Liste complète de la bibliographie . . . . .	41
A.1	En Révision - Revues internationales avec comité de lecture . . . . .	41
A.2	Revue internationale avec comité de lecture . . . . .	41
A.3	Conférences internationales avec comité de lecture . . . . .	43
A.4	Communications nationales avec comité de lecture . . . . .	47
A.5	Ouvrages . . . . .	49
B	Textes complets des publications les plus significatives . . . . .	50
B.1	Simulation Monte-Carlo sur architecture GPU . . . . .	50
B.2	La plateforme de simulation Monte-Carlo GGEMS . . . . .	69
B.3	Extension de GGEMS pour l'imagerie TEMP . . . . .	72
B.4	Application de GGEMS en curiethérapie de la prostate . . . . .	90
B.5	Géométrie hybride en simulation Monte-Carlo . . . . .	110
B.6	Modélisation et validation du système IntraBeam . . . . .	128
B.7	Modélisation des systèmes en radiothérapie externe . . . . .	137
B.8	Modélisation biomécanique de la prostate . . . . .	145
B.9	Recalage en imagerie multimodale pour la radiothérapie . . . . .	161





## 1 Curriculum vitae

**Nom :** Julien Bert  
**Date et lieu de de naissance :** 16 juin 1980, Saint Rémy, Saône et Loire (71)  
**Nationalité :** Française  
**Adresse personnelle :** 39 rue Robespierre, 29200 Brest  
**Téléphone :** 06 29 48 02 35  
**Adresse professionnelle :** LaTIM, INSERM UMR1101  
 Faculté de médecine, bâtiment IBRBS, étage R+1  
 22, Av. Camille Desmoulins, 29238 Brest  
**Téléphone :** 02 98 01 81 99  
**e-mail :** [julien.bert@univ-brest.fr](mailto:julien.bert@univ-brest.fr)

### 1.1 Expériences professionnelles

- Depuis 2013** **Mise à disposition** de 10% de mes activités à l'Institut de Recherche Technologique b<>com au *Augmented Healthcare Lab*.
- Depuis 2012** **Ingénieur de recherche**. Poste d'Ingénieur Hospitalier Principal titulaire. *Délégation à la Recherche Clinique et à l'Innovation du CHRU de Brest*. Rattaché au *Laboratoire de Traitement de l'Information Médicale (LaTIM - INSERM UMR1101)*, dans l'équipe de recherche ACTION (ACtion Thérapeutique guidée par l'Imagerie multimodale en ONcologie) de Dimitris Visvikis (DR1 INSERM).
- 2010-2012** **Postdoctorant**. Projet ANR h-GATE (ANR-09-COSI-004-01), *LaTIM, INSERM UMR1101, Brest*. Travaux en simulation Monte-Carlo dédiés aux applications médicales sur architecture GPU.
- 2007-2010** **Postdoctorant**. Projet de recherche en reconstruction tomographique de structure 3D de protéine par cryo-microscopie électronique. Financé par le *National Institutes of Health project (NIH Ro1 GM 60635)*. *Department of Biochemistry & Molecular Biology, Houston Medical School, Texas Medical Center, Houston, USA*.
- 2004-2007** **Doctorant**. Projet de recherche en vision par ordinateur pour la synthèse de vues à partir d'images de microscope optique, application à la micromanipulation. *CNRS Laboratoire d'Automatique de Besançon (devenu le département AS2M de l'institut FEMTO-ST)*.

### 1.2 Formations

- 2007** **Doctorat en Automatique**. *CNRS Laboratoire d'Automatique de Besançon, université de Franche-Comté*. Intitulé du mémoire : Synthèse de vues à partir d'images de microscopes photoniques pour la micromanipulation (<http://tel.archives-ouvertes.fr/tel-00195867>). Thèse financée par une allocation ministérielle.
- 2004** **DEA en Informatique, Automatique et Productique option Microrobotique et Micromécatronique**. *UFR Sciences et techniques, université de Franche-Comté, Besançon*. Intitulé du mémoire : Synthèse de comportements coopératifs dans les systèmes multi-agents par apprentissage par renforcement, application à la microrobotique mobile. Mention Bien.
- 2003** **Licence et Maîtrise en Électronique, Électrotechnique et Automatique**. *UFR Sciences et techniques, université de Franche-Comté, Besançon*. Mention Bien, bourse au mérite.
- 1997-2001** **CAP, BEP, BAC et DUT Génie Électrique et Informatique Industrielle**. *Lycée technique Nicéphore Niépce, Chalon sur Saône (71), IUT Le Creusot (université de Bourgogne)*.

## 2 Enseignements et encadrements

**2008** **Qualification** aux fonctions de maître de conférences en **section 61** du Conseil National des Universités : génie informatique, automatique, et traitement du signal.

### 2.1 Enseignements et présentations invitées

**2017** **Journée scientifique du réseau vectorisation et radiothérapie**, Rennes, France : *Innovative planning and guidance system for focal prostate brachytherapy* **15min**

**2016** **Séminaire Calcul/Imagerie**, INSERM, Biopark, Paris, France : *Fast and accurate medical image simulation using GPU-accelerated computing* **30min**

**2016** **37e Forum ORAP**, le nouveau paysage européen du HPC, retour d'expériences sur les accélérateurs et autres many-cores, Paris, France : *GPU-based high-performance computing for radiotherapy applications* **20min**

**2015** **Master2 recherche** signal, image, systèmes embarqués, automatique, Télécom Bretagne, Brest : *Reconstruction tomographique en imagerie médicale* **3h**

**2015** 20th Geant4 **Collaboration Meeting**, Fermi Lab, Illinois USA : *GATE on GPU* **30min**

**2015** **International Training School** on PET-MRI Engineering, COST Action TD1007, University of Leeds, United Kingdom : *Simulation Theory on PET* **1h30**, *PET Simulation Software Demonstration* **1h30**

**2015** **Ecole d'hiver** du LabEx CAMI, LaTIM, Brest : *GPU-based high performance computing for intraoperative medical applications* **1h30**

**2014** **Workshop** à l'université de Clemson USA : *Monte Carlo simulation in medical radiation physics : theory* Physics department **1h30**, *Monte Carlo simulation in medical radiation physics : application* Physics department **1h30**, *GPU computing in medical applications* Computer science department **1h30**

**2014** **International Training School** on PET-MRI Engineering. COST Action TD1007, Technological Education Institute of Athens, Greece : *Simulation Theory on PET* **1h30**, *PET Simulation Software Demonstration* **1h30**

**2014** **Séminaire** GdR STIC-Santé sur la simulation numérique, Paris : *The use of GPU simulation in biomedical applications*

**2013** **Workshop** on Numerical Modeling and Simulation of Inverse Problems in Medical Imaging, Grenoble : *3D PET list-mode reconstruction including all information provided by the detector* **1h**

**2013** **Ecole d'été** francophone de traitement d'images sur GPU, GIPSA-Lab, Institut polytechnique de Grenoble : *Simulation Monte Carlo sur GPU appliquée à la curiethérapie* **1h**

**2012** **Workshop** on Numerical Modeling and Simulation of Inverse Problems in Medical Imaging, Grenoble : *Optimisation of the projector in 3D PET list-mode reconstruction on GPU* **1h**

**2011** **Ecole d'été** francophone de traitement d'images sur GPU, GIPSA-Lab, Institut polytechnique de Grenoble : *Simulation Monte-Carlo sur GPU pour les applications médicales* **1h**

**2010** **Ecole d'été** francophone de traitement d'images sur GPU, GIPSA-Lab, Institut polytechnique de Grenoble : *Le GPU dans les sciences du vivant et de la santé* **1h**

**2004-2007** **Moniteur d'initiation à l'enseignement supérieur** à l'IUT de Besançon, Département d'Information et de Communication, Enseignement de **192h** de travaux dirigés en informatique en première année de DUT.

## 2.2 Encadrements

### 2.2.1 Post doctorants

- 2017-** **Konstantinos Mountris** Système de planification de traitement en Curiethérapie.
- 2016-** **Vincent Jaouen** Traitement de l'image en imagerie ultrason de la prostate.
- 2017-2018** **Abdeslam Behlouli** Réduction de variance pour la Simulation Monte Carlo sur GPU.
- 2017-2018** **Iyas Hamdan** Système de planification de traitement en Curiethérapie.
- 2015-2017** **Didier Benoit** Dosimétrie in-vivo par EPID en radiothérapie externe.
- 2015-2016** **Marie-Paule Garcia** *Computer Assisted for Prostate BRachytherapy Intervention (CAPRI)*.
- 2013-2015** **Eric Garrido** Modélisation de système de traitement en radiothérapie externe.

### 2.2.2 Doctorants

- 2016-** **Franklin Okoli** Optimisation de plans de traitement de faisceaux non-coplanaires en radiothérapie externe (encadrant). Financement LabEx CAMI et FHU TecSan. Co-direction avec le LIRMM (Salih Abdelaziz).
- 2015-** **Mozert Djohossou** Assistance en curiethérapie prostate par guidage robotisé (encadrant). Financement projet intégré CAPRI (LabEx CAMI).
- 2015-2018** **Nicolas Loy Rodas** Context-aware radiation protection for the hybrid operating room (co-encadrant). Thèse effectuée à l'ICUBE (Strasbourg) sous la supervision de Nicolas Padoy, financé par le LabEx CAMI.
- 2014-2017** **Konstantinos Mountris** Simulation biomécanique de la prostate pour l'optimisation de la planification en curiethérapie (encadrant). Financement région Bretagne et LabEx CAMI. Co-direction avec le TIMC-IMAG (Jocelyne Troccaz).
- 2013-2017** **Laurence Autret** Dosimétrie in-vivo temps réel en radiothérapie externe par simulation Monte-Carlo (encadrant). Financement région Bretagne et LabEx CAMI. Co-direction avec le TIMC-IMAG (Laurent Desbat).
- 2013-2016** **Iyas Hamdan** Planification adaptative en curiethérapie par l'imagerie multimodale TDM / IRM / échographie 3D (co-encadrant). Financement IRT b<>com, responsable Guillaume Dardenne.
- 2012-2016** **Yannick Lemaréchal** Simulation Monte-Carlo Geant4 sur architecture GPU (encadrant). Financement région Bretagne et CHRU de Brest.
- 2011-2015** **Awen Autret** Modélisation précise du détecteur en reconstruction TEP mode liste sur architecture GPU (encadrant). Financement Futur & Ruptures Fondation Télécom, collaboration avec Olivier Strauss (LIRMM).
- 2011-2015** **Dounia Bouzid** Simulation Monte Carlo GATE et dosimétrie en radiothérapie peropératoire pour le cancer du sein (co-encadrant). Financement région Bretagne et INSERM.

### 2.2.3 Echanges scientifiques (entrants)

- 2015** **Donald Medlin** Doctorant (université de Clemson, USA) Conception d'un nouvel irradiateur de traitement médical par simulation Monte-Carlo **4 semaines**.
- 2014** **Michaela Gaens** Doctorante (Institute of Neuroscience and Medicine, Allemagne), Correction de la diffusion par simulation Monte-Carlo sur GPU en reconstruction TEP **7 semaines**.
- 2013** **Marie-Paule Garcia** Post doctorante (CRCT, Toulouse), simulation Monte-Carlo sur GPU en imagerie SPECT **1 semaine**.
- 2012** **Didier Benoit** Doctorant (IMNC, Orsay), simulation Monte-Carlo sur GPU en imagerie SPECT **1 semaine**.

**2012** Vesna Cuplov Post doctorante (CEA SHFJ, Orsay), simulation Monte-Carlo de photon optique sur GPU **1 semaine**.

#### 2.2.4 Masters et ingénieurs

**2016** Elric Caill Stage ingénieur, Institut Supérieur de l'Electronique et du Numérique, Brest.

**2015** Erwann Kassis Master 1 informatique, université de Bretagne occidentale (UBO), Brest.

**2014** Stéphanie Beuil Master 2 signaux et images en biologie et médecine, UBO, Brest.

**2014** Marc Pouliquen Stage ingénieur, Institut Supérieur de l'Electronique et du Numérique, Brest.

**2014** Fabien Grassiot Projet de fin d'études ingénieur en mécatronique, Ecole Nationale Supérieure d'Ingénieurs de Bretagne Sud, Brest.

**2013** Stéphanie Beuil Master 2 signaux et images en biologie et médecine, UBO, Brest.

**2013** Jingyu Chen 2ième année Ingénieur Ecole des Mines de Nantes.

**2013** Tely Rakotondrajaona Master 2 signal, imageries et applications, université Toulouse III Paul Sabatier.

**2013** Khadim Sall Master 2 physique biologique et médicale, université Lille 1.

**2007** Laurent Lebocq Master recherche en mécatronique, Ecole Nationale Supérieure de Mécanique et des Microtechniques (ENSMM), Besançon.

**2007** Laurent Lebocq Projet de fin d'études ingénieur, ENSMM, Besançon.

**2007** Benjamin Doumenc Projet de fin d'études ingénieur, ENSMM, Besançon.

**2006** Mamadou Bah Master recherche en mécatronique, université de Franche-Comté (UFC), Besançon.

**2006** El Hani Boumaraf Master recherche en mécatronique, UFC, Besançon.

**2005** Mamadou Bah Master recherche en électronique et optique, UFC, Besançon.

**2005** Frédéric Esmilaire Master recherche en mécatronique, ENSMM, Besançon.

**2005** Cyril Chanel Master recherche en mécatronique, ENSMM, Besançon.

**2005** Ali Harbane Master recherche en mécatronique, UFC, Besançon.

## 3 Activités de recherche

### 3.1 Bourses de mobilité

**2015** **Mission scientifique à court terme.** Université de Bretagne Occidentale 1900€. K. Mountris, 3 mois à l'Universitat Pompeu Fabra, Barcelone, équipe du Pr Miguel A. Gonzalez Ballester.

**2015** **Mission scientifique à court terme.** Union Européenne COST Action TD1007 : European cooperation in science and technology 1400€. *Coopération avec Kris Thielemans d'une semaine, University College London, Londres.*

**2014** **Financement.** France Life Imaging 10k€. *Mission d'échange entre partenaires Français de la reconstruction TEP.*

**2014** **Bourse de mobilité.** Cancéropole Grand Ouest 1700€. *Une semaine à Québec à l'occasion d'un workshop international sur la simulation Monte Carlo.*

**2014** **Bourse de mobilité.** Cancéropole Grand Ouest 1500€. Y. Lemaréchal, *une semaine à Québec à l'occasion d'un workshop international sur la simulation Monte Carlo.*

**2014** **Mission scientifique à court terme.** Union Européenne COST Action TD1007 : European cooperation in science and technology 4500€. M. Gaens, *7 semaines au LaTIM, Brest.*

**2013** **Mission scientifique à court terme.** Université de Bretagne Occidentale 1600€. Y. Lemaréchal, *4 semaines au CHU de Québec, dans l'équipe de Philippe Després.*

**2012** **Bourse de mobilité.** Cancéropole Grand Ouest 1500€. A. Autret, *une semaine à Anaheim (USA) pour la conférence IEEE MIC 2012.*

### 3.2 Financements de thèses

- 2018-2021** Bourse CIFRE (Koelis), recrutement en cours.
- 2018-2021** Contrat Doctoral d'Établissement et Région Bretagne (FHU TecSan), étudiante Aziza Ben Halima.
- 2016-2019** Région Bretagne (FHU TecSan) et LabEx CAMI, étudiant Franklin Okoli.
- 2014-2017** Région Bretagne et LabEx CAMI, étudiant Konstantinos Mountris.
- 2013-2016** Institut de recherche technologique b<>com, étudiant Iyas Hamdan.
- 2013-2016** Région Bretagne et LabEx CAMI, étudiante Laurence Autret.
- 2011-2014** Institut Telecom, programme Future et Ruptures, étudiant Awen Autret.

### 3.3 Projets

- 2018-2022** Projet ANR OptimiX (Agence Nationale de la Recherche ANR-18-CE45-xxxx), Projets de Recherche Collaborative (PRC), *Radiation dose optimization for X-ray guided procedures*, 498k€, **Coordinateur**.
- 2016-2020** Projet ANR FOCUS (Agence Nationale de la Recherche ANR-16-CE19-0011), Projets de Recherche Collaborative - Entreprise (PRCE), *FOCUS – Innovative planning and guidance system for focal prostate brachytherapy*, 765k€, **Coordinateur**.
- 2016-2019** Projet Needleware, IRT b<>com (ANR), *Assistance au geste médical en Curiethérapie prostate*, 100k€, **Responsable de tâches**.
- 2014-2018** Projet intégré du LabEx CAMI, *CAPRI : Computer Assisted for Prostate BRachytherapy Intervention*, 340k€, **Responsable de projet**.
- 2014-2018** Projet ANR t-GATE (ANR-14-CE23-0008), *t-GATE : a unique integrative simulation platform for theranostics modeling*, 730k€, **Responsable de tâches**.
- 2013-2016** Projet GestChir, IRT b<>com (ANR), *Curiethérapie guidée par l'image multimodale*, 150k€, **Encadrement de thèse**.
- 2013-2016** Union Européenne FP7, *MINDView : Multimodal Imaging of Neurological Disorders*, 150k€, **Collaborateur**.
- 2010-2013** Union Européenne ITEA 2 : Information Technology for European Advancement, *MEDIATE : Patient friendly medical intervention*, 165k€, **Responsable de tâches**.
- 2009-2012** Projet ANR h-GATE (Agence Nationale de la Recherche ANR-09-COSI-004-01), *Hybrid GATE : Monte Carlo simulations on graphics processing units (GPU) for medical applications*, 700k€, **Responsable de tâches**.

### 3.4 Développement de logiciels

- Depuis 2017** **TiTAN** : opTimized Treatment pLANning system, logiciel en cours de déposition
- Depuis 2013** **BrachyPlan** et **BrachyLive**. Partenaire, license avec copyright (IRT b<>com).
- Depuis 2013** **GGEMS** : GPU GEant4-based Monte carlo Simulation. Responsable et développeur. Logiciel déposé : IDDN.FR.001.180017.000.S.P.2017.000.31230  
<http://ggems.fr>
- Depuis 2010** **GATE Monte Carlo Simulation Platform**. Membre de la collaboration Open Gate. Logiciel open source avec licenses GPL et LGPL.  
<http://www.opengatecollaboration.org>



### 3.5 Brevets

- 2017** Nicolas Padoy, Nicolas Loy Rodas, Michel de Mathelin, Julien Bert and Dimitris Visvikis, **Method for determining a configuration setting of a source of ionizing radiation**, *EU application*

### 3.6 Autres activités

#### 3.6.1 Administratives

- 2018** Membre du comité de direction du laboratoire *LaTIM*  
**2018** Responsable de l'axe Radiothérapie et Dosimétrie de l'équipe *ACTION*

#### 3.6.2 Jury de thèse

- 2018** Daniel Maneval, université Laval, Canada, *examineur*  
**2017** Nicolas Loy Rodas, université de Strasbourg, *invité*  
**2015** Benjamin Spencer, université de Grenoble, *invité*  
**2013** Michele Arcangelo Quinto, université de Grenoble, *examineur*

#### 3.6.3 Organisation d'événements

- 2018** CAMI Days, rencontre annuelle du LabEx Computer Assisted Medical Intervention, Brest, Dec. 2018  
**2017** Journées Scientifiques France Life Imaging WP3 - Imagerie Interventionnelle, Brest, 11-12 Dec. 2017

#### 3.6.4 Relecteur

- IEEE Transactions on Nuclear Science
- IEEE Transactions on Information Technology in BioMedicine
- IEEE Transactions on Radiation and Plasma Medical Sciences
- IEEE International Symposium on Biomedical Imaging
- IEEE Engineering in Medicine and Biology
- IEEE Nuclear Science Symposium and Medical Imaging Conference
- Nuclear Science and Techniques (Springer)
- Physica Medica : European Journal of Medical Physics (Elsevier)
- Medical Physics (AAPM), *reviewer* et *associate editor*
- EURASIP Journal on Image and Video Processing (Springer)
- Computer Physics Communications (Elsevier)
- Computer Methods in Biomechanics and Biomedical Engineering : Imaging & Visualization (Taylor & Francis)

## 4 Revues, communications et ouvrages

### 4.1 Revues internationales avec comité de lecture

23 publications de revues internationales dont voici une sélection. La liste complète est en Annexe [A.2](#). La liste des articles en révision se trouve en Annexe [A.1](#) :

1. Mountris K A, **Bert J**, Noailly J, Rodriguez Aguilera A, Valeri A, Pradier O, Schick U, Promayon E, Gonzalez Ballester M A, Troccaz J, Visvikis D, (2017). Modeling the impact of prostate edema on LDR brachytherapy : a Monte Carlo dosimetry study based on a 3D biphasic finite element biomechanical model *Physics in Medicine and Biology* 62 pp 2087-2102
2. **Bert J**, Lemaréchal Y, Visvikis D, (2016). New hybrid voxelized/analytical primitive in Monte Carlo simulations for medical applications *Physics in medicine and biology* 61 pp 3347-3364
3. Lemarechal Y, **Bert J**, Falconnet C, Despres P, Valeri A, Schick U, Pradier O, Garcia M-P, Boussion N, Visvikis D, (2015). GGEMS-Brachy : GPU GEant4-based Monte Carlo simulation for brachytherapy applications *Physics in Medicine and Biology* 60 pp 4978-5006
4. Bouzid D, **Bert J**, Dupre P-F, Benhalouche S, Pradier O, Boussion N, Visvikis D, (2015). Monte-Carlo dosimetry for intraoperative radiotherapy using a low energy x-ray source *Acta Oncologica* 54 pp 1788-1795
5. **Bert J**, Perez-Ponce H, El Bitar Z, Jan S, Boursier Y, Vintache D, Bonissent A, Morel C, Brasse D, Visvikis D, (2013). Geant4-based Monte Carlo simulations on GPU for medical applications *Physics in medicine and biology* 58 pp 5593-5611

#### 4.2 Conférences internationales avec comité de lecture

76 publications de conférences internationales dont voici une sélection. L'ensemble des publications est listé à l'Annexe A.3 :

1. **Bert J**, Visvikis D, (2018). Smooth mesh for accurate Monte Carlo simulation in medical applications *IEEE Nuclear Science Symposium and Medical Imaging Conference* (**présentation orale**)
2. Behlouli A, **Bert J**, Visvikis D, (2017). Improved Woodcock tracking on Monte Carlo simulations for medical applications *International Conference on Monte Carlo Techniques for Medical Applications* (**présentation orale**)
3. Mountris K, **Bert J**, Visvikis D, (2016). Prostate brachytherapy optimization using simulated annealing and Monte Carlo dose simulation *IEEE Nuclear Science Symposium and Medical Imaging Conference* (**présentation orale**)
4. **Bert J**, Lemaréchal Y, Visvikis D, (2014). Particle navigator for hybrid voxelized/analytical phantoms in Monte Carlo simulation for medical applications *International Workshop on Monte Carlo Techniques in Medical Physics* (**présentation orale**)
5. Benhalouche S, **Bert J**, Autret A, Visvikis D, Pradier O, Boussion N, (2013). Imaging and Radiation Therapy : GATE Monte Carlo Simulation of a Megavolt Cone Beam CT *IEEE Nuclear Science Symposium and Medical Imaging Conference* (**présentation orale**)
6. Bouzid D, Boussion N, Dupré P-F, **Bert J**, Pradier O, Visvikis D, (2013). Dosimetric validation of an Intrabeam<sup>TM</sup>GATE model, based on Monte Carlo GEANT4 toolkit, for IORT applications *American Association of Physicists in Medicine Annual Meeting*
7. **Bert J**, Perez-Ponce H, Jan S, El Bitar Z, Gueth P, Cuplov V, Chekatt H, Benoit D, Sarrut D, Boursier Y, Brasse D, Buvat I, Morel C, Visvikis D, (2012). Hybrid GATE : A GPU/CPU implementation for imaging and therapy applications *IEEE Nuclear Science Symposium and Medical Imaging Conference* pp 2247-2250 (**présentation orale**)

#### 4.3 Conférences nationales avec comité de lecture

La liste complète des 26 publications de conférences nationales est à l'Annexe A.4.

#### 4.4 Ouvrages

1. **Bert J**, (2010). Synthèse de vues à partir d'images de microscopes optiques, application à la micromanipulation *Editions Universitaires Européennes, ISBN 6131544018*



2. Bert J, (2007). Synthèse de vues à partir d'images de microscopes photoniques pour la micro-manipulation *Mémoire de thèse de doctorat, université de Franche-Comté*
3. Bert J, (2004). Synthèse de comportements coopératifs dans les systèmes multi-agents par apprentissage par renforcement, application à la microrobotique mobile *Mémoire de DEA, université de Franche-Comté*

## 5 Travaux de recherches

Cette section principale est dédiée à la présentation de mes travaux de recherches, passés, présents et futurs. Mes travaux de thèse seront brièvement mentionnés, tout comme ceux de post doctorat, pour laisser la place principale à mes activités de recherche actuelle et futurs. Depuis le début de ma thèse, j'ai été confronté à des thématiques assez variées (micro-robotique, biologie structurale, radiothérapie). Cependant, l'objectif scientifique sous-jacent de ces travaux reste dans une cohérence liée au domaine de l'automatisme, qui est ma formation académique initiale. Pour en comprendre le fondement, une brève introduction de ma vision de l'automatisme va être présentée dans la section suivante.

### 5.1 Introduction

L'automatique est la science qui traite de la modélisation, de l'analyse, de l'identification et de la commande des systèmes. L'objectif principal est de contrôler tout système conçu par et pour l'homme afin qu'il exécute ce pourquoi il a été conçu, le tout avec un certain niveau de robustesse et de précision dans l'interaction qu'il a avec l'environnement qui l'entoure. En aérospatial, c'est par exemple le pilotage automatique d'un avion de ligne ou le guidage d'une fusée. La robotique est aussi une bonne illustration. Domaine des sciences de l'ingénieur, l'automatisme fait appel à un ensemble de sous domaines : l'informatique, l'électronique, la mécanique, le traitement du signal, etc. Le contrôle d'un système (sa commande) peut se formaliser par la boucle *sensori motrice* (Fig. 1).

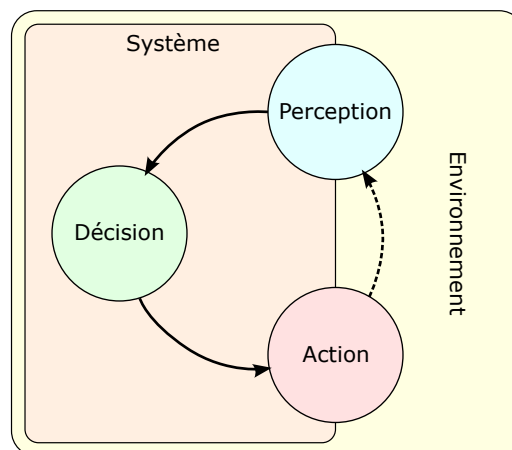


Figure 1 – Un fondement en automatique : la boucle *sensori motrice*.

Cette boucle est définie par trois fondements : perception, décision et action. Ils ont été introduits en Europe par (Couffignal, 1963) sont issus des travaux de Wiener dans les années 50 avec la cybernétique (Wiener, 1948). La cybernétique était la science qui étudie les mécanismes de communications et de contrôle dans les machines et chez les êtres vivants. Ce courant de réflexion est à l'origine notamment de l'automatisme et de l'intelligence artificielle. Ces trois fondements définissent ensemble un mécanisme intelligent qui se caractérise par la planification et la réflexion de ses actes en vue de modifier son environnement en se basant sur ses perceptions. En terme de définition, tout ce qui n'appartient pas au système est considéré comme étant son environnement. Le fondement *perception* représente tous types de détecteurs permettant d'observer et de percevoir l'environnement : caméra, capteur, microscope, etc. L'élément *décision* est la partie intelligente de la boucle, c'est le contrôleur

à proprement parler. Il peut prendre différentes fonctions : traitement des données, reconstruction de l'information, intelligence artificielle, optimisation, régulation, etc. Le dernier fondement *action* correspond à la partie qui interagit directement avec l'environnement : moteurs, vérins, interfaces graphiques, etc.

On distingue deux types de boucle *sensori motrice* : la boucle ouverte et la boucle fermée. Un système en boucle ouverte, appelée aussi proaction, n'a pas de fondement de perception. L'action du système sur l'environnement n'est pas observée. Ce type de système, très simple, ne permet pas de compenser l'erreur qu'il pourrait y avoir entre la consigne et la résultante de l'action. De même, dans cette configuration, le système ne peut pas réagir à une perturbation induite par un élément extérieur. Lorsque le système est dit à boucle fermée, appelée aussi rétroaction, tous les fondements sont présents et communicants. Le système réagit avec son environnement, c'est-à-dire qu'il y a un ajustement de l'action en fonction de la résultante obtenue sur son environnement. C'est le principe de l'asservissement. Un système en boucle fermée, sera plus robuste et précis. La comparaison entre la consigne et la résultante de l'action perçue permet de calculer une erreur qui sera utilisée pour corriger tous biais et perturbations.

Ce formalisme théorique restera un socle pour mes travaux de recherche, quelque soit le domaine d'étude. Fondamentalement, je cherche à améliorer les différents fondements de la boucle *sensori motrice* qui gouvernent maintenant l'automatisme moderne. L'objectif est de mieux contrôler, en terme de vitesse, de précision et de robustesse, un système soumis à une consigne donnée.

## 5.2 Travaux de thèse et de postdoctorat

### 5.2.1 Thèse (2004-2007)

Durant mes trois années de thèses, j'ai bénéficié d'une bourse ministérielle au Laboratoire d'Automatique de Besançon (CNRS) et d'un poste de moniteur à l'IUT de Besançon. Mes travaux de thèse ont été essentiellement consacrés au domaine de la vision par ordinateur pour la robotique, l'élément *perception* de la boucle *sensori-motrice*. L'application ciblée est le micro-assemblage, c'est-à-dire la manipulation et l'assemblage de pièces mécaniques de dimension micrométrique.

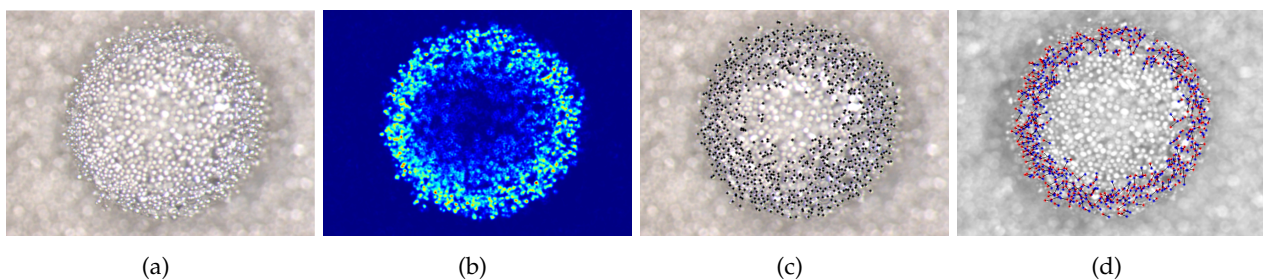


**Figure 2** – (a) Exemple de mire de calibration stéréoscopique : goutte d'eau recouverte de limaille de nickel (diamètre de  $300\ \mu\text{m}$ ). (b)-(c) Détection automatique des points d'intérêt et (d) mise en correspondance robuste des points. L'estimation du calibration se fait en utilisant plusieurs profondeurs de champ.

La combinaison de microscope photonique et de caméra est largement utilisée en micro-assemblage. Cet instrument indispensable comporte des inconvénients (faible champ de vision, faible profondeur de champ, encombrement important, nombre de vues limité, etc.). La conséquence directe à cela est l'utilisation d'un système de vision distribué composé d'imageurs qui ont des caractéristiques différentes et complémentaires. Cela augmente le coût de la supervision du micro-assemblage. La complexité de la station augmente aussi, son accès est restreint car encombré de tout côté par des systèmes d'imageries. Mes travaux de thèse ont consisté à supprimer ou déplacer certains imageurs en reconstruisant virtuellement les vues utiles au contrôle d'une station de micro-assemblage. L'utilisation de microscopes en configuration stéréoscopie a été privilégiée. Pour cela j'ai développé de nouvelles approches pour le calibration automatique et robuste dédié à la micro-stéréoscopie, comme notamment la création de mires de calibration à base d'une goutte d'eau (Fig. 2

Bert et al., 2007).

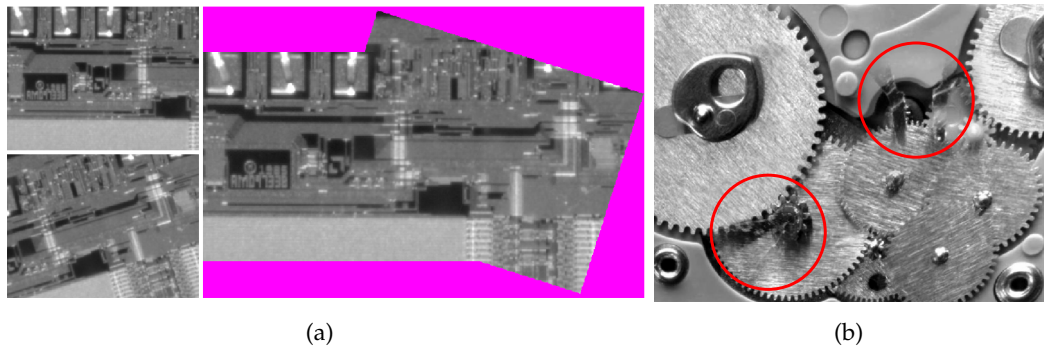


**Figure 3** – (a) Exemple du recalage et de la fusion automatique de deux images d’une puce EPROM (résolution  $2,51 \mu\text{m}/\text{pixel}$ ). (b) Incrustation et suivi en temps réel de deux pinces en cours de micromanipulation.

J’ai également proposé une nouvelle approche de construction d’images mosaïques et de suivi dynamique par incrustation afin de superviser un micro-assemblage (Bert et al., 2006b). Ici la problématique est de fusionner une vue large champ (statique) et une vue rapprochée (dynamique). La première étape est de pré-construire une carte de fond de l’espace de travail (statique) par recalage et fusion automatique via une acquisition par balayage (Fig. 3-a). Ensuite la vue locale dynamique (vidéo live), qui observe la tâche de micromanipulation exécutée par une pince, est suivie en temps réel par des méthodes de détection automatique et d’incrustation dans la carte de l’espace de travail obtenue précédemment par mosaïque (Fig. 3-b).

Pour observer des scènes inaccessibles, souvent liées à l’encombrement du matériel de la station, une reconstruction virtuelle de cette vue a été proposée. L’idée consiste à utiliser un stéréo-microscope en vue de dessus de la station pour reconstruire virtuellement n’importe quelle vue latérale. Classiquement, en reconstruction stéréoscopique, l’information 3D explicite est calculée à partir des images 2D stéréo, puis la vue désirée est projetée à partir du modèle 3D (2D-3D-2D). J’ai proposé une méthode basée sur le transfert trifocal (Bert et al., 2006a) qui permet de s’affranchir de l’étape de reconstruction 3D. La vue virtuelle est construite directement à partir des deux autres vues stéréoscopiques sans le besoin de l’information 3D explicite, c’est-à-dire de reconstruction. Cela permet principalement d’obtenir une vue virtuelle avec un faible temps de calcul (Fig. 4-a,b), ce qui n’est pas possible avec une méthode classique. Après un éclaircissement sur la théorie du tenseur trifocal avec singularité, j’ai utilisé cette méthode pour contrôler le déplacement en profondeur d’une micro-pince par une vue virtuelle latérale (Fig. 4-c).

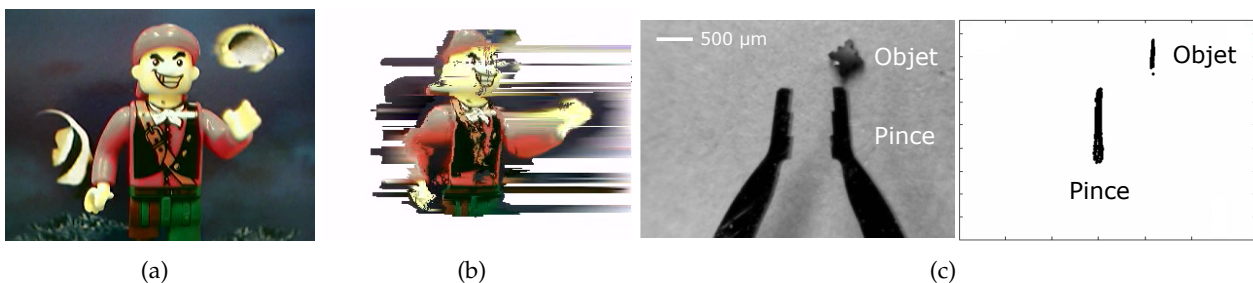


**Figure 4** – Exemple de création de vue virtuelle par transfert trifocal avec (a) une des images stéréoscopiques et (b) la vue virtuelle latérale. (c) La méthode a été appliquée pour l’asservissement en position d’un pince par rapport à un objet, avec la vue latérale pour le contrôle est purement virtuelle.

### 5.2.2 Post doctorat (2007-2010)

A l’issue de ma thèse, j’ai voulu me rapprocher du domaine médical par un premier contact à mi-chemin avec la biologie structurale. J’ai effectué un post doctorat de 3 ans aux Etats Unis dans le

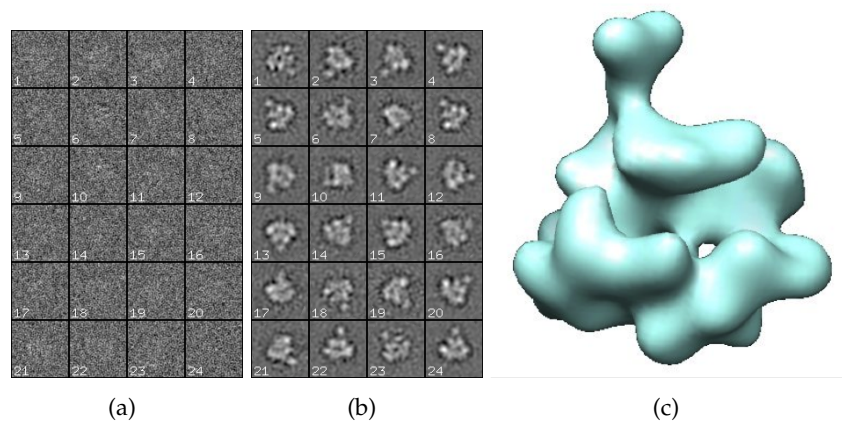


**Figure 5** – Exemples de (a) projection d’images par cryo-microscopie électronique ( $4,11 \text{ \AA}/\text{pixel}$ , parmi 66000 images), (b) images moyennes après classification des projections (parmi 316 images), et (c) reconstruction 3D de la densité électronique de la protéine, ici l’ARN polymérase II ( $18 \text{ nm}$  de hauteur pour  $14 \text{ nm}$  de large).

plus grand complexe de santé au monde : le *Texas Medical Center* à *Houston*. Le but de mon travail a consisté à améliorer les méthodes de reconstruction 3D de la structure de protéine imagé par microscopie électronique cryogénique (cryo-EM) à des fins de recherche fondamentale en biologie. Si la reconstruction 3D semble éloignée de l’automatisme, elle a en fait toute sa place notamment dans la boucle *sensory motrice*. En effet la reconstruction 3D, peut-être considérée comme une analyse des données issues de la perception. Elle fait intervenir le fondement *perception*, mais aussi celui de *décision*, ici au sens interprétation.

La microscopie électronique cryogénique consiste à cryogéniser rapidement des macromolécules du même type dans une solution. Cette solution “glacée” est ensuite imagée par le faisceau d’électrons du microscope qui est de faible énergie pour éviter la détérioration des éléments biologiques. Comme les macromolécules ont été figées dans des orientations différentes, il est possible de reconstruire sa structure 3D par tomographie via les milliers d’images obtenues de la macromolécule (Fig. 5), exactement comme en imagerie tomodensitométrie (TDM). Cependant la reconstruction est plus complexe car constituée de nombreuses étapes de traitement. Une des difficultés principales provient du fait que l’orientation aléatoire de chaque macromolécule est inconnue. Un autre problème est lié à la macromolécule qui a une densité électronique quasi identique à celle de la solution qui la contient, impliquant des images avec un rapport signal-sur-bruit extrêmement faible (Fig. 5-a).

Parmi l’ensemble des étapes de reconstruction, mes travaux ont consisté à améliorer la classification d’images en cryo-EM (Bert et al., 2009), le but étant de regrouper les vues identiques pour les moyenner, et donc d’améliorer le rapport signal-sur-bruit. Dans un premier temps, j’ai proposé une amélioration de l’algorithme de classification *K-means* avec un concept de recuit simulé et de sélection par voisinage adaptatif de type *Roulette-Wheel*, issue des méthodes d’algorithmes génétiques. Ceci a permis d’améliorer la propriété de convergence de *K-means* et donc sa reproductibilité. J’ai utilisé cet algorithme dans une nouvelle méthode itérative pour recueillir les groupes les plus consistants (stables) et homogènes. La procédure, qui est entièrement automatique sur architecture GPU, afin d’améliorer la vitesse d’exécution, est constituée d’alignements du jeu de données, de classifications répétées avec différentes initialisations, d’extractions des groupes stables, et de leurs évaluations (homogénéité). J’ai validé la procédure avec un jeu de données expérimentales de la protéine humaine ARN polymérase II. Les résultats montrent des moyennes obtenues d’une rare définition. Il est même possible de distinguer l’absence de sous-unités sur certaines structures détériorées. Ceci n’avait jamais été possible avant sur ce jeu de données avec des méthodes classiques.

### 5.3 Travaux au LaTIM (depuis 2010)

En 2010, je me rapproche définitivement du domaine médical, notamment par le biais d’un post doctorat effectué au LaTIM (INSERM-UMR1101) sur une problématique qui va me suivre jusqu’à



aujourd'hui. C'est pour cette raison que j'engloberai ces travaux effectués entre (2010-2012) avec mon activité de recherche actuelle. J'ai intégré l'équipe de recherche de D. Visvikis (DR INSERM), dont un des axes de recherche est la radiothérapie guidée par l'imagerie multimodale.

### 5.3.1 Problématique générale

La radiothérapie est une modalité de traitement contre le cancer qui consiste à utiliser des rayonnements ionisants pour détruire les cellules cancéreuses en bloquant leur capacité à se multiplier. Le traitement doit aussi préserver au mieux les tissus sains et les organes avoisinants. La radiothérapie peut être de nature externe, c'est-à-dire avec un faisceau de particules provenant de l'extérieur et qui traverse le patient pour atteindre la tumeur. C'est le traitement le plus utilisé en radiothérapie via un accélérateur linéaire de particules (LINAC : *LI*Near *AC*celerator), voir Fig. 6-a. Elle peut être également interne, appelée aussi curiethérapie (Fig. 6-b), avec des sources radioactives qui sont placées de façons permanentes ou transitoires à l'intérieur du corps du patient. Cet acte médical peut être employé également avec d'autres traitements comme la chirurgie et peut intervenir soit avant ou après la résection de la tumeur. Dans le cas d'une irradiation pendant la chirurgie, par exemple pour traiter les berges du lit tumoral après résection, elle est qualifiée de peropératoire (Fig. 6-c). Près de la moitié des personnes atteintes de cancer sont traitées par radiothérapie. Les chiffres et les indications cliniques de la radiothérapie ne seront pas détaillés dans ce mémoire. Des données actualisées sont accessibles sur différents sites qui font office de références (voir [e-cancer.fr](http://e-cancer.fr), [gco.iarc.fr](http://gco.iarc.fr), [cancerresearchuk.org](http://cancerresearchuk.org)). La radiothérapie est d'une importance socio-économique qui n'est plus à démontrer.

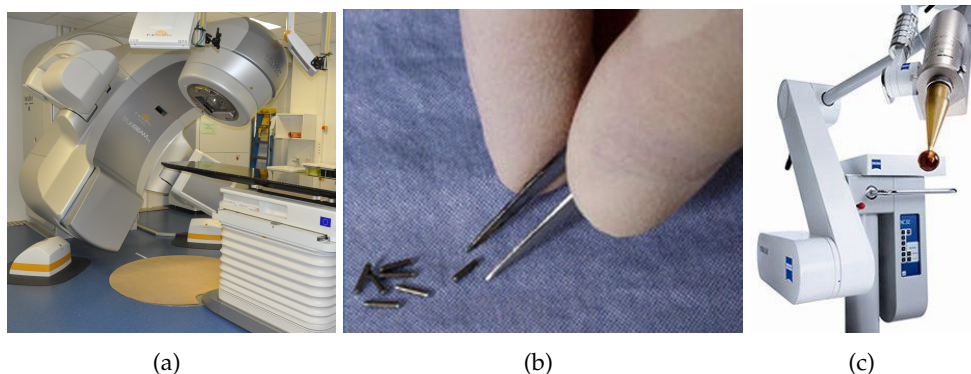


**Figure 6** – (a) Accélérateur linéaire TrueBeam Novalis (Varian) pour la radiothérapie externe. (b) Grain d'iode 125 utilisé en curiethérapie de la prostate. (c) Source à rayon X faible énergie (système IntraBeam, Zeiss) pour la radiothérapie per-opératoire.

La radiothérapie peut être formalisée par la boucle *sensory motrice*. Le fondement *action* correspond à l'action d'irradier les tissus et le fondement *décision* à celui de contrôler cette irradiation. Comme consignes de traitement, le clinicien définit des zones d'irradiations avec des critères de doses (minimum et maximum). La spécificité de la radiothérapie est qu'il n'existe pas de fondement *perception*, car il n'est pas possible de façon précise, complète et en temps réel de mesurer la dose déposée à l'intérieur du patient. La boucle est donc ouverte (voir Fig. 7), ce qui est le mode de fonctionnement le moins précis et le moins robuste. Faire un traitement à l'aveugle impliquerait un biais systémique entre les zones traitées et celles ciblées, avec des conséquences graves pour le patient. Pour répondre à ce problème un autre fondement est introduit dans la boucle *sensory motrice*, c'est celui de la *simulation* (voir Fig. 7). Comme l'environnement réel n'est pas observable, un environnement virtuel sera simulé *in silico* pour mesurer la résultante de l'irradiation sur le patient. Une étape de planification permet d'optimiser le traitement de façon *a priori* par la simulation comme si le système était en boucle fermée. La boucle d'asservissement habituelle décision/action/perception est remplacée par un asservissement virtuel et interne au système par les fondements décision/simulation, où la simulation émule le couplage action/perception. Lorsque les consignes dosimétriques sont satisfaites,

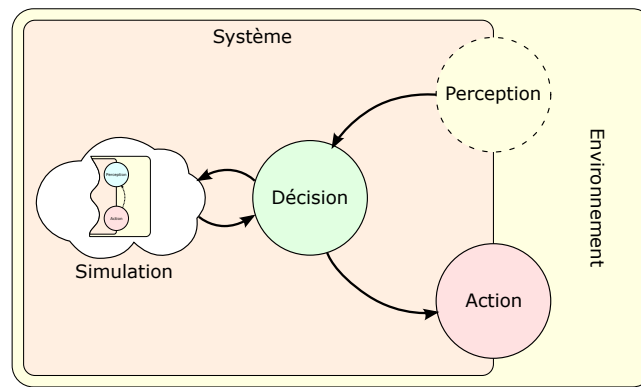


**Figure 7** – La boucle ouverte en radiothérapie, le lien manquant entre *action* et *perception* est compensé par celui de *simulation*.

le traitement optimal (virtuel) est sauvegardé dans un plan de traitement qui sera utilisé pour traiter le vrai patient. En fonction des applications cliniques, ce plan de traitement peut être déterminé de quelques minutes à quelques jours avant de traiter le patient en une ou plusieurs séances.

Si cette mécanique de planification permet de déterminer au mieux les paramètres d'irradiation, elle n'est pas exempte d'imprécisions non négligeables avec pour conséquence de diminuer l'efficacité du traitement, mais aussi d'accroître la présence des effets secondaires. Toute la difficulté en radiothérapie réside dans la capacité à prédire un plan de traitement qui soit le plus proche possible de ce que sera la réalité. Il y a des imprécisions qui proviennent de la simulation qui est réalisée avec plus ou moins de réalisme en fonction du niveau de modélisation : calcul de la dose, système de traitement, anatomie du patient, mouvement physiologique du patient, etc. En pratique, notamment en radiothérapie externe, le traitement est personnalisé en modélisant l'anatomie du patient via une image tomодensitométrie (TDM). Cependant les mouvements physiologiques (respiratoire, cardiaque, péristaltique) ne sont pas considérés. En radiothérapie peropératoire la planification du traitement est réalisée à la volée pendant l'intervention chirurgicale et doit être par conséquent très rapide. Dans la plupart des cas, le traitement n'est pas spécifique au patient. Par exemple, en curiethérapie de la prostate, on considère le patient comme étant un volume d'eau liquide infinie. Un autre ensemble d'imprécisions provient de la non stationnarité des modèles. C'est-à-dire l'évolution du modèle entre le moment de la planification et le jour où le traitement est délivré. C'est par exemple le changement anatomique du patient, les jeux mécaniques dans certains systèmes, la dérive de certaines sources, etc.

Toutes ces imprécisions n'ont probablement pas d'impact sur le taux de succès du traitement. La toxicité, c'est-à-dire l'irradiation des tissus sains est ici à mettre en avant. Les effets secondaires sont la conséquence directe de ce manque de précision dans le traitement. Ces imprécisions sont aussi un verrou pour mettre en place de nouveaux protocoles de traitement. Par exemple en radiothérapie externe, être plus précis dans la balistique permettrait une escalade de la dose et peut être de diminuer le nombre de séances ou dans certains cas peut-être d'améliorer les chances de rémission. Un autre exemple, être précis sur la prédiction de l'irradiation en curiethérapie permettrait de mettre en place des traitements plus ciblés (focal) avec moins d'effets secondaires et des temps opératoires moindres. Combattre les imprécisions dans la planification du traitement en radiothérapie permettrait au patient de mieux vivre pendant et après son cancer, tout en répondant aussi à un enjeu socio-économique important. En effet, une meilleure précision dans la planification du traitement aura pour conséquence de diminuer les effets secondaires, réduisant ainsi les coûts des soins post traitement, et de permettre de proposer de nouveaux protocoles plus optimisés avec des traitements plus courts, donc moins chers. La diminution des imprécisions de traitement en radiothérapie par la simulation a été le moteur initial de mes travaux de recherche depuis mon arrivé au LaTIM. Les sections suivantes seront consacrées à la présentation de mes travaux autour de cette problématique.

Optimiser le traitement du patient se résume en premier lieu à améliorer la simulation utilisée dans l'étape de planification. L'élément principal de cette simulation est le modèle utilisé pour le

calcul de la dose dans le patient. En effet, la plupart des logiciels cliniques utilisent des modèles de calcul analytique avec une précision suffisante dans la plupart des situations, mais révèlent des imprécisions dans certaines configurations. C'est le cas au niveau des interfaces de tissus hétérogènes de densités très différentes (tissu/air, tissu/os, tissu/métaux). Cette erreur d'estimation de la dose peut atteindre 6% dans une région osseuse et 10 % dans une région pulmonaire (Han et al., 2011; Calvo et al., 2012).

En physique médicale, l'outil méthodologique qui fait office de référence en matière de calcul de dose est la simulation Monte-Carlo (SMC). La SMC utilise des méthodes d'échantillonnage aléatoire pour résoudre le problème de transport des particules dans un milieu donné. Elle joue un rôle clé dans les applications de recherche médicale en modélisant avec précision les différents processus physiques d'interaction entre les particules et la matière (tissus et/ou détecteurs). En radiothérapie la SMC permet des calculs de dosimétrie précis pour la planification d'un traitement (Verhaegen and Seuntjens, 2003; Flampouri et al., 2006; Rassiah-Szegedi et al., 2007). Ce type de simulation permet de modéliser n'importe quel système de traitement utilisant des particules (Sarrut et al., 2014). Toutefois, cette méthode a un défaut majeur : son temps de calcul. En effet chaque particule est transportée indépendamment des autres dans le milieu afin d'enregistrer la dose qu'elle va déposer pendant son parcours. Cette méthode d'échantillonnage suit la loi des grands nombres. Pour obtenir un résultat statistiquement satisfaisant, il faut simuler un nombre de particules très important.

La simulation Monte-Carlo n'est pas utilisée en routine clinique à cause des temps de calcul trop importants. Dans l'objectif de démocratiser son utilisation en clinique, le premier angle d'attaque est donc de réduire ces temps de calcul.

### 5.3.2 Simulation Monte-Carlo sur architecture GPU

Une solution potentielle pour résoudre ce problème de calcul intensif est d'utiliser un cluster d'ordinateurs. Cependant, cette solution est difficile à déployer au sein d'une structure de santé, notamment quand elle est de taille moyenne. En effet, une telle solution demande un coût d'achat important ainsi qu'un coût de maintenance et de fonctionnement non négligeable, sans oublier la logistique associée (infrastructure informatique, zone de stockage, etc.).

Au début des années 2000, les cartes graphiques (GPU) sont devenues dans de nombreux domaines une alternative intéressante pour obtenir une puissance de calcul élevée avec un coût et un encombrement assez faible (Nickolls and Dally, 2010). Ce type d'architecture est capable de transformer n'importe quel ordinateur conventionnel en un petit cluster. L'utilisation de GPU dans la SMC représente une solution intéressante pour diminuer les temps de calcul associés à cette méthode, et *in fine* la porter en clinique.

Dans le cadre d'un projet ANR (hGATE, 2009-2012), nous avons proposé de développer des éléments simples de SMC sur GPU et de les intégrer dans le logiciel GATE (Jan et al., 2011), qui est un logiciel de référence dans le domaine de la SMC pour les applications médicales. GATE s'appuie sur la librairie de physique des particules Geant4 (Allison et al., 2006), développée dans le cadre d'une collaboration du CERN. Dans ce projet, nous nous sommes focalisé uniquement sur les effets physiques du photon : diffusion Compton, diffusion Rayleigh et photoélectrique. Pour le transport des photons, appelé aussi navigation, nous avons choisi d'implémenter uniquement le volume géométrique de type voxélisé, qui permet de modéliser le patient via une image TDM. Un GPU est constitué de *threads*, qui sont des unités de données à traiter. Ces threads sont ensuite regroupés en *warp* et ordonnancés pour être exécutés en parallèle par les cœurs de calcul du GPU, en nombre de plusieurs milliers sur les cartes graphiques les plus récentes. Le paradigme de solution a été choisi pour que chaque *thread* représente une particule à transporter. Ainsi, un nombre important de particules sont traitées de façon parallèle.

Ce module GPU, qui ne gère que la navigation des particules dans le patient, a été inséré à l'intérieur du logiciel GATE afin de bénéficier des autres éléments nécessaires à la simulation (source, détecteur, etc.). Un système de mise en mémoire tampon des particules a été utilisé pour faire communiquer GATE, qui est séquentiel avec le module GPU. Les particules qui entrent dans le

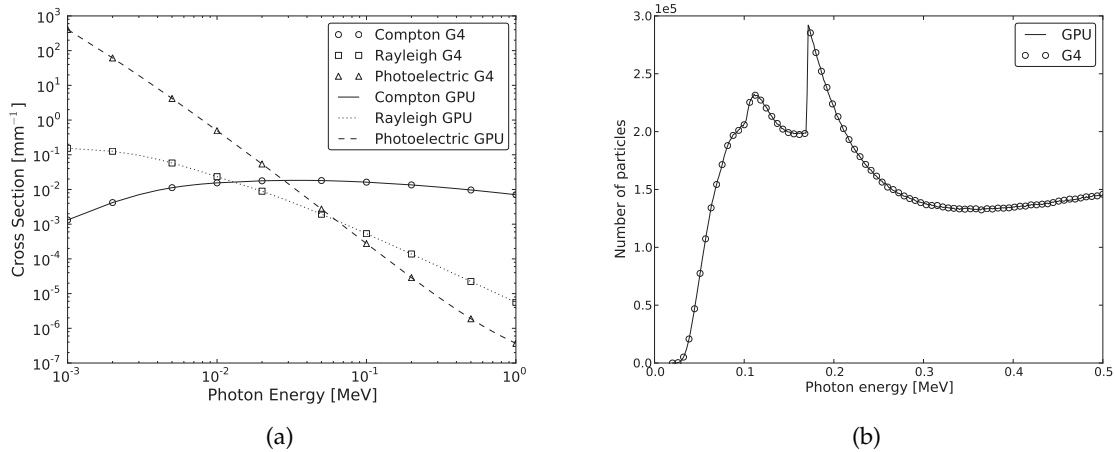


**Figure 8** – (a) Comparaison des sections efficaces dans l’eau des effets physiques des photons (modèle Livermore) entre le code GPU et Geant4 (CPU). (b) Comparaison de la distribution de l’énergie de diffusion des photons d’une simulation en tomographie d’émission entre le code GPU et Geant4 (CPU).

volume du patient sont stockées dans un tampon. Lorsque que ce tampon est plein, le GPU est déclenché et transporte toutes les particules en parallèle dans le patient. Idem pour les particules sortantes : elles sont retirées du tampon du GPU pour être réintroduites dans la simulation GATE une par une séquentiellement. Nos premiers résultats d’implémentation et de validation (Perez-Ponce et al., 2011; Bert et al., 2012, 2013a,c) ont montré une équivalence entre simulation GPU et CPU (GATE) (voir Fig. 8). Pour plus de détails voir l’article Bert et al. (2013c) en Annexe B.1. Ces premiers tests ont montré que le temps d’exécution du GPU pour la navigation des photons à l’intérieur du patient a été 500 fois plus rapide que le code standard de GATE sur CPU. Ce facteur d’accélération est la résultante de deux facteurs : d’une part de la réécriture du code de façon plus simple sur le GPU ( $\sim \times 10$ ) et d’autre part de la puissance propre de parallélisation du GPU ( $\sim \times 50$ ). Si l’on compare le temps de calcul global entre une simulation GATE avec et sans le module GPU, on note que la simulation est à peine  $\times 1,5$  plus rapide. Cela peut s’expliquer par le temps perdu par la mécanique de mise en tampon utilisé pour interfacer GATE et le module GPU. Mais l’explication principale est mise en évidence par la loi d’Amdhal. Il n’y a pas assez de code parallélisé à l’intérieur d’un logiciel globalement séquentiel. Le gain maximal ne peut être atteint que lorsque la simulation est entièrement parallélisée.

Après ce projet, nous avons poursuivi ces travaux prometteurs en proposant une nouvelle plateforme de SMC sur GPU. Pour bénéficier de toute la puissance de calcul de la carte graphique, la simulation Monte-Carlo est entièrement parallélisée sur l’architecture GPU. Cette plateforme appelée GGEMS (GPU GEant4-based Monte Carlo Simulation) est dédiée aux applications médicales (Bert et al., 2014). La physique a été étendue pour permettre la simulation des électrons et par conséquent les applications en radiothérapie externe (Fig. 9). L’objectif de GGEMS est double : apporter la SMC dans un contexte clinique et capitaliser nos différents travaux autour de la SMC. Il existe dans la littérature plusieurs codes GPU où chacun est dédié à une application médicale. La programmation GPU, liée à son architecture et à son langage de programmation (proche du C), ne permet pas autant de souplesse qu’un logiciel standard développé pour un processeur CPU. Pour chaque nouvelle application clinique, il faut un code dédié pour espérer avoir un gain d’accélération maximal. L’ensemble des travaux dans le domaine (Jia et al., 2014) font le même constat : chaque application clinique pour être performante doit avoir un code GPU dédié.

Pour répondre à cette problématique, la structure du code de GGEMS a évolué en profondeur. L’objectif a été de proposer la première plateforme flexible permettant la simulation de diverses applications médicale. Pour cela nous avons généralisé et proposé un nouveau concept de simulation Monte-Carlo sur GPU (Bert et al., 2016a, en Annexe B.2) appelé *source-phantom-detector* (SPD). Ce concept décompose de façon hybride la SMC en trois ensembles (Fig. 10-a) qui sont simulés



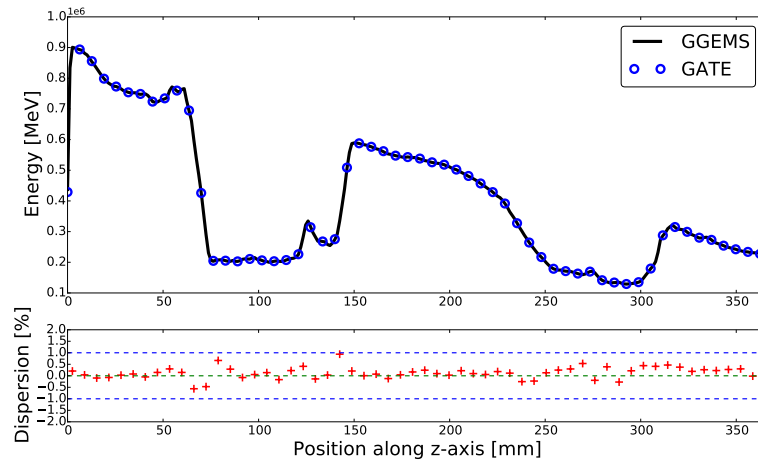


**Figure 9** – Comparaison de l'énergie totale déposée le long de l'axe z d'un faisceau de photons conformés provenant d'un système de radiothérapie externe (TrueBeam Novalis) à l'intérieur d'un thorax de patient entre GATE et GGEMS. Le facteur d'accélération obtenu par GGEMS a été de  $\times 156$  (NVIDIA GTX980Ti vs un cœur Intel i7-2600).

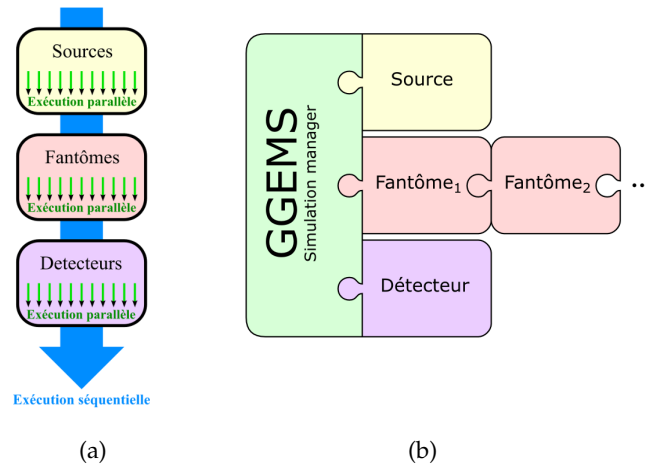


**Figure 10** – (a) Simulation hybride (séquentielle / parallèle), (b) modularité de l'architecture de GGEMS.

séquentiellement l'un après l'autre : sources, puis fantômes et enfin détecteurs. Cette configuration représente 99% des cas de SMC dans le médical. Chaque entité de l'ensemble SPD est quant à elle simulée de façon parallèle sur GPU. Cela permet au sein de la plateforme de SMC d'avoir une ossature fixe avec une flexibilité dans le choix des éléments à utiliser. En d'autres termes, la plateforme permet de facilement combiner différents types de sources, de fantômes et de détecteurs sans changer l'ossature principale du code (Fig. 10-b). Cela permet d'ajouter rapidement de nouveaux éléments (sources, fantômes, détecteurs) qui viennent directement se brancher sur l'ossature principale et de cibler de nouvelles applications.

Bien que dédié initialement à la radiothérapie, ce concept SPD nous a permis d'étendre facilement GGEMS à l'imagerie médicale et d'en évaluer les bénéfices (Fig. 11), pour la TDM (Bert et al., 2016a), pour la tomographie par émission monophotonique (TEMP) Garcia et al. (2014, 2015), Garcia et al. (2016) (en Annexe B.3) et pour la tomographie par émission de positons (TEP) (Gaens et al., 2013). En 2017, la plateforme GGEMS a été protégée par un dépôt logiciel (Bert and Visvikis, 2017).

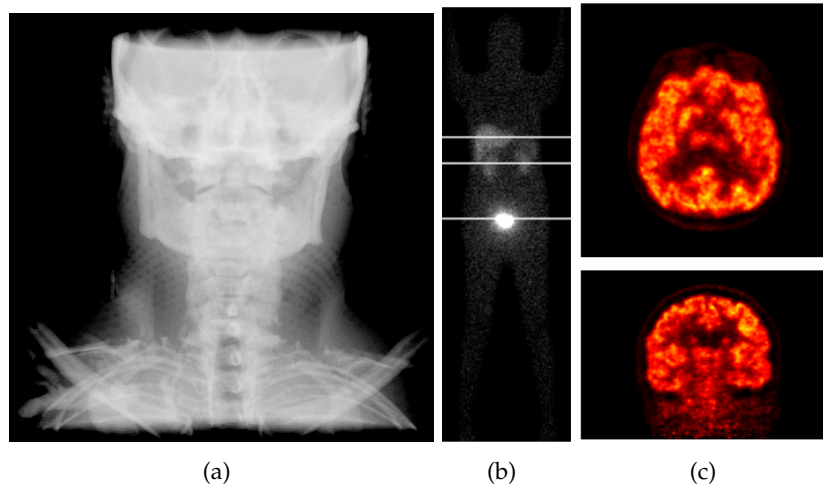


**Figure 11** – Simulation GGEMS en (a) TDM d’un fantôme de la tête avec un détecteur plan, en (b) imagerie TEMP du fantôme XCAT avec le radio-traceur  $^{111}\text{In}/\text{MEGP}$  et en (c) de l’image du cerveau d’un patient en imagerie TEP avec le radio-traceur  $^{18}\text{F}\text{-FDG}$ .

Pour évaluer l’impact et l’utilité d’une telle plateforme dans un contexte clinique, nous avons choisi une application qui a un réel enjeu en terme de rapidité et de précision dosimétrique. La curiethérapie bas débit de la prostate répond parfaitement aux besoins d’amélioration que peut apporter la SMC sur GPU. En effet la planification doit être rapide car réalisée à la volée en peropératoire et le modèle de calcul de dose est très perfectible. Nous avons facilement accès aux données des patients grâce aux collaborations avec les cliniciens du service d’urologie et de radiothérapie du CHRU de Brest.

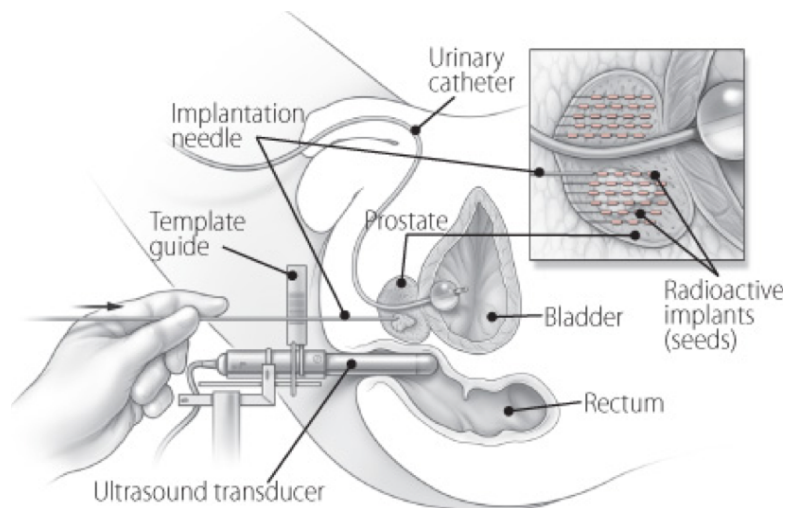


**Figure 12** – Procédure de la curiethérapie bas débit de la prostate. Les grains radioactifs sont insérés par le périnée manuellement aidé par un guide et l’imagerie échographique transrectale.

La curiethérapie de la prostate est une modalité de radiothérapie interne où plusieurs grains radioactifs ( $\sim 80$ ) sont insérés par abord périnéal et de façon permanente dans l’organe pour traiter le site tumoral. La méthode de calcul pour la dose repose sur un modèle de plus de 20 ans appelé le TG43 (Nath et al., 1995). Ce modèle, très simple et analytique, simplifie le patient comme un volume d’eau liquide de dimension infinie et la source radioactive comme une source ponctuelle constituée d’eau également. Le *workflow* clinique, présenté en Fig. 12, consiste à faire l’acquisition de la prostate par une sonde échographique endorectale puis à segmenter la glande et les organes à risque (urètre et rectum). Chaque volume est associé à un critère dosimétrique, puis une planification est réalisée en utilisant le TG43 comme fonction de coût pour déterminer les positions optimales des grains. Les

grains sont ensuite insérés par le périnée de façon manuelle sous contrôle échographique et guidés par une grille de repérage.

Si ce traitement permet d'obtenir de bon résultats sur les cancers précoces de la prostate (8 - 10% de récurrence), des effets secondaires transitoires et/ou permanents non négligeables de type urinaire, érectil, et rectal sont présents. Les approximations du calcul de dose contribuent à ces effets secondaires. Dans certains cas, notamment sur les régions de la prostate qui ont été sous dosées, les approximations dosimétriques peuvent potentiellement contribuer à une récurrence. Notre objectif a été d'utiliser la SMC pour personnaliser, améliorer et étudier le calcul de dose en curiethérapie. Les méthodes nécessaires pour réaliser ces travaux ont été développées dans le cadre d'un travail de thèse (Y. Lemaréchal).

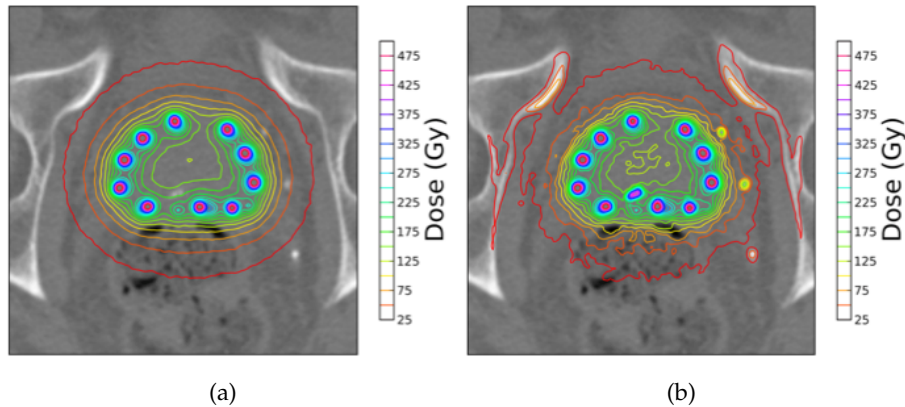


**Figure 13** – Image TDM du pelvis d'un patient avec en surimpression les isodoses provenant (a) du formalisme TG43 et (b) de la SMC avec GGEMS.

Nous avons proposé dans ces travaux de prendre en considération l'hétérogénéité des tissus du patient par le biais de l'image TDM du pelvis et de simuler l'interaction entre les grains. Pour cela, il a notamment fallu modéliser et valider le modèle du grain radioactif utilisé pour le traitement (ici de l'Iode 125). La simulation GGEMS a été validée avec le logiciel de référence Geant4 (sur CPU). Nous montrons une équivalence des résultats de simulation (erreur moyenne relative de 0,68%). Les données de 12 patients ont été utilisées pour comparer notre solution avec celle clinique (TG43). La SMC permet bien de prendre en considération les différents tissus du patient. Comme le montre la Fig. 13-a, le formalisme TG43 distribue la dose dans la prostate de façon homogène car il considère tout le volume comme étant de l'eau. Pour la SMC avec GGEMS, on remarque que la distribution spatiale de la dose est différente avec des points chauds notamment sur les calcifications présentes dans et autour de la prostate (Fig. 13-b). Au centre de la prostate, on note également que la dose est plus faible, indiquant une surestimation provenant du TG43.

Nous montrons que ces écarts de dose, conformes à la littérature (Beaulieu et al., 2012), atteignent une différence de 10% sur le D90 (dose minimum déposée à 90% du volume de la prostate), impliquant donc des zones sous dosées lorsque le TG43 est utilisé et donc un probable risque de récurrence du cancer. Les organes à risque, comme le montre les histogrammes dose-volume à la Fig. 14, reçoivent également moins de dose que prévu. L'os du pubis reçoit une dose bien plus importante que prévu par le TG43, il n'est à ce jour pas considéré comme un organe à risque. GGEMS nous a permis également de tester différentes configurations de simulation. Cela nous a permis de conclure que sur les 10% de différence entre le TG43 et la SMC, la moitié est liée à la différence de la définition du tissu de la glande entre eau et prostate, et l'autre moitié provient de l'interaction entre les grains. Etant composés de matériaux atténuants, les  $\sim 80$  grains font office de bouclier et atténuent la propagation des particules dans la glande. Concernant le temps de calcul, l'estimation de la dose avec une incertitude  $< 2\%$  dans la prostate pour le traitement complet (avec tous les grains) se fait en une seconde avec GGEMS (une seule carte graphique NVIDIA GTX980Ti), ce qui est compatible pour une utilisation clinique. Les validations et les résultats ont été publiés dans Lemaréchal et al. (2013a,b, 2014) et Lemaréchal et al. (2015) (voir Annexe B.4).

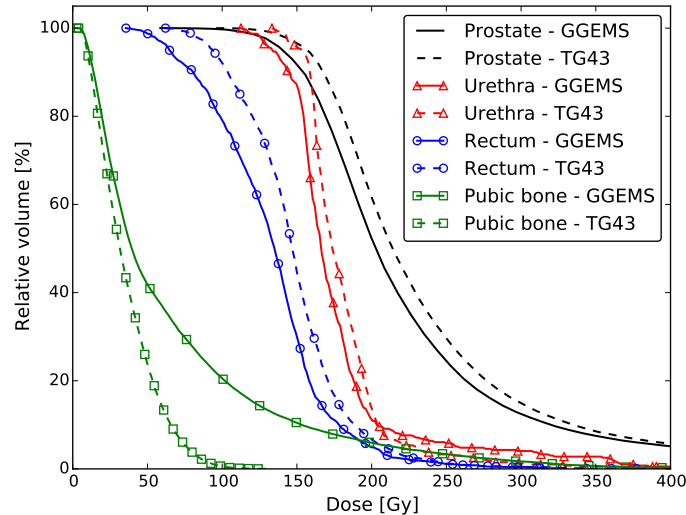


**Figure 14** – Histogramme dose-volume pour la prostate et les organes environnants entre une dosimétrie obtenue par le formalisme TG43 et une SMC obtenue par GGEMS.

### 5.3.3 Simulation Monte-Carlo pour les applications médicales

Les travaux effectués en curiethérapie de la prostate nous ont permis de mettre en évidence un manque d'outils spécifiques pour la SMC d'applications médicales. Par exemple, dans le cas de la curiethérapie, il manque des méthodes efficaces et génériques pour le transport des particules dans des objets analytiques, tels que par exemple les grains radioactifs, à l'intérieur d'un volume voxelisé (le patient). Ce problème se pose dans de nombreuses applications médicales où l'on veut simuler la présence d'objets mécaniques (prothèse, applicateur, vis, etc.) ou simuler une partie du patient plus finement avec une représentation analytique issue d'une segmentation d'une autre modalité d'image comme l'IRM (moelle épinière, organe à risque, vaisseau sanguin, etc.).

La solution consistant à voxeliser les objets contenus dans le patient n'est pas viable, car la quantité de données nécessaires pour une représentation fine de ces petits objets est trop importante, augmentant aussi le temps de calcul de la simulation. L'autre solution, qui est de convertir le patient en modèle analytique, n'est pas non plus exploitable, car on ne serait pas capable de simuler pleinement l'hétérogénéité des tissus dans le patient, chaque volume analytique étant constitué de matériaux homogènes. Il existe cependant une solution dans l'état de l'art appelée *Layered Mass Geometry (LMG)* (Yegin, 2003; Enger et al., 2012) implémentée notamment dans Geant4. Elle consiste à réaliser en même temps deux simulations, l'une avec l'objet voxelisé et l'autre avec l'objet analytique. Cette méthode fonctionnelle n'est pas optimale, du fait de la réplification de la simulation et de la synchronisation du transport entre ces deux mondes. De plus, elle nécessite de toucher au cœur de l'architecture de la simulation (la navigation des particules), compliquant la mise en place de la méthode dans d'autres plateformes de SMC.

Pour répondre à ce problème, j'ai proposé un nouveau type de primitive géométrique appelé YVAN (*hYbrid Voxelized/ANalytical*) qui permet de combiner de façon générique et optimale des objets analytiques à l'intérieur d'un objet voxelisé à des fins d'applications médicales Bert et al. (2013b, 2016b), voir l'article complet en Annexe B.5. Comme c'est une primitive, un nouveau type d'objet, les méthodes de transport des particules n'ont pas besoin d'être modifiées ni dupliquées comme dans le LMG. La méthode est donc facilement utilisable dans n'importe quel code de SMC, en plus de GGEMS, elle a été notamment implémentée dans GATE. Cette primitive YVAN peut être considérée comme une géométrie polymorphique où le navigateur qui transporte la particule traverse différents types de géométrie (analytique ou voxelisé) en fonction des situations.

Afin d'évaluer et de valider cette proposition, un fantôme analytique simple constitué d'un bac d'eau, d'une sphère d'air et d'une paroi en os a été simulé avec GATE en utilisant une source

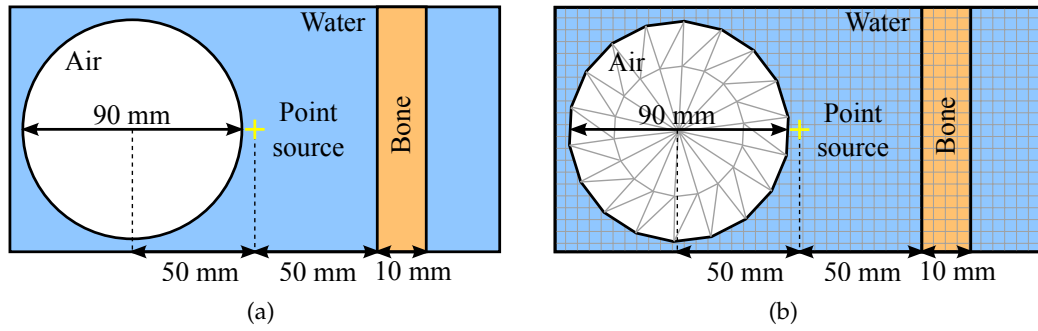


**Figure 15** – Configuration des fantômes de simulation utilisés pour l'évaluation de la méthode proposée YVAN avec (a) que des objets analytiques et (b) des objets voxélisés et maillés.

ponctuelle de photons au centre du fantôme (voir Fig. 15-a). Ce fantôme a été ensuite digitalisé, la sphère d'air est devenue un maillage triangulaire sphérique, le bac d'eau et la paroi d'os, des volumes voxélisés (Fig. 15-b). Ce fantôme digital a été simulé en utilisant la méthode du LMG et notre méthode YVAN. Différents paramètres, notamment d'échantillonnages de la sphère maillée ont été utilisés afin d'étudier l'impact sur les résultats.

La distribution des particules sortant du fantôme numérique entre YVAN et l'approche LMG est identique avec une erreur relative moyenne de 0,28 % (Fig. 16-a). La différence majeure est que la navigation optimisée avec YVAN permet une simulation  $\times 2$  plus rapide que la méthode LMG. La finesse de l'échantillonnage de la sphère d'air peut apporter un biais de simulation. En effet, plus la sphère est constituée de triangles et plus la forme géométrique de la sphère va se rapprocher de celle analytique. C'est ce qui est illustré sur la (Fig. 16-b), où YVAN, avec une sphère composée de 16 128 triangles est identique en terme de simulation à une sphère analytique simulée avec GATE, ce qui n'est pas le cas pour un maillage de 224 triangles. Il faut donc être attentif à l'échantillonnage de chaque volume pour éviter tout biais de simulation. A noter que la simulation avec YVAN utilisant une sphère de 16 128 triangles n'est que 4,3% plus longue que celle utilisant une sphère constituée de 224 triangles. Un travail préliminaire est en cours pour trouver des solutions au problème de définition des maillages triangulaires. Ce type de géométrie est souvent utilisé pour modéliser des formes complexes continues (organes, implants, etc), mais avec la numérisation, il est difficile de garder leur forme originale sans augmenter considérablement le nombre de triangles. Ce travail

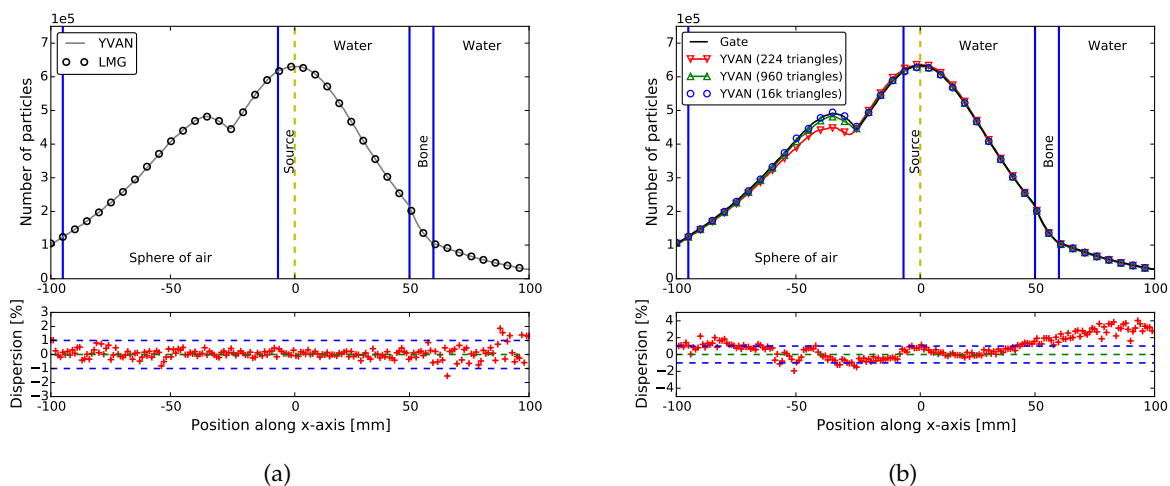


**Figure 16** – Distribution de la position des photons le long de l'axe x obtenue par SMC en utilisant (a) une simulation LMG avec la primitive YVAN et (b) une simulation GATE avec une géométrie analytique et une simulation avec YVAN en utilisant une géométrie numérique avec différents échantillonnages pour le maillage de la sphère.



préliminaire utilise des méthodes d'interpolation basées sur les vecteurs normaux des faces pour simuler une surface continue sans augmenter le nombre de triangles (Fig. 17 Bert and Visvikis, 2018).

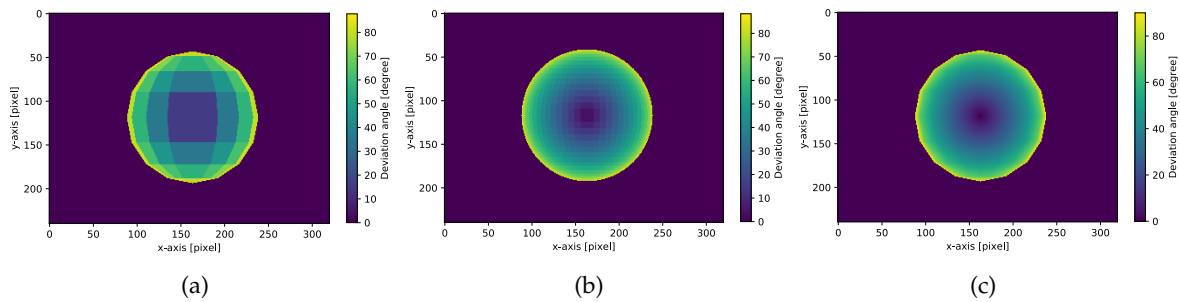


**Figure 17** – Carte de l'angle de réflexion d'un faisceau parallèle de photons optiques sur une sphère réfléchissante utilisant un maillage triangulaire composé de (a) 224 triangles, et (b) 3968 triangles, et (c) 224 triangles avec notre méthode d'interpolation de surface.

La méthode YVAN que nous avons proposée ouvre de nouvelles perspectives de simulation et d'étude. Par exemple, elle a été utilisée dans une application clinique en radiothérapie peropératoire pour le cancer du sein avec le système IntraBeam<sup>TM</sup>. Ce système consiste à traiter par une source de rayons X de faible énergie le lit tumoral après l'exérèse d'une tumeur cancéreuse. YVAN nous a permis dans ce contexte d'étudier par simulation l'utilisation de bouclier de protection interne (objet analytique en forme de cupule) dans le lit tumoral (patiente voxélisée). Comme pour la curiethérapie, l'objectif a été de mesurer la diminution de la dose aux organes à risque par le biais de cette protection (Fig. 18). Les résultats, dans le contexte d'une thèse, ont été publiés dans Bouzid et al. (2015).

L'image TDM du patient est un élément clé pour la SMC car elle permet une personnalisation de la simulation en utilisant les différentes densités électroniques des tissus. Dans la simulation, cette image composée de valeurs d'atténuation en unité Hounsfield est labélisée en différents matériaux (os, foie, prostate, poumon, etc.). Le volume voxélisé est en quelque sorte un ensemble de boîtes analytiques (voxel) constituées de matériaux homogènes. L'inconvénient provient de la navigation où chaque particule doit traverser tous les voxels, impliquant de tester la frontière entre chaque voxel et d'effectuer des mises à jour physiques pour considérer le matériau traversé. En fonction du nombre de voxels et de l'application, la navigation dans un volume voxélisé est responsable d'une proportion non négligeable du temps total de la simulation.

Toujours dans un objectif d'améliorer la SMC dans un contexte médical, nous avons travaillé dans le cadre d'un post doctorat (A. Behloui) sur l'optimisation du transport des particules dans les volumes voxélisés (le patient). Dans la littérature, il existe différentes stratégies, mais une méthode

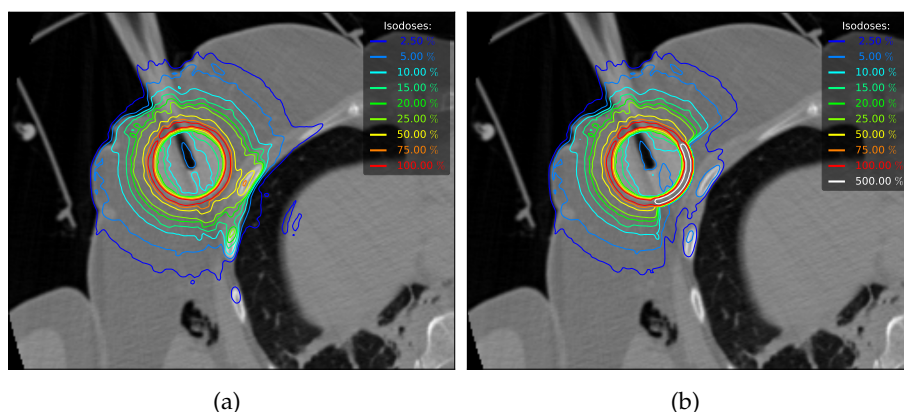


**Figure 18** – TDM d'une patiente traitée par radiothérapie peropératoire avec en surimpression les isodoses données en pourcentage de la dose de prescription obtenue par SMC utilisant (a) un fantôme voxélisé sans blindage de protection et (b) avec la protection modélisée par un maillage tétraédrique avec YVAN.

de réduction de variance fait office de référence : c'est la méthode appelée Woodcock (Woodcock et al., 1965) (ou *delta tracking* ou *fictitious method*). Cette méthode sans biais supprime tous les tests nécessaires aux frontières des voxels, améliorant la rapidité de la navigation. Le transport de la particule suit un échantillonnage aléatoire dirigé par le matériau le plus atténuant dans le volume. A chaque déplacement de la particule, une méthode de réjection utilisant le matériau courant traversé par la particule et le matériau le plus atténuant permet de déterminer si une interaction a lieu.

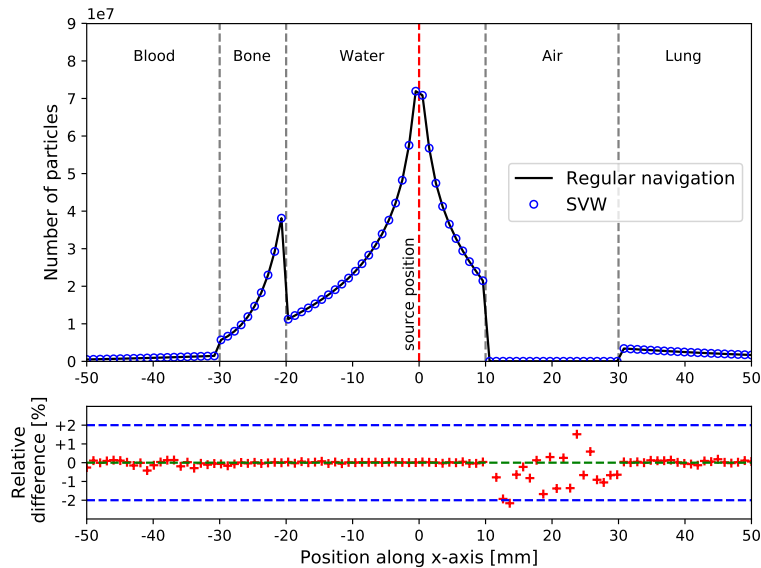


**Figure 19** – Distribution de la position des photons le long de l'axe x obtenue par une simulation GGEMS utilisant une méthode de navigation standard et le Super-Voxel Woodcock.

Cependant, l'échantillonnage des rejections est directement lié au matériau le plus atténuant dans le patient. Dans un contexte médical où implants métalliques et structures osseuses sont présents dans des tissus beaucoup moins denses, le gain d'amélioration du Woodcock en terme de vitesse de calcul sera limité. Le transport des particules sera sur-échantillonné même si elles traversent des zones de faible densité. Pour résoudre ce problème, nous avons proposé une amélioration du Woodcock en utilisant le concept de Super-Voxel (SV), concept utilisé dans le domaine du rendu d'images de synthèse. Cela consiste à regrouper virtuellement certaines caractéristiques entre les voxels sans pour autant les fusionner. Le Super-Voxel, de même forme que le voxel, stocke des métadonnées qui caractérisent les voxels contenus dans celui-ci. La métadonnée qui caractérisera le SV sera pour nous la valeur locale du matériau le plus atténuant trouvé dans les voxels contenus par ce SV. C'est équivalent à avoir un Woodcock indépendant dans chaque SV qui utilisera la valeur locale du matériau le plus atténuant. Le but est d'adapter l'échantillonnage de la navigation de la particule en fonction des différentes zones du volume via les SV, et donc d'améliorer globalement la navigation. Le Super-Voxel Woodcock (SVW) ne supprime pas le problème du sur-échantillonnage du transport de la particule, il ne fait que le contenir au niveau du SV. Dans un premier temps le Super-Voxel Woodcock a été validé et évalué dans GGEMS avec un fantôme voxelisé constitué de différentes couches de matériaux (sang, os, eau, air et poumon), avec une source ponctuelle de photons en son centre. Différents paramètres ont été utilisés, comme par exemple la taille du Super-Voxel exprimé en voxels. Deux simulations, l'une avec la navigation voxelisée standard et l'autre avec le SVW ont été réalisées. Les résultats en Fig. 19 montrent des résultats identiques entre une navigation standard et la méthode proposée. Le SVW tout comme le Woodcock n'apportent pas de biais dans la simulation. Dans cet exemple la taille du SV utilisé était de  $30 \times 30 \times 30$  voxels.

Deux applications médicales ont été utilisées pour évaluer le SVW. La première est une simulation en imagerie avec la radiographie du thorax et de la tête d'un patient et la deuxième en dosimétrie pour la curiethérapie de la prostate. Pour chaque simulation GGEMS, la navigation standard, la méthode Woodcock et le SVW ont été utilisés. Plusieurs dimensions de SV ont été testées afin de trouver la valeur optimale, c'est-à-dire là où la simulation est la plus rapide. Dans le cas de la

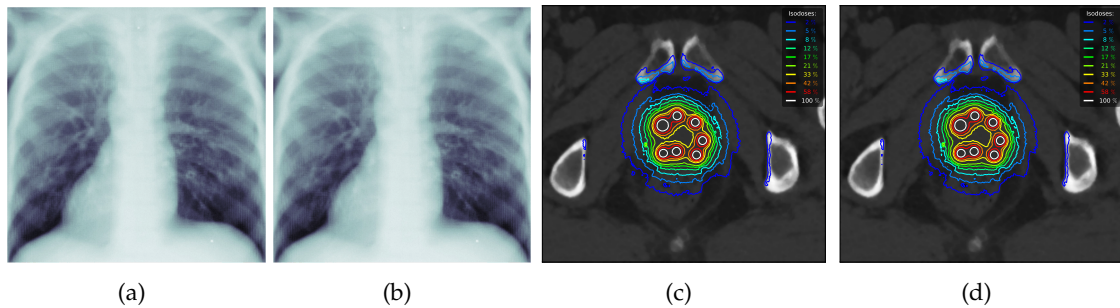


**Figure 20** – SMC d’une radiographie du thorax avec (a) la navigation standard et (b) le Super-Voxel Woodcock (SVW); les isodoses obtenues par SMC d’un traitement par curiethérapie de la prostate entre le (c) navigateur standard et (d) le SVW.

simulation en imagerie, la taille de SV optimale était de  $20 \times 20 \times 20$  voxels et celle en dosimétrie de  $25 \times 25 \times 25$  voxels. Les résultats montrent que la méthode Woodcock et le SVW sont complètement équivalents et non biaisées par rapport à une navigation standard voxélisée (Fig. 20). Concernant l’application en imagerie du thorax, le Woodcock a été  $\times 2,46$  fois plus rapide que la navigation standard et le SVW  $\times 7,75$  plus rapide. Lorsqu’on compare les mêmes résultats pour l’image de la tête avec des implants dentaire, le Woodcock n’est que  $\times 1,57$  fois plus rapide que la navigation standard alors que le SVW reste autour d’un facteur de  $\times 7,1$ . Dans le cas de la dosimétrie, le facteur d’accélération comparé à la navigation standard n’est que de  $\times 1,3$  pour le Woodcock et de  $\times 5,6$  pour notre méthode SVW. Quelle que soit l’application médicale, notre proposition d’amélioration de Woodcock permet d’augmenter son efficacité. L’ensemble de nos résultats sont en cours de publication [Behlouli et al. \(2017\)](#).

#### 5.3.4 Modélisation des systèmes de traitement

Si améliorer la vitesse de la SMC est capital pour son exploitation dans un contexte clinique, la modélisation des éléments de la simulation (effets physiques, source de particules, système mécanique, patient, etc.) est la pierre angulaire pour garantir une exactitude des résultats. En SMC, on a pour habitude de dire qu’il ne faut pas faire confiance à sa simulation. En effet, quelles que soient les données d’entrée définies par l’utilisateur, même si elles sont erronées, la simulation donnera toujours un résultat quel qu’il soit. Toute la difficulté est de définir le niveau de précision à atteindre pour que les résultats soient valides par rapport à une application donnée. Pour cela le seul moyen consiste à faire une modélisation simple, puis de simuler et de confronter les résultats avec des données expérimentales. Si la précision n’est pas suffisante, on complexifie alors le modèle et on recommence jusqu’à satisfaction.

Dans ce contexte, nous avons travaillé sur la modélisation et la validation de systèmes de traitement d’irradiation utilisés dans nos études de SMC en radiothérapie. Le premier système est celui de l’IntraBeam<sup>TM</sup> (voir section précédente). Ce système peropératoire est utilisé au CHRU de Brest pour le cancer du sein en remplacement des sessions traditionnelles de radiothérapie externe. L’objectif des travaux autour de ce système, dans le cadre de la thèse de D. Bouzid, a été d’optimiser et de personnaliser la planification dosimétrique pré/peropératoire en utilisant la SMC. Pour cela, un modèle valide du système pour la SMC a dû être établi. Le système de traitement, qui comprend les parties mécaniques, la source de rayons X et la géométrie des applicateurs a été modélisé dans GATE le plus fidèlement possible par rapport aux données techniques du constructeur. Les résultats de simulation dans un contexte simple (bac d’eau) ont été confrontés aux mesures expérimentales. Cette étape n’est pas simple étant donné l’ensemble des incertitudes à prendre en compte en terme de modèle, mais également sur les mesures expérimentales obtenues. Ces résultats ainsi que l’étude des incertitudes (modèle et mesure) montrent un accord très suffisant pour une utilisation clinique, ([Bouzid et al., 2013, 2015](#), voir Annexe B.6). Pour évaluer ce modèle dans un contexte clinique *in vivo*, une acquisition TDM d’une patiente pendant l’intervention a été nécessaire. Un protocole de



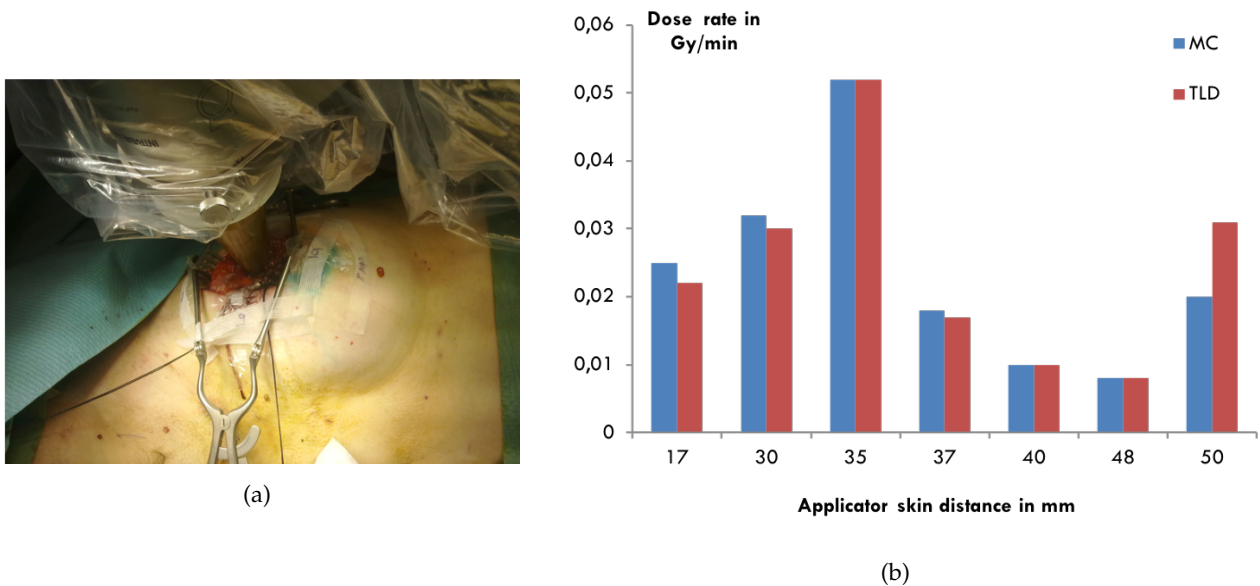


**Figure 21** – (a) Placement des TLD sur la peau avant l'irradiation. (b) Comparaison entre des débits de dose obtenus par les données expérimentales des TLD placés à différentes distances de l'applicateur d'irradiation et ceux obtenus par simulation Monte-Carlo (MC).

calibrage et de validation a été mis en place pour utiliser des dosimètres à thermoluminescence (TLD) sur la peau de la patiente autour de l'applicateur d'irradiation (Fig. 21-a). Ces données cliniques ont été confrontées à nos résultats *in silico* par SMC (Fig. 21-b). Un travail sur le calcul de la dose absolue par simulation et l'estimation de l'incertitude associée a été nécessaire pour montrer une cohérence entre valeurs cliniques et simulées avec une erreur de dose autour de 6%.

Le même type de modélisation et de validation a été réalisé pour différents systèmes de radiothérapie externe, notamment ceux que nous utilisons pour nos travaux au CHRU de Brest. La modélisation d'un accélérateur linéaire est assez délicat compte tenu des nombreux éléments qui le composent et de leurs formes complexes. Par exemple, nous avons modélisé l'accélérateur TrueBeam Novalis STX (Varian) utilisé par le LaTIM et le CHRU de Brest, où le collimateur multi-lames compte pas moins de six types de lames différentes. Chacune d'entre elles a été modélisée avec précision par un maillage triangulaire réalisé avec l'aide des données du constructeur (Fig. 22-a).

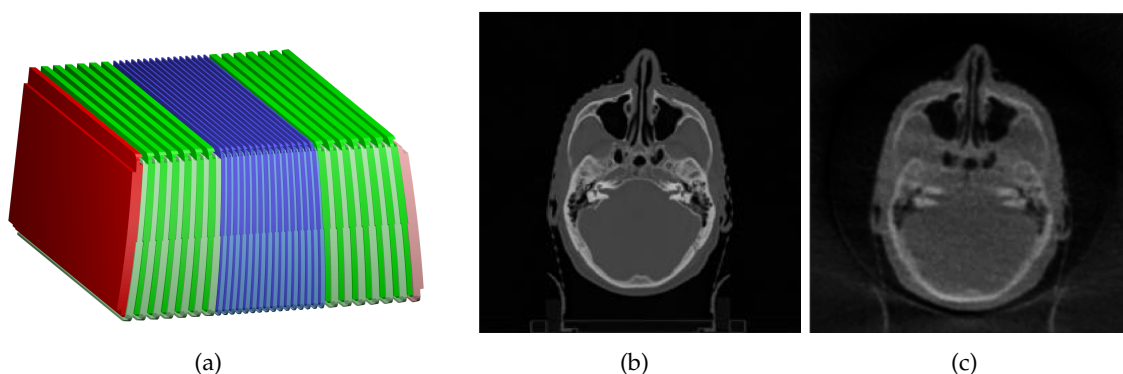


**Figure 22** – (a) Maillages 3D dans GGEMS des lames d'une banque du collimateur multi-lames (MLC) du TrueBeam Novalis (Varian). Le MLC est composé d'un total de 120 lames avec six types de lames différentes (couleurs différentes sur l'image). Coupe de la reconstruction 3D de la tête d'un patient en utilisant le mode MV-CBCT du système de radiothérapie externe avec les acquisitions obtenues par (b) le vrai système et (c) la simulation Monte-Carlo.

La même stratégie a été adoptée pour les mâchoires de collimation. Après chaque modélisation, une étape de validation est nécessaire avec des données expérimentales provenant de la machine. Il en va de même pour la source du faisceau. Le système d'imagerie embarqué EPID (*electronic portal imaging device*) a également été modélisé avec précision. Ce système permet d'obtenir des images standard (kV), mais également des images en utilisant le faisceau de traitement comme source (MV). Nous avons validé les différents modes d'acquisition pour que nos SMC soient réalistes par rapport aux machines utilisées en clinique (Fig. 22-b,c). Nos résultats ont été publiés dans [Benhalouche et al. \(2017\)](#), article en Annexe B.7.

Le même type de travail a été réalisé pour valider la géométrie et l'émission des sources radioactives utilisées en curiethérapie de la prostate. Les données expérimentales pour la source utilisée, notamment les fonctions de dose radiale et anisotropique, sont facilement accessibles sur internet et nous ont simplifié la validation sans devoir recourir à l'expérimentation. Les résultats sont accessibles dans [Lemarechal et al. \(2015\)](#).

### 5.3.5 Modélisation du patient

Le patient, tout comme le système de traitement, est une partie centrale de la simulation. Si aujourd'hui en SMC l'utilisation d'images TDM est courante pour modéliser le patient en fantôme numérique, certaines de ses caractéristiques restent non modélisées, notamment les aspects dynamiques et non stationnaires (mouvements, changements anatomiques, etc.). On suppose que le jour du traitement, le patient est parfaitement identique à sa TDM de planification, ce qui est très loin de la vérité et le devient encore plus tout au long du traitement. Une solution serait d'introduire une étape re-planification pour tenir compte des changements anatomiques, et cela à différents moments clés du traitement.

Nous nous sommes intéressés à cette problématique dans le contexte de la curiethérapie de la prostate, problème qui a été mis en évidence avec nos précédents travaux. Au cours du traitement, un œdème au niveau de la prostate se crée, qui est principalement dû à l'insertion des aiguilles pendant l'intervention chirurgicale et à l'irradiation issue des grains. Le volume maximal de la prostate est atteint le lendemain de l'opération et se réduit lentement jusqu'à retrouver sa taille normale au bout d'un mois. La curiethérapie n'est pas à proprement parler une radiothérapie peropératoire, car elle est initiée au bloc opératoire, mais le traitement sera délivré pendant plusieurs jours après l'intervention. En curiethérapie bas débit de la prostate, l'Iode 125 est utilisé et a une demi vie de 59,4 jours. Cela signifie que pendant toute la durée du traitement, la prostate va continuellement changer de volume.

Ce changement anatomique n'est pas pris en compte dans la planification au moment de

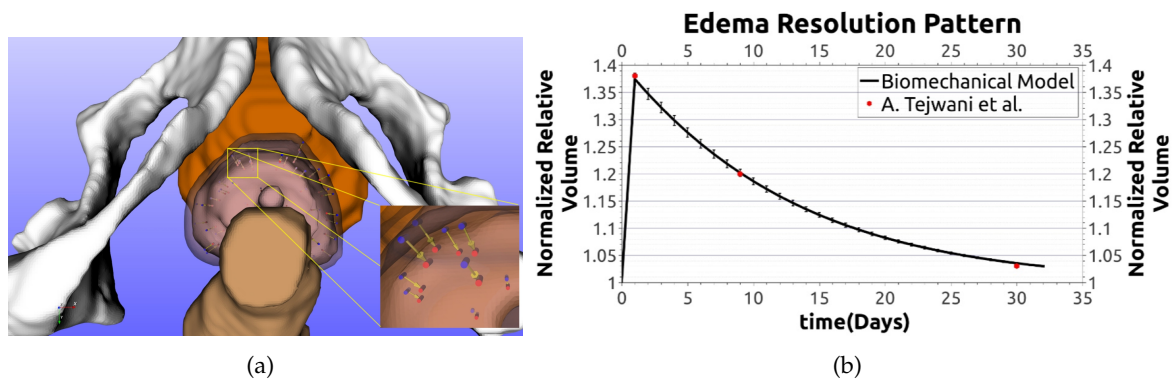


**Figure 23** – (a) Visualisation 3D du modèle de la prostate avec le changement de volume et le déplacement des grains provoqué par l'œdème. (b) Moyenne du changement du volume de la prostate pour 15 patients prédit par le modèle biomécanique de l'œdème de la prostate. Les barres d'erreur correspondent à l'écart-type de la valeur en considérant les 15 patients. Les points rouges à jour 1, 9 et 30 jours correspondent à la moyenne du volume de la prostate mesurée dans [Tejwani et al. \(2012\)](#).

l'intervention. On considère que la prostate aura le même volume tout au long du traitement, induisant naturellement des biais dosimétriques. Dans le cadre d'un travail de thèse (K. Mountris), nous avons proposé de considérer l'œdème de la prostate dans le calcul de dose. Comme il n'est pas possible de suivre l'évolution du volume de la glande pendant le traitement, ni même de changer le traitement en cours, nous avons fait le choix de proposer un modèle prédictif, qui permet de déterminer le changement du volume dans le temps. Nous avons modélisé l'œdème en développant un modèle biomécanique 3D bi-phasique par éléments finis (Fig. 23-a). Ce modèle est basé sur la théorie de la poroélasticité, c'est-à-dire la théorie élastique du comportement mécanique des matériaux poreux. L'œdème est principalement un problème de fluide apporté pendant le traumatisme des aiguilles/grains et qui se résorbe dans le temps. La prostate se comporte un peu comme une éponge. Le modèle proposé permet de bien retrouver le comportement de l'œdème et a notamment été validé avec des données issues de la littérature (Fig. 23-b). Dans le but de conforter ces résultats, notamment avec plus de valeurs temporelles, j'ai mis en place une étude clinique avec le CHRU de Brest. Nous allons récolter les images IRM de 25 patients à différents jours de leur traitement (jour 0, 1, 15 et 30) que nous pourrons comparer avec la prédiction de notre modèle. Chaque modèle sera également personnalisé via les données d'élastographie obtenues par échographie de chaque patient.

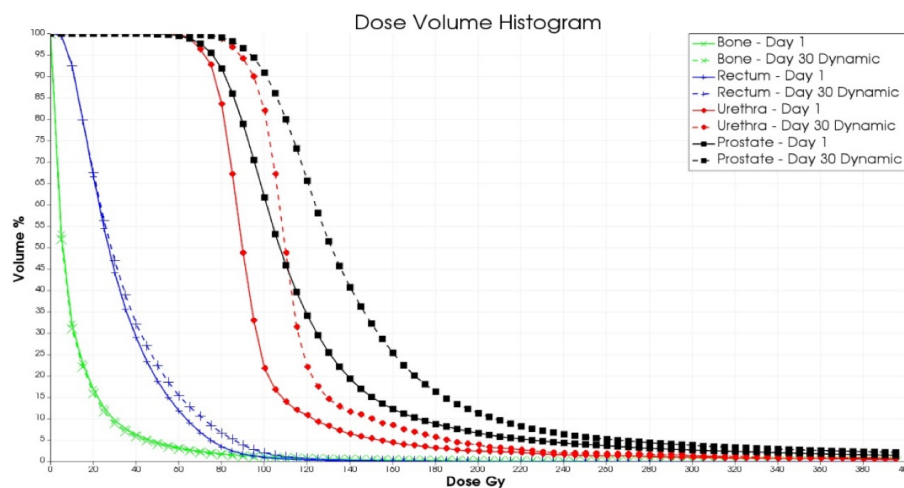


**Figure 24** – Comparaison des histogrammes dose-volume de la prostate et des organes à risque pour un patient représentatif entre une dosimétrie simulée le jour du traitement et après 30 jours en considérant le déplacement des grains lié à l'œdème de la prostate.

Nous avons aussi étudié comment les paramètres du modèle affectaient l'évolution de l'œdème, comme par exemple la valeur d'élasticité des tissus, le volume de départ, le nombre d'aiguilles, etc. L'impact dosimétrique a également été étudié en utilisant des données TDM (préopératoire et post-opératoire après 30 jours) de 15 patients qui ont été traités par curiethérapie. Une dosimétrie dynamique qui prend en compte le déplacement des grains et un ré-échantillonnage des TDM avec différents scénarios de l'œdème a été développée et simulée avec GGEMS (Fig. 24).

Les résultats pour un patient représentatif montrent que la réduction de l'œdème pendant le traitement est à l'origine d'une élévation des paramètres dosimétriques à la fois dans la prostate ( $D_{90} 22,0 \pm 1,9\%$ ), mais également dans les organes à risque (urètre  $D_{10} 19,2 \pm 2,1\%$  et rectum  $D_{2cc} 9,3 \pm 2,5\%$ ). Ceci s'explique par le fait que les sources se rapprochent du centre de la prostate lorsque l'œdème se réduit. Par conséquent, la prise en compte de l'œdème dans la planification du traitement permettrait de réduire la toxicité et donc les effets secondaires. Le modèle proposé pourrait être utilisé pour ajuster le plan de traitement en adaptant les positions des grains afin de compenser la réduction du volume prostatique lié à l'œdème. L'ensemble des résultats a été publié dans [Mountris et al. \(2017c\)](#), l'article complet se trouve en Annexe [B.8](#).

Prendre en considération le changement anatomique dans la planification en radiothérapie est essentiellement un problème d'imagerie. C'est par l'image que l'on est capable de mettre à jour le

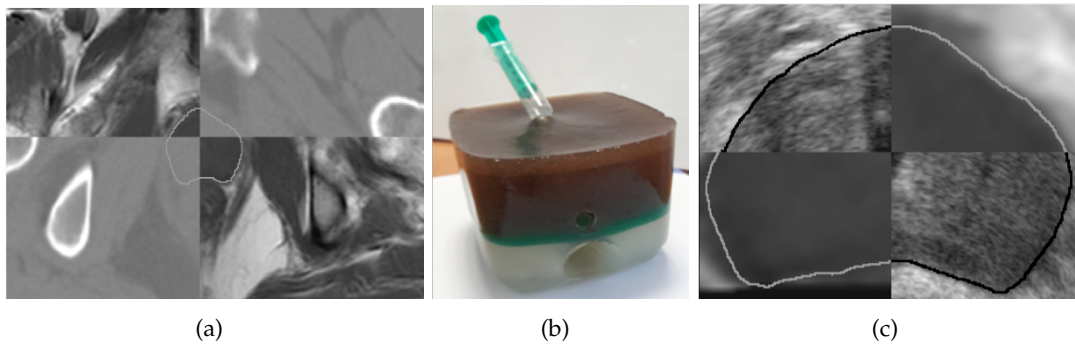


**Figure 25** – (a) Mosaïque de l'image IRM et TDM de la prostate avec son contour après notre méthode de recalage automatique non-rigide. (b) Fantôme fait maison en PVC du pelvis, incluant prostate, urètre et rectum. (c) Mosaïque de l'image IRM et US de la prostate avec son contour après notre méthode de recalage automatique non-rigide.

modèle qui représente le patient. La SMC pour la curiethérapie nécessite une image TDM du pelvis du patient qui est obtenue en plus du protocole de soins standard. La seule image disponible le jour de l'intervention est l'image échographique. Par conséquent, pour utiliser la SMC en routine clinique il faut absolument adapter l'image TDM préopératoire à l'image par ultrasons (US) peropératoire le jour du traitement. Ce n'est plus un problème de simulation ou de modélisation, mais un problème de recalage d'images multimodales. Nous avons travaillé sur cet aspect dans le cadre de la thèse de I. Hamdan. L'objectif était de mettre à jour les images préopératoires (TDM et IRM) en fonction de la forme réelle de la prostate le jour de l'intervention obtenue par l'image échographique. Un point particulier a été mis en avant : celui de proposer des solutions de recalage élastique entièrement automatisé sans aucune intervention du clinicien. Nous avons proposé une première méthode de recalage élastique automatique TDM/IRM basée sur l'information mutuelle, puis une deuxième méthode IRM/US basée sur un critère calculé en utilisant une corrélation et une combinaison des gradients des images. Ces deux méthodes permettent d'exprimer TDM, IRM et US dans un même référentiel où la forme et le volume prostatique sont les mêmes dans chaque modalité. La première méthode TDM/IRM a été validée avec un jeu de données de 8 patients et le contourage de la prostate par deux experts (Fig. 25-a). Nous avons montré que la solution proposée permet un recalage avec une erreur maximum de 2 mm, ce qui est suffisant pour l'application clinique ciblée. Concernant la solution de recalage IRM/US, nous avons validé dans un premier temps la méthode en utilisant des fantômes faits maison de la prostate (Fig. 25-b). Une étude est en cours pour valider la méthode sur des données cliniques (Fig. 25-c). Les premiers résultats montrent une erreur de recalage maximal de 2 mm, mais doivent être confirmés avec plus de données cliniques. Les travaux sur le recalage TDM/IRM ont été publiés dans (Hamdan et al., 2017, voir Annexe B.9), ceux en IRM/US sont en cours de validation.

#### 5.4 Travaux en cours et futurs

Cette section est consacrée aux travaux en cours et à venir à l'horizon de quatre ans et au-delà. Si l'axe de recherche autour de l'amélioration et du développement de nouveaux outils pour la SMC dans un contexte médical reste bien présent, deux ouvertures thématiques ont été entreprises.

D'après nos travaux précédents, l'amélioration et la proposition de nouveaux outils de simulation ne sont pas suffisants pour utiliser la SMC dans un contexte clinique. Si la SMC est un élément important pour optimiser le traitement en radiothérapie, elle n'est en réalité qu'une pièce d'un puzzle bien plus complet et complexe. Par exemple, la modélisation du patient afin d'obtenir une simulation personnalisée nécessite de s'intéresser aussi à l'imagerie médicale multimodale et à tous les problèmes inhérents à cela (segmentation, recalage, acquisition, etc.). De même, la planification nécessite de mettre en place des méthodes d'optimisation car la SMC permet uniquement d'estimer une fonction de coût. Nous pouvons également nous poser la question de l'intérêt d'estimer un plan



de traitement le plus optimal et précis possible si le système de traitement n'est pas capable de le restituer avec véricité.

Pour résumer, vouloir optimiser le traitement en radiothérapie par l'utilisation de la SMC nécessite globalement d'améliorer toute la chaîne de la boucle *sensori motrice*. C'est ce que j'ai entrepris autour de deux applications médicales. Si elles ont pour base la SMC, des méthodologies aux thématiques différentes seront proposées pour compléter le puzzle par les pièces manquantes afin d'améliorer les applications cliniques visées.

Compte tenu de nos précédentes collaborations avec le CHRU de Brest et de nos différents travaux sur le sujet, la thématique autour de la curiethérapie de la prostate assistée par ordinateur s'est naturellement imposée. Ces travaux en cours ont bénéficié d'un financement provenant de plusieurs projets que je coordonne, dont les deux principaux sont financés d'une part par le LabEx CAMI (*Computer Assisted Medical Intervention*) — projet CAPRI (*Computer Assisted Prostate brachytherapy Intervention*) et d'autre part par l'ANR — projet FOCUS (*Innovative planning and guidance system for focal prostate brachytherapy*). Ce dernier est une collaboration entre la société Koelis, le CHRU de Brest, le CHU Grenoble Alpes et le laboratoire TIMC de Grenoble. Un aperçu des travaux en cours et futurs sera présenté dans les sections suivantes.

La deuxième application clinique est une ouverture thématique qui résulte d'une collaboration dans l'encadrement de thèse de N. Loy Rodas effectué au laboratoire ICube de Strasbourg. Le sujet est l'optimisation de la dose d'irradiation pendant les procédures chirurgicales guidées par l'imagerie de rayons X. Cette optimisation cible aussi bien le patient sous le faisceau que les cliniciens autour du système. Ce sujet est assez proche de nos travaux précédents, à savoir obtenir une simulation Monte-Carlo rapide, personnalisée au patient, mais aussi à la configuration de la salle opératoire. Dans ce contexte, je coordonne un projet ANR OptimiX (*Radiation dose optimization for X-ray guided procedures*) récemment acquis avec pour partenaire le CHRU de Brest, l'IHU de Strasbourg et le laboratoire ICube de Strasbourg. Un aperçu des travaux prévus dans le projet sera exposé dans les sections suivantes.

#### 5.4.1 Curieothérapie de la prostate assistée par ordinateur

La procédure de planification et d'intervention de la curiethérapie de la prostate n'a pas vraiment évolué depuis les années 80. Notre objectif est de mettre à jour la procédure en utilisant les moyens modernes en termes de technologie et de méthodologie. Comme vu précédemment, nous avons déjà travaillé sur le sujet. Nous avons amélioré la simulation Monte-Carlo pour qu'elle soit plus rapide, mais aussi plus précise en considérant le changement anatomique de l'œdème de la prostate. Maintenant, nous nous intéressons à la scène globale du traitement, avec pour objectif final de diminuer la toxicité du traitement (effets secondaires), notamment par l'introduction de la thérapie focale. Pour cela, la précision et la maîtrise du traitement doivent être améliorées afin de ne traiter qu'une partie de la prostate, là où la tumeur est présente. Un ensemble d'innovations a été défini pour constituer le nouveau protocole de la curiethérapie 2.0 de la prostate où chaque élément présenté à la Fig. 26 répond à un défi particulier.

Le premier point innovant est l'utilisation de l'imagerie multimodale dans le protocole. La TDM sera utilisée pour la SMC, l'IRM et la TEP pour identifier la cible tumorale, et l'US (b-mode et élastographie) pour le suivi, l'identification et la personnalisation du traitement en peropératoire. Ces images seront recalées et segmentées automatiquement afin d'obtenir le contourage des organes. La détection automatique des grains dans l'image US permettra de re-planifier le plan de traitement à la volée pendant l'intervention pour compenser toutes erreurs de positionnement des grains par rapport au plan de départ. Nous envisageons d'utiliser un système de planification de traitement basé sur la SMC avec la prise en compte de l'œdème de la prostate. Un autre élément innovant de cette nouvelle procédure est la mise en place du traitement. Contrairement à un guidage manuel par image échographique, nous voulons utiliser un système robotique par retour d'effort. Le but est d'aider le geste du chirurgien pour atteindre de façon précise la position d'implantation des grains telle que définie dans le plan de traitement. Le suivi visuel pourra se faire également sur

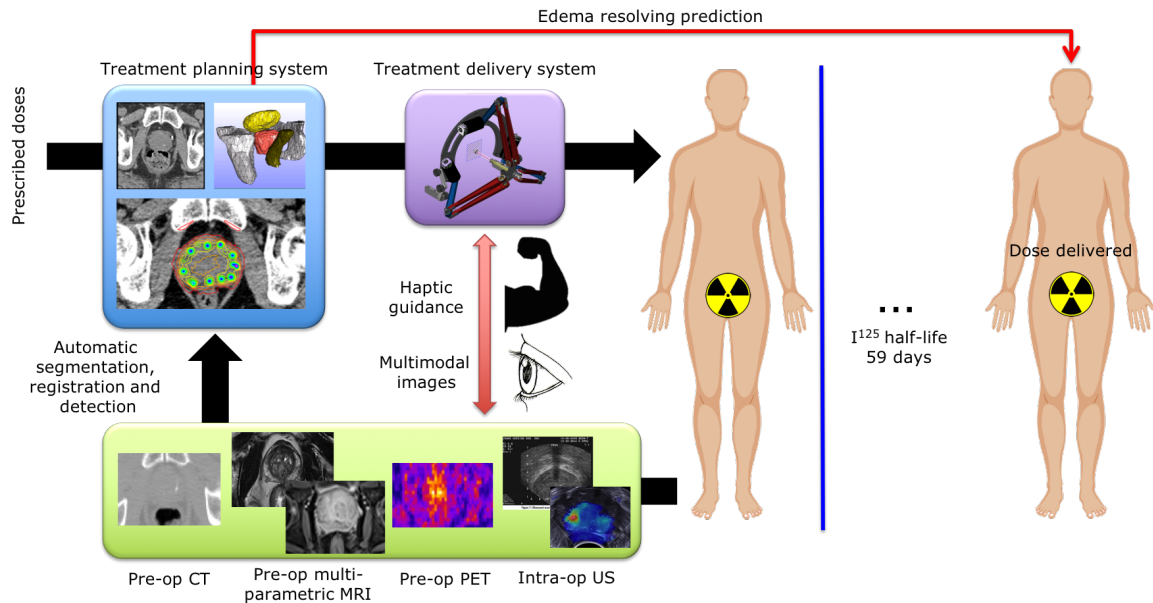


**Figure 26** – Vision de la procédure proposée pour la curiethérapie de la prostate assistée par ordinateur.

l'image échographique avec la visualisation de la trajectoire de l'aiguille, mais aussi des informations anatomiques issues de l'IRM comme par exemple le site tumoral. Cette procédure s'effectuera en boucle fermée permettant à tout moment de demander une re-planification en cours d'intervention pour garantir un contrôle optimal du traitement. Les sections suivantes présentent les travaux qui sont en cours et prévus à plus long terme sur cette thématique.

### Imagerie multimodale

Les images US sont faiblement contrastées et contiennent un important niveau de bruit. Cette modalité d'imagerie n'est pas la plus idéale, mais c'est la seule qui permet une supervision de la prostate en temps réel sans irradier le patient. Un autre inconvénient est que la sonde n'est pas à balayage 3D. Elle est déplacée dans le rectum de façon linéaire par un système appelé *stepper* de telle façon à acquérir les différentes coupes 2D de la prostate et de reconstituer un volume 3D. En plus d'être encombrant, le *stepper* nécessite un temps d'acquisition important et peu répétable. Conséquence de cela, il est difficile d'obtenir plusieurs volumes US 3D de la prostate pendant l'intervention. Cela limite un certain nombre d'options en termes de supervision et de contrôle. Pour palier cette limitation, notre partenaire industriel Koelis dans le cadre de notre projet ANR a développé avec Vermon, constructeur de sonde échographique, une nouvelle sonde endorectale 3D à balayage latéral (Fig. 27).

Cette sonde permet en une seconde d'acquérir le volume total de la prostate, ouvrant ainsi de nouvelles perspectives en terme de protocole. Après l'acquisition d'une telle sonde au LaTIM et sur la plateforme associée par le CHRU de Brest, nous envisageons de tester ces bénéfices cliniques et méthodologiques en termes d'imageries, d'algorithmes et de supervisions dans un futur proche.

Après les travaux sur le recalage de l'image de la prostate TDM/IRM/US, nous nous sommes orientés vers le traitement des images US, notamment dans le cadre des travaux d'un post doctorat (V. Jaouen). L'objectif est de préparer ces images pour aider les futurs traitements tels que la segmentation. Une nouvelle méthode d'amélioration des images a notamment été développée permettant à la fois de filtrer les images mais aussi de renforcer leurs contours. Cette méthode est très rapide, ce qui permettra par la suite de l'utiliser dans un *workflow* clinique sans problème. Les améliorations ont été testées et comparées avec les méthodes de l'état de l'art sur un jeu de données cliniques de 14 patients (Fig. 28-a,b). La description de ces travaux est en cours de révision dans *IEEE Transactions Image Processing*. Ensuite, une méthode de segmentation quasi automatique de la prostate a été développée (Fig. 28-c). Cette méthode s'appuie sur des approches de surface active hybride en



**Figure 27** – (a) Sonde endocavitaire latérale 2D avec son *stepper* permettant l’acquisition du volume prostatique en plusieurs coupes. (b) Sonde endocavitaire 3D à balayage latéral de Koelis ([koelis.com](http://koelis.com)) développée dans le cadre du projet ANR FOCUS.

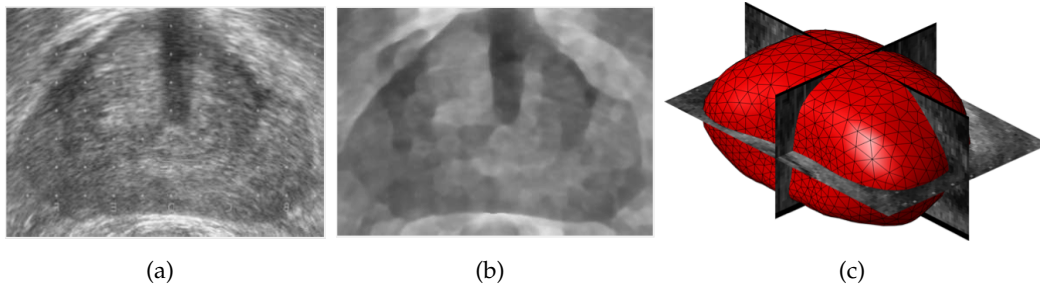


**Figure 28** – Coupe centrale de la prostate d’un patient (a) de l’image US originale et (b) après filtrage par la méthode proposée. (c) Maillage de la segmentation 3D de la prostate par la méthode proposée.

utilisant les contours pour la précision et les régions pour la robustesse. L’évaluation a été réalisée en utilisant comme référence la segmentation manuelle de deux experts cliniciens des images US 3D de la prostate de 36 patients. Les résultats montrent que les métriques quantitatives de la qualité de la segmentation sont identiques à celles des cliniciens. C’est-à-dire que notre méthode propose des résultats similaires à une segmentation manuelle 3D avec pour avantage de nécessiter seulement la sélection de l’image délimitant la base et l’apex de la prostate. Les travaux préliminaires ont été publiés dans [Jaouen et al. \(2017\)](#) et les résultats complets sont en cours de révision dans *IEEE Transactions on Biomedical Engineering*.

Sur les aspects de traitement des images US, un travail a débuté pour détecter de façon automatique la position des grains qui sont déjà implantés dans la prostate. Cette tâche, très difficile à cause des artefacts provoqués par les grains, doit permettre de déterminer si les positions des sources radioactives sont correctes par rapport au plan de traitement. Une première méthode a été proposée et nous sommes en cours d’évaluation.

### Système de planification du traitement

Le système de planification de traitement (TPS) est responsable d’optimiser itérativement le plan de traitement en utilisant le calcul de la dose comme fonction de coût. Dans nos travaux, l’estimateur de dose sera assuré par la SMC rapide obtenue par GGEMS. La majorité des TPS cliniques utilisent le recuit simulé comme optimiseur. Cette méthode nécessite un nombre important d’itérations pour converger, mais permet d’éviter les minimums locaux. Pour des raisons de temps de calcul, les systèmes de planification inverses en curiethérapie de la prostate utilisent une fonction de coût partielle. C’est-à-dire que la dose n’est pas estimée pour toute la prostate mais seulement pour quelques points caractéristiques. Ces points de contrôle sont souvent localisés entre les grains et à

la surface de la prostate. Un tel plan de traitement ne permet pas d'atteindre toutes les contraintes dosimétriques préétablies. Dans la pratique, il est courant que le radiophysicien vienne affiner manuellement le plan de traitement pour respecter tous les critères dosimétriques. Cette opération peut durer plusieurs dizaines de minutes. L'optimisation inverse est principalement utilisée pour estimer un premier jet d'implantation des grains.

Pour améliorer ce processus de planification, nous avons proposé d'une part de calculer la dose pour toute la prostate et les organes à risque avec la SMC et GGEMS et d'autre part de définir une nouvelle fonction de coût calculée directement par l'histogramme dose-volume. Les critères sont définis par des valeurs caractéristiques de l'histogramme dose-volume. Par exemple, 90% du volume de la prostate doit recevoir une dose minimale de 160 Gy. Le même type de critère est défini pour les organes à risque. Ceci permet de tenir compte de toutes les valeurs de dose dans chaque organe. Pour répondre au problème de temps de calcul, la méthode d'optimisation par recuit simulé a également été développée sur architecture GPU. Nous montrons qu'il est possible d'obtenir un plan de traitement par SMC en 45 s (NVIDIA GTX Titan X). Grâce à la nouvelle fonction de coût proposée, il n'est plus utile de retoucher manuellement le plan de traitement, ce qui permet un gain de temps en salle opératoire. Après convergence, tous les critères dosimétriques sont respectés. L'évaluation de ces méthodes a été réalisée en comparant les plans de traitement clinique de 18 patients avec les critères dosimétriques issus des recommandations TG137 (Nath et al., 2009).

Contrairement à un plan de traitement clinique où les critères dosimétriques sont surestimés à cause du formalisme analytique TG43 (de 8 à 10%), notre logiciel de planification n'a pas de biais grâce à la simulation Monte-Carlo. C'est un avantage, mais c'est aussi un inconvénient, notamment pour les organes à risque. Pour ne pas augmenter la toxicité, certains critères dosimétriques devront être ajustés et callés par rapport aux doses habituelles obtenues par le TG43. L'ensemble de ces travaux a été implémenté dans un logiciel de planification de traitement appelé TiTAN (*opTimized Treatment plANning system*) qui est en cours d'être protégé par un dépôt logiciel (Fig. 29). Ce logiciel sera notre plateforme d'intégration où chaque méthodologie future sera capitalisée et validée dans TiTAN. Certains résultats préliminaires sur le TPS ont été publiés dans Mountris et al. (2016, 2017b,a, 2018b). La présentation des méthodes et des résultats complets est en révision dans *International Journal of Radiation Oncology*.

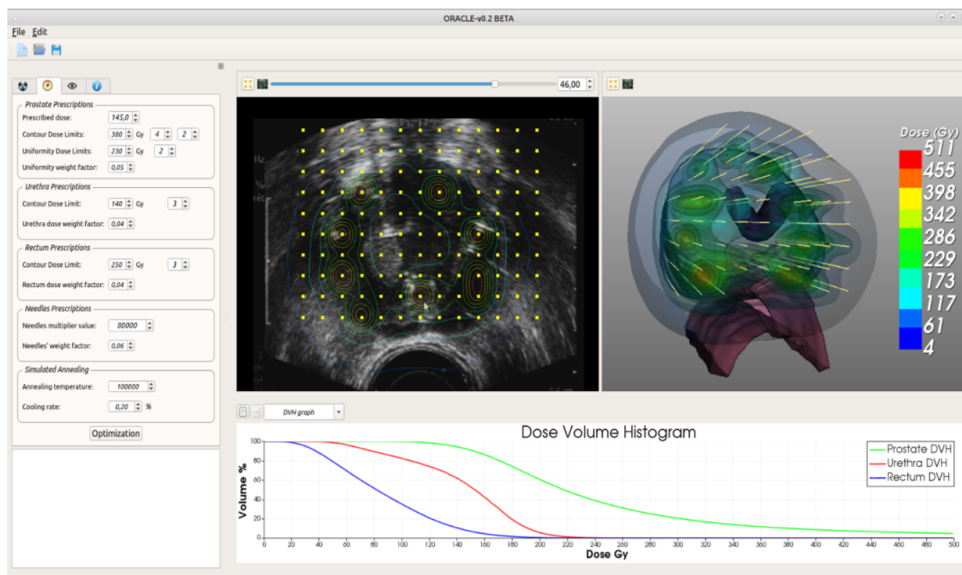


**Figure 29** – Capture d'écran de l'interface du logiciel TiTAN, système de planification de traitement pour la curiethérapie de la prostate que nous avons développé.

Les travaux que nous menons actuellement portent sur la prise en compte de l'œdème de la prostate dans le TPS et la SMC. Le but est de minimiser les calculs nécessaires pour la simulation de l'œdème, notamment dans son échantillonnage temporel. Plusieurs scénarios ont été envisagés et sont en cours d'évaluation. Des résultats préliminaires ont été présentés dans Mountris et al. (2018a).



Nous sommes également en train d'étudier la possibilité d'utiliser l'intelligence artificielle de type réseau de neurones, outil méthodologique populaire en ce moment, pour améliorer la convergence du TPS dans un contexte de curiethérapie de la prostate. Nous allons travailler sur ce sujet dans un futur proche, notamment dans le cadre d'une thèse qui débutera en octobre 2018.

### Système de délivrance du traitement

Un plan de traitement précis et optimal ne sert à rien si nous ne sommes pas capables de le mettre en place exactement tel qu'il a été défini. C'est notamment le cas en curiethérapie de la prostate. L'insertion manuelle, qui nécessite un très bon entraînement, n'est pas précise. L'utilisation de l'image échographique permet globalement d'aider l'urologue mais aucune information n'est délivrée sur l'image pour identifier la cible d'insertion. La précision d'implantation n'est pas une priorité dans un traitement standard. En effet, les erreurs de placement sont estompées par une implantation globale, c'est-à-dire que l'on met des grains partout afin de couvrir le moindre volume de la prostate.

Cependant, c'est un véritable frein à l'évolution du protocole standard, notamment en traitement ciblé (appelé aussi focal) où l'on cherche à traiter une zone plus petite avec différents scénarios de traitement possibles : la demi-glande, le quart de glande, uniquement le site tumoral, une dose de fond prostatique avec un boost sur la tumeur, etc. Le but est de diminuer les effets secondaires, le temps opératoire et le coût de l'intervention (un grain coûte cher). On ne cherche plus à effectuer un tir de zone sur l'ensemble de la prostate, mais un tir précis sur la tumeur. Ceci implique qu'il n'y a pas de place à l'erreur, il ne faut pas manquer sa cible. Dans ce contexte la précision de placement du grain doit être de l'ordre de un à deux millimètres. Précision impossible à obtenir aujourd'hui avec les méthodes et les technologies du protocole standard.

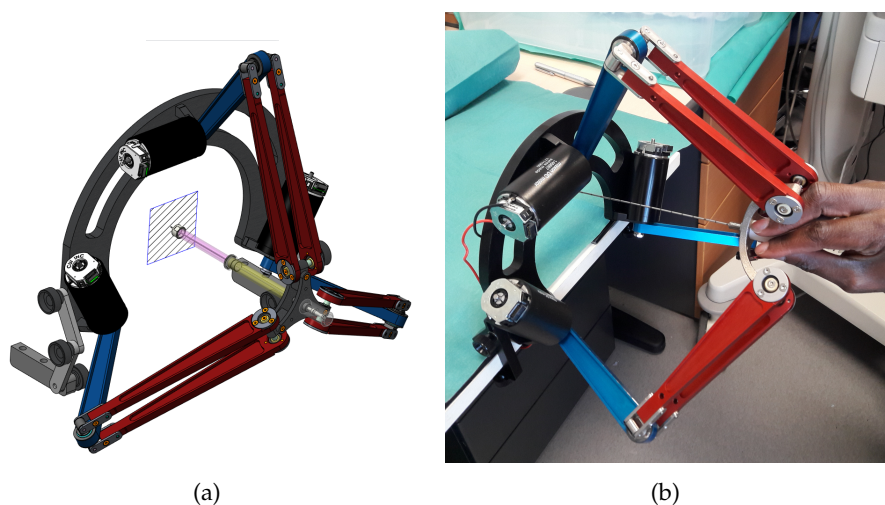


**Figure 30** – Robot médical collaboratif à architecture parallèle, dédié à l'insertion d'aiguille par retour d'effort en curiethérapie de la prostate. (a) Visualisation 3D de sa conception, (b) prototype après réalisation.

Pour répondre à ce défi, dans le cadre d'une thèse qui est en cours (M. Djohossou), nous avons proposé une approche de robot collaboratif (CoBot) dédié à la curiethérapie. Le CoBot est un robot qui travaille main dans la main dans un espace partagé avec l'utilisateur. Ce choix résulte d'un constat de l'état de l'art où toutes les solutions robotiques proposées pour la curiethérapie de la prostate sont d'une part calquée sur une géométrie mécanique conventionnelle imposante et sont d'autre part automatiques ou semi-automatiques (Podder et al., 2014). C'est-à-dire que l'urologue appuie sur un bouton et c'est la machine qui s'occupe de l'insertion. Notre philosophie est tranchée par rapport à ce qui existe. Nous voulons proposer d'une part un robot avec une géométrie dédiée à son application clinique et d'autre part un système qui a un niveau d'acceptabilité clinique plus élevé. Après l'étude de différents designs, nous avons développé un prototype de CoBot parallèle par retour d'effort avec une géométrie spécialement conçue pour la curiethérapie de la prostate (Fig. 30). C'est-à-dire qu'il tient compte de l'accès à l'abord périnéal, de la position du patient sur

la table opératoire et de la présence de la sonde endorectale. Le CoBot et le chirurgien agissent ensemble, l'un guidant l'autre par un retour d'effort. Un premier prototype a été réalisé par la société d'étude et de réalisation mécanique EIMA (Guipavas, Bretagne). Nous avons également développé l'architecture électronique permettant la commande du système. Les modèles théoriques ont été calculés (géométrie directe et inverse, dynamique, singularités) permettant une commande haptique par retour d'effort en fonction d'une consigne de position d'implantation. Le CoBot est en cours d'évaluation au laboratoire, notamment avec l'achat récent d'un système de suivi d'aiguille par champ électromagnétique. Ce premier prototype a pour but de valider nos différents choix stratégiques sur la solution d'aide au geste en curiethérapie de la prostate. Le CoBot est pour l'instant limité à 3 degrés de liberté, ne permettant pas de guider l'aiguille sur des trajectoires complexes. Une future version de ce système sera proposée dans les années à suivre dans le cadre d'une thèse qui débutera en octobre 2018. L'objectif, après les résultats concluants sur le premier prototype, est d'ajouter les degrés de liberté manquants pour un guidage complexe de la trajectoire de l'aiguille et de la prise en considération des contraintes cliniques (matériaux, ergonomie du préhenseur, carter, etc.). Notre objectif à plus long terme est de tester le système dans un contexte *in vivo* en salle opératoire.

## Conclusion

L'ensemble des travaux entrepris pour la curiethérapie de la prostate a pour l'instant un horizon de financement jusqu'en 2021. Avec autour de 2020, un objectif qui sera de réaliser un démonstrateur mettant en scène chaque élément du nouveau protocole proposé. Le but est de montrer la faisabilité d'un tel protocole et de vérifier la cohérence, l'importance et la maturité de chaque solution.

En terme de brique technologique, beaucoup d'éléments restent encore à améliorer, que ce soit pour les approches du traitement des images, de la planification du traitement, de la simulation Monte-Carlo ou de l'aide au geste pour l'insertion d'aiguille dans la prostate. Il reste donc beaucoup à faire et cela jalonnait mes différents travaux futurs. De nouvelles technologies d'imagerie semblent aussi intéressantes à évaluer dans le contexte de la curiethérapie de la prostate. Il existe par exemple un prototype de sonde échographique endo-urétrale permettant d'imager la glande de l'intérieur (Voros et al., 2013). Il existe aussi un projet pour l'instant fondamental en vibro-acoustographie (Mehrmohammadi et al., 2014), permettant de visualiser les grains dans la prostate sans aucun artefact via des ondes acoustiques basses fréquences. L'acquisition et la collaboration avec les groupes travaillant sur ces sujets constitueront des travaux futurs.

A plus long terme, nos approches devront être évaluées par des essais cliniques. Ceux mis en place pour l'instant ont pour but uniquement d'évaluer et de valider certaines briques du protocole, comme le modèle de l'œdème de la prostate par exemple. Nous sommes encore loin de modifier le protocole de traitement clinique. Cela devra se faire par palier en introduisant une à une les solutions proposées dans le protocole standard en fonction de leur maturité et de leur bénéfice potentiel. Il faudra aussi cibler progressivement des zones de traitement de plus en plus petite, afin de valider l'utilité clinique de la thérapie ciblée, ce qui aujourd'hui reste encore à démontrer.

### 5.4.2 Optimisation de la dose pour les procédures guidées par rayons X

Nos travaux futurs vont être également conditionnés par le projet ANR OptimiX sur l'optimisation et l'enseignement de la dose d'irradiation reçue pendant les procédures chirurgicales guidées par l'imagerie par rayons X. Tout comme pour la curiethérapie de la prostate, nous voulions aller au delà du fondement *simulation* de la boucle *sensori motrice* et appliquer nos outils pour améliorer et optimiser une application clinique. Cette application ne figure pas dans un contexte de radiothérapie. Cependant, les méthodes nécessaires sont les mêmes car toutes basées sur une dosimétrie peropératoire, précise, rapide et personnalisée. Des travaux préliminaires de moindre ampleur avaient été menés dans ce domaine via le co-encadrement d'une thèse (N. Loy Rodas effectuée à Strasbourg au laboratoire ICube. Travaux qui ont débouché sur une publication (Loy Rodas et al., 2017) et un brevet. Le projet OptimiX portera nos travaux jusqu'en 2022, et je l'espère fera effet

de levier pour continuer dans cette thématique.

Pour résumer, l'imagerie médicale par rayons X joue un rôle fondamental dans plusieurs domaines de la médecine, notamment en chirurgie. Cependant, son utilisation est associée à un risque inhérent d'exposition aux rayonnements ionisants (RI) nocifs pour le patient et les membres du personnel médical. De nombreuses études ont montré que toute exposition augmente le risque de réactions tissulaires radio-induites (épilation, nécrose cutanée, cataracte) et d'effets stochastiques potentiels tels que les tumeurs malignes. Alors que l'exposition d'un patient peut être justifiée par une indication médicale et se produit généralement en un seul épisode, le personnel médical fournissant les soins peut être exposé quotidiennement. La nature répétitive de cette exposition, même à faibles doses, augmente le risque de développer des effets biologiques négatifs et ce risque augmente lorsque l'exposition est accumulée au fil du temps. Des études ont rapporté que le dosage de RI le plus élevé enregistré pour tout personnel médical travaillant avec des rayons X est celui des praticiens en chirurgie interventionnelle. En effet, la plupart des procédures sont réalisées sous guidage radioscopique (imagerie radiographique continue) avec le besoin pour le personnel de rester à côté du patient pendant la procédure. Même si la majeure partie de leur corps est protégée par des vêtements protecteurs en plomb, la dose délivrée aux zones non couvertes telles que les mains, les yeux et les jambes peut atteindre les limites maximales autorisées. La dose du patient peut également devenir alarmante pendant des procédures complexes où les temps de fluoroscopie sont prolongés et/ou une acquisition d'un grand nombre de clichés de la même zone est nécessaire. D'autre part, plusieurs études ont rapporté une quantité considérable d'expositions inutiles résultant d'un manque de sensibilisation, d'un intérêt réduit pour les risques à long terme et d'une mauvaise connaissance du comportement des RI. Des travaux récents ont proposé des approches en quasi temps réel pour estimer l'exposition du patient/personnel au rayonnement dans la salle opératoire. Cependant, de telles approches ne sont pas compatibles avec une utilisation clinique ou pour l'enseignement, car elles sont associées à des approximations substantielles. En raison du coût de calcul élevé requis, elles utilisent de larges bases de données de simulation pré-calculées pour un ensemble de configurations données en utilisant un modèle générique du patient. L'ambition du projet Optimix est d'éliminer les approximations inhérentes à de telles approches en développant des méthodologies qui permettent un calcul de la dose en temps réel pour n'importe quelle configuration du système d'imagerie, de la salle opératoire, du personnel et aussi de n'importe quel patient.



**Figure 31** – Le projet ANR Optimix : (a) optimisation de la position du système d'imagerie par rayons X afin de minimiser la dose d'irradiation reçue par le patient et le personnel médical, (b) visualisation 3D par réalité augmentée/virtuelle des zones d'irradiation en procédure chirurgicale guidée par rayons X pour l'éducation et l'enseignement.

L'objectif global du projet Optimix est d'améliorer la sécurité radiologique du patient et du personnel en développant de nouvelles approches pour simuler le RI de façon rapide et précis en considérant des modèles réalistes et personnalisés du patient et du personnel, mais aussi de

proposer des méthodes pour optimiser la configuration du dispositif d'imagerie par rayons X afin de minimiser la dose délivrée sans compromettre la qualité de l'image (Fig. 31-a) et enfin de développer un système de visualisation par réalité augmentée/virtuelle pour faciliter l'enseignement, de façon engagée et intuitive, du comportement des RI en salle opératoire (Fig. 31-b). Les méthodes qui seront développées dans ce projet pourront être facilement transférées à l'industrie de la santé et pourront également profiter à la communauté scientifique. Enfin, Optimix a le potentiel pour devenir un standard en termes de formation et d'enseignement pour la radioprotection.

### 5.4.3 Radiothérapie externe

S'il n'y a pas de travaux de recherche en radiothérapie externe dans ce document, je ne les écarte pas néanmoins de mes objectifs futurs. En effet, l'ouverture de la thématique de la curiethérapie de la prostate a nécessité un effort particulier pour la mettre en œuvre, estompant de ce fait certains sujets tout aussi intéressants. Cependant, ces dernières années et de façon marginale, des travaux ont été entrepris dans l'optimisation de la planification en radiothérapie externe non-coplanaire (ou  $4\pi$ ). C'est la dernière innovation des traitements par arc-thérapie permettant le déplacement du lit du patient en même temps que la tête de l'accélérateur. L'objectif est d'augmenter les possibilités balistiques et normalement de mieux optimiser le traitement. Les travaux menés dans le cadre de la thèse de F. Okoli utilisent la SMC avec GGEMS et l'optimisation par recuit simulé combinée à la méthode du *compressed sensing* pour améliorer la planification du traitement, notamment en prenant en compte le temps du traitement (la trajectoire). Il est trop tôt pour définir si ce sujet nous amènera à des projets de plus grande envergure. En effet, le domaine très fourni dans la littérature nécessite un travail très conséquent de développement (TPS en radiothérapie externe) pour des bénéfices par rapport à l'état de l'art en demi-teinte. L'exploration de nouvelles méthodes, technologies et sujets de recherche font partie intégrante de la recherche.

Un de mes arguments pour appuyer l'utilisation de la simulation en radiothérapie était l'absence de système de perception. En réalité, les systèmes de radiothérapie externe embarquent un système d'imagerie électronique (EPID : *Electronic Portal Imaging Device*). Ce système sous exploité en routine clinique est capable d'acquérir l'image du faisceau d'irradiation par transmission, c'est-à-dire à travers le patient. Il est donc possible d'estimer la dose déposée dans le patient en 3D en analysant l'intensité et la forme de l'image du faisceau. Ce n'est pas une représentation complète en temps réel telle qu'elle serait nécessaire pour s'affranchir de la simulation et fermer la boucle *sensori motrice*. Mais il est possible de développer des méthodes innovantes par SMC pour la sécurité et le suivi du traitement du patient. La dosimétrie *in vivo* par imagerie EPID est un des sujets qui pourrait être entrepris dans un futur horizon de développement des thématiques en radiothérapie externe.

## 6 Conclusion

Ce rapport a pour objectif de montrer mes capacités à entreprendre, diriger et faire vivre des activités de recherche au sein d'un groupe. Depuis mon arrivée en tant que post doctorant au LaTIM en 2010, j'ai rédigé, entrepris, mis en place et participé à de nombreux projets ANR, LabEx, IRT, projets européens avec l'objectif de développer nos activités en radiothérapie. Je suis actuellement responsable de l'axe de recherche "Radiothérapie et dosimétrie", qui comptera à la rentrée universitaire de 2018, 4 post doctorants, 5 thésards et quelques permanents cliniciens. Ce document s'inscrit dans une continuité stratégique qui est de pérenniser et de consolider nos activités de recherche au sein de l'axe Radiothérapie et dosimétrie. Pendant ces 8 années, j'ai encadré 9 thèses et 7 post doctorants. L'ensemble de ces travaux a été valorisé par des publications et des logiciels. Certains travaux préliminaires et en marge à nos activités habituelles m'ont permis d'entreprendre des ouvertures thématiques afin de renouveler et d'envisager le futur, tout en gardant comme socle fondateur la radiothérapie et la dosimétrie. Les travaux que j'ai réalisés ou dirigés ont eu pour but de répondre globalement aux défis soulevés par certaines applications cliniques. Ceci a nécessité de proposer des solutions innovantes au regard de l'état de l'art pour chaque brique méthodologique constituante de ces applications. C'est pour cette raison que beaucoup de thèmes de recherche ont été abordés : SMC, segmentation, recalage, optimisation, système d'imagerie, architecture GPU, robotique, etc.

Pendant ces années de recherche de nombreuses collaborations ont été mises en place, qu'elles soient académiques ou industrielles. La plupart des thèses et tous les projets sont en collaboration avec d'autres chercheurs externes au laboratoire. Les réseaux provenant du LabEx CAMI, de l'IRT b<>com, FLI, et du FHU TECHSAN, sans compter ceux de la communauté de la SMC (notamment de GATE) dont je fais partie ont largement contribué à cela.

Jusqu'à l'horizon 2022, mes travaux de recherche sont bien définis, car dirigés par mes projets de recherche actuels (ANR FOCUS et Optimix). La priorité est d'une part le développement de la curiethérapie 2.0 de la prostate et d'autre part la mise en place au sein de notre groupe de recherche les fondements concernant la thématique de l'optimisation de la dose pour les procédures utilisant des rayons X. Les travaux en radiothérapie externe, bien que marginaux pour l'instant, vont se poursuivre tout comme ceux en simulation Monte-Carlo. Certains de ces résultats prendront peut-être de l'ampleur dans un futur proche autour d'un ou plusieurs projets structurants.

Il est difficile d'avoir une vue des recherches à très long terme, la seule certitude étant que les évaluations cliniques des méthodologies que nous sommes en train de proposer nécessiteront de nombreuses années de recul pour dresser une conclusion sur leurs impacts. Par exemple, en curiethérapie de la prostate, un recul de 10 ans est nécessaire pour conclure à l'efficacité d'un protocole particulier. Les sujets dans le domaine de la technologie de la santé qui répondent à un enjeu sociétal majeur sont nombreux, surtout en radiothérapie et il y a largement de quoi remplir une vie... En général, les thématiques cliniques qui émergent dans un laboratoire sont issues de collaborations fructueuses et de volontés mutuelles entre cliniciens et chercheurs, souvent locales. C'est le cas entre le LaTIM et le CHRU de Brest. En effet, sans accès à la clinique (données, patients, experts, matériels, etc.), il est difficile de faire des projets autour de la technologie pour la santé. Pour conclure, l'émergence d'une thématique ou d'un sujet de recherche particulier est pour un chercheur la résultante de plusieurs ingrédients qu'il est difficile de prédire à un horizon lointain. Mais c'est aussi, ce qui fait la richesse de ce métier. Il n'y a pas de routes toutes tracées en avances, nous explorons un terrain libre et inconnu. Et que malgré les difficultés, il y a une grande satisfaction à regarder derrière soi et de voir qu'à partir de nos pas, un chemin a fini par émerger de lui-même. C'est le résultat des efforts de plusieurs personnes, qui année après année, ont réussi à installer une dynamique autour d'un même objectif de recherche.



## Références bibliographiques

- Allison, J., Amako, K., Apostolakis, J., Araujo, H., Arce Dubois, P., Asai, M., Barrand, G., Capra, R., Chauvie, S., Chytracsek, R., Cirrone, G. A. P., Cooperman, G., Cosmo, G., Cuttone, G., Daquino, G. G., Donszelmann, M., Dressel, M., Folger, G., Foppiano, F., Generowicz, J., Grichine, V., Guatelli, S., Gumplinger, P., Heikkinen, A., Hrivnacova, I., Howard, A., Incerti, S., Ivanchenko, V., Johnson, T., Jones, F., Koi, T., Kokoulin, R., Kossov, M., Kurashige, H., Lara, V., Larsson, S., Lei, F., Link, O., Longo, F., Maire, M., Mantero, A., Mascialino, B., McLaren, I., Mendez Lorenzo, P., Minamimoto, K., Murakami, K., Nieminen, P., Pandola, L., Parlati, S., Peralta, L., Perl, J., Pfeiffer, A., Pia, M. G., Ribon, A., Rodrigues, P., Russo, G., Sadilov, S., Santin, G., Sasaki, T., Smith, D., Starkov, N., Tanaka, S., Tcherniaev, E., Tome, B., Trindade, A., Truscott, P., Urban, L., Verderi, M., Walkden, A., Wellisch, J. P., Williams, D. C., Wright, D., and Yoshida, H. (2006). Geant4 developments and applications. *IEEE Transactions on Nuclear Science*, 53(1) :270–278.
- Beaulieu, L., Carlsson Tedgren, A., Carrier, J.-F., Davis, S. D., Mourtada, F., Rivard, M. J., Thomson, R. M., Verhaegen, F., Wareing, T. A., and Williamson, J. F. (2012). Report of the Task Group 186 on model-based dose calculation methods in brachytherapy beyond the TG-43 formalism : current status and recommendations for clinical implementation. *Medical Physics*, 39(10) :6208–6236.
- Behloul, A., Bert, J., and Visvikis, D. (2017). Improved Woodcock tracking on Monte Carlo simulations for medical applications. In *International Conference on Monte Carlo Techniques for Medical Applications*.
- Benhalouche, S., Bert, J., Bousson, N., Autret, A., Pradier, O., and Visvikis, D. (2017). GATE Monte-Carlo simulation of a MV-CBCT flat panel for synergistic imaging and dosimetric applications in radiotherapy. *IEEE Transactions on Radiation and Plasma Medical Sciences*.
- Bert, J., Dembélé, S., and Lefort-Piat, N. (2006a). Trifocal transfer based novel view synthesis for micromanipulation. *Lecture Notes in Computer Science*, 4291 :411–420.
- Bert, J., Dembélé, S., and Lefort-Piat, N. (2006b). Virtual Camera Synthesis for Mircomanipulation and Mircoassembly. In *IEEE International Conference on Intelligent Robots and Systems*, pages 1390–1395.
- Bert, J., Dembélé, S., and Lefort-Piat, N. (2007). Performing Weak Calibration at the Microscale. Application to Micromanipulation. In *IEEE International Conference on Robotics and Automation*, pages 4937–4942.
- Bert, J., Asturias, F., and Penczek, P. A. (2009). *Iterative Step Wise Clustering of 2D EM Projection Data*. Houston Medical School, Texas Medical Center, USA.
- Bert, J., Perez-Ponce, H., Jan, S., Bitar, Z. E., Gueth, P., Cuplov, V., Chekatt, H., Benoit, D., Sarrut, D., Boursier, Y., Brasse, D., Buvat, I., Morel, C., and Visvikis, D. (2012). Hybrid GATE : A GPU/CPU implementation for imaging and therapy applications. In *IEEE Nuclear Science Symposium and Medical Imaging Conference*, pages 2247–2250.
- Bert, J., Dubois, A., Jan, S., Gueth, P., Garrido, E., Benoit, D., Sarrut, D., Bitar, Z. E., Cuplov, V., Boursier, Y., Brasse, D., Buvat, I., Morel, C., and Visvikis, D. (2013a). Hybrid CPU/GPU GATE : towards GATE V7. In *Geant4 International User Conference*.
- Bert, J., Lemaréchal, Y., Bousson, N., and Visvikis, D. (2013b). New particle navigator for hybrid voxelized/analytical phantoms in Monte Carlo simulations for medical applications. In *IEEE Nuclear Science Symposium and Medical Imaging Conference*.
- Bert, J., Perez-Ponce, H., Bitar, Z. E., Jan, S., Boursier, Y., Vintache, D., Bonissent, A., Morel, C., Brasse, D., and Visvikis, D. (2013c). Geant4-based Monte Carlo simulations on GPU for medical applications. *Physics in Medicine and Biology*, 58 :5593–5611.
- Bert, J., Lemaréchal, Y., Garrido, E., and Visvikis, D. (2014). GGEMS platform : GPU Geant4-based Monte Carlo Simulation. In *International Workshop on Monte Carlo Techniques in Medical Physics*.
- Bert, J., Benoit, D., Garcia, M.-P., and Visvikis, D. (2016a). GGEMS : GPU GEant4-based Monte Carlo Simulation platform. In *IEEE Nuclear Science Symposium and Medical Imaging Conference*.
- Bert, J., Lemaréchal, Y., and Visvikis, D. (2016b). New hybrid voxelized/analytical primitive in Monte

- Carlo simulations for medical applications. *Physics in Medicine and Biology*, 61(9) :3347–3364.
- Bert, J. and Visvikis, D. (2017). Ggems version 1.385, iddn.fr.001.180017.000.s.p.2017.000.31230.
- Bert, J. and Visvikis, D. (2018). Smooth mesh for accurate Monte Carlo simulation in medical applications. In *IEEE Nuclear Science Symposium and Medical Imaging Conference*.
- Bouzzid, D., Bert, J., Dupré, P.-F., Benhalouche, S., Visvikis, D., Pradier, O., and Boussion, N. (2013). Monte Carlo simulation of the Intrabeam<sup>TM</sup> system with the platform GATE for breast cancer. *Physica Medica : European Journal of Medical Physics*, 29.
- Bouzzid, D., Bert, J., Dupre, P.-F., Benhalouche, S., Pradier, O., Boussion, N., and Visvikis, D. (2015). Monte-Carlo dosimetry for intraoperative radiotherapy using a low energy x-ray source. *Acta Oncologica*, 54(10) :1788–1795.
- Calvo, O. I., Gutiérrez, A. N., Stathakis, S., Esquivel, C., and Papanikolaou, N. (2012). On the quantification of the dosimetric accuracy of collapsed cone convolution superposition (CCCS) algorithm for small lung volumes using IMRT. *Journal of Applied Clinical Medical Physics*, 13(3) :3751.
- Couffignal, L. (1963). *La Cybernétique*. Presses Universitaire de France.
- Enger, S. A., Landry, G., D'Amours, M., Verhaegen, F., Beaulieu, L., Asai, M., and Perl, J. (2012). Layered mass geometry : a novel technique to overlay seeds and applicators onto patient geometry in Geant4 brachytherapy simulations. *Physics in medicine and biology*, 57 :6269–6277.
- Flampouri, S., Jiang, S. B., Sharp, G. C., Wolfgang, J., Patel, A. A., and Choi, N. C. (2006). Estimation of the delivered patient dose in lung IMRT treatment based on deformable registration of 4D-CT data and Monte Carlo simulations. *Physics in Medicine and Biology*, 51 :2763–2779.
- Gaens, M., Bert, J., Pietrzyk, U., Shah, N. J., and Visvikis, D. (2013). GPU-accelerated Monte Carlo Base Scatter Correction in Brain PET/MR. In *IEEE Nuclear Science Symposium and Medical Imaging Conference*.
- Garcia, M.-P., Bert, J., Vilhoing, D., Reilhac, A., Grégoire, M.-C., Visvikis, D., and Bardies, M. (2014). Hybrid CPU/GPU SPECT Monte Carlo Simulations : The Hexagonal Hole Collimator Case. In *IEEE Nuclear Science Symposium and Medical Imaging Conference*.
- Garcia, M.-P., Bert, J., Benoit, D., Bardies, M., and Visvikis, D. (2015). Accelerated GPU based SPECT Monte Carlo Simulations using GGEMS. In *IEEE Nuclear Science Symposium and Medical Imaging Conference*.
- Garcia, M.-P., Bert, J., Benoit, D., Bardies, M., and Visvikis, D. (2016). Accelerated GPU based SPECT Monte Carlo simulations. *Physics in Medicine and Biology*, 61 :4001–4018.
- Hamdan, I., Bert, J., Rest, C. C. L., Tasu, J. P., Boussion, N., Valeri, A., Dardenne, G., and Visvikis, D. (2017). Fully automatic deformable registration of pre-treatment MRI/CT for image-guided prostate radiotherapy planning. *Medical Physics*.
- Han, T., Mikell, J. K., Salehpour, M., and Mourtada, F. (2011). Dosimetric comparison of Acuros XB deterministic radiation transport method with Monte Carlo and model-based convolution methods in heterogeneous media. *Medical Physics*, 38(5) :2651–2664.
- Jan, S., Benoit, D., Becheva, E., Carlier, T., Cassol, F., Descourt, P., Frisson, T., Grevillot, L., Guigues, L., Maigne, L., Morel, C., Perrot, Y., Rehfeld, N., Sarrut, D., Schaart, D. R., Stute, S., Pietrzyk, U., Visvikis, D., Zahra, N., and Buvat, I. (2011). GATE V6 : a major enhancement of the GATE simulation platform enabling modelling of CT and radiotherapy. *Physics in Medicine and Biology*, 56 :881–901.
- Jaouen, V., Bert, J., Hamdan, I., Valeri, A., Schick, U., Boussion, N., and Visvikis, D. (2017). Purely edge-based prostate segmentation in 3D TRUS images using deformable models. In *SURGETICA*.
- Jia, X., Ziegenhein, P., and Jiang, S. B. (2014). GPU-based high-performance computing for radiation therapy. *Physics in Medicine and Biology*, 59(4) :R151–182.
- Lemaréchal, Y., Bert, J., Boussion, N., and Visvikis, D. (2013a). GGEMS-Brachy : Fully GPU Geant4-Based Efficient Monte Carlo Simulation for Brachytherapy Applications. In *Medical Physics AAPM*,

volume 40, page 88.

- Lemaréchal, Y., Bert, J., Lefur, E., Bousson, N., and Visvikis, D. (2013b). Monte Carlo simulations on GPU for brachytherapy applications. In *IEEE Nuclear Science Symposium and Medical Imaging Conference*.
- Lemaréchal, Y., Bert, J., Bousson, N., and Visvikis, D. (2014). GGEMS-brachy : Fully GPU Geant4-based Monte Carlo Simulation for Brachytherapy Applications. In *European Society for Radiotherapy and Oncology (ESTRO)*.
- Lemarechal, Y., Bert, J., Falconnet, C., Despres, P., Valeri, A., Schick, U., Pradier, O., Garcia, M.-P., Bousson, N., and Visvikis, D. (2015). GGEMS-Brachy : GPU GEant4-based Monte Carlo simulation for brachytherapy applications. *Physics in Medicine and Biology*, 60 :4978–5006.
- Loy Rodas, N., Bert, J., Visvikis, D., de Mathelin, M., and Padoy, N. (2017). Pose optimization of a C-arm imaging device to reduce intraoperative radiation exposure of staff and patient during interventional procedures. pages 4200–4207.
- Mehrmohammadi, M., Alizad, A., Kinnick, R. R., Davis, B. J., and Fatemi, M. (2014). Feasibility of vibro-acoustography with a quasi-2d ultrasound array transducer for detection and localizing of permanent prostate brachytherapy seeds : A pilot *ex vivo* study : Q2d VA for detection of PPB seeds. *Medical Physics*, 41(9) :092902.
- Mountris, K., Bert, J., and Visvikis, D. (2016). Prostate brachytherapy optimization using simulated annealing and Monte Carlo dose simulation. In *IEEE Nuclear Science Symposium and Medical Imaging Conference*.
- Mountris, K. A., Bert, J., Bousson, N., Valeri, A., Schick, U., and Visvikis, D. (2017a). DVH-based optimization of LDR prostate brachytherapy using GPU-accelerated MC dosimetry. In *SURGETICA*.
- Mountris, K. A., Bert, J., Bousson, N., Valeri, A., Schick, U., and Visvikis, D. (2017b). ORACLE : A DVH-based inverse planning system for LDR prostate brachytherapy using MC dosimetry. In *International Conference on Monte Carlo Techniques for Medical Applications*.
- Mountris, K. A., Bert, J., Noailly, J., Aguilera, A. R., Valeri, A., Pradier, O., Schick, U., Promayon, E., Ballester, M. A. G., Troccaz, J., and Visvikis, D. (2017c). Modeling the impact of prostate edema on LDR brachytherapy : a Monte Carlo dosimetry study based on a 3D biphasic finite element biomechanical model. *Physics in Medicine and Biology*, 62(6) :2087–2102.
- Mountris, K. A., Bert, J., and Visvikis, D. (2018a). Edema adapted treatment plan in LDR prostate brachytherapy : beyond common inverse treatment planning. In *European Society for Radiotherapy & Oncology (ESTRO)*.
- Mountris, K. A., Bert, J., and Visvikis, D. (2018b). LDR prostate brachytherapy inverse planning including dose-volume relation and tissue heterogeneity. In *European Society for Radiotherapy & Oncology (ESTRO)*.
- Nath, R., Anderson, L. L., Luxton, G., Weaver, K. A., Williamson, J. F., and Meigooni, A. S. (1995). Dosimetry of interstitial brachytherapy sources : recommendations of the AAPM Radiation Therapy Committee Task Group No. 43. American Association of Physicists in Medicine. *Medical Physics*, 22(2) :209–234.
- Nath, R., Bice, W. S., Butler, W. M., Chen, Z., Meigooni, A. S., Narayana, V., Rivard, M. J., and Yu, Y. (2009). AAPM recommendations on dose prescription and reporting methods for permanent interstitial brachytherapy for prostate cancer : Report of Task Group 137 : AAPM TG-137 Report. *Medical Physics*, 36(11) :5310–5322.
- Nickolls, J. and Dally, W. J. (2010). The GPU Computing Era. *IEEE Micro*, 30(2) :56–69.
- Perez-Ponce, H., Bitar, Z. E., Boursier, Y., Vintache, D., Bonissent, A., Morel, C., Brasse, D., Visvikis, D., and Bert, J. (2011). Implementing Geant4 on GPU for medical applications. In *IEEE Nuclear Science Symposium and Medical Imaging Conference*, pages 2703–2707.
- Podder, T. K., Beaulieu, L., Caldwell, B., Cormack, R. A., Crass, J. B., Dicker, A. P., Fenster, A.,

- Fichtinger, G., Meltsner, M. A., Moerland, M. A., Nath, R., Rivard, M. J., Salcudean, T., Song, D. Y., Thomadsen, B. R., Yu, Y., American Association of Physicists in Medicine Brachytherapy Subcommittee and Therapy Physics Committee, and Groupe Européen de Curiethérapie-European Society for Radiotherapy & Oncology BRAPHYQS Subcommittee (2014). AAPM and GEC-ESTRO guidelines for image-guided robotic brachytherapy : report of Task Group 192. *Medical Physics*, 41(10) :101501.
- Rassiah-Szegedi, P., Fuss, M., Sheikh-Bagheri, D., Szegedi, M., Stathakis, S., Lancaster, J., Papanikolaou, N., and Salter, B. (2007). Dosimetric evaluation of a Monte Carlo IMRT treatment planning system incorporating the MIMiC. *Physics in Medicine and Biology*, 52 :6931–6941.
- Sarrut, D., Bardiès, M., Bousson, N., Freud, N., Jan, S., Létang, J.-M., Loudos, G., Maigne, L., Marcatili, S., Mauxion, T., Papadimitroulas, P., Perrot, Y., Pietrzyk, U., Robert, C., Schaart, D. R., Visvikis, D., and Buvat, I. (2014). A review of the use and potential of the GATE Monte Carlo simulation code for radiation therapy and dosimetry applications. *Medical Physics*, 41(6) :064301.
- Tejwani, A., Bieniek, E., Puckett, L., Lavaf, A., Guirguis, A., Bennish, A., and Ashamalla, H. (2012). Case series analysis of post-brachytherapy prostate edema and its relevance to post-implant dosimetry. post-implant prostate edema and dosimetry. *Journal of Contemporary Brachytherapy*, 4(2) :75–80.
- Verhaegen, F. and Seuntjens, J. (2003). Monte Carlo modeling of external radiotherapy photon beams. *Physics in Medicine and Biology*, 48 :107–164.
- Voros, S., Moreau-Gaudry, A., Tamadzate, B., Custillon, G., Heus, R., Montmasson, M.-P., Giroud, F., Gaiffe, O., Pieralli, C., Fiard, G., Long, J.-A., Descotes, J.-L., Vidal, C., Nguyen-Dinh, A., and Cinquin, P. (2013). Devices and systems targeted towards augmented robotic radical prostatectomy. *IRBM*, 34(2) :139–146.
- Wiener, N. (1948). *Cybernetics*. Hermann, Paris.
- Woodcock, E., Murphy, T., Hemmings, P., and Longworth, S. (1965). Techniques used in the gem code for monte carlo neutronics calculations in reactors and other systems of complex geometry. In *Proc. Conf. on Applications of Computing Methods to Reactor Problems*, page 557.
- Yegin, G. (2003). A new approach to geometry modeling for Monte Carlo particle transport : An application to the EGS code system. *Nuclear Instruments and Methods in Physics Research*, 211 :331–338.

## ANNEXES

### A Liste complète de la bibliographie

#### A.1 En Révision - Revues internationales avec comité de lecture

- R1 Mountris K A, Visvikis D, **Bert J**, (2018). DVH-based Inverse Planning using Monte Carlo Dosimetry for LDR Prostate Brachytherapy *International Journal of Radiation Oncology Biology Physics*
- R2 Behloul A, Visvikis D, **Bert J**, (2018). Improved Woodcock tracking on Monte Carlo simulations for medical applications *Physics in Medicine and Biology*
- R3 Jaouen V, **Bert J**, Mountris K, BouSSION N, Shick U, Pradier O, Valeri A, Visvikis D, (2018). Prostate Volume Segmentation in TRUS using Hybrid Edge- Bhattacharyya Active Surfaces *Transactions on Biomedical Engineering*
- R4 Merlin T, Stute S, Benoit D, **Bert J**, Carlier T, Comtat C, Filipovic M, Lamare F, Visvikis D, (2018). CASToR : A Generic Data Organization and Processing Code Framework for Multi-Modal and Multi-Dimensional Tomographic Reconstruction *Physics in Medicine and Biology*
- R5 Jaouen V, **Bert J**, BouSSION N, Fayad H, Hatt M, Visvikis D, (2017). Image enhancement with PDEs and nonconservative advection flow fields *Transactions on Image Processing*

#### A.2 Revues internationales avec comité de lecture

- J1 Virone L, Acounis S, Beaupère N, Beney J-L, **Bert J**, Bouvier S, Briend P, Butterworth J, Carlier T, Chérel M, Crespi P, Cussonneau J-P, Diglio S, Gallego Manzano L, Giovagnoli D, Gossiaux P-B, Kraeber-Bodéré F, Le Ray P, Lefèvre F, Marty P, Masbou J, Morteau E, Picard G, Roy D, Staempflin M, Stutzmann J-S, Visvikis D, Xing Y, Zhu Y, Thers D, (2018). Gravity assisted recovery of liquid xenon at large mass flow rates *Nuclear Instruments and Methods in Physics Research Section A : Accelerators, Spectrometers, Detectors and Associated Equipment* 893 pp 10–14
- J2 Salah H, Lapuyade-Lahorgue J, **Bert J**, Benoit D, Lambin P, Baardwijk A V, Monfrini E, Pieczynski W, Visvikis D, Hatt M, (2017). A framework based on hidden Markov trees for multimodal PET/CT image co-segmentation *Medical Physics* 44 pp 5835–5848
- J3 Hamdan I, **Bert J**, Cheze Le Rest C , Tasu J P, BouSSION N, Valeri A, Dardenne G, Visvikis D, (2017). Fully automatic deformable registration of pre-treatment MRI/CT for image-guided prostate radiotherapy planning *Medical Physics* 44 pp 6447–6455
- J4 Cussonneau JP, Abaline JM, Acounis S, Beaupère N, Beney JL, **Bert J**, Bouvier S, Briend P, Butterworth J, Carlier T, Chanal H, Cherel M, Dahoumane M, Diglio S, Gallego-Manzano L, Giovagnoli D, Idier J, Kraeber-Bodere F, Lefebvre F, Lemaire O, Le Ray P, Manen S, Masbou J, Mathez H, Morteau E, Pillet N, Royer L, Staempflin M, Stutzmann JS, Vandaele R, Virone L, Visvikis D, Xing Y, Zhu Y, Thers D, (2017).  $3\gamma$  Medical Imaging with a Liquid Xenon Compton Camera and  $^{44}\text{Sc}$  Radionuclide *Acta Physica Polonica B* 48 pp 1661
- J5 Benhalouche S, **Bert J**, BouSSION N, Autret A, Pradier O, Visvikis D, (2017). GATE Monte-Carlo simulation of a MV-CBCT flat panel for synergistic imaging and dosimetric applications in radiotherapy *IEEE Transactions on Radiation and Plasma Medical Sciences*
- J6 Mountris K A, **Bert J**, Noailly J, Rodriguez Aguilera A, Valeri A, Pradier O, Schick U, Promayon E, Gonzalez Ballester M A, Troccaz J, Visvikis D, (2017). Modeling the impact of prostate edema on LDR brachytherapy : a Monte Carlo dosimetry study based on a 3D biphasic finite element biomechanical model *Physics in Medicine and Biology* 62 pp 2087–2102
- J7 Gilles M, Fayad H, Miglierini P, Clement J F, Scheib S, Cozzi L, **Bert J**, BouSSION N, Schick U, Pradier O, Visvikis D, (2016). Patient positioning in radiotherapy based on surface imaging using time of flight cameras. *Medical physics* 43 pp 4833



- J8 **Bert J**, Lemaréchal Y, Visvikis D, (2016). New hybrid voxelized/analytical primitive in Monte Carlo simulations for medical applications *Physics in medicine and biology* 61 pp 3347–3364
- J9 Gonzalez A J, Majewski S, Sanchez F, Aussenhofer S, Aguilar A, Conde P, Hernandez L, Vidal L F, Pani R, Bettiol M, Fabbri A, **Bert J**, Visvikis D, Jackson C, Murphy J, O'Neill K, Benlloch J M, (2016). The MINDView brain PET detector, feasibility study based on SiPM arrays *Nuclear Instruments and Methods in Physics Research Section A : Accelerators, Spectrometers, Detectors and Associated Equipment* 818 pp 82–90
- J10 Garcia M-P, **Bert J**, Benoit D, Bardies M, Visvikis D, (2016). Accelerated GPU based SPECT Monte Carlo simulations *Physics in Medicine and Biology* 61 pp 4001-4018
- J11 Monnier F, Fayad H, **Bert J**, Schmidt H, Visvikis D, (2015). Validation of a simultaneous PET/MR system model for PET simulation using GATE *EJNMMI Physics* 2 pp A45
- J12 Mota A M, Cuplova V, Drobnjak I, Dickson J, **Bert J**, Burgos N, Cardoso J M, Modat M, Ourselin S, Schott J, Erlandsson K, Hutton B, Thielemans K, (2015). Erratum to : Establishment of an open database of realistic simulated data for evaluation of partial volume correction techniques in brain PET/MR. *EJNMMI physics* 2 pp 30
- J13 Bouzid D, **Bert J**, Dupre P-F, Benhalouche S, Pradier O, Boussion N, Visvikis D, (2015). Monte-Carlo dosimetry for intraoperative radiotherapy using a low energy x-ray source *Acta Oncologica* 54 pp 1788-1795
- J14 Lemarechal Y, **Bert J**, Falconnet C, Despres P, Valeri A, Schick U, Pradier O, Garcia M-P, Boussion N, Visvikis D, (2015). GGEMS-Brachy : GPU GEant4-based Monte Carlo simulation for brachytherapy applications *Physics in Medicine and Biology* 60 pp 4978-5006
- J15 Bouzid D, Boussion N, **Bert J**, Pradier O, Visvikis D, (2014). A simulation based dosimetric study for a Kypho-IORT treatment using Intrabeam(TM) *Translational Cancer Research* 3 pp 83-87
- J16 Visvikis D, Monnier F, **Bert J**, Hatt M, Fayad H, (2014). PET/MR attenuation correction : where have we come from and where are we going? *European Journal of Nuclear Medicine & Molecular Imaging*
- J17 Monnier F, Fayad H, **Bert J**, Lapuyade-Lahorgue J, Hatt M, Veit-Haibach P, Delso G, Visvikis D, (2014). Generation of pseudo-CT from a single MRI for PET/MR attenuation correction purposes *EJNMMI Physics* 1 pp A74
- J18 Bouzid D, **Bert J**, Dupré P-F, Benhalouche S, Visvikis D, Pradier O, Boussion N, (2013). Monte Carlo simulation of the Intrabeam<sup>TM</sup> system with the platform GATE for breast cancer *Physica Medica : European Journal of Medical Physics* 29
- J19 **Bert J**, Perez-Ponce H, El Bitar Z, Jan S, Boursier Y, Vintache D, Bonissent A, Morel C, Brasse D, Visvikis D, (2013). Geant4-based Monte Carlo simulations on GPU for medical applications *Physics in medicine and biology* 58 pp 5593-5611
- J20 Benhalouche S, **Bert J**, Pradier O, Visvikis D, Boussion N, (2013). Tomographie conique de 6 MV : simulation et évaluation GATE v6.2 Monte-Carlo d'un imageur portal avec application spécifique en radiothérapie ORL *Journal Cancer/Radiothérapie* 17 pp 620
- J21 Wentz T, Fayad H, **Bert J**, Pradier O, Clément J-F, Boussion N, Visvikis D, (2012). Accuracy of dynamic patient surface monitoring using a Time-of-Flight camera and B-splines modeling for respiratory motion characterization *Physics in medicine and biology* 57 pp 4175-4193
- J22 Dembélé S, **Bert J**, Tamadazte B, Lefort-Piat N, (2010). A Trifocal Transfer Based Virtual Microscope for Robotic Manipulation of MEMS Components *International Journal of Optomechatronics* 4 pp 342-361
- J23 **Bert J**, Dembélé S, Lefort-Piat N, (2006). Trifocal Transfer Based Novel View Synthesis for Micromanipulation *Lecture Notes in Computer Science* 4291 pp 411-420

### A.3 Conférences internationales avec comité de lecture

- C1 **Bert J**, Visvikis D, (2018). Smooth mesh for accurate Monte Carlo simulation in medical applications *IEEE Nuclear Science Symposium and Medical Imaging Conference*
- C2 Mountris K A, **Bert J**, Visvikis D, (2018). LDR prostate brachytherapy inverse planning including dose-volume relation and tissue heterogeneity *European Society for Radiotherapy & Oncology (ESTRO)*
- C3 Mountris K A, **Bert J**, Visvikis D, (2018). Edema adapted treatment plan in LDR prostate brachytherapy : beyond common inverse treatment planning *European Society for Radiotherapy & Oncology (ESTRO)*
- C4 Jaouen V, Gaubert L, **Bert J**, Hatt M, Visvikis D, (2018). Image Filtering with Advectors *IEEE International Conference on Image Processing*
- C5 Merlin T, Stute S, Benoit D, **Bert J**, Carlier T, Comtat C, Lamare F, Visvikis D, (2017). CAS-ToR : A Generic Data Organization and Processing Code Framework for Multi-Modal and Multi-Dimensional Tomographic Reconstruction *Fully Three-Dimensional Image Reconstruction in Radiology and Nuclear Medicine*
- C6 Loy Rodas N, **Bert J**, Visvikis D, de Mathelin M, Padoy N, (2017). Pose optimization of a C-arm imaging device to reduce intraoperative radiation exposure of staff and patient during interventional procedures *IEEE International Conference on Robotics and Automation*
- C7 Behlouli A, **Bert J**, Visvikis D, (2017). Improved Woodcock tracking on Monte Carlo simulations for medical applications *International Conference on Monte Carlo Techniques for Medical Applications*
- C8 Mountris K A, **Bert J**, Boussion N, Valeri A, Schick U, Visvikis D, (2017). ORACLE : A DVH-based inverse planning system for LDR prostate brachytherapy using MC dosimetry *International Conference on Monte Carlo Techniques for Medical Applications*
- C9 Behlouli A, **Bert J**, Visvikis D, (2017). Improved Woodcock tracking on Monte Carlo simulations for medical applications *IEEE Nuclear Science Symposium and Medical Imaging Conference*
- C10 Iborra A, **Bert J**, Merlin T, Sanchez S, Conde P, Gonzalez A J, Rodriguez-Alvarez M J, Visvikis D, (2017). IRIS Projector Adaptation for PET Scanner Based on Monolithic Crystals *IEEE Nuclear Science Symposium and Medical Imaging Conference*
- C11 Benoit D, Merlin T, **Bert J**, Carlier T, Lamare F, Visvikis D, (2017). CT iterative reconstruction within the CASToR platform using GPU architecture *IEEE Nuclear Science Symposium and Medical Imaging Conference*
- C12 Hamdan I, Dardenne G, **Bert J**, Visvikis D, (2016). Non-rigid MRI/CT registration for effective planning of prostate brachytherapy *IEEE Engineering in Medicine and Biology Society*
- C13 Autret A, **Bert J**, Preziosi E, Gonzalez A J, Benlloch J M, Visvikis D, (2016). Accurate detector response modeling in PET reconstructions for systems using monolithic scintillators *IEEE Nuclear Science Symposium and Medical Imaging Conference*
- C14 Merlin T, Stute S, Benoit D, **Bert J**, Carlier T, Comtat C, Lamare F, Visvikis D, (2016). CASToR : A Generic Data Organization and Processing Code Framework for Multi-Modal and Multi-Dimensional Tomographic Reconstruction *IEEE Nuclear Science Symposium and Medical Imaging Conference*
- C15 Mountris K, **Bert J**, Visvikis D, (2016). Prostate brachytherapy optimization using simulated annealing and Monte Carlo dose simulation *IEEE Nuclear Science Symposium and Medical Imaging Conference*
- C16 Gonzalez A J, Gonzalez-Montoro A, Aguilar A, Conde P, Canizares G, Hernandez L, Iborra A, Moliner L, Vidal L F, Sanchez S, Sanchez F, Garcia R, Barbera J, Correcher C, Aussenhofer S, Gareis D, Galasso M, Fabbri A, Preziosi E, Visvikis D, **Bert J**, Autret A, Benlloch J M, (2016). A Brain PET Insert MR Compatible : Final Design and First Results *IEEE Nuclear Science Symposium and Medical Imaging Conference*

- C17 **Bert J**, Lemaréchal Y, Benoit D, Garcia M-P, Visvikis D, (2016). GGEMS : GPU GEant4-based Monte Carlo Simulation platform *IEEE Nuclear Science Symposium and Medical Imaging Conference*
- C18 Autret A, Moreau M, Carlier T, Strauss O, **Bert J**, Visvikis D, (2015). Detector Modeling in PET List-Mode Reconstruction : Comparison Between Pre-calculated and On-the-Fly Computed System Matrices *Society of Nuclear Medicine and Molecular Imaging Annual Meeting*
- C19 Hamdan I, **Bert J**, Hamitouche C, Dardenne G, Visvikis D, (2015). 3D MRI/CT non-rigid registration for image-guided prostate brachytherapy *International Congress of Computer Assisted Radiology and Surgery*
- C20 Lemaréchal Y, **Bert J**, Boussion N, Falconet C, Pradier O, Visvikis D, (2015). GGEMS-brachy : GPU GEant4-based Monte Carlo Simulation for brachytherapy applications *Varian research partnership symposium*
- C21 Autret L, **Bert J**, Desbat L, Visvikis D, (2015). 3D dose reconstruction in external beam radiotherapy using portal imaging *IEEE Nuclear Science Symposium and Medical Imaging Conference*
- C22 Autret A, Moreau M, Carlier T, Strauss O, **Bert J**, Visvikis D, (2015). Detector modeling in PET list-mode reconstruction : comparison between pre-calculated and GPU capable on-the-fly computed system matrix *Fully Three-Dimensional Image Reconstruction in Radiology and Nuclear Medicine*
- C23 Autret A, Moreau M, Carlier T, Strauss O, **Bert J**, Visvikis D, (2015). Detector Modeling in PET List-Mode Reconstruction : Comparison Between Pre-calculated and On-the-Fly Computed System Matrices *IEEE Nuclear Science Symposium and Medical Imaging Conference*
- C24 Monnier F, Fayad H, **Bert J**, Schmidt H, Visvikis D, (2015). Validation of a combined PET/MR system model for PET simulation using GATE *International Conference on MR-PET and MR-SPECT (PSMR)*
- C25 Monnier F, Fayad H, **Bert J**, Schmidt H, Visvikis D, (2015). Development and Evaluation of a Simultaneous PET/MR Scanner Model Using GATE *IEEE Nuclear Science Symposium and Medical Imaging Conference*
- C26 Mota A M, Cuplova V, Drobnjak I, Dickson J, **Bert J**, Burgos N, Cardoso J M, Modat M, Ourselin S, Schott J, Erlandsson K, Hutton B, Thielemans K, (2015). Establishment of an open database of realistic simulated data for evaluation of partial volume correction techniques in brain PET/MR *International Conference on MR-PET and MR-SPECT (PSMR)*
- C27 Garcia M-P, **Bert J**, Benoit D, Bardies M, Visvikis D, (2015). Accelerated GPU based SPECT Monte Carlo Simulations using GGEMS *IEEE Nuclear Science Symposium and Medical Imaging Conference*
- C28 Garcia M-P, **Bert J**, Villoing D, Reilhac A, Grégoire M-C, Visvikis D, Bardies M, (2014). Hybrid CPU/GPU SPECT Monte Carlo Simulations : The Hexagonal Hole Collimator Case *IEEE Nuclear Science Symposium and Medical Imaging Conference*
- C29 Gaens M, **Bert J**, Lohmann P, Jon Shah N, Visvikis D, Pietrzyk U, (2014). Evaluation of Full Monte Carlo Based Scatter Correction in Brain PET/MR *IEEE Nuclear Science Symposium and Medical Imaging Conference*
- C30 Benhalouche S, **Bert J**, Autret A, Boussion N, Pradier O, Visvikis D, (2014). Imaging and Radiation Therapy : GATE Monte Carlo Simulation of a 6 MV photon beam LINAC and its MV-CBCT Flat Panel for IMRT applications *International Workshop on Monte Carlo Techniques in Medical Physics*
- C31 **Bert J**, Lemaréchal Y, Visvikis D, (2014). Particle navigator for hybrid voxelized/analytical phantoms in Monte Carlo simulation for medical applications *International Workshop on Monte Carlo Techniques in Medical Physics*
- C32 Dupré P-F, Bouzid D, Miglierini P, Pradier O, Visvikis D, **Bert J**, Boussion N, (2014). External dosimetry and in vivo measurements improve surgical comprehension of intraoperative radiotherapy using Intrabeam(TM) *San Antonio Breast Cancer Symposium*

- C33 **Bert J**, Lemaréchal Y, Garrido E, Visvikis D, (2014). GGEMS platform : GPU Geant4-based Monte Carlo Simulation *International Workshop on Monte Carlo Techniques in Medical Physics*
- C34 Gaens M, **Bert J**, Pietrzyk U, Jon Shah N, Visvikis D, (2014). GPU-accelerated Monte Carlo Based Scatter Correction in Brain PET/MR *International Conference on MR-PET and MR-SPECT (PSMR)*
- C35 Lemaréchal Y, **Bert J**, Bousson N, Visvikis D, (2014). GGEMS-brachy : Fully GPU Geant4-based Monte Carlo Simulation for Brachytherapy Applications *European Society for Radiotherapy and Oncology (ESTRO)*
- C36 Monnier F, Fayad H, **Bert J**, Lapuyade-Lahorgue J, Hatt M, Veit-Haibach P, Delso G, Visvikis D, (2014). MR-based PET attenuation correction through the generation of pseudo-CT data from a single MRI sequence *IEEE Nuclear Science Symposium and Medical Imaging Conference*
- C37 Monnier F, Fayad H, **Bert J**, Lapuyade-Lahorgue J, Hat M, Veit-Haibach P, Delso G, Visvikis D, (2014). Generation of pseudo-CT from a single MRI for PET/MR attenuation correction purposes *International Conference on MR-PET and MR-SPECT (PSMR)*
- C38 Gonzalez A J, Sanchez F, Conde P, Aussenhofer S, Gareis D, Pani R, Pellegrini R, Bettiol M, Fabbri A, Majewski S, Stolin A, **Bert J**, Visvikis D, (2014). A Novel Brain PET Insert for the MINDView Project *IEEE Nuclear Science Symposium and Medical Imaging Conference*
- C39 Autret A, **Bert J**, Strauss O, Visvikis D, (2013). Incorporation of Time-of-Flight information in PET List-Mode reconstruction using a projector with accurate detector PSF modeling *IEEE Nuclear Science Symposium and Medical Imaging Conference*
- C40 Autret A, **Bert J**, Strauss O, Visvikis D, (2013). Fully 3D PET List-Mode reconstruction including an accurate detector modeling on GPU architecture *Fully Three-Dimensional Image Reconstruction in Radiology and Nuclear Medicine*
- C41 **Bert J**, Lemaréchal Y, Bousson N, Visvikis D, (2013). New particle navigator for hybrid voxelized/analytical phantoms in Monte Carlo simulations for medical applications *IEEE Nuclear Science Symposium and Medical Imaging Conference*
- C42 **Bert J**, Dubois A, Jan S, Gueth P, Garrido E, Benoit D, Sarrut D, El Bitar Z, Cuplov V, Boursier Y, Brasse D, Buvat I, Morel C, Visvikis D, (2013). Hybrid CPU/GPU GATE : towards GATE V7 *Geant4 International User Conference*
- C43 Bahi Z, **Bert J**, Visvikis D, (2013). Volume Splitting Based Multi-GPUs Implementation for 3D List-Mode PET Reconstruction *Fully Three-Dimensional Image Reconstruction in Radiology and Nuclear Medicine*
- C44 Benhalouche S, **Bert J**, Visvikis D, Pradier O, Bousson N, (2013). Imaging and radiation therapy : GATE Monte Carlo simulation of a MV-CBCT flat panel with specific application in head and neck cancer *American Association of Physicists in Medicine Annual Meeting*
- C45 Benhalouche S, **Bert J**, Bouzid D, Autret A, Visvikis D, Bousson N, (2013). Imaging and Radiation Therapy : GATE Monte Carlo Simulation of a Megavolt Cone Beam CT *Geant4 International User Conference*
- C46 Benhalouche S, **Bert J**, Autret A, Visvikis D, Pradier O, Bousson N, (2013). Imaging and Radiation Therapy : GATE Monte Carlo Simulation of a Megavolt Cone Beam CT *IEEE Nuclear Science Symposium and Medical Imaging Conference*
- C47 Benhalouche S, **Bert J**, Autret A, Visvikis D, Pradier O, Bousson N, (2013). Imaging and radiation therapy : GATE Monte Carlo simulation of a MV-CBCT flat panel with specific application in head and neck cancer *The future of radiation oncology workshop : Imaging, Dosimetry, Biology & Therapy*
- C48 Bouzid D, **Bert J**, Dupré P-F, Benhalouche S, Pradier O, Visvikis D, Bousson N, (2013). Monte Carlo simulation of the Intrabeam<sup>TM</sup> system with the platform GATE for breast cancer *DEGRO 19th Annual Congress*

- C49 Bouzid D, Visvikis D, Dupré P-F, **Bert J**, Pradier O, Boussion N, (2013). Dosimetric validation of an Intrabeam™ GATE model, based on Monte Carlo GEANT4 toolkit, for IORT applications *The future of radiation oncology workshop : Imaging, Dosimetry, Biology & Therapy*
- C50 Bouzid D, Boussion N, Dupré P-F, **Bert J**, Pradier O, Visvikis D, (2013). Personalized 3D dose prediction for Intrabeam™ treatments based on patient CT imaging with Monte Carlo GATE simulations *Geant4 International User Conference*
- C51 Bouzid D, Boussion N, Dupré P-F, **Bert J**, Pradier O, Visvikis D, (2013). Personalized 3D dose prediction for Intrabeam™ treatments based on patient CT imaging with Monte Carlo GATE simulations *The future of radiation oncology workshop : Imaging, Dosimetry, Biology & Therapy*
- C52 Bahi Z, **Bert J**, Visvikis D, (2013). Volume Splitting Based Multi-GPUs Implementation for 3D List-Mode PET Reconstruction *Fully Three-Dimensional Image Reconstruction in Radiology and Nuclear Medicine*
- C53 Lemaréchal Y, **Bert J**, Lefur E, Boussion N, Visvikis D, (2013). GGEMS-brachy : Fully GPU GEant4-based Monte Carlo Simulation for brachytherapy applications *The future of radiation oncology workshop : Imaging, Dosimetry, Biology & Therapy*
- C54 Lemaréchal Y, **Bert J**, Lefur E, Boussion N, Visvikis D, (2013). GGEMS-brachy : Fully GPU GEant4-based Monte Carlo Simulation for brachytherapy applications *Geant4 International User Conference*
- C55 Lemaréchal Y, **Bert J**, Lefur E, Boussion N, Visvikis D, (2013). Monte Carlo simulations on GPU for brachytherapy applications *IEEE Nuclear Science Symposium and Medical Imaging Conference*
- C56 Lemaréchal Y, **Bert J**, Boussion N, Visvikis D, (2013). GGEMS-Brachy : Fully GPU Geant4-Based Efficient Monte Carlo Simulation for Brachytherapy Applications *Medical Physics AAPM* 40 pp 88
- C57 Garrido E, **Bert J**, Chekatt H, Brasse D, Visvikis D, (2013). GPU implementation of Geant4 process for use in proton therapy *Geant4 International User Conference*
- C58 Gaens M, **Bert J**, Pietrzyk U, Shah N J, Visvikis D, (2013). GPU Framework Allowing Fast Monte Carlo Based Scatter Correction for the MR-BrainPET *International Conference on MR-PET and MR-SPECT (PSMR)*
- C59 Gaens M, **Bert J**, Pietrzyk U, Shah N J, Visvikis D, (2013). GPU-accelerated Monte Carlo Base Scatter Correction in Brain PET/MR *IEEE Nuclear Science Symposium and Medical Imaging Conference*
- C60 Gaens M, **Bert J**, Pietrzyk U, Shah N J, Visvikis D, (2013). GPU Framework Allowing Fast Monte Carlo based Scatter Correction for the MR-BrainPET *Geant4 International User Conference*
- C61 Bouzid D, Boussion N, Dupré P-F, **Bert J**, Pradier O, Visvikis D, (2013). Dosimetric validation of an Intrabeam™ GATE model, based on Monte Carlo GEANT4 toolkit, for IORT applications *American Association of Physicists in Medicine Annual Meeting*
- C62 Autret A, **Bert J**, Bahi Z, Strauss O, Visvikis D, (2013). Accurate fully 3D list-mode PET reconstruction on Multi-GPUs *Recherche en Imagerie et Technologies pour la Santé*
- C63 Bouzid D, Boussion N, Dupré P-F, **Bert J**, Pradier O, Visvikis D, (2013). Personalized 3D dose prediction for Intrabeam™ treatments based on patient CT imaging with Monte Carlo GATE simulations *7th Intrabeam User Meeting*
- C64 Bouzid D, Boussion N, Dupré P-F, **Bert J**, Pradier O, Visvikis D, (2013). Personalized 3D dose prediction for Intrabeam™ treatments based on patient CT imaging with Monte Carlo GATE simulations *American Association of Physicists in Medicine Annual Meeting*
- C65 Bouzid D, **Bert J**, Dupré P-F, Pradier O, Visvikis D, Boussion N, (2013). Dosimetric validation of an Intrabeam™ GATE model, based on Monte Carlo GEANT4 toolkit, for IORT applications *7th Intrabeam User Meeting*



- C66 Autret A, **Bert J**, Strauss O, Visvikis D, (2012). Projector with Realistic Detector Scatter Modelling for PET List-Mode Reconstruction *IEEE Nuclear Science Symposium and Medical Imaging Conference* pp 3333-3336
- C67 Bouzid D, **Bert J**, Benhalouche S, Pradier O, Visvikis D, Bousson N, (2012). Monte Carlo simulation on GATE V6.1 of an intraoperative device Intrabeam<sup>TM</sup> for early breast cancers *6th Intrabeam User's Meeting*
- C68 **Bert J**, Perez-Ponce H, Jan S, El Bitar Z, Gueth P, Cuplov V, Chekatt H, Benoit D, Sarrut D, Boursier Y, Brasse D, Buvat I, Morel C, Visvikis D, (2012). Hybrid GATE : A GPU/CPU implementation for imaging and therapy applications *IEEE Nuclear Science Symposium and Medical Imaging Conference* pp 2247-2250
- C69 Bahi Z, **Bert J**, Autret A, Visvikis D, (2012). High Performance Multi-GPU Acceleration for Fully 3D List-Mode PET Reconstruction *IEEE Nuclear Science Symposium and Medical Imaging Conference* pp 3390-3393
- C70 **Bert J**, Visvikis D, (2011). A Fast CPU/GPU Ray Projector for Fully 3D List-Mode PET Reconstruction *IEEE Nuclear Science Symposium and Medical Imaging Conference* pp 4126-4130
- C71 Perez-Ponce H, El Bitar Z, Boursier Y, Vintache D, Bonissent A, Morel C, Brasse D, Visvikis D, **Bert J**, (2011). Implementing Geant4 on GPU for medical applications *IEEE Nuclear Science Symposium and Medical Imaging Conference* pp 2703-2707
- C72 **Bert J**, Dembélé S, Lefort-Piat N, (2008). Novel View Synthesis by Trifocal Tensor : Improvement of View Placement and Application to Microassembly *Mali Symposium on Applied Sciences*
- C73 **Bert J**, Dembélé S, Lefort-Piat N, (2007). Performing Weak Calibration at the Microscale. Application to Micromanipulation *IEEE International Conference on Robotics and Automation* pp 4937-4942
- C74 **Bert J**, Dembélé S, Lefort-Piat N, (2006). Virtual Camera Synthesis for Mircomanipulation and Mircoassembly *IEEE International Conference on Intelligent Robots and Systems* pp 1390-1395
- C75 **Bert J**, Dembélé S, Lefort-Piat N, (2006). Synthesizing a Virtual Imager with a Large Field of View and a High Resolution for Micromanipulation *Proceeding of International Workshop on Microfactories*
- C76 **Bert J**, Dembélé S, Lefort-Piat N, (2006). Toward the Vision Based Supervision of Microfactories Trough Images Mosaicing *International Precision Assembly Seminar 239* pp 250

#### A.4 Communications nationales avec comité de lecture

- c1 Mountris K A, **Bert J**, Bousson N, Valeri A, Schick U, Visvikis D, (2017). DVH-based optimization of LDR prostate brachytherapy using GPU-accelerated MC dosimetry *SURGETICA*
- c2 Djohossou M, **Bert J**, Visvikis D, (2017). Assistance in Prostate Brachytherapy by haptic guidance *SURGETICA*
- c3 Jaouen V, **Bert J**, Hamdan I, Valeri A, Schick U, Bousson N, Visvikis D, (2017). Purely edge-based prostate segmentation in 3D TRUS images using deformable models *SURGETICA*
- c4 Merlin T, Stute S, Benoit D, **Bert J**, Carlier T, Comtat C, Lamare F, Visvikis D, (2017). CASToR : Evaluation of an efficient Data Organization and Processing Code Framework for Multi-modal and Multi-Dimensional Tomographic Reconstruction *Recherche en Imagerie et Technologies pour la Santé*
- c5 Lemaréchal Y, **Bert J**, Bousson N, Garcia M-P, Falconnet C, Pradier O, Visvikis D, (2015). GGEMS-Brachy : GPU Geant4-Based Monte Carlo Simulation for brachytherapy applications *Recherche en Imagerie et Technologies pour la Santé*
- c6 Autret L, **Bert J**, Lemarechal Y, Desbat L, Visvikis D, (2015). 3D dose reconstruction in external beam radiotherapy using portal imaging *Recherche en Imagerie et Technologies pour la Santé*

- c7 Hamdan I, **Bert J**, Hamitouche C, Dardenne G, Visvikis D, (2014). 3D MRI/CT non-rigid registration for image-guided prostate brachytherapy *SURGETICA*
- c8 Lemaréchal Y, **Bert J**, BouSSION N, C Falconnet, Visvikis D, (2014). GGEMS-Brachy : Fully GPU Geant4-Based Monte Carlo Simulation pour des applications en curiethérapie *Journée des doctorants de l'école doctorale SICAM*
- c9 Autret L, **Bert J**, Benhalouche S, Desbat L, Visvikis D, (2014). Reconstruction of 3D dose distribution in external beam radiotherapy using portal imaging *SURGETICA*
- c10 Benhalouche S, **Bert J**, Visvikis D, Pradier O, BouSSION N, (2013). Imagerie en Megavolt cone-beam computed Tomography MV CBCT 6 MV : Simulation et évaluation GATE v6.2 Monte Carlo d'un imageur portal avec application spécifique en ORL *7èmes Journées du Cancéropole Grand Ouest*
- c11 **Bert J**, Perez-Ponce H, Jan S, El Bitar Z, Gueth P, Cuplov V, Chekatt H, Benoit D, Sarrut D, Boursier Y, Brasse D, Buvat I, Morel C, Visvikis D, (2013). Hybrid GPU/CPU modules for GATE platform : imaging and therapy applications *Recherche en Imagerie et Technologies pour la Santé*
- c12 Autret A, **Bert J**, Strauss O, Visvikis D, (2013). Amélioration qualitative et quantitative de reconstruction TEP basée sur architecture graphique *7èmes Journées du Cancéropole Grand Ouest*
- c13 Benhalouche S, **Bert J**, Visvikis D, Pradier O, BouSSION N, (2013). Imagerie en Megavolt Cone-Beam Computed Tomography MV CBCT 6 MV : Simulation et évaluation GATE v6.2 Monte Carlo d'un imageur portal avec application spécifique en ORL *52èmes Journées Scientifiques de Physique Médicale*
- c14 Bouzid D, **Bert J**, Dupré P-F, Benhalouche S, Pradier O, Visvikis D, BouSSION N, (2013). Simulation Monte Carlo du système Intrabeam<sup>TM</sup> avec la plateforme GATE (Geant4) pour le cancer du sein *52èmes Journées Scientifiques de Physique Médicale*
- c15 Wentz T, Fayad H, **Bert J**, BouSSION N, Pradier O, Visvikis D, (2013). Suivi du mouvement respiratoire externe avec une caméra temps-de-vol : application pour la prédiction de la déformation interne *Recherche en Imagerie et Technologies pour la Santé*
- c16 Lemaréchal Y, **Bert J**, Lefur E, BouSSION N, Visvikis D, (2013). Amélioration de la planification du traitement en curiethérapie de prostate par simulation Monte-Carlo complète et rapide utilisant les processeurs graphiques *Journée des doctorants et post-doctorants en biosanté de Bretagne*
- c17 Lemaréchal Y, **Bert J**, BouSSION N, Visvikis D, (2013). Amélioration de la planification du traitement en curiethérapie de prostate par simulation Monte-Carlo complète et rapide utilisant les processeurs graphiques *7èmes Journées du Cancéropole Grand Ouest*
- c18 Gaens M, **Bert J**, Pietrzyk U, Shah N J, Visvikis D, (2013). Grafikprozessorbeschleunigte Monte Carlo Simulation für die Streustrahlkorrektur des MR- BrainPET Scanners *Deutschen Gesellschaft für Medizinische Physik Conference*
- c19 Bouzid D, BouSSION N, **Bert J**, Pradier O, Visvikis D, (2013). Modélisation et validation sur Monte Carlo d'un traitement de métastases vertébrales sur fantôme par Kyphoplastie et RT peropératoire *52èmes Journées Scientifiques de Physique Médicale*
- c20 Bouzid D, **Bert J**, Dupré P-F, Benhalouche S, Visvikis D, Pradier O, BouSSION N, (2013). Simulation Monte Carlo du système Intrabeam<sup>TM</sup> sur GATE et application au cancer du sein *Journée des doctorants et post-doctorants en biologie-santé en Bretagne*
- c21 Bouzid D, **Bert J**, Dupré P-F, Benhalouche S, Visvikis D, Pradier O, BouSSION N, (2013). Simulation Monte Carlo du système Intrabeam<sup>TM</sup> avec la plateforme GATE (Geant4) pour le cancer du sein *7èmes Journées du Cancéropole Grand Ouest*
- c22 Wentz T, Fayad H, **Bert J**, BouSSION N, Visvikis D, (2012). Utilisation d'une camera TOF pour la synchronisation et la modélisation du mouvement respiratoire *Journées scientifiques Nouvelles méthodologies en imagerie du vivant*

- c23 Bouzid D, **Bert J**, Dupré P-F, Benhalouche S, Pradier O, Visvikis V, BouSSION N, (2012). Simulation Monte Carlo du système Intrabeam<sup>TM</sup> avec la plateforme GATE pour le cancer du sein *2ème Journée des doctorants de l'ED SICMA*
- c24 Bouzid D, **Bert J**, Dupré P-F, Benhalouche S, Pradier O, Visvikis D, (2012). Simulation Monte Carlo du système Intrabeam<sup>TM</sup> avec la plateforme GATE pour le cancer du sein *23ème Congrès National de la Société Française de Radiothérapie Oncologique (SFRO)*
- c25 **Bert J**, Dembélé S, Lefort-Piat N, (2006). Vers la Supervision de Microfactories par Mosaicing d'Images *Atelier du Laboratoire Européen Associé*
- c26 **Bert J**, Dembélé S, Lefort-Piat N, (2005). Synthèse de Microimageurs Virtuels pour la Micromanipulation *Atelier du Laboratoire Européen Associé*

## A.5 Ouvrages

- O1 **Bert J**, (2010). Synthèse de vues à partir d'images de microscopes optiques, application à la micromanipulation *Editions Universitaires Européennes, ISBN 6131544018*
- O2 **Bert J**, Asturias F, Penczek P A, (2009). Iterative Step Wise Clustering of 2D EM Projection Data *Houston Medical School, Texas Medical Center, USA*
- O3 **Bert J**, (2007). Synthèse de vues à partir d'images de microscopes photoniques pour la micromanipulation *Mémoire de thèse de doctorat, université de Franche-Comté*
- O4 **Bert J**, (2004). Synthèse de comportements coopératifs dans les systèmes multi-agents par apprentissage par renforcement, application à la microrobotique mobile *Mémoire de DEA, université de Franche-Comté*

## B Textes complets des publications les plus significatives

### B.1 Simulation Monte-Carlo sur architecture GPU

## Geant4-based Monte Carlo simulations on GPU for medical applications

**Julien Bert**<sup>1,5</sup>, **Hector Perez-Ponce**<sup>2,5</sup>, **Ziad El Bitar**<sup>3</sup>, **Sébastien Jan**<sup>4</sup>,  
**Yannick Boursier**<sup>2</sup>, **Damien Vintache**<sup>3</sup>, **Alain Bonissent**<sup>2</sup>,  
**Christian Morel**<sup>2</sup>, **David Brasse**<sup>3</sup> and **Dimitris Visvikis**<sup>1</sup>

<sup>1</sup> LaTIM, UMR 1101 INSERM, CHRU Brest, Brest, France

<sup>2</sup> CPPM, Aix-Marseille Université, CNRS/IN2P3, Marseille, France

<sup>3</sup> IPHC, UMR 7178—CNRS/IN2P3, Strasbourg, France

<sup>4</sup> DSV/I2BM/SHFJ, Commissariat à l’Energie Atomique, Orsay, France

E-mail: [julien.bert@univ-brest.fr](mailto:julien.bert@univ-brest.fr)

Received 31 December 2012, in final form 6 June 2013

Published 29 July 2013

Online at [stacks.iop.org/PMB/58/5593](http://stacks.iop.org/PMB/58/5593)

### Abstract

Monte Carlo simulation (MCS) plays a key role in medical applications, especially for emission tomography and radiotherapy. However MCS is also associated with long calculation times that prevent its use in routine clinical practice. Recently, graphics processing units (GPU) became in many domains a low cost alternative for the acquisition of high computational power. The objective of this work was to develop an efficient framework for the implementation of MCS on GPU architectures. Geant4 was chosen as the MCS engine given the large variety of physics processes available for targeting different medical imaging and radiotherapy applications. In addition, Geant4 is the MCS engine behind GATE which is actually the most popular medical applications’ simulation platform. We propose the definition of a global strategy and associated structures for such a GPU based simulation implementation. Different photon and electron physics effects are resolved on the fly directly on GPU without any approximations with respect to Geant4. Validations have shown equivalence in the underlying photon and electron physics processes between the Geant4 and the GPU codes with a speedup factor of 80–90. More clinically realistic simulations in emission and transmission imaging led to acceleration factors of 400–800 respectively compared to corresponding GATE simulations.

(Some figures may appear in colour only in the online journal)

<sup>5</sup> The first two authors contributed equally to this work.

## 1. Introduction

Monte Carlo simulations (MCS) are using random sampling methods for representing and solving physical and mathematical problems. They play a key role in medical applications, both for imaging and radiotherapy by accurately modelling the different physical processes and interactions between particles and matter (tissues and/or detectors). For example in the medical imaging field, MCS are used in the design of imaging systems, optimization of acquisition protocols, as well as in the development and assessment of image reconstruction processes and associated correction algorithms (Barret *et al* 2005, Rehfeld *et al* 2005, Zhang *et al* 2010). On the other hand, the use of MCS in radiotherapy allows accurate dosimetry calculations within the treatment planning stage (Verhaegen and Seuntjens 2003, Flampouri *et al* 2006, Rassiah-Szegedi *et al* 2007). However, MCS are also associated with long execution times, which is one of the major issues preventing their use in routine clinical practice for both image reconstruction and dosimetry applications. A potential solution to the intensive computational issues of MCS can be based on the use of computer clusters, although this solution may be less realistic within a routine clinical environment given the associated cost and logistics issues (necessary space and informatics infrastructures).

Recently, graphics processing units (GPU) have become in many different domains a low cost alternative solution for the acquisition of high computation power (Nickolls and Dally 2010). Their architecture is able to provide any conventional computer with the computation power of a small cluster. A few studies (Jia *et al* 2010, Toth and Magdics 2010, Hissoiny *et al* 2011, Lippuner and Elbakri 2011, Perez-Ponce *et al* 2011, Jahnke *et al* 2012) have shown that the use of GPU in MCS represents the best way to decrease associated computation time. In all these studies different physics processes extracted from various Monte Carlo simulation codes have been used and implemented on GPU targeting specific applications. The objective of this work was to develop an efficient framework for the implementation of MCS on GPU architectures for medical applications, including both medical imaging and radiation therapy. The main differences between our work and recent publications (Hissoiny *et al* 2011, Lippuner and Elbakri 2011, Jahnke *et al* 2012) is that our simulation framework is common for both imaging and therapy applications, based on the well-validated Geant4 (Allison *et al* 2006) platform. Furthermore, the different physics effects are resolved on the fly directly on GPU without any approximations with respect to Geant4. Finally, in this work we propose an alternative to the Mersenne twister (MT) random number generator, used in all of the other recent implementations, which runs faster and generates random numbers in a more compatible fashion to the GPU architecture and associated memory restrictions.

## 2. Materials and methods

### 2.1. GPU architecture

GPUs are designed as a numerical computing engine taking advantage of a large number of execution threads. Within this context the GPU architecture is conceived for computation intensive highly parallel execution. As such they are designed so that more transistors are devoted to data processing rather than data caching and flow control, as is the case in a CPU. A GPU is organized in several streaming multiprocessors (SMs) each composed of numerous stream processors (SPs) that share control logic and cache. Most recent GPU architectures contain more than 2000 such streaming processors (2688 SPs for a NVIDIA GTX Titan). Every SM handles a number of threads which are organized in blocks, with each thread representing a basic data element to be processed.



As a single instruction multiple data device, all threads of a GPU are executing the same code, called kernel. Once a kernel is launched, the GPU architecture automatically schedules all blocks of threads on the different SMs. Each block assigned to a SM is further divided into units called warps, which can be considered as the smallest executable unit of code. Recent GPU architectures have at least 32 SPs per SM, meaning that a SM processes a single instruction over all of the threads in a warp at a time. This capability to process warps in a parallel way over thousands of SPs renders the GPU a highly parallel computing device.

Threads may access data from multiple memory spaces during their execution. Each thread has private local memory, while each block of threads has shared memory visible to all threads of a block. Although both memory types, local and shared, have a quick access, their size per block remains rather small (16–64 kB per block). In addition, all threads have access to the same global memory. This global memory is the largest one (up to 6 GB), and although it has a high latency compared to the local and shared memory, its bandwidth is still higher than the one provided by recent CPU processors (192 GB s<sup>-1</sup> for a NVIDIA GTX680 and only 25.6 GB s<sup>-1</sup> for an Intel Core i7-3770). Finally, there are also two additional read-only memory spaces, namely the constant and texture memory, accessible by all threads residing within the global memory but cached for efficient access. The constant memory, which is usually limited in size (<65 kB for recent NVIDIA GPU architectures) is often used for variables that provide input values to kernel functions, since these values can be accessed by all threads. On the other hand, texture memory is an alternative way to use cached data residing on the global memory, without the memory size limitation of the constant memory. For a more detailed description of GPU architectures the reader is referred to (Blythe 2008, Nickolls and Dally 2010).

In the case of MCS GPU implementation, the simulation has to be divided into different kernels representing specific processes that will be performed at the same time by all the particles tracked within a voxelized volume. Therefore, any implementation strategy has to be particularly adapted to perfectly fit the specifications and constraints of the GPU architecture. In our applications these aspects govern how variables and constants used for cross-section estimations, tracked particle phase-space information and voxelized phantom materials must be stored. In this work we have used the NVIDIA GPU parallel computing platform CUDA, which allows harnessing in an efficient manner the power of recent GPU architectures.

## 2.2. Global strategy

Our implementation was designed to handle voxelized phantoms and sources that are essential for the medical applications targeted in this work. Similarly to Lippuner and Elbakri (2011), our GPU implementation was conceived to make use of one thread per particle, i.e. a thread handles a given particle from its ‘birth’ to its ‘death’. Using thousands of processing units, thousands of particles can be simulated in parallel by executing the same code on the GPU. This is equivalent to processing in parallel a stack of particles. For an efficient implementation, particles are simulated in different stages of processing stacks. These stages are associated with particle generation, navigation, physics interaction and extraction. This stacking approach computes the same process for every particle available in the stack. This synchronization reduces the impact of conditional branching due to the pseudo-stochastic nature of MCS and allows for a better occupancy of the GPU computation. The simulation runs all these stages in a loop until it simulates the total number of particles requested. The strategy follows the same principle as in Jahnke *et al* (2012), by activating flags for each particle to enable or disable the physics interaction that must be applied. This means that no copying or sorting is performed by the CPU before each kernel call. Therefore all processes are completely handled by the GPU.

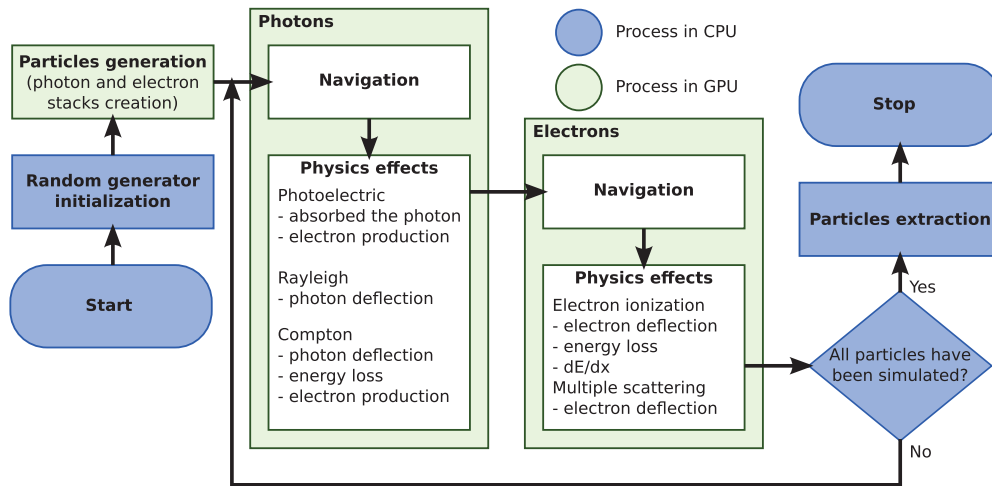


Figure 1. Flowchart of the GPU implementation used in the presented framework.

In our implementation, two stacks of particles are used, one for photons and another for electrons. A thread accesses to the same slot position within both stacks. The electron stack can be considered as a temporary particle buffer. During the photon tracking if an electron is produced, the same thread will pause the photon simulation to handle the new secondary particle stored temporarily within the electron stack. Once the electron tracking is done, the particle is removed from the electron stack and the thread re-activates the photon tracking. This hierarchical tracking process is repeated each time an electron is created as a secondary particle from a photon interaction. This approach has the advantage of handling any number of electrons produced by a photon with a minimum memory requirement. Since each electron is associated to a photon and handled one by one requiring a single memory slot at a time both photon and electron stacks have the same size.

Different physics processes are involved during the photon/electron tracking. When a photoelectric effect occurs, the photon is absorbed and an electron is created. The electron tracking is then simulated by following the electron ionization or multiple scattering effect until its energy is lower than the energy cut defined by the user. In our implementation, secondary particles are only produced by photon interactions. Electron interactions do not produce secondary electrons. Considering a Compton scatter, the photon will be deflected and part of its energy lost. The particle is then paused and the corresponding electron is created and activated (like for the photoelectric effect). Once the electron is simulated, the simulation of the photon is re-activated so that it continues its 'travel'. On the other hand, Rayleigh scattering does not produce any secondary particles. Figure 1 gives a flowchart of the global approach used in this work. The whole simulation is processed on GPU until the total number of simulated photons has been reached. This implies that every electron produced by a photon has been completely simulated.

### 2.3. Pseudo-random number generator

MCS are based on the quality of the sequence of pseudo-random numbers used for sampling. A reference in MCS is the MT generator (Matsumoto and Nishimura 1998). This pseudo-random number generator (PRNG) provides a period of  $2^{19937} - 1$ . However, within the context of

**Table 1.** Comparison of PRNGs selected from TESTU01.

	Park–Miller	MT	Brent
Period	$2^{31} - 1$	$2^{19937} - 1$	$2^{256} - 1$
Number of failed tests	45	4	0
Size of the state (number of 32bits)	1	624	8
Execution time in CPU (s)	3.9	4.3	4.2
Execution time in GPU (ms)	4.0	546.0	12.0
Acceleration factor between GPU codes (versus MT)	$\times 137$	$\times 1$	$\times 46$

efficient MCS implementation on GPU architectures, there are a number of issues associated with the use of this PRNG. Each time that a number is required, this generator will provide 624 numbers. In a GPU, the memory allocated per thread is too small to store all these numbers and they must be stored into the global memory, which is equivalent to computational efficiency losses since access to the global memory penalizes computational performance. For this reason, the search for an alternative PRNG that best fits the GPU architecture was undertaken in this work. Within this context we based our research on the battery test TESTU01 (L’Ecuyer and Simard 2007) using the following selection criteria:

- high periodicity;
- low number of failed tests within the battery test;
- fast times for the generation of  $10^8$  random numbers.

From this battery test, two PRNGs were selected; namely the Park–Miller generator (Park and Miller 1988) particularly for its easiness of GPU implementation, and Brent-XOR256s generator (Brent 2007) for its performance in all of the tests considered. Despite the fact that the Park–Miller is faster than the Brent-XOR256s generator, its low periodicity has led us to select the latter for our implementation showing the best compromise in terms of overall performance in the battery tests (table 1).

The most significant difference between the Brent-XOR256s PRNG and the GPU version of the MT PRNG implemented in L’Ecuyer and Simard (2007) is that the Brent-XOR256s PRNG allows the calculation of random numbers one at a time, meaning that each thread can handle its own PRNG. This is performed without need of pre-calculations, storage and so-called ‘atomic operations’ that are used to determine what random number has already been used in the MT implementation (L’Ecuyer and Simard 2007). In addition MT PRNG failed at four tests provided by the battery test TESTU01, clearly demonstrating the relative superiority of the Brent PRNG.

#### 2.4. Physics effects

Different physical processes have been implemented. These include the main physical interactions of photons with matter, provided by the Livermore and standard models available in Geant4. The two models are accurate within different particle energy ranges. These correspond to 250 eV up to 1 GeV and from 1 keV to 10 PeV for the Livermore (mainly used for low-energy particle simulations) and the standard models respectively. Both models are well validated within Geant4 (Allison *et al* 2006) and users can chose a model according to their application requirements. From the Livermore model, the Compton and Rayleigh scattering were implemented, in addition to the photoelectric effect for low energy. From the standard model, only the Compton scattering and the photoelectric effect were included, since the Rayleigh scattering is defined only for the Livermore model in Geant4. Their implementations are based on an adaptation of the Geant4 code for GPU. Secondary particles (for instance  $e^-$ )

**Table 2.** GPU memory overview for the Livermore model.

Effect	Data type	Constant memory (bytes)	Texture memory (kbytes)
Photoelectric	Cross-sections	808	841
	Sample $e^-$	6 564	–
Compton	Cross-sections	12 780	89
	Scattering	20 348	119
	Sample $e^-$	0 <sup>a</sup>	–
Rayleigh	Cross-sections	11 280	855
	Scattering	808	115

<sup>a</sup> Same data used for the Compton scattering.

**Table 3.** GPU memory overview for the standard model.

Effect	Data type	Constant memory (bytes)	Texture memory (kbytes)
Photoelectric	Cross-sections	20 832	–
	Sample $e^-$	6 564	–
Compton	Cross-sections		Klein–Nishina model
	Scattering		
	Sample $e^-$		
eIonization	Cross-sections		Möller model
	Scattering		
	$dE/dx$		
Multiple scattering	Cross-sections	1 588	Urban model
	Scattering		

are considered as well in our implementation. Within this context, only the standard model of electron ionization and multiple scattering effects based on the Möller model and Urban model respectively were implemented. All cross-sections, scattering angles and energy loss for photons and electrons are calculated on the fly according to the particle energy and interaction medium, exactly as in Geant4 without introducing any approximations from the use of pre-calculated tables.

For both the Livermore and standard models, the photoelectric cross-sections are calculated by log–log interpolation from a database stored in the constant memory of the GPU. Secondary electrons are computed based on shell data (number of shells, binding energies, etc) stored in the constant memory as well. The same approach is used for Rayleigh scattering, except that the data is stored in the texture memory. Compton cross-sections determined with the Livermore model also use data stored in the texture memory. In the case of the standard model, Compton cross-sections, scattering angles and delta ray secondary electrons are computed analytically by using the Klein–Nishina formula and therefore there is no need for specific memory allocation. Coherent scattering is determined with the Livermore model by using form factors stored in the texture memory. Basically, the computation of the Rayleigh cross-section is similar to the Compton cross-section computation, but additional data stored in the GPU constant memory are used to compute the Doppler broadening effect. Data used for the computation of photon cross-sections were assigned to different types of GPU memory according to their sizes. For the electron ionization (eIonization) from the standard model, cross-sections, scattering angles and ionization energy loss per path length ( $dE/dx$ ) are computed analytically by using the Möller model. Similarly the Urban model from the standard model is used to compute analytically cross-sections and scattering angles for the multiple scattering effect. Tables 2 and 3 summarize all the physics effects implemented on GPU together with their corresponding GPU memory assignments. In the case of using

analytical models associated with no specific memory requirements, the corresponding model is instead mentioned in table 3.

### 2.5. Particle navigation

The navigation of each particle consists in determining its mean free path within the voxelized phantom before its next interaction. This distance is randomly defined according to the total cross-section. In order to avoid intensive computation associated with new calculations every time a particle finds a new material, the Woodcock tracking method (Woodcock *et al* 1965, Carter *et al* 1972) was implemented. This method allows for a regular sampling along the particle pathway without computing cross-sections for every voxel. The definition of materials has been implemented in the same way as handled in Geant4, with materials' mixture and elements' properties described in constant memory, thus allowing navigation within complex voxelized phantoms. New materials can be easily added by defining their compositions similar to Geant4.

### 2.6. Particle interaction

Once the navigation of the particle is finished, a GPU kernel selects and applies one type of interaction on every particle. According to the particle current location and energy, cross-sections are computed for all physics effects and the cumulative probabilities are determined for the entire process. Then a random number is used to select one type of interaction according to the cumulative probability values. If a scatter is selected to be the next interaction, quaternion geometry is used to quickly deflect the particle while using a minimum number of GPU operations. In order to reproduce the Geant4 implementation, particle deflection calculations have been extracted from the CLHEP software and implemented on GPU.

### 2.7. GPU implementation

The data structure on CPU architectures is usually defined as an array of structures. Within such a structure definition, a particle stack is defined as a data vector containing particles, themselves defining a structure containing data (particle energy, position, etc). Such a data structure is not optimized for GPU architectures due to the way a thread accesses memory. A GPU stack of particles was instead defined as a structure of arrays allowing a coalesced memory access by the threads. In this case the particle stack is a structure containing separate data vectors, each one containing for every particle the same kind of information. The final stack residing on the global memory contains multiple arrays; namely one for every particle energy, three for every position, three for every direction, eight for every PRNG state, one that contains every particle status and a last array containing every flag that defines whether the particle has completed the simulation. Considering this implementation each particle requires 62 bytes on the global memory. For example a simulation using two stacks (photons and electrons) with a total of  $5 \times 10^6$  particles requires 620 MB of global memory. The stack size is adjusted according to the global memory available on the GPU.

In terms of the random number handling, each individual thread can get a random number on the fly by calling the Brent PRNG device function anywhere within a kernel. For every particle a thread has to read the current PRNG state residing on the particle stack, get a new random number and finally update the PRNG state. Since each particle maintains individual PRNG state, each thread is allowed to have its own PRNG independently of the others threads. Different random seeds are used for every independent PRNG, hence producing an

uncorrelated series of random numbers. Within this context, the user firstly provides a global seed represented by an integer number. This number is used to initialize a random generator on CPU (the one provided by the C standard library). From this random generator a list of random numbers is generated. This list is finally copied to the GPU, with each of these values being used as a random seed for the GPU PRNGs.

In terms of kernels only three were defined, one to fill the particle stack with new particles, one to perform the navigation within the voxelized phantom and a last one for the application of the physics interaction after each step. All kernels are performed sequentially, and repeated until no particle remains on the stack. Due to the complexity of the MCS each kernel does not use shared memory. The number of threads per block was defined by using the CUDA occupancy calculator provided by NVIDIA. Within this context the occupancy calculator provides an optimal configuration of block thread size according to the number of registers used for each kernel, the card computational capability and the required shared memory. The number of threads per block is architecture dependent and must be chosen for each GPU (for the NVIDIA GTX580 a block of 256 threads was used for all kernels). The number of blocks is then calculated according to the number of threads per block and the size user defined particle stack. The materials that can be used in the definition of the voxelized phantoms are stored using 1D texture bound to the linear memory. Each element was defined using a 2 bytes format limiting the number of materials to 65 536 (which is largely sufficient for the medical applications targeted). A voxelized anthropomorphic phantom of  $200 \times 200 \times 200$  voxels needed only 16 MB of texture memory.

The final GPU code was compiled with CUDA 5.0 by using the fast math option and single precision float numbers. The choice of the CUDA language for the proposed implementation has been motivated by the numerous features associated with the maturity of CUDA relative to the OpenCL GPU programming language. However, the actual CUDA code proposed in this work will be easy to migrate since the code structure framework chosen is close to the OpenCL language. Other GPU related portability issues may be associated to overall memory requirements. Considering the proposed implementation a complete simulation using the Livermore model requires 53 kB and 2 MB of constant and texture memory respectively, whereas the standard model including electron processes requires only 29 kB of constant memory. This is largely manageable considering that most current GPUs have a 65 kB of constant memory available. On the other hand, the use of atomic operations on 32 bits float numbers imposes a minimum GPU requirement. The proposed code is then compatible with the Fermi (in use from 2010 onwards) or more recent NVIDIA GPU architectures.

## 2.8. Validation study: physics

**2.8.1. Cross-sections.** Validation consisted in assessing GPU interaction calculations by comparing it to the cross-sections determined by Geant4. For this purpose, we computed separately on GPU water cross-sections of seven different implementations of cross-section calculations, three from the Livermore model (Photoelectric, Rayleigh and Compton), and four from the standard model (Photoelectric, Compton, eIonization and multiple scattering). Cross-sections were estimated within an energy range between 1 keV and 1 MeV.

**2.8.2. Photon scattering and energy distribution.** We used a voxelized water cube phantom of  $100 \times 100 \times 100$   $4^3$  mm<sup>3</sup> voxels with a centrally positioned source that emits 60 keV photons isotropically.  $5 \times 10^6$  particles both with the GPU and Geant4 codes were simulated. Scattered particle data were stored only for the first interaction. Based on independent runs for



Rayleigh (Livermore model only) and Compton scattering (Livermore and standard models), physics interactions were cross validated between the GPU and Geant4 implementations.

A last experiment based on the previous voxelized water cube and its isotropically emitting source was used to assess the energy distribution of particles escaping the voxelized phantom. This validation assessed the full simulation framework that involved physics interactions and navigation. A first batch of ten independent runs with different seeds and  $10^7$  photons per run was simulated. This simulation included all the physics effects from the Livermore model (photoelectric effect, Compton and Rayleigh scattering). These simulations were repeated in a second batch by replacing the photoelectric effect and Compton scattering with the ones provided by the standard model. During simulation, the number of interactions for each interaction type was counted. Average and standard deviations were then computed from the ten independent simulations. Finally, the energy distribution was plotted for each simulation from energies stored for every particle.

*2.8.3. Electron scattering and energy distribution.* In this case a larger voxelized water cube phantom of  $400 \times 400 \times 400 \text{ } 2^3 \text{ cm}^3$  voxels was simulated, including a centrally arranged source isotropically emitting photons with a uniform energy distribution between 10 keV and 8 MeV. From the standard model, photoelectric and Compton interactions were activated separately but always associated with the eIonization effect. A total of  $5 \times 10^6$  photons were simulated. Secondary electrons' energies and emission angles, i.e. the solid angles between the incident photons direction and the produced electrons direction, were stored as a function of the precursor photon energies. During simulation, scattering angles and ionization energy loss per path length ( $dE/dx$ ) were stored for every electron. GPU results were compared against Geant4 results.

*2.8.4. Computation time evaluation.* Run time of each GPU simulation was compared against the same configuration Geant4 simulations under the same conditions in terms of parameters and physics effects. A NVIDIA GTX580 GPU with 512 cores operated at a clock frequency of 1.23 GHz was used. For the Geant4 simulations, a single core of an Intel Core i7 with a frequency of 3.4 GHz was used.

## 2.9. Validation study: applications

*2.9.1. Emission tomography.* The first application based validation study of the proposed GPU implementation was in emission tomography. The thoracic and abdominal regions of the NCAT (NURBS based Cardiac Torso) (Segars 2001) voxelized phantom were used, involving a total of  $46 \times 63 \times 128$  voxels ( $4 \times 4 \times 4 \text{ mm}^3$ ). For this phantom displayed in figure 2, organs are associated with a label defining an activity level and an attenuation coefficient corresponding to the different tissue characteristics (12 different tissue types were used in this work). A lung tumour was included in the digital phantom based on previously proposed methodology (Le Maitre *et al* 2009). The activity levels used for each structure, emitting pairs of gamma rays of 511 keV, were derived from region of interest analysis on corresponding clinical images used as a model for designing the simulated phantom. The simulation was performed by considering photoelectric and Compton scattering processes provided by the standard model and Woodcock tracking (same for CPU and GPU implementations). The overall simulated activity was 28.7 MBq and a 10 min acquisition was modelled, with all particles escaping the phantom stored in a phase-space file.

In the case of the medical imaging simulation examples the comparison was based on the use of the GATE (Geant4 Application for Tomographic Emission) MCS platform (Jan *et al*



**Figure 2.** A transaxial slice from the digital phantom used for the emission tomography application showing, (a) tissue attenuation (12 different tissue types), and (b) normalized activity distribution maps.

2011). Based on the Geant4, GATE is an international collaborative development providing an open source platform able to perform complex MCS based on simple micro-commands. GATE uses Geant4 as the MCS engine concerning physics processes, particle navigation, materials definition, etc. It has been used in the past for the generation of realistic medical image simulations in emission tomography considering the use of clinical datasets based anthropomorphic voxelized phantoms (Le Maitre *et al* 2009) and accurate modelling of complete imaging devices (Lamare *et al* 2006).

Within the context of this comparison the simulation of the same voxelized volume was considered using the proposed GPU implementation and standard GATE. For both the standalone GPU and standard GATE simulations common characteristics were used in terms of simulation (phantom geometry, activity distribution, tissue attenuation characteristics, physics and navigation processes), eliminating the potential for run time discrepancies based on differences in the simulation setups. For each simulation the total run time was evaluated.

**2.9.2. Transmission tomography.** A second application based validation was designed to perform transmission tomography based on a close to cone beam CT geometry, by simulating a single x-ray projection. A realistic x-ray spectrum was generated using the TASMIP model (Boone and Seibert 1997) considering a classic tube voltage of 120 kVp and a 2 mm aluminium filter. This spectrum was directly used by the GPU implemented source. The cone beam source had a rectangular shape of  $1.3 \times 1.3 \text{ mm}^2$ , emitting particles from an  $8^\circ$  aperture. From a thoracic patient CT, a phantom was built by automatically transforming Hounsfield units into materials through density conversion given by (Schneider *et al* 2000). The final phantom consisted of 42 materials and  $275 \times 230 \times 175$  voxels with a spacing of  $1.27 \times 1.27 \times 2.0 \text{ mm}^3$ . Finally, a flat panel detector was simulated (field of view of  $350 \times 350 \text{ mm}^2$ , pixel size of  $1 \times 1 \text{ mm}^2$ ) and used to count the number of detected particles. The phantom was placed over the detector, with a distance of 1.8 m between the x-ray source and the detector. Similar to the emission tomography example, the same simulation set up and configuration was performed using standard GATE and the proposed standalone GPU implementation. In contrast to the emission tomography example where the comparison concentrated only on the particle tracking within a voxelized volume, in the transmission tomography the standard GATE/standalone GPU comparisons involved the complete simulation process (source, phantom and flat panel detector tracking). 2D projection images were recovered for both simulations considering a total of  $2 \times 10^9$  photons emitted from the x-ray source. Finally, for each implementation the total run time associated with the complete simulation was measured.

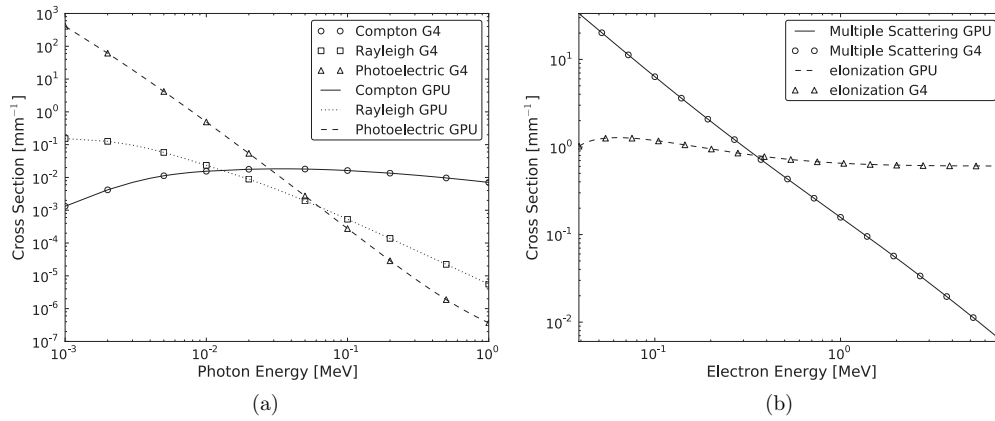


**Figure 3.** Water cross-sections given by (a) photon effects from the Livermore model and (b) electron effects from the standard model calculated by the Geant4 and GPU implementations plotted as a function of particle energy.

### 3. Results

#### 3.1. Cross-sections

The comparison of the resulting cross-sections from the Livermore model are plotted as a function of photon energy in figure 3(a). Identical cross-section values were obtained for the Geant4 and GPU implementations. The same evaluation for the cross-sections provided by the standard model was performed. Values were also identical for the Geant4 and GPU implementations (data not shown). A similar conclusion can be drawn by comparing the cross-sections for eIonization and multiple scattering between Geant4 and GPU simulations in figure 3(b).

#### 3.2. Photon scattering and energy distribution

Histograms of coherent scattering angles determined with the Livermore model are plotted in figure 4(a). Identical distributions were obtained for the Geant4 and GPU codes. Figure 4(b) represents the same histogram for Compton scattering angles determined with the Livermore model. Scattering angle distributions for both the Geant4 and the GPU implementations also match perfectly. Corresponding distributions of Compton scattering angles were also determined for the standard model (data not shown). In addition to the assessment of incoherent scattering angle distributions, the energy of the scattered photons as a function of the scattering angle was measured. Energy losses versus scattering angle were the same for the Geant4 and GPU implementations for both the Livermore and standard models (data not shown).

From the first batch of full simulations, interaction statistics during the simulation for the Livermore model were computed. The run time of one amongst the ten simulations performed was 4320 s for Geant4, compared to 51 s for the GPU implementation, corresponding to a speedup of  $\times 84$ . Based on the ten simulations, all photon phase-space statistics were merged together for a total of  $13 \times 10^6$  particles. The resulting phase-space was used to plot the histogram of particle energy over 400 bins. To improve comprehension only the energy of the scattered photon was plotted in figure 5(a). As can be seen both distributions derived from the Geant4 and GPU implementations fit perfectly. Statistics values between the Geant4 and GPU implementations are compared in table 4. The average number of interactions

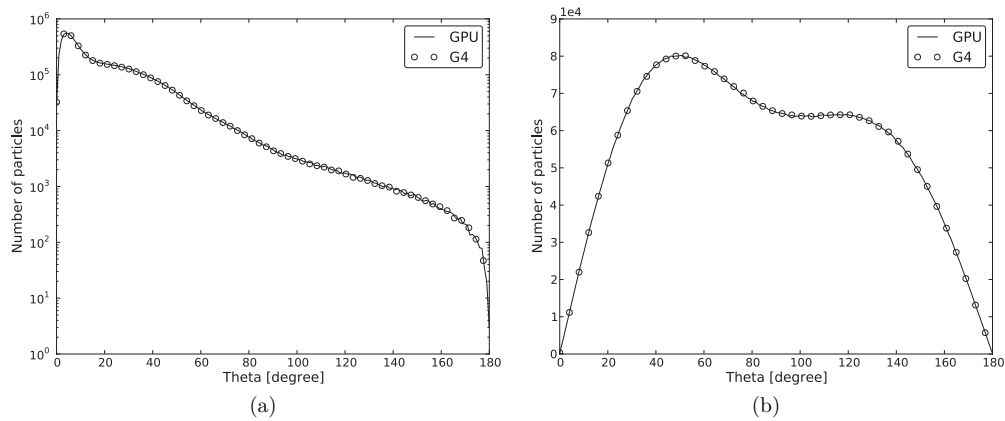


**Figure 4.** Distributions of the (a) Rayleigh scattering angles and (b) Compton scattering angles simulated by the Geant4 and GPU implementations based on the Livermore model.

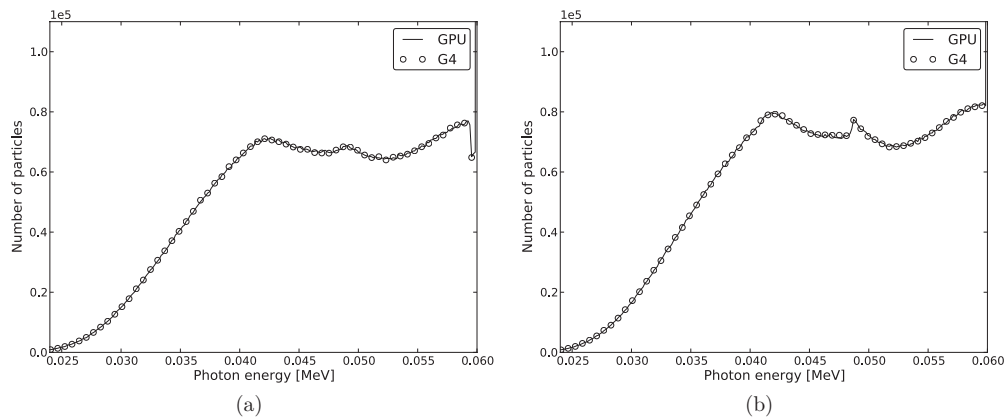


**Figure 5.** Scattered photon energy distributions simulated with the photoelectric, Compton and Rayleigh effects by the Geant4 and GPU implementations based on the (a) Livermore model and (b) standard model.

**Table 4.** Statistics from complete simulations based on the Livermore model. Based on ten simulations.

		Geant4	GPU	$ \epsilon $
Number of PE	ave	8689 483	8690 738	1255
	$\sigma$	117.1	979.3	
Number of Compton	ave	40 514 346	40 509 366	4980
	$\sigma$	11 003.0	9539.8	
Number of Rayleigh	ave	4909 328	4908 793	535
	$\sigma$	2679.4	1756.2	

were about the same for the Geant4 and GPU codes. Most of the standard deviations ( $\sigma$ ) were equivalent, except for the value of the photoelectric effect that was slightly different. Indeed, the small number of simulations (10) used to estimate standard deviations involve estimation errors that are consistent with the differences observed between the standard deviation values.

**Table 5.** Statistics from complete simulations based on the standard model. Based on ten simulations.

		Geant4	GPU	$ \varepsilon $
Number of PE	ave	8577 230	8578 760	1530
	$\sigma$	1058.5	913.6	
Number of Compton	ave	41 696 249	41 699 577	3328
	$\sigma$	6793.6	7046.5	
Number of Rayleigh	ave	5032 059	5032 840	781
	$\sigma$	2167.9	2577.2	

The difference ( $\varepsilon$ ) between the number of interactions in each type of effect did not exceed 0.014% for the photoelectric effect, where the average number of interactions was 8689 483 for Geant4 and 8690 738 for the GPU code.

The same analysis was repeated with the second batch simulations, where Compton scattering and photoelectric effects were provided by the standard model. The run time for a simulation was 4200 s for Geant4 and 49 s for the proposed GPU implementation, leading to a speed up factor of nearly 86. Statistics of interactions determined over ten simulations are summarized in table 5. Similarly to previous interaction statistics simulated with the Livermore model, values were closely identical. The larger difference between the number of interactions considering the photoelectric effect was 0.017% with an average of 8577 230 and 8578 760 interactions estimated from Geant4 and from the GPU implementation respectively. In this comparison, standard deviations were nearly the same. After merging all the ten simulations into one, we obtained a file containing  $14 \times 10^6$  particles. Histograms of the energy distributions of the scattered photons are given in figure 5(b). Both plots determined from the Geant4 and GPU codes are identical. Energy distributions plotted in figure 5 highlight the difference between the Livermore and standard models for a given simulation.

Overall, this study validates the proposed GPU implementation of the main physics effects extracted from both the Livermore and standard models. Considering that these experiments were based on a complete simulation including navigation, these results provide a global assessment of our GPU implementation against Geant4, considering the same physical processes. This evaluation shows that calculations from the proposed GPU implementation have not introduced any bias on physical effects compared to the corresponding Geant4 results.

### 3.3. Electron scattering and energy distribution

Mean energy distributions of secondary electrons given by the photoelectric and Compton scattering provided by the standard model were plotted in figure 6(a) as a function of photon energy. This distribution was obtained by averaging the electrons energy over photon energy bins of 10 keV. Results from Geant4 and the GPU implementation show a complete agreement. A similar conclusion can be drawn by comparing the mean of the emission electron angles relative to the primary incident photon direction, considering photon energy bins of 10 keV in figure 6(b). From data obtained during the simulation on every electron, histograms of the electron ionization scattering angles given by the Geant4 and the GPU implementations based on the standard model are plotted in figure 7(a). Identical distributions were obtained for the Geant4 and GPU codes. The final assessment for the electron ionization was a comparison between Geant4 and the GPU code for the ionization energy loss per path length ( $dE/dx$ ) regarding electron energy. The resulted plot in figure 7(b) shows a perfect agreement.

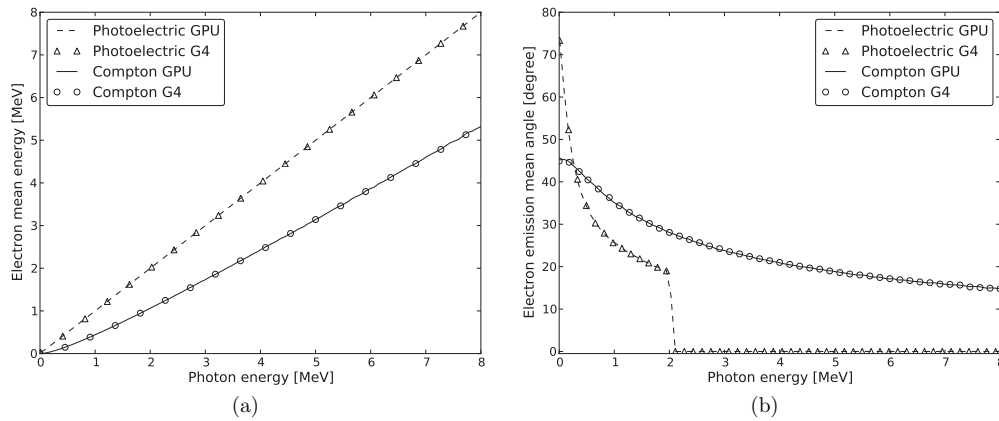


**Figure 6.** Distributions of the (a) mean energy and (b) mean angle of secondary electrons produced by photoelectric and Compton effects by the Geant4 and GPU implementations based on the standard model. The distribution was obtained by averaging electron energy and emission angle values over photon energy bins of 10 keV.

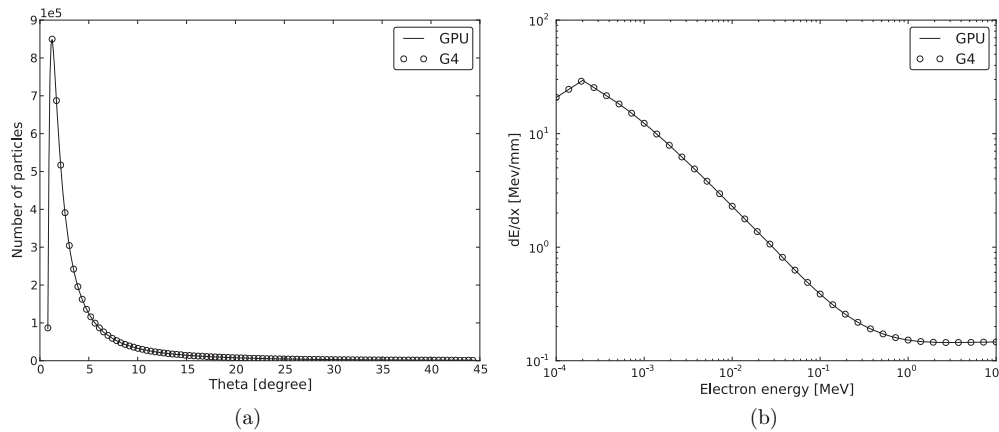


**Figure 7.** Distributions of the (a) electron ionization scattering angles and (b) ionization energy loss per path length ( $dE/dx$ ) simulated by the Geant4 and GPU implementations based on the standard model.

### 3.4. Validation studies: applications

**3.4.1. Emission tomography.** For the emission tomography simulation, the total run time for simulating one million particles on GATE was 151 s against only 385 ms for the standalone GPU implementation, thus an acceleration factor of 392. Using the phase-space files given by both simulations, figure 8 shows a comparison of the scattered photon energy distribution by plotting the number of particles as a function of the detected photon energy. Results show a very good agreement between GATE and the proposed standalone Geant4 GPU implementation.

**3.4.2. Transmission tomography.** Similar conclusions in terms of accuracy and execution times can be drawn for the transmission imaging application. The total run time for simulating the  $2 \times 10^9$  photons was 12 days on GATE compared with only 22 min on the corresponding GPU simulation. This corresponds to 532.8 s and 650 ms for simulating one million photons



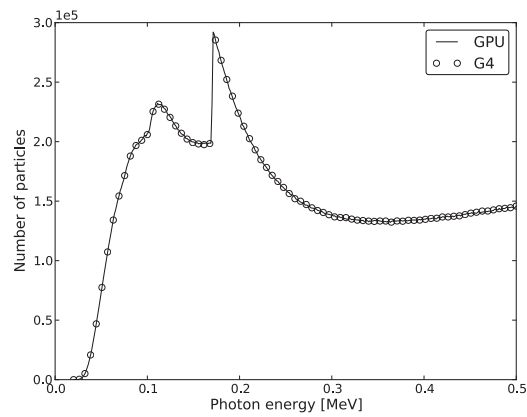


**Figure 8.** Energy distribution for scattered photons from emission tomography imaging simulation using GATE and the Geant4 GPU implementation.

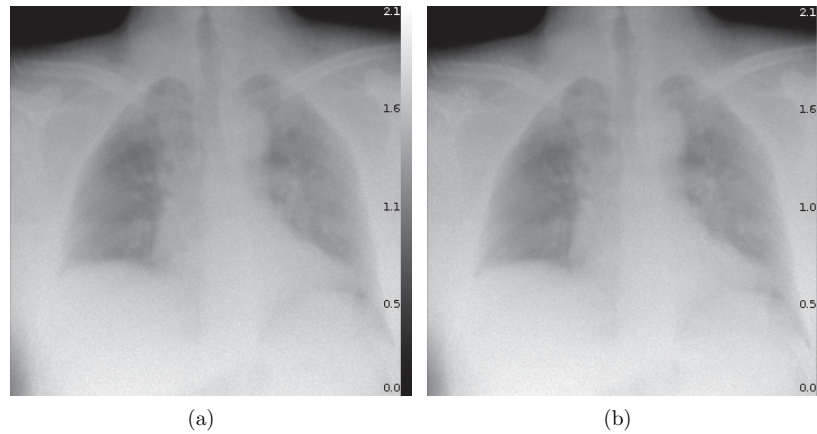


**Figure 9.** 2D projections recovered by the detector of the transmission imaging application using the (a) GPU simulation and (b) GATE simulation.

using GATE and the GPU code respectively. The GPU implementation was 819 times faster than running conventional CPU simulations with GATE. Projections from both simulations are shown on figure 9. Profiles shown in figure 10 through the 2D projections obtained using GATE and the standalone GPU implementation demonstrate the close agreement between the two simulations.

#### 4. Discussion

Despite the potential key role that MCS can play in medical imaging and therapy applications their widespread use in clinical practice has been largely hampered by the long associated calculation times. Different solutions have been proposed including the use of computer clusters and more recently GPUs, which have the advantage of high computational power per unit cost. However, the implementation of physics Monte Carlo simulation calculations

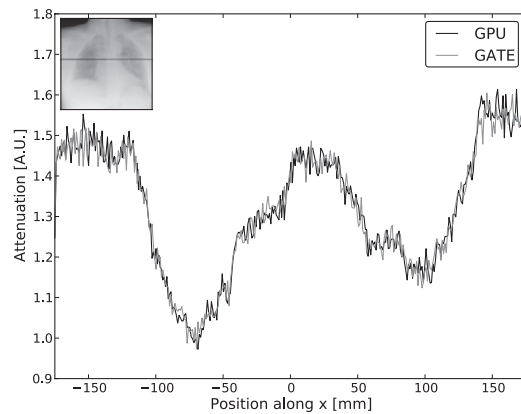


**Figure 10.** Profiles through the 2D projections obtained using GATE and the GPU implementation for the transmission imaging application. To the upper left, the horizontal line on the 2D projection indicates the location of the profiles.

on GPU architectures poses certain challenges if one is to allow the full GPU potential to be realized and its power to be harnessed in an efficient and optimized manner.

Within this context a number of recent works have described GPU implementations considering various physics effects provided by different Monte Carlo codes, with examples including EGS (Lippuner and Elbakri 2011) and PENELOPE (Hissoiny *et al* 2011, Badal and Badano 2009). In each of these cases a single particular application was targeted (imaging or radiotherapy) associated with the implementation of only the corresponding physics processes. In this work we have privileged the use of the well-validated Geant4 platform offering a wide variety of processes, providing the potential for the use of more than standard photon and electron physics effects (protons, optical photons, hadrons). Although, only photon and electron physics processes were implemented in this work, the proposed GPU implementation framework of the MCS structure, facilitates a straightforward addition of other Geant4 physics processes. In addition, our GPU implementation proposes, similarly to Geant4, an easy way to describe tissue properties by defining material mixtures, allowing larger flexibility in terms of simulations especially for medical applications.

A recent work in Jahnke *et al* (2012) has also proposed the GPU implementation of some physics effects provided by Geant4. However, there are fundamental differences with our work residing in the manner the particle physics processes have been implemented on GPU. Firstly, in our work the computational codes from Geant4 and CLHEP libraries, involved in the estimation of the physics and particle tracking, have been extracted from the Geant4 source code. They have been subsequently adapted for the GPU environment implementation and validated against Geant4. These validations have shown, as expected, a very close agreement between the Geant4 physics processes and the GPU implementation for both photons and electrons considering the standard and Livermore models. Differences between the Geant4 CPU and GPU implementations in terms of the number of particle interactions, considering both photon and electron processes, were below 0.018%. The direct use of the Geant4 source code avoids any approximations that may be associated with the alternative approach (Jahnke *et al* 2012), where pre-calculated values extracted from Geant4 are inserted as tables in the GPU. Consequently the proposed method is less susceptible to introducing bias on the MCS results. Secondly, there are also differences associated with the way electrons and photons are processed. In our proposed implementation, photons and electrons are stored in different

stacks, rather than the same stack. Using two stacks, resolves the issue related to the choice of the number of empty slots needed to store secondary particles. As the same thread alternatively tracks the photon and its associated electron, any number of electrons can be considered in the simulation process. A thread is always tracking a particle (photon or electron) avoiding the case of idle threads, hence maximizing the GPU occupancy when few electrons are produced. On the other hand each thread handles different particles and resolves different physics effects, leading to a thread divergence, which has a negative impact on the overall computation time. We have estimated that 40% of the simulation run time is lost as a result of thread divergence. However due to the nature of the simulation it is difficult to avoid thread divergence in an efficient manner. A potential solution would consist of sorting particles according to their energies, physics effects or positions. However, as previously explained by Jahnke *et al* (2012), such a solution does not improve overall global run times due to the cost associated with the sorting process repeated during the simulation. In this work we have also concentrated efforts in the adaptation to the GPU environment of an appropriate PRNG for physics MCS considering the medical applications targeted. Within this context our proposed version of the mixed combined PRNG (Brent-XOR256s) for GPU has shown good acceleration ( $\times 46$ ) as compared to the NVIDIA MT PRNG version. In contrast the modified version of the MT PRNG proposed in Jahnke *et al* (2012) was  $\times 4$  faster than the NVIDIA MT implementation. On the other hand, the re-utilization of random numbers proposed as an alternative to improve acceleration rates (Jahnke *et al* 2012) could indeed bias simulation results.

For a volume comprising 1 million voxels filled with water, the computational gain relative to Geant4, considering the use of either standard or Livermore physics models, was a factor of between 80 and 90. In terms of clinical applications an anthropomorphic phantom simulation ( $371 \times 10^3$  voxels and 12 different tissue type properties), based on a typical activity distribution and acquisition times encountered in clinical PET imaging practice, led to nearly a factor of 400 in terms of computational time improvement relative to the use of GATE. In the case of projection transmission imaging, and within the same comparison framework, an acceleration factor of 819 was obtained for a phantom based on a clinical acquisition ( $11 \times 10^6$  voxels and 42 different tissue types).

The larger acceleration factors obtained for the simulations associated with the clinical applications relative to that associated with the simple water box phantom simulation is related to a number of factors. Firstly different physical processes were considered during these simulations. While all physics processes were used in the case of the water box phantom simulation, only Compton scatter and photoelectric interactions were considered in the case of the PET and CT imaging simulations. The use of different physics effects may lead to different speedup factors according to their requirement in terms of random numbers and memory access. Using only Compton scattering and photoelectric effects allows an increase in the speed-up factors since both effects require few memory accesses.

Secondly, in contrast to the simple water phantom simulation both clinical imaging simulation examples were realized within the GATE/Geant4 environment. This choice was based on the fact that GATE is currently the most popular MCS platform for imaging applications. The speed-up factors realized for both clinical imaging examples were superior to the computing capability of a single GPU as a result of the combination of two sources of acceleration. The first was related to a purely hardware acceleration given by the massively parallel GPU architecture. The GATE programming model provided the second source of acceleration since no specific optimization strategies were considered within the GATE/Geant4 codes. Both these codes are based on an object-oriented programming model using C++ involving multiple interleaved library calls and classes, in contrast to the optimized GPU applications implementation developed using CUDA (extended C code) where data structures

are well defined without the possibility to use object programming. Finally, the acceleration factor was more important with the x-ray imaging example compared to the PET imaging simulation since all of the components associated with the x-ray imaging simulation case (x-ray source, patient volume and flat panel detector tracking) were implemented on the GPU. In contrast in the case of the PET imaging the GPU implementation was limited on the patient volume navigation simulation component. These results clearly demonstrate the interest of implementing the entire simulation process within the GPU environment relative to a hybrid CPU/GPU approach.

These significant improvements in computational time in combination with an uncompromised accuracy show the potential impact of the proposed GPU implementation of Geant4 physics processes for medical applications. One of the advantages of the proposed implementation framework is the potential of its incorporation within GATE, which is currently the most popular Monte Carlo simulation platform for medical imaging and therapy applications using Geant4. Since the major disadvantage of the GATE platform is its long execution times, the proposed GPU implementation will provide an efficient solution without the need for major modifications in the existing GATE platform structure.

## 5. Conclusions

The global aim of our work was to develop a MCS framework for medical applications on GPU based on the use of Geant4. Within this context, we proposed and presented the definition of a novel global strategy and the associated structure for such a GPU based Geant4 simulation implementation. An extensive validation study has shown equivalence in the underlying implemented physics processes for both photons and electrons. The GPU version of the Brent-XOR256s PRNG introduced in our implementation has shown to be a good choice for an optimized GPU pseudo-random number generation. Its period is high enough for the targeted medical applications in MCS with a superior performance compared to the traditionally used MT PRNG.

A speedup factor of  $\times 85$  was obtained for simplistic simulations using the photoelectric effect and the Compton and Rayleigh scattering, with no associated precision biases. In the case of more clinically realistic imaging simulations acceleration factors of 400–800 were obtained compared to the use of the GATE platform.

Future work will include extending the proposed GPU framework by adding further Geant4 physics effects for a complete electron interactions modelling (bremsstrahlung effect), as well as considering optical photon and proton physics effects. In terms of validation further work will involve the validation of the GPU implementation for radiotherapy dosimetry applications. Finally, the incorporation of the proposed GPU implementation within a hybrid version of the GATE platform is also under way.

## Acknowledgment

This work was funded by the French National Research Agency through hGATE project (ANR-09-COSI-004-01).

## References

- Allison J *et al* 2006 Geant4 developments and applications *IEEE Trans. Nucl. Sci.* **53** 270–8
- Badal A and Badano A 2009 Accelerating Monte Carlo simulations of photon transport in a voxelized geometry using a massively parallel graphics processing unit *Med. Phys.* **36** 4878–80

- Barret O, Carpenter T A, Clark J C, Ansorge R E and Fryer T D 2005 Monte Carlo simulation and scatter correction of the GE advance PET scanner with SimSET and Geant4 *Phys. Med. Biol.* **50** 4823–40
- Blythe D 2008 Rise of the graphics processor *Proc. IEEE* **96** 761–78
- Boone J M and Seibert J A 1997 An accurate method for computer-generating tungsten anode x-ray spectra from 30 to 140 kV *Med. Phys.* **24** 1661–71
- Brent R P 2007 Some long-period random number generators using shifts and XORS *Aust. N.Z. Indust. Appl. Math. J.* **48** 1–11
- Carter L L, Cashwell E D and Taylor W M 1972 Monte Carlo sampling with continuously varying cross sections along flight paths *Nucl. Sci. Eng.* **48** 403–11 (available at [www.ans.org/pubs/journals/nse/a\\_14304](http://www.ans.org/pubs/journals/nse/a_14304))
- Flampouri S, Jiang S B, Sharp G C, Wolfgang J, Patel A A and Choi N C 2006 Estimation of the delivered patient dose in lung IMRT treatment based on deformable registration of 4D-CT data and Monte Carlo simulations *Phys. Med. Biol.* **51** 2763–79
- Hissoiny S, Ozell B, Bouchard H and Després P 2011 GPUMCD: a new GPU-oriented Monte Carlo dose calculation platform *Med. Phys.* **38** 754–64
- Jahnke L, Fleckenstein J, Wenz F and Hesser J 2012 GMC: a GPU implementation of a Monte Carlo dose calculation based on Geant4 *Phys. Med. Biol.* **57** 1217–29
- Jan S *et al* 2011 GATE V6: a major enhancement of the Gate simulation platform enabling modelling of CT and radiotherapy *Phys. Med. Biol.* **56** 881–901
- Jia X, Gu X, Sempau J, Choi D, Majumdar A and Jiang S B 2010 Development of a GPU-based Monte Carlo dose calculation code for coupled electron–photon transport *Phys. Med. Biol.* **55** 3077–86
- Lamare F, Turzo A, Bizais Y, Le Rest C C and Visvikis D 2006 Validation of a Monte Carlo simulation of the Philips Allegro/GEMINI PET systems using GATE *Phys. Med. Biol.* **51** 943–62
- L'Ecuyer P and Simard R 2007 TestU01: A C library for empirical testing of random number generators *ACM Trans. Math. Softw.* **33** 1–38
- Le Maitre A, Segars W P, Marache S, Reilhac A, Hatt M, Tomei S, Lartizien C and Visvikis D 2009 Incorporating patient specific variability in the simulation of realistic whole body 18F-FDG distributions for oncology applications *Proc. IEEE* **97** 2026–38
- Lippuner J and Elbakri I A 2011 A GPU implementation of EGSNRC's Monte Carlo photon transport for imaging applications *Phys. Med. Biol.* **56** 7145–62
- Matsumoto M and Nishimura T 1998 Mersenne twister: a 623-dimensionally equidistributed uniform pseudo-random number generator *ACM Trans. Modeling Comput. Simul.* **8** 3–30
- Nickolls J and Dally W J 2010 The GPU computing era *IEEE Micro* **30** 56–69
- Park S K and Miller K W 1988 Random number generators: good ones are hard to find *Commun. ACM* **31** 1192–201
- Perez-Ponce H, Bitar Z E, Boursier Y, Vintache D, Bonissent A, Morel C, Brasse D, Visvikis D and Bert J 2011 Implementing Geant4 on GPU for medical applications *NSS/MIC: IEEE Nucl. Sci. Symp. and Med. Imaging Conf. Rec.* pp 2703–7
- Rassiah-Szegedi P, Fuss M, Sheikh-Bagheri D, Szegedi M, Stathakis S, Lancaster J, Papanikolaou N and Salter B 2007 Dosimetric evaluation of a Monte Carlo IMRT treatment planning system incorporating the mimic *Phys. Med. Biol.* **52** 6931–41
- Rehfeld N, Fippel M and Alber M 2005 Reconstruction of PET images with a compressed Monte Carlo based system matrix—a comparison to other Monte Carlo based algorithms *NSS/MIC: IEEE Nucl. Sci. Symp. and Med. Imaging Conf. Rec.* vol 4 pp 2286–90
- Schneider W, Bortfeld T and Schlegel W 2000 Correlation between CT numbers and tissue parameters needed for Monte Carlo simulations of clinical dose distributions *Phys. Med. Biol.* **45** 459–78
- Segars W P 2001 Development and application of the new dynamic NURBS-based cardiac-torso (NCAT) phantom *PhD Thesis* The University of North Carolina
- Toth B and Magdics M 2010 Monte Carlo radiative transport on the GPU *5th Hungarian Conf. on Computer Graphics and Geometry* pp 1–8
- Verhaegen F and Seuntjens J 2003 Monte Carlo modeling of external radiotherapy photon beams *Phys. Med. Biol.* **48** 107–64
- Woodcock E, Murphy T, Hemmings P and Longworth S 1965 Techniques used in the gem code for Monte Carlo neutronics calculations in reactors and other systems of complex geometry *Proc. Conf. on Applications of Computing Methods to Reactor Problems* p 557
- Zhang L, Staelens S, Holen R V, Beenhouwer J D, Verhaeghe J, Kawrakow I and Vandenberghe S 2010 Fast and memory-efficient Monte Carlo-base image reconstruction for whole-body pet *Med. Phys.* **37** 3667–76

## B.2 La plateforme de simulation Monte-Carlo GGEMS

*IEEE Nuclear Science Symposium and Medical Imaging Conference (2016)*

1

# GGEMS: GPU GEant4-based Monte Carlo Simulation platform

Julien Bert, Yannick Lemaréchal, Didier Benoit, Marie-Paule Garcia, and Dimitris Visvikis

### I. INTRODUCTION

**M**ONTE Carlo Simulations (MCS) are associated with long execution times, which is one of the major issues preventing their use in routine clinical practice for both image reconstruction and dosimetry applications. Recently, graphics processing units (GPU) have become in many different domains [1], especially in medical physics [2], a low cost alternative solution for the acquisition of high computation power. Within this context different Monte Carlo simulation codes have been used and implemented on GPU targeting specific applications. Most of them are focused on dose calculation [3]–[7], and few of them on CT imaging applications [8]–[10]. Each of these codes has different implementation strategies.

Although, on standard CPU programming several Monte Carlo frameworks gather a large spectrum of applications such Geant4 [11] and GATE [12], there is today no equivalent in GPU programming. The objective of this work was to develop a unique solution in terms of flexibility and coverage for both therapy and imaging applications. The proposed efficient MCS toolkit for GPU architectures named GGEMS (GPU GEant4-based Monte Carlo Simulation) was partially based on the already implemented framework proposed by [13] and based on the well-validated Geant4 toolkit. GGEMS is a modular simulation platform and proposes hardware adapted solutions for the different components of MCS with advanced mechanisms allowing numerous medical applications (PET, SPECT, CT imaging; photon, low x-rays, electron based radiotherapy).

### II. MATERIALS AND METHODS

#### A. Architecture of GGEMS

The GGEMS architecture was based on a source-phantom-detector (SPD) concept. Every MCS is composed by these basic simulation elements. There is at least a source or/and a phantom or/and a detector. Therefore, three programming objects (abstract classes) were developed to describe a generic source, phantom and detector. Each of these classes has mandatory GPU functions to perform a MCS. For instance a source must absolutely have a function that generates particles. Any new object targeting a specific application is created by inheritance with the corresponding generic object. Subsequently, mandatory functions are written to consider the specificities of the new object. In this way the GGEMS main core is capable of using any SPD object by calling the necessary mandatory functions required to perform a MCS on GPU. The GGEMS software architecture allows plugging different SPDs together to perform versatile MCS on GPU architectures.

#### B. GGEMS features

1) *Physics*: Photon processes were based on the previous framework proposed by [13], which includes the Compton and Rayleigh

All authors are with the INSERM UMR1101, LaTIM, CHRU Brest, France (e-mail: julien.bert@univ-brest.fr).

scattering and the photoelectric effect. Electron processes namely Bremsstrahlung, eIonization and Multiple scattering, were extracted from Geant4 and implemented into GGEMS. Each GPU thread handles the complete primary particle history including the associated secondary particles which are managed using a particle queue on the graphics card global memory.

2) *Sources*: Different kinds of sources were developed in GGEMS. Cone beam source and voxelized source using energy spectra are mostly used for imaging applications. Phase space sources and parametric source models were implemented for dosimetry applications, especially considering linear accelerator sources.

3) *Object navigation*: The GPU computational power is higher while using simple-precision floating-point (FP32). Therefore, for a fast GPU particle transport, the regular Geant4 double-precision floating-point (FP64) transport model was converted into a FP32 model. Interval arithmetic was used to control rounding-errors and ensure accurate particle navigation within a given geometry. Similarly to Geant4, GGEMS uses particle energy cut mechanisms to avoid undesirable stepping of low energy particles and thus improve overall computational efficiency. GGEMS uses both voxelized and analytical phantom descriptions. The new hybrid primitive [14] allowing accurately mixing voxelized and analytical phantom within the same MCS was also implemented in GGEMS. Similarly to GATE, GGEMS is capable of using a realistic voxelized phantom by deriving Hounsfield units from patient CT images into material data using [15]. Material properties calculation and definition were implemented on GGEMS using the same methods provided by Geant4.

4) *Detector and dosimetry*: Different kinds of detector were implemented to cover the different imaging applications. Flat panel detectors were developed for transmission imaging, PET and SPECT cameras for emission imaging. Regarding dosimetry, two dose kerma were implemented on GPU namely the analog and the Track Length Estimator [16]. Dose and energy map and the corresponding uncertainties based on a history by history statistical estimation from [17] are recorded during a GGEMS simulation. The dose scoring on GPU uses a scheme based on FP64 (double-precision) in order to avoid accumulation bias from rounding-errors.

#### C. Implementation

GGEMS is a static library and a self-consistent code that does not require any third-library software. However, NVIDIA CUDA environment (CUDA 7.0 or newest) is required to execute code with the GGEMS library. GGEMS was designed considering architecture that has a minimal compute compatibility version (ccv) of 3.0. Therefore, any architecture from Kepler (ccv 3.0, ex. GTX650) to Maxwell (ccv 5.2, ex. GTX TITAN X or GTX980Ti) is capable to run GGEMS.



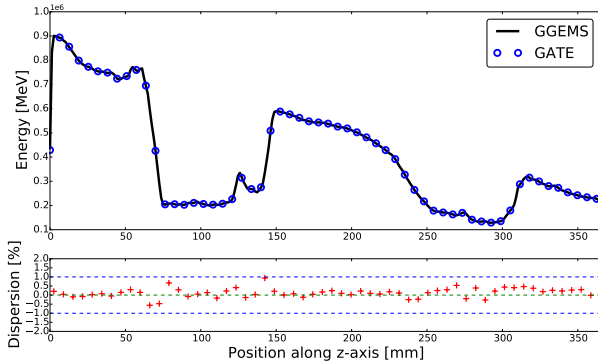


Fig. 1: Total energy deposited to the phantom along the z-axis from the dosimetry simulation using GATE and GGEMS.

#### D. Examples of GGEMS simulations

Among the different possibilities offered by GGEMS in term of simulation only two applications are presented here due to space constraints: one in MeV dosimetry and one in transmission imaging.

1) *Photon beam dosimetry*: The first application based validation study of the proposed GGEMS platform was in dosimetry. A cone beam source emitting photon particles of 1 MeV from an  $1^\circ$  aperture targeting a thoracic patient CT composed of  $288 \times 241 \times 164$  voxels with a spacing of  $1.26 \times 1.26 \times 2 \text{ mm}^3$  was simulated. This phantom was placed over the source with a distance of 1 m. All for photon and electron physics effects were enabled with a particle range cut of  $100 \mu\text{m}$ . A total of  $200 \times 10^6$  primary photons were simulated. The same simulation was performed using GGEMS with a NVIDIA GTX980Ti and GATE (7.2)/Geant4 (10.01) with one CPU core of Intel i7-2600 processor. Run time and the energy deposited to the phantom were recorded for both simulations.

2) *Cone Beam CT*: Another application of the GGEMS software was the transmission tomography. A cone beam CT (CBCT) geometry was designed using a rectangular shape of  $0.6 \times 1.2 \text{ mm}^2$ , emitting particles from an  $13^\circ$  aperture, and a polychromatic spectrum with a classic tube voltage of 120 kVp and 2 mm aluminum filter. A head and neck phantom consisted of 5 materials and  $512 \times 512 \times 228$  voxels with a spacing of  $0.4 \times 0.4 \times 0.8 \text{ mm}^3$  was built by segmenting the tissues from a patient CT. Finally, a flat panel detector was simulated with a field of view of  $430 \times 430 \text{ mm}^2$  and pixel size of  $0.444 \times 0.444 \text{ mm}^2$  by counting the number of detected particles. For a high statistics acquisition ( $\sim 10000 \text{ count/pixel}$ ) a total of  $14 \times 10^9$  primary photons were simulated. Run times and 2D projections from GGEMS simulation were estimated with the same graphics cards used in example 1 above.

### III. RESULTS

For the dosimetry application, the total run time using GATE and GGEMS simulation was 4222 min and 27 min respectively, with GGEMS being 156 times faster than GATE. Fig. 1 shows a comparison of the total energy deposited to the phantom along the photon beam axis from both simulations. The overall dispersion of the energy relative error between GGEMS and GATE was below 1 %, showing a good agreement. The total run time for the CBCT simulation was 10h when using GGEMS. The final high statistics 2D projection recovered from the simulation is shown on Fig. 2.

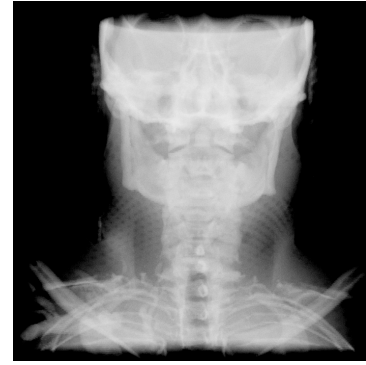


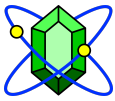
Fig. 2: High statistical 2D projection recover from GGEMS CBCT simulation.

### IV. CONCLUSION

GGEMS is a new GPU MCS platform targeting multiple dosimetry and imaging applications. Physics models were based on the well-validated Geant4 toolkit. This new platform proposes a hardware adapted solution for the different components of MCS with advanced mechanisms targeting numerous of MCS medical applications.

### REFERENCES

- [1] J. Nickolls and W. J. Dally, "The GPU Computing Era," *IEEE Micro*, vol. 30, no. 2, pp. 56–69, Mar. 2010.
- [2] G. Pratz and L. Xing, "GPU computing in medical physics: a review," *Medical Physics*, vol. 38, no. 5, pp. 2685–2697, May 2011.
- [3] S. Hissoiny, B. Ozell, H. Bouchard, and P. Desprs, "GPUMCD: A new GPU-oriented Monte Carlo dose calculation platform," *Medical Physics*, vol. 38, no. 2, pp. 754–764, Feb. 2011.
- [4] L. Jahnke, J. Fleckenstein, F. Wenz, and J. Hesser, "GMC: a GPU implementation of a Monte Carlo dose calculation based on Geant4," *Physics in Medicine and Biology*, vol. 57, no. 5, pp. 1217–1229, Mar. 2012.
- [5] X. Jia, P. Ziegenhein, and S. B. Jiang, "GPU-based high-performance computing for radiation therapy," *Physics in Medicine and Biology*, vol. 59, no. 4, pp. 151–182, Feb. 2014.
- [6] Z. Tian, F. Shi, M. Folkerts, N. Qin, S. B. Jiang, and X. Jia, "A GPU OpenCL based cross-platform Monte Carlo dose calculation engine (goMC)," *Physics in Medicine and Biology*, vol. 60, no. 19, pp. 7419–7435, Oct. 2015.
- [7] E. Bonenfant, V. Magnoux, S. Hissoiny, B. Ozell, L. Beaulieu, and P. Desprs, "Fast GPU-based Monte Carlo simulations for LDR prostate brachytherapy," *Physics in Medicine and Biology*, vol. 60, no. 13, pp. 4973–4986, Jul. 2015.
- [8] J. Lippuner and I. A. Elbakri, "A GPU implementation of EGSnrc's Monte Carlo photon transport for imaging applications," *Physics in Medicine and Biology*, vol. 56, no. 22, pp. 7145–7162, Nov. 2011.
- [9] X. Jia, H. Yan, L. Cervino, M. Folkerts, and S. B. Jiang, "A GPU tool for efficient, accurate, and realistic simulation of cone beam CT projections," *Medical Physics*, vol. 39, no. 12, pp. 7368–7378, Dec. 2012.
- [10] K. Kim, et al., "Fully iterative scatter corrected digital breast tomosynthesis using GPU-based fast Monte Carlo simulation and composition ratio update," *Medical Physics*, vol. 42, no. 9, pp. 5342–5355, Sep. 2015.
- [11] J. Allison, et al., "Geant4 developments and applications," *IEEE Transactions on Nuclear Science*, vol. 53, no. 1, pp. 270–278, Feb. 2006.
- [12] S. Jan, et al., "GATE V6: a major enhancement of the GATE simulation platform enabling modelling of CT and radiotherapy," *Physics in Medicine and Biology*, vol. 56, no. 4, pp. 881–901, Feb. 2011.
- [13] J. Bert, et al., "Geant4-based Monte Carlo simulations on GPU for medical applications," *Physics in Medicine and Biology*, vol. 58, no. 16, pp. 5593–5611, Aug. 2013.
- [14] J. Bert, Y. Lemarchal, and D. Visvikis, "New hybrid voxelized/analytical primitive in Monte Carlo simulations for medical applications," *Physics in Medicine and Biology*, vol. 61, no. 9, 2016.
- [15] W. Schneider, T. Bortfeld, and W. Schlegel, "Correlation between CT numbers and tissue parameters needed for Monte Carlo simulations of clinical dose distributions," *Physics in Medicine and Biology*, vol. 45, no. 2, pp. 459–478, Feb. 2000.
- [16] J. F. Williamson, "Monte Carlo evaluation of kerma at a point for photon transport problems," *Medical Physics*, vol. 14, no. 4, pp. 567–576, Aug. 1987.
- [17] B. R. B. Walters, I. Kawrakow, and D. W. O. Rogers, "History by history statistical estimators in the BEAM code system," *Medical Physics*, vol. 29, no. 12, pp. 2745–2752, Dec. 2002.



# GGEMS: GPU GEant4-based Monte Carlo Simulation platform

Julien Bert, Didier Benoit, Marie-Paule Garcia and Dimitris Visvikis  
LaTIM, INSERM UMR1101, CHRU Brest, France

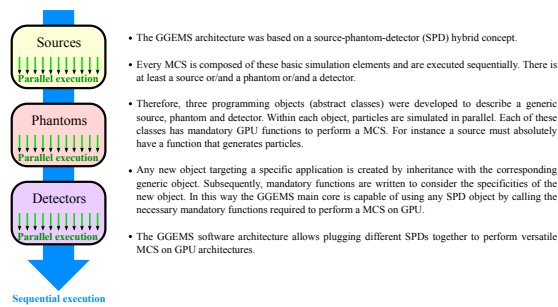
## I Introduction

Monte Carlo Simulations (MCS) are associated with long execution times, which is one of the major issues preventing their use in routine clinical practice for both image reconstruction and dosimetry applications. Recently, graphics processing units (GPU) have become in many different domains, especially in medical physics, a low cost alternative solution for the acquisition of high computation power. Within this context different Monte Carlo simulation codes have been used and implemented on GPU targeting specific applications. Most of them are focused on dose calculations [Hisoyny 2011, Jahnke 2012, Jia 2014, Tian 2015, Bonenfant 2015], and few of them on CT imaging applications [Lippuner 2011, Jia 2012, Kim 2015]. Each of these codes has different implementation strategies.

Although, on standard CPU programming several Monte Carlo frameworks gather a large spectrum of applications such as Geant4 [Allison 2006] and GATE [Jan 2011], there is today no equivalent in GPU programming. The objective of this work was to develop a unique solution in terms of flexibility and coverage for both therapy and imaging applications. The proposed efficient MCS toolkit for GPU architectures named GGEMS (GPU GEant4-based Monte Carlo Simulation) was partially based on the already implemented framework proposed by [Bert 2013] and based on the well-validated Geant4 toolkit. GGEMS is a modular simulation platform and proposes hardware adapted solutions for the different components of MCS with advanced mechanisms allowing numerous medical applications (PET, SPECT, CT imaging; photon, low x-rays, electron based radiotherapy).

## II Materials and methods

### A Architecture of GGEMS



### B GGEMS features

#### 1. Physics model from Geant4

- Photon processes
  - Compton and Rayleigh scattering and photoelectric effect
- Electron processes
  - Bremsstrahlung, elomization and Multiple scattering
- Range cuts
  - Production and tracking cuts

#### 2. Sources

- Cone beam source
- Voxelized source
  - Phase space (IAEA)
- Parametric model (LINAC, brachytherapy seed)

#### 3. Phantoms

- Fast navigation in single-precision floating-point (FP32)
- Navigation uses interval arithmetic to control rounding-errors
- Voxelized and analytical phantoms (CT patient or meshed object)
- Material properties and definition derived from Geant4

#### 4. Detectors and dosimetry

- Flat panel detector (transmission imaging)
- PET and SPECT cameras (emission imaging)
- Dose and energy map in double-precision floating-point (FP64)
- Dose uncertainty based on history by history statistical estimation

#### 5. Miscellaneous

- Export the simulation scene in VRML
- Object description using local and global frames
- Easy to add new simulation object (source, detector, etc.)

#### Easy simulation settings

```
#include <ggems.cuh>

// Creating a cone beam CT (CB-CT) source
ConeBeamCTSource *Source = new ConeBeamCTSource;
Source->set_particle_type("gamma");
Source->set_beam_aperture(0.01 * mm, 0.01 * mm);
Source->set_beam_aperture(0.7 * deg);
Source->set_position(0.0 * mm, 0.0 * mm, 0.0 * mm);
Source->set_rotation(0.0 * deg, 0.0 * deg, 0.0 * deg);
Source->set_energy_spectrum("data/spectrum_220kVp_2mmAl.dat");

// Creating a voxelized phantom
...

// Creating a detector
...

// GGEMS simulation
GGEMS *simu = new GGEMS;

// GPU parameters
simu->setHardwareTarget("GPU");
simu->setGPU_ID(0);

// Physics parameters
simu->setProcess("Compton");
simu->setProcess("PhotoElectric");
simu->setProcess("Rayleigh");
simu->setParticleCut("photon", 0.5 * mm);

// Random and particles
simu->setSeed(123456789);
simu->setNumberofParticles(100000);

// Source, phantom and detector
simu->setSource(*Source);
simu->setPhantom(*phantom);
simu->setDetector(*detector);

// Run the simulation
simu->runSimulation();
simu->startSimulation();

// Export results
...
```

#### Include the GGEMS library

Simulation object is created separately by instantiating one of the classes provided by GGEMS. Here, a new cone beam source is creating and set up.

Different basic objects for MCS are provided by GGEMS, and can be added to the simulation (phantoms and detectors).

A main GGEMS simulation is then created and the different parameters are setting up.

GGEMS is capable of running the same MCS on standard CPU or GPU. This has to be defined at the beginning.

Physics processes are added to the physics list. Then the random seed and the number of particles required are

Simulation objects previously created (sources, phantoms and detectors) are passed to the main simulation.

A first step of initialization is required, in order to process and copy data from the computer to the graphics device. Then, the simulation is started, and all particles required are simulated.

### C Evaluation study

GGEMS is a static library and a self-consistent code that does not require any third-library software. However, NVIDIA CUDA environment (CUDA 7.0 or newest) is required to execute code with the GGEMS library. GGEMS was designed considering architecture that has a minimal compute compatibility version (ccv) of 3.0. Therefore, any architecture from Kepler (ccv 3.0, ex. GTX650) to Maxwell (ccv 5.2, ex. GTX TITAN X or GTX980Ti) is capable to run GGEMS.

[Hisoyny 2011] *Med. Phys.* 38(2) pp. 2685  
[Jahnke 2012] *Phys. Med. Biol.* 57(9) pp. 217  
[Jia 2014] *Phys. Med. Biol.* 59(4) pp. 151  
[Tian 2015] *Phys. Med. Biol.* 60(19) pp. 7419

[Bonenfant 2015] *Phys. Med. Biol.* 60(13) pp. 4973  
[Lippuner 2011] *Phys. Med. Biol.* 56(23) pp. 7145  
[Jia 2012] *Med. Phys.* 39(12) pp. 7368  
[Kim 2015] *Med. Phys.* 42(9) pp. 5342

[Jan 2011] *Phys. Med. Biol.* 56(4) pp. 881  
[Allison 2006] *IEEE Trans. on Nuclear Science* 53(1) pp. 270  
[Bert 2013] *Phys. Med. Biol.* 58(16) pp. 5593

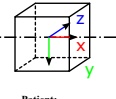
## III Results: examples of GGEMS simulations

### Photon beam dosimetry



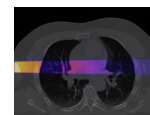
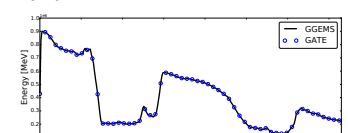
**CBCT source:**

- emitting photon particles
- 1° aperture
- mono energy: 1 MeV



**Simulation:**

- photon and electron physics list
- particle range cut of 0.1 mm
- 200 millions of primary photons
- GGEMS (NVIDIA GTX690)
- GATE 7.2/Geant4 10.01 (one cpu core Intel i7-2600)
- dose deposition in FP64



4222 mins 27 mins

x156

**Patient:**

- thoracic patient CT
- 288x241x164 voxels
- spacing of 1.26x1.26x2 mm<sup>3</sup>

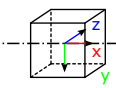
Total energy deposited to the phantom along the z-axis from the dosimetry simulation using GATE and GGEMS

### Cone Beam CT



**CBCT source:**

- rectangular shape 0.6x1.2mm<sup>2</sup>
- emitting photon particles
- 13° aperture
- polychromatic spectrum
- 120 kVp, 2 mm aluminum filter



**Patient:**

- head and neck CT phantom
- 512x512x228 voxels
- spacing of 0.4x0.4x0.8 mm<sup>3</sup>

**CT detector:**

- flat panel detector
- field of view 430x430 mm<sup>2</sup>
- pixel size of 0.44x0.444 mm<sup>2</sup>
- counting mode

**Simulation:**

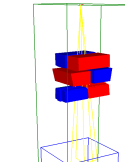
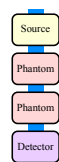
- photon physics list
- particle range cut of 0.5 mm
- 14 billions of primary photons (high statistics)
- NVIDIA GTX690

10 hours



Projection from GGEMS with high statistics (-10000 count/pixel)

### External beam radiotherapy

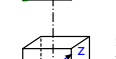


**Virtual source:**

- source model from phase space data
- TrueBeam™ Novalis (Varian Medical System)
- photon beam 6MV

**LINAC head:**

- accurate jaws modeling using mesh-based object
- accurate multileaf collimator (120 mesh-based leaves)
- particles navigation through collimator



**Patient:**

- thoracic phantom CT
- 200x200x178 voxels
- spacing of 2x2x2 mm<sup>3</sup>

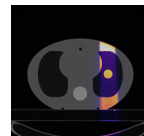
**EPID detector:**

- 1024x768 pixels
- pixel size of 0.392x0.392 mm<sup>2</sup>
- record energy

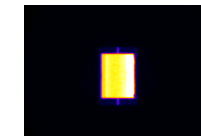
**Simulation:**

- one VMAT field from TPS
- photon and electron physics list
- particle range cut of 0.1 mm
- 1 billion of primary photons
- GGEMS (NVIDIA GTX690)
- dose deposition in FP64

2h 37 mins



Dose distribution map from GGEMS over phantom CT



EPID projection from GGEMS

## IV Conclusions

GGEMS is a new GPU MCS platform targeting multiple dosimetry and imaging applications. Physics models were based on the well-validated Geant4 toolkit. This new platform proposes a hardware adapted solution for the different components of MCS with advanced mechanisms targeting numerous of MCS medical applications.



A first public release is planned for the middle of 2017



## B.3 Extension de GGEMS pour l'imagerie TEMP

# Accelerated GPU based SPECT Monte Carlo simulations

Marie-Paule Garcia<sup>1</sup>, Julien Bert<sup>1</sup>, Didier Benoit<sup>1</sup>,  
Manuel Bardiès<sup>2</sup> and Dimitris Visvikis<sup>1</sup>

<sup>1</sup> LaTIM, UMR 1101, INSERM, CHRU Brest, France

<sup>2</sup> UMR 1037 INSERM/UPS, Centre de Recherche en Cancérologie de Toulouse, France

E-mail: [marie-paule.garcia@univ-brest.fr](mailto:marie-paule.garcia@univ-brest.fr)

Received 12 February 2016, revised 28 March 2016

Accepted for publication 1 April 2016

Published 10 May 2016



CrossMark

### Abstract

Monte Carlo (MC) modelling is widely used in the field of single photon emission computed tomography (SPECT) as it is a reliable technique to simulate very high quality scans. This technique provides very accurate modelling of the radiation transport and particle interactions in a heterogeneous medium. Various MC codes exist for nuclear medicine imaging simulations. Recently, new strategies exploiting the computing capabilities of graphical processing units (GPU) have been proposed. This work aims at evaluating the accuracy of such GPU implementation strategies in comparison to standard MC codes in the context of SPECT imaging. GATE was considered the reference MC toolkit and used to evaluate the performance of newly developed GPU Geant4-based Monte Carlo simulation (GGEMS) modules for SPECT imaging. Radioisotopes with different photon energies were used with these various CPU and GPU Geant4-based MC codes in order to assess the best strategy for each configuration. Three different isotopes were considered:  $^{99m}\text{Tc}$ ,  $^{111}\text{In}$  and  $^{131}\text{I}$ , using a low energy high resolution (LEHR) collimator, a medium energy general purpose (MEGP) collimator and a high energy general purpose (HEGP) collimator respectively. Point source, uniform source, cylindrical phantom and anthropomorphic phantom acquisitions were simulated using a model of the GE infinia II 3/8" gamma camera. Both simulation platforms yielded a similar system sensitivity and image statistical quality for the various combinations. The overall acceleration factor between GATE and GGEMS platform derived from the same cylindrical phantom acquisition was between 18 and 27 for the different radioisotopes. Besides, a full MC simulation using an anthropomorphic phantom showed the full potential of the GGEMS platform, with a resulting acceleration factor up to 71. The good agreement with reference codes and the acceleration factors obtained support the use

of GPU implementation strategies for improving computational efficiency of SPECT imaging simulations.

Keywords: Monte Carlo simulation, single photon emission computed tomography, graphical processing unit

(Some figures may appear in colour only in the online journal)

## 1. Introduction

Monte Carlo (MC) simulation in emission tomography is a powerful technique to generate high quality single photon emission computed tomography (SPECT) scans. MC modelling allows the accurate simulation of radiation transport physics as well as that of particle interactions with tissues or detector components. Many studies have assessed such accuracy for different existing MC codes such as SIMIND (Ljungberg and Strand 1989), SimSET (Harrison *et al* 1993) or GATE (Jan *et al* 2004). Within this context many gamma camera system models have been validated considering a combination of various radioisotopes (Staelens *et al* 2003, Assié *et al* 2005, Autret *et al* 2005, Crespo *et al* 2008, Holstenson *et al* 2010, Brolin *et al* 2013). One of the advantages of the GATE simulation toolkit is its use of the Geant4 libraries for the physics models (Agnostinelli *et al* 2003, Allison *et al* 2006) that have been tested and validated over many years by a large scientific community. In addition to the physics models, the simulation quality relies also on the ability to model accurately and in detail the various elements of a gamma camera detector and its associated electronics. In SPECT, the precise modelling of the collimator is crucial to properly account for all interactions associated with the emissions of each radioisotope and subsequent overall image qualitative and quantitative accuracy. In clinical practice, different parallel hole collimators are predominantly used according to the radioisotope of interest, such as low-energy high-resolution (LEHR) collimators for the 140 keV photons in  $^{99m}\text{Tc}$  imaging, or high energy general purpose (HEGP) collimators for the 364 keV photons in  $^{131}\text{I}$  imaging. They consist of thousands of hexagonal holes, leading to a highly inefficient photon tracking process. Indeed, photon tracking in such complex structure is extremely time consuming, especially for higher energy photons where septal penetration and scattering are prominent. In Dewaraja *et al* (2000), the authors demonstrated that 73% of events occurring in  $^{131}\text{I}$  point source imaging are not primary particles. On the other hand, low-energy photons such as those of  $^{99m}\text{Tc}$  are quickly absorbed when reaching lead septa which considerably decreases the number of tracking steps inside the collimator.

Therefore in order to overcome computational efficiency issues associated with SPECT MC simulations and accelerate the simulation process of gamma-camera acquisitions, several approaches have been investigated in the last few years. Amongst such solutions the most popular involve the use of variance reduction techniques (VRT). Most of these methods rely on a probabilistic approximation, which efficiently reduces the number of tracking steps but also results in a lack of accuracy. One such approach is the concept of convolution-based forced detection (CFD) which has been investigated for several MC simulation codes. For example, in De Beenhouwer *et al* (2008), the authors made use of this technique within GATE to accelerate  $^{99m}\text{Tc}$  SPECT imaging where septal penetration can be neglected. Another popular VRT technique is based on fictitious interactions as in Ljungberg *et al* (2005), where the authors proposed the use of the delta-scattering technique in the SIMIND simulation toolkit in order to improve computational efficiency of ray tracing in hexagonal hole collimators. A third common approach known as angular response functions (ARF) was first introduced in

Song *et al* (2005). In Descourt *et al* (2010), the authors incorporated the ARF technique within GATE for  $^{131}\text{I}$  imaging.

Recently, many efforts have been made to exploit the computing capabilities of graphical processing units (GPU) within the context of MC simulations. They offer the possibility of reproducing full MC simulations with a substantially decreased associated computation time. To our knowledge, for imaging applications, two MC simulation codes have been recently implemented on GPU (Lippuner and Elbakri 2011, Bert *et al* 2013). The platform presented in Lippuner and Elbakri (2011) is based on the EGSnrc library (Kawrakow *et al* 2010) while the second solution (Bert *et al* 2013) offers a global GPU based implementation strategy using the validated Geant4 physics models. Neither of these two works has referred to SPECT imaging and particular issues associated with navigation within physical collimators.

The objective of this work was to develop the framework for SPECT MC simulations using GPU architectures. Within this context a secondary objective was to evaluate the performance of the different proposed implementation strategies for different combinations of radioisotopes and collimators. To achieve this goal, a new GPU SPECT module dealing with the widely used hexagonal hole collimator was implemented using the previously proposed GPU Geant4-based Monte Carlo simulations (GGEMS) general framework. Radioisotopes with different photon energies (for  $^{99m}\text{Tc}$ ,  $^{111}\text{In}$  and  $^{131}\text{I}$ ) were considered to assess the performance of both CPU and GPU Geant4-based MC simulations implementations.

## 2. Materials & methods

### 2.1. SPECT GPU implementation

The proposed implementation relies on the generic GPU GGEMS framework (Bert *et al* 2013) that has been previously proposed for various medical applications. The key idea behind this framework is to address particle tracking for a huge number of photons in parallel using as many GPU threads as the number of simulated photons. In other words, each particle runs simultaneously on a separate thread from its birth to its death and each of them execute the same program. At each step, the particles are moved according to the minimal distance between the next physics effect (Compton or Photoelectric) and the hexagonal hole or septum boundary. Regarding physics effects, cross sections tables covering the different photon interactions (Photoelectric, Compton and Rayleigh) have been implemented using the Geant4 physics lists.

Based on this global framework, a workflow has been designed for SPECT imaging purposes, as described in figure 1. A first stage implemented in CPU handles the analytical description of the scene geometry, the cross section tables, material tables and source data definitions. The scene geometry commonly consists of a voxelized phantom, a source and one or several gamma camera heads. Once the simulation scene has been defined, the simulation process is handled by the GPU threads which make use of the same navigation code for each particle. For this purpose the previously defined simulation parameters are copied to the GPU memory to be accessible for each thread when running the code. Two main steps are processed by the GPU threads: 1. the generation of the primaries with respect to the source data; 2. the photon navigation for the entire scene (from the source to the generation of the pulses list at the detection level). Finally, the resulting detected photons list is transferred back to the CPU memory, from which singles are processed to account for the photomultiplier and overall readout performance.

Considering the overall camera head simulation: each layer is defined analytically. Most layers are represented as parallelepipeds with specific dimensions, orientation and material.



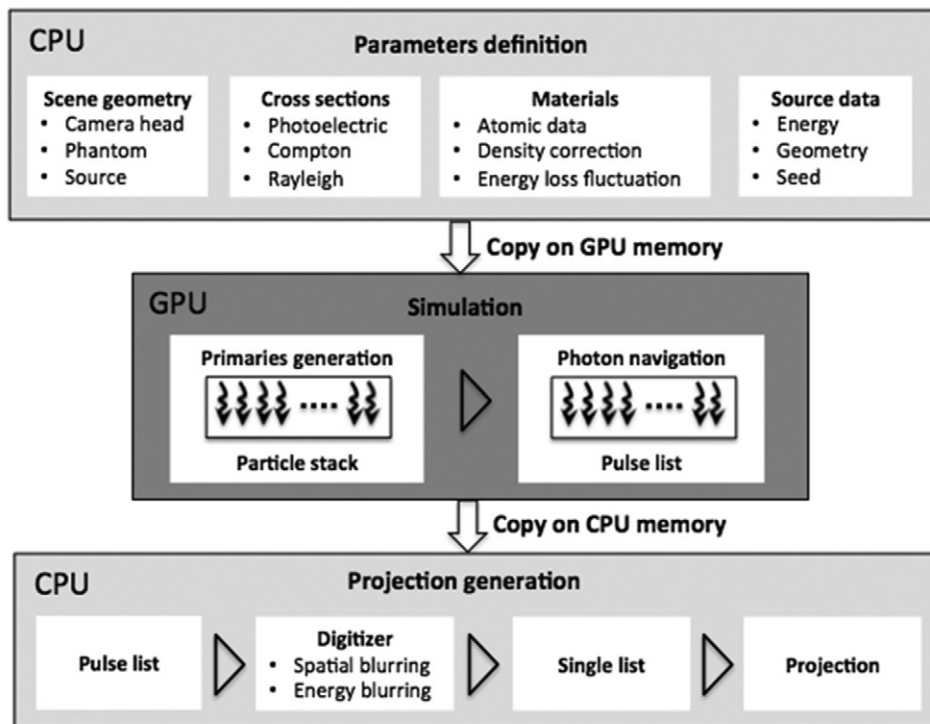


**Figure 1.** Overall workflow of the developed SPECT module: 1. Scene geometry is first defined in CPU as well as the cross section table for each physics effect, material table for each material of the scene and source information; 2. Each simulation parameter is transferred to the GPU memory to be used in the simulation process which starts with the generation of the primaries gathered in a particle stack, then each particle is tracked inside the scene geometry using one thread for each photon from its birth to its death; 3. The resulting pulse list is transferred back to the CPU memory from which singles are processed after some spatial and energy blurring to finally get a realistic projection.

Given that the collimator is a more complex component with numerous hexagonal holes and septa, a particular description has been implemented to facilitate the location of the particles within this structure as described in section 2.2.1. Moreover, a new navigation methodology for such structures has been developed within the proposed SPECT module (section 2.2.2).

## 2.2. Hexagonal hole collimator

**2.2.1. Analytical description.** A user can design their own hexagonal hole collimator by specifying the length and diameter of a single hexagonal hole, and the repetition parameters to obtain the correct imbricated hexagons (figure 2). First, the original hole is reproduced in a cubic array with  $num_y$  translations along the  $y$ -axis (with a  $Y_{cubic}$  displacement) and  $num_z$  translations along the  $z$ -axis (with a  $Z_{cubic}$  displacement). Then, each raw line is translated linearly to obtain the shifted hole lines (with a  $Y_{linear}$  and  $Z_{linear}$  displacements). From the user's initial inputs, the local coordinates of each hexagonal hole center in the collimator referential can be computed. Each hole is given an index following its location in the collimator grid, so that each hexagonal hole can be easily accessed and its local position derived.



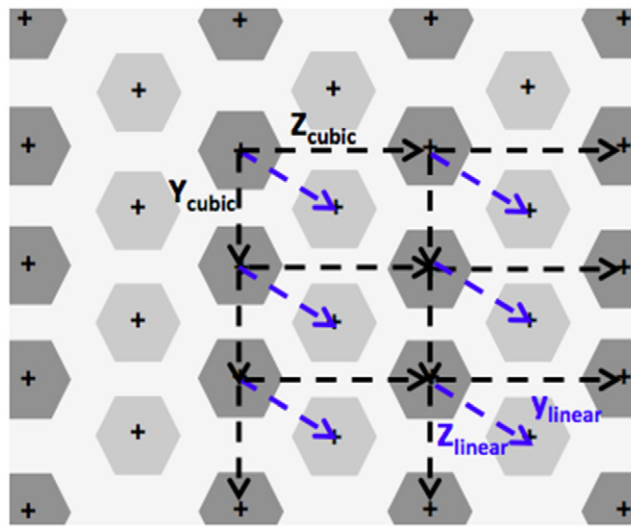


**Figure 2.** Construction of the hexagonal hole collimator grid: holes are first reproduced in a cubic array (dark grey holes) and then linearly translated to obtain the shifted holes (light grey holes). The grid is copied to the GPU memory as a structure of arrays gathering the center coordinates of each hexagonal hole.

The structure of arrays containing the center coordinates of each hexagonal hole is copied to the GPU memory along with the hole length and diameter.

**2.2.2. Geometric navigation.** The relative position of a given particle to the closest hexagon can be found using the previous collimator description. Firstly, a reduced search area is derived using the following equations to determine a cell in the collimator grid specified by a column  $C$  and a line  $L$ :

$$L = \text{round} \left( \frac{(Y_{\text{cubic}} \times (\text{num}_Y - 1)/2) - P_y}{Y_{\text{cubic}}} \right) \quad (1)$$

$$C = \text{round} \left( \frac{(Z_{\text{linear}} \times (\text{num}_Z - 1) - P_z)}{Z_{\text{linear}}} \right) \quad (2)$$

where  $P_y$  and  $P_z$  are point  $P$  coordinates on the  $yz$  plane (collimator plane) and  $\text{round}$  is a function computing the nearest integer value. The collimator grid is presented in figure 4. The total number of lines and columns are  $\text{num}_Y$  and  $2 \times \text{num}_Z$  respectively. A cell contains up to five holes whose indexes can be easily derived. Subsequently a simple test based on hexagonal shape features is performed to define if the particle is located in one of the holes. Otherwise, the particle is located in a septum.

The geometric navigation yields the distance between the current particle position and the next geometric interaction (septum or hole) with respect to the current particle direction. Two different ray tracing algorithms have been developed to solve this problem for hexagonal holes or septa. For the hexagonal hole case, an adaptation of classical oriented bounding box (OBB) ray tracing was implemented to deal with the hexagonal shape. Indeed, the  $x$ -,  $y$ -,  $z$ - coordinates used for a square bounding box have been completed to account for the six sides of a hexagon. In this adapted OBB algorithm, two supplementary axes  $e1$  and  $e2$  are considered by

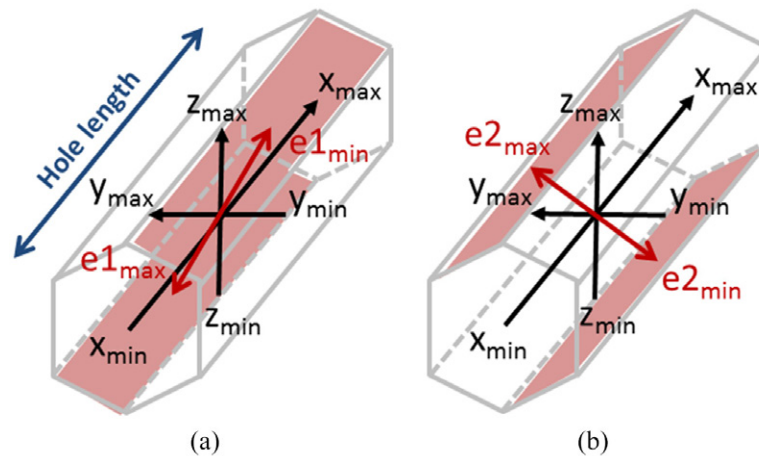


**Figure 3.** Adaptation of the classical bounding box ray tracing algorithm to the specific hexagonal shape: two new axes  $e1$  and  $e2$  (in red) in addition to the classical  $x$ ,  $y$  and  $z$  axes. (a)  $60^\circ$  rotation in  $yz$ -plane, (b)  $-60^\circ$  rotation in  $yz$ -plane.

rotation in the  $yz$ -plane as shown in figure 3. Each direction is then tested by the algorithm to define the next boundary interaction with respect to the particle position and direction. For the septa case, the problem is different as the particle is not contained in a bounding box. Instead, ray plane intersection tests are applied to the surrounding holes as illustrated in figure 4. First, intersection tests are applied to the six sides of the closest hexagonal hole considering the photon position  $P$  and direction  $\vec{d}$ . If no intersection is detected, the same tests are performed with holes of the first ring (blue holes in figure 4) and then with holes of the second ring (orange holes in figure 4). Indeed, as shown for the particle  $P$  and its direction  $\vec{d}$ , the next intersection can also occur with a hole located on the second ring.

### 2.3. Evaluation study

The performance of the implemented SPECT module (described in sections 2.1 and 2.2) within the GGEMS framework (GPU\_SPECT) was compared with GATE v7 (GATE\_SPECT). An additional module also implemented within GGEMS, to perform simple ray tracing inside the collimator without taking into account septal penetration (GPU\_rtcoll), was also included in the comparative evaluation study.

**2.3.1. SPECT camera modelling.** Three models based on the widely used GE infinia II 3/8" gamma camera were designed in this study. With this system, three collimators are classically available to deal with various photon energies: the low energy high resolution (LEHR), medium energy general purpose (MEGP) and high energy general purpose (HEGP) collimators. They are all made of lead and have the same length and width ( $54 \times 40 \text{ cm}^3$ ), but they differ from each other according to hole length, hole diameter and septal thickness. Table 1 includes the main characteristics of these three collimators.

Modeling of the GE infinia II 3/8" gamma camera has been previously validated in Garcia *et al* (2015) using the GATE platform. The camera head is composed of a  $12.925 \times 56 \times 42 \text{ cm}^3$  lead head shielding, a  $0.15 \times 54 \times 40 \text{ cm}^3$  head protection in aluminum, a 0.025 cm thick crystal cover in aluminum, a 3/8" NaI crystal and a  $5 \times 54 \times 40 \text{ cm}^3$  back compartment

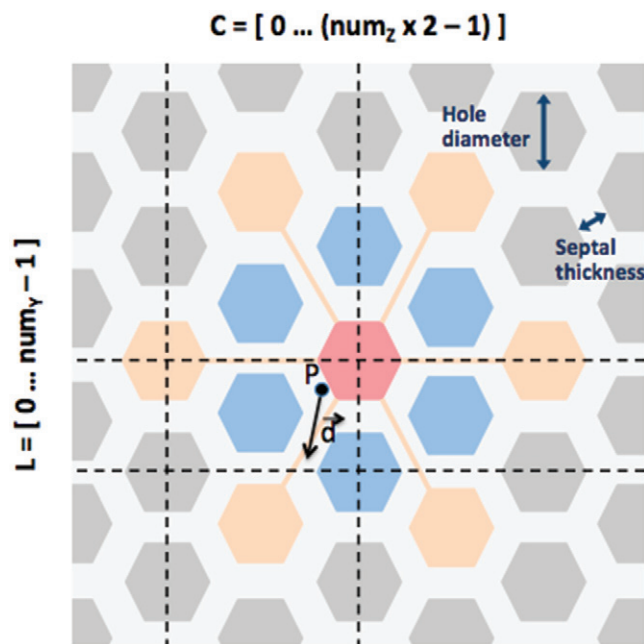


**Figure 4.** Resolution of the next hole photon interaction if current photon  $P$  is located inside a septum: 1.  $P$  coordinates are used to define the current cell of the grid (equations (1) and (2)); 2. the closest hexagonal hole (in red) is derived amongst the holes contained in the cell; 3. test is implemented for occurrence of an intersection with the closest hexagonal hole with respect to the photon position  $P$  and direction  $\vec{d}$ ; 4. if not, test is repeated with holes of the first ring (blue hexagons); 5. otherwise, test is repeated with holes of the second ring (orange hexagons).

**Table 1.** Characteristics of the three modeled collimators for the GE infinia II 3/8" gamma camera simulations.

Collimator	LEHR	MEGP	HEGP
Number of hexagonal holes	85 139	14 973	7123
Hole length (mm)	35	58	66
Hole diameter (mm)	1.5	3	4
Septal thickness (mm)	0.2	1.05	1.8

(figure 5(b)). The back compartment representing photomultipliers and associated electronics was made of a hybrid material of density  $2.5 \text{ g} \cdot \text{cm}^{-3}$  to account for potential interactions between photons and photomultipliers. An overall intrinsic spatial blurring of 2.5 mm FWHM was considered at the level of the electronics. Finally an energy resolution of 9.65% for an energy of reference at 140 keV was considered. Identical detector configurations, including detector material, characteristics, dimensions and performance, were considered for all simulations.

**2.3.2. Acquisition modelling.** Several sources of  $^{99m}\text{Tc}$ ,  $^{111}\text{In}$  and  $^{131}\text{I}$  were simulated for LEHR, MEGP and HEGP collimators respectively. Energy windows of  $140 \text{ keV} \pm 10\%$  and  $364 \text{ keV} \pm 15\%$  were considered for  $^{99m}\text{Tc}$  and  $^{131}\text{I}$  sources respectively. For the  $^{111}\text{In}$  two

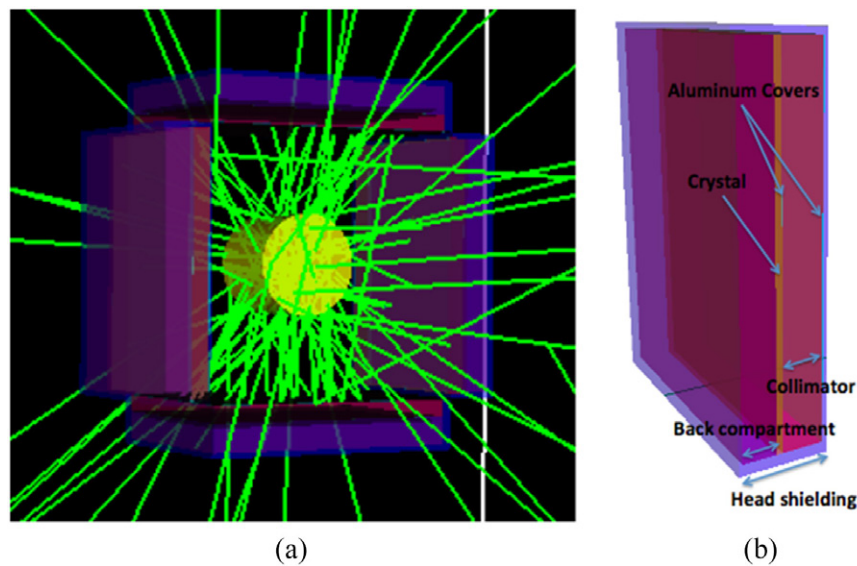


**Figure 5.** Modelling of the GE infinia II 3/8" gamma camera using the developed SPECT GPU module: (a) cylindrical phantom acquisition with a virtual 4-head gamma camera, (b) layers composing the gamma camera head.

emission windows ( $171 \text{ keV} \pm 10\%$  and  $245 \text{ keV} \pm 10\%$ ) were considered. An identical simulation set up was used for each of the three radioisotope/collimator combinations considered:

- (i) ten independent 3 MBq point source acquisitions of 16 s;
- (ii) a 1 GBq uniform source acquisition ( $30 \times 30 \text{ cm}^2$ ) with all photons forced in the solid angle of the detector plane;
- (iii) a SPECT acquisition (64 projections) of a cylindrical phantom (diameter: 21.6 cm, length: 18.6 cm) uniformly filled with 1 GBq activity.

The point and uniform sources were placed 20 cm away from the camera head for the three combinations. For the SPECT cylindrical phantom acquisition, a 4-head gamma camera was designed as shown in figure 5(a). This way, four projections are acquired during a single run, and therefore only 16 runs are needed to simulate 64 projections. The cylinder was placed at the center of the 4-head system with respect to the overall head thickness (cylinder/head distance: 334.625, 349.625 and 365.625 cm for LEHR, MEGP and HEGP collimators, respectively).

In terms of image dimensions for point and uniform source acquisitions, projections of  $256 \times 256$  (pixel size:  $2.21 \times 2.21 \text{ mm}^2$ ) were simulated with the LEHR collimator, whereas projections of  $128 \times 128$  (pixel size:  $4.42 \times 4.42 \text{ mm}^2$ ) were simulated with the MEGP and HEGP collimators. For SPECT cylindrical phantom acquisitions,  $128 \times 128$  projections (pixel size:  $4.42 \times 4.42 \text{ mm}^2$ ) and  $64 \times 64$  projections (pixel size:  $8.84 \times 8.84 \text{ mm}^2$ ) were simulated with the LEHR and MEGP/HEGP collimators respectively. The simulated projections were subsequently reconstructed using OSEM (2 iterations, 8 subsets) with a voxel size of  $4.42 \times 4.42 \times 4.42 \text{ mm}^3$  for LEHR collimator and  $8.84 \times 8.84 \times 8.84 \text{ mm}^3$  for MEGP and HEGP collimators.

**2.3.3. Performance evaluation.** The modelling accuracy of the developed SPECT GPU implementation was first benchmarked against the reference code GATE v7.0 using three classical metrics:

- *Root Mean Squared Difference (RMSD)* characterizing the difference between two projections, providing a score between 0 and 1 (0 for no detected differences):

$$\text{RMSD} = \sqrt{\frac{1}{N} \sum_{k=1}^N (B_k^{\text{GPU\_SPECT}} - B_k^{\text{GATE\_SPECT}})^2} \quad (3)$$

where  $B_k^{\text{GPU\_SPECT}}$  and  $B_k^{\text{GATE\_SPECT}}$  are voxel<sub>k</sub> value in GPU and GATE projections respectively. This metric was applied on the uniform source projections;

- *SPECT system sensitivity* (counts/MBq/s) corresponding to the total number of detected counts divided by the number of emitted particles computed from the ten independent point source acquisitions.
- *Image statistical quality* defined as the standard deviation divided by the mean over a region of interest (ROI) ( $60 \times 60$  pixels for  $^{99m}\text{Tc}$  and  $30 \times 30$  pixels for  $^{111}\text{In}$  and  $^{131}\text{I}$  imaging) within the uniform source projections. Similarly, a mean noise value was derived from the 64 cylindrical phantom projections (using a  $20 \times 20$  pixels ROI for  $^{99m}\text{Tc}$  and a  $10 \times 10$  pixels ROI for  $^{111}\text{In}$  and  $^{131}\text{I}$ ).

An additional analysis aimed at evaluating the impact of using single or double precision for the kernel codes launched on GPU threads. Each of the point source, uniform source and cylindrical phantom simulations were also performed both for the GPU\_SPECT strategy with simple precision and double precision. The associated metrics were also derived for accuracy comparison between single and double precision.

For visual comparison, profiles were also drawn across the point source projections simulated with the different simulation strategies. Similar tests were performed through the reconstructed volumes of the cylindrical phantom simulations. The GPU based ray tracing strategy (GPU\_rtcolli) was also considered in order to evaluate the relative impact of ignoring septal penetration for the three radioisotope/collimator combinations using the similar metrics obtained from the point source, uniform source and cylindrical phantom projections.

The full potential of the proposed GPU SPECT simulation code was assessed by simulating an acquisition using the XCAT anthropomorphic phantom (Segars *et al* 2010). A whole-body planar acquisition of this voxelized phantom was simulated using the  $^{111}\text{In}$ /MEGP combination, following the simulation set-up described in Garcia *et al* (2015). In this previous work, Octreoscan<sup>TM</sup> pharmacokinetics data were used to derive a 6-compartment model composed of urinary bladder, blood, liver, kidneys, spleen and the rest of the body organs and tissues. From that model, it is possible to compute the cumulated activity (number of emissions in Bq.s) at every time interval of interest for each compartment. For this study, cumulative activity maps using the XCAT model were generated to simulate a 20 minutes ‘step & shoot’ acquisition at 4h post-injection (5 axial steps to cover the whole phantom). The resulting maps consisted of 128 columns, 128 lines and 500 slices, with voxel dimensions of  $4.0 \times 4.0 \times 4.0 \text{ mm}^3$ . Anterior and posterior views were both simulated with a resulting image format of  $128 \times 512$  pixels and a pixel size of  $4.42 \times 4.42 \text{ mm}^2$ . Profiles through the XCAT simulated views using both the GPU\_SPECT and GATE\_SPECT simulations were subsequently used to compare the resulting projections. Quantitative measurements were also made from ROI placed in the different organs composing the XCAT model from the GPU\_SPECT and GATE\_SPECT projections.

Finally, computational efficiency was evaluated for the different strategies using the cylindrical phantom and the XCAT model. Simulations were run on a NVIDIA GeForce GTX 980 (2048 cores—4 GB RAM) or a single core of an Intel Core i5 (3.5 GHz) for GPU and CPU strategies respectively. Acceleration factors were derived between the two full MC simulation codes either on GPU (GPU\_SPECT) or CPU (GATE\_SPECT) for each combination and between the

**Table 2.** SPECT system sensitivity for the three radioisotope/collimator combinations from point source projections obtained with the different simulation strategies.

Sensitivity (counts/MBq/s)	<sup>99m</sup> Tc/LEHR (Avg. ± SD)	<sup>111</sup> In/MEGP (Avg. ± SD)	<sup>131</sup> I/HEGP (Avg. ± SD)
GATE_SPECT	86.9 ± 0.85	60.5 ± 1.0	38.63 ± 1.3
GPU_SPECT (double precision)	86.65 ± 1.65	60.06 ± 1.42	38.61 ± 1.56
GPU_SPECT (simple precision)	86.66 ± 1.66	60.08 ± 1.34	38.55 ± 1.54
GPU_rtcolli	81.94 ± 1.41	54.69 ± 1.19	24.96 ± 0.80

GPU\_rtcolli and GPU\_SPECT simulation codes for <sup>99m</sup>Tc and <sup>111</sup>In. For the whole body XCAT phantom simulations different hardware configurations were considered for the GPU\_SPECT simulations; namely three NVIDIA GeForce GPU cards: GTX 690 (3072 cores—2 GB RAM), GTX 980 (2048 cores—4 GB RAM), GTX 980 Ti (2816 cores—6 GB RAM). The corresponding GATE\_SPECT simulations were run on a single Intel Core i5 (3.5 GHz).

### 3. Results

#### 3.1. Point source simulations

In table 2, the measurements obtained from the 10 independent point source acquisitions, show that the implemented GPU\_SPECT simulations yield identical system sensitivities compared to GATE for all three radioisotope/collimator combinations considered. No difference is notable between the GPU\_SPECT simulations with single and double precision. Sensitivity values obtained with GPU ray-tracing strategy for <sup>99m</sup>Tc and <sup>111</sup>In images are slightly lower (−5%) relative to the strategies for which septal penetration is not neglected (i.e. GPU\_SPECT and GATE\_SPECT). This difference suggests that 5% of the counts in the final projection obtained with the full MC strategies come from diffused photons within the collimator septa. For the <sup>131</sup>I case, the 14% difference in the sensitivity values between full MC strategies and the GPU\_rtcolli strategy show that a much larger fraction of photons are diffused within collimator septa.

Line profiles were drawn on the center of the 1 GBq point source images obtained with the different simulation strategies considered (figure 6). A logarithmic scale was applied to the point source projections to better visualize the diffused photons around the point source. Both for <sup>99m</sup>Tc and <sup>111</sup>In point sources, projections using the full MC simulations are identical whereas the projection obtained with the GPU ray tracing strategy shows marginally lower counts (−5%). Despite this quantitative difference, the simulated images are visually very similar. Finally, <sup>131</sup>I point source projections exhibit the common star structure with the full MC strategies. As expected for the ray-tracing strategy, the star branches do not appear on the resulting projection. The line profiles confirm that the diffused photons composing the star branches cannot be neglected for such high energy photon isotopes and as such the simplistic ray tracing approach is not sufficiently accurate for such isotopes.

#### 3.2. Uniform source simulations

In table 3, the measurements obtained from the 30 × 30 cm<sup>2</sup> uniform source simulations show that the GPU\_SPECT module yields images with statistical quality very close to the



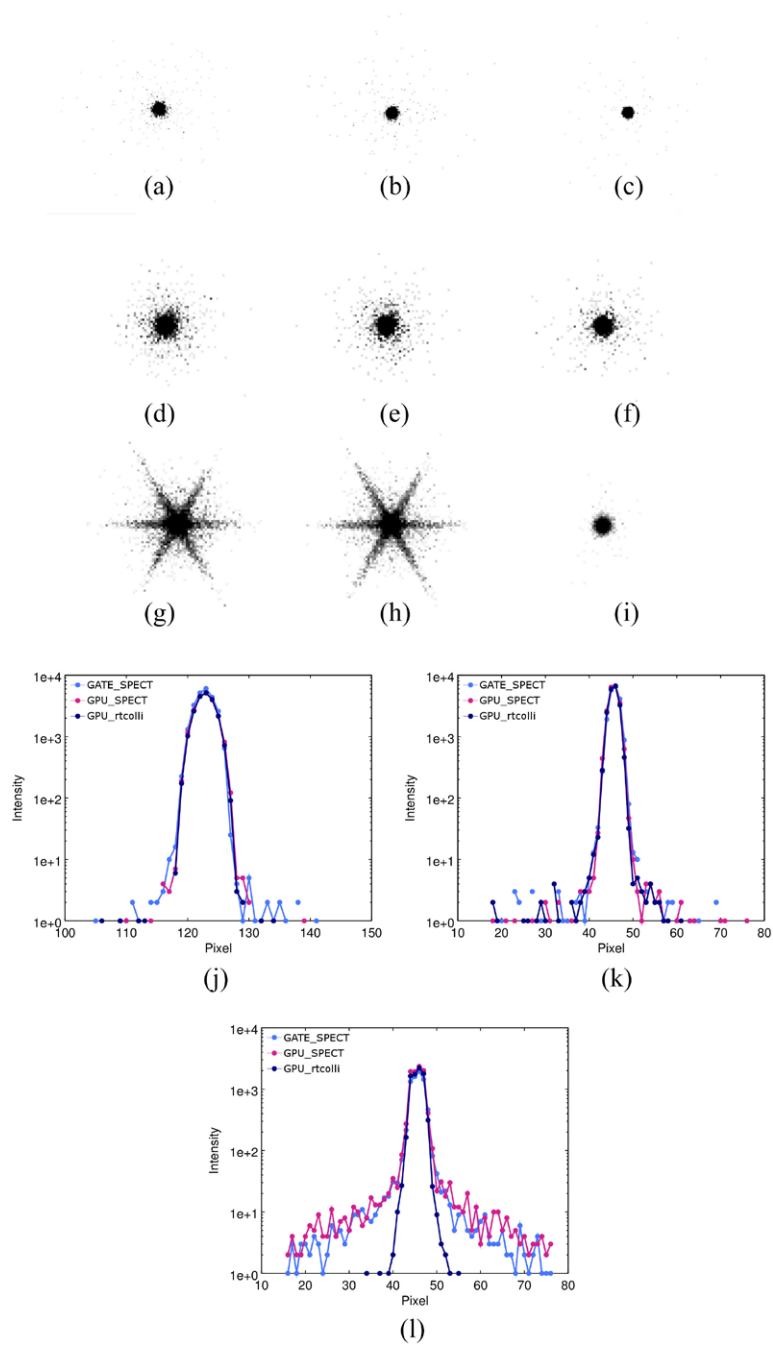


**Figure 6.** Point source projections and line profiles (drawn through the center of the corresponding point sources) with the different simulation strategies and imaging configurations: ((a)–(c), (j))  $^{99m}\text{Tc}$ ; ((d)–(f), (k))  $^{111}\text{In}$ ; ((g)–(i), (l))  $^{131}\text{I}$ . (a) GATE\_SPECT. (b) GPU\_SPECT. (c) GPU\_rtcolli. (d) GATE\_SPECT. (e) GPU\_SPECT. (f) GPU\_rtcolli. (g) GATE\_SPECT. (h) GPU\_SPECT. (i) GPU\_rtcolli.

**Table 3.** Noise level and root mean squared difference (RMSD) measurements for the three radioisotope/collimator combinations from uniform source projections obtained with the different simulation strategies.

Isotope/collimator	<sup>99m</sup> Tc/ LEHR	<sup>111</sup> In/ MEGP	<sup>131</sup> I/ HEGP
Noise level (%)			
GATE_SPECT	31.9	19.3	23.4
GPU_SPECT (double precision)	32.0	19.6	24.3
GPU_SPECT (simple precision)	32.0	18.8	25.1
GPU_rtcolli	33.2	20.1	31.5
RMSD (%)			
GATE_SPECT versus GPU_SPECT	12.15	11.25	11.17
GATE_SPECT(1) versus GATE_SPECT(2)	12.43	10.04	11.18

GATE simulations for all three radioisotope/collimator combinations. A similar noise level is also obtained between the GPU\_SPECT simulations with single and double precision for the three combinations. RMSD values are <12% for each combination between the two projections. They are of similar magnitude to the RMSD values obtained when comparing two GATE independent simulations (GATE\_SPECT(1) versus GATE\_SPECT(2)), which demonstrates that the observed differences between the proposed GPU\_SPECT implementation and GATE are equivalent to the variations from two identical MC simulation runs using the same simulation platform. Finally, <sup>99m</sup>Tc and <sup>111</sup>In images simulated with the GPU ray tracing approach exhibit a noise level slightly higher than images obtained with the full MC simulations taking into account septal penetration. This can be essentially attributed to the 5% difference in the number of counts within final projections between the projections obtained using the two simulation strategies. The noise level is even higher for the <sup>131</sup>I/HEGP combination due to the even smaller amount of counts in the GPU\_rtcolli simulated images.

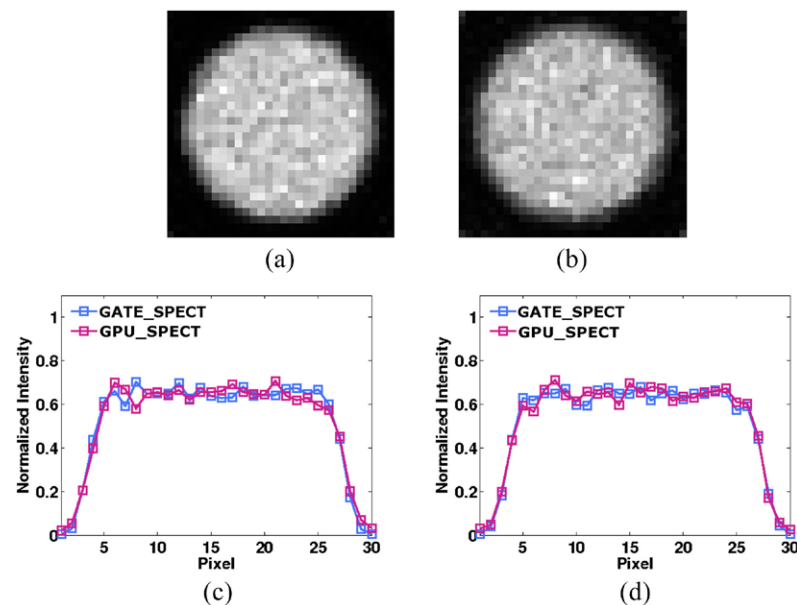
### 3.3. Cylindrical phantom simulations

Table 4 shows the computational efficiency obtained from the SPECT cylindrical phantom acquisitions for the three radioisotope/collimator combinations. The SPECT\_GPU strategy with simple precision was chosen for the remainder of the study as we demonstrated a good agreement with the GATE simulations in terms of sensitivity and statistical quality. For <sup>99m</sup>Tc/LEHR, the complete SPECT simulation was executed in  $\approx 66$  h with GATE, whereas simulations took  $\approx 3$  h with the GPU\_SPECT and 1 h with the GPU\_rtcolli simulations leading to acceleration factors for MC SPECT simulations within the GPU framework of over two orders of magnitude (22 and 66) using the full MC simulation and the ray-tracing approaches respectively. For <sup>111</sup>In/MEGP, the acceleration factor is even higher (27). Finally for <sup>131</sup>I/HEGP, the complete SPECT simulation was completed in  $\approx 71$  h with GATE and  $\approx 4$  h with GPU\_SPECT, corresponding to an acceleration factor of almost two orders of magnitude. Besides, an equivalent level of noise was found with the relevant strategy for each radioisotope/collimator combination.

Figure 7 shows images and line profiles through the reconstructed volumes from <sup>111</sup>In cylindrical phantom simulations for GATE\_SPECT and GPU\_SPECT strategies. For each volume, two lines were drawn through the cylinder center and the resulting profiles show a very good agreement between the results of the two strategies (figures 7(c) and (d)).

**Table 4.** Computational efficiency and noise levels for the three radioisotope/collimator combinations from the 64 cylindrical phantom projections obtained with the different simulation strategies.

Isotope/collimator	$^{99m}\text{Tc}/\text{LEHR}$	$^{111}\text{In}/\text{MEGP}$	$^{131}\text{I}/\text{HEGP}$
Total duration time (h)			
GATE_SPECT	66	67	71
GPU_SPECT	3	2.5	4
GPU_rtcolli	1	1	—
Acceleration factor			
GPU_SPECT	<b>22</b>	<b>27</b>	<b>18</b>
GPU_rtcolli	<b>66</b>	<b>67</b>	—
Noise level (%)			
GATE_SPECT	14.29	9.23	11.48
GPU_SPECT	14.44	9.47	12.54
GPU_rtcolli	14.84	9.81	—



**Figure 7.**  $^{111}\text{In}$  cylindrical phantom simulations: ((a), (b)) transaxial slices through the reconstructed volumes, ((c), (d)) line profiles plotted through the cylinder center in the transaxial slices. (a) GATE\_SPECT. (b) GPU\_SPECT. (c) Line 1. (d) Line 2.

### 3.4. Whole-body planar simulations

The anterior and posterior whole-body images obtained from the XCAT model with the  $^{111}\text{In}/\text{MEGP}$  combination using both GATE\_SPECT and GPU\_SPECT strategies are shown in figure 8. Line profiles were drawn through different organs on the resulting whole-body planar images. The resulting profile plots are shown in figure 9, for both CPU and GPU strategies. Although the comparative profile shapes for the different organs are in good agreement, the low statistical quality of the projection images are responsible for the noisy appearance of the plots and resulting differences in the number of counts. To further validate the GPU\_SPECT

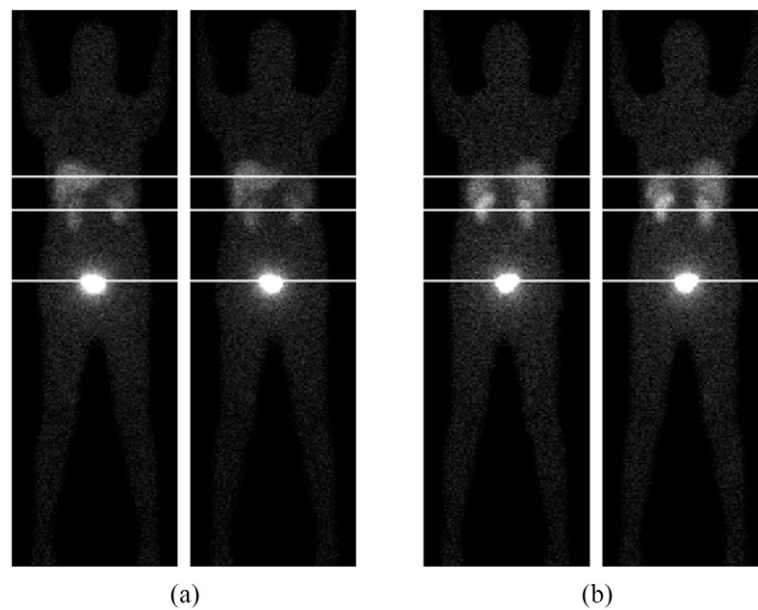


**Figure 8.** Anterior and posterior whole-body planar simulations of the XCAT phantom with the  $^{111}\text{In}$ /MEGP combination using GATE\_SPECT and GPU\_SPECT codes (left and right images respectively for each view). Location of three profile lines are also shown on the images (resulting plots are depicted in figure 9). (a) Anterior view. (b) Posterior view.

performance, a ROI analysis performed within different organs also demonstrates a good agreement in the intensity ranges for both strategies (table 5).

Table 6 shows the computational efficiency obtained from XCAT-WB phantom acquisitions for different GPU hardware. Five different simulations were performed for each step with the appropriate axial location of the gamma-camera heads. The total number of emitted photons was about  $7.6 \times 10^9$  for each axial location. For GATE, simulations of each step were performed in about 17–18 days, depending on the number of counts detected by the heads in each axial position. Indeed, the third step takes a little longer given that the head is located on the bladder which exhibits a higher activity. The corresponding execution times for the GPU\_SPECT simulations were 15–17 h, 8–9 h and 5–6 h with the GTX 690 GPU card, GTX 980 GPU card and GTX 980 ti GPU card respectively. The resulting acceleration factor compared with GATE on CPU is therefore 26, 49 and 71 for each of the three GPU cards considered.

#### 4. Discussion

Our main objective in this work was to implement a GPU-based solution for SPECT Monte Carlo simulations and evaluate its performance for various combinations of radioisotopes and collimators. To our knowledge, this is the first time that a GPU strategy has been developed for the Monte Carlo simulation of SPECT imaging. Various CPU-based solutions have been proposed to accelerate SPECT Monte Carlo simulations associated with various approximations that should be considered carefully according to the radioisotope of interest. The proposed GPU strategy was conceived to reproduce full Monte Carlo simulations applicable to any radioisotope. To ensure accurate Monte Carlo simulations, our implementation

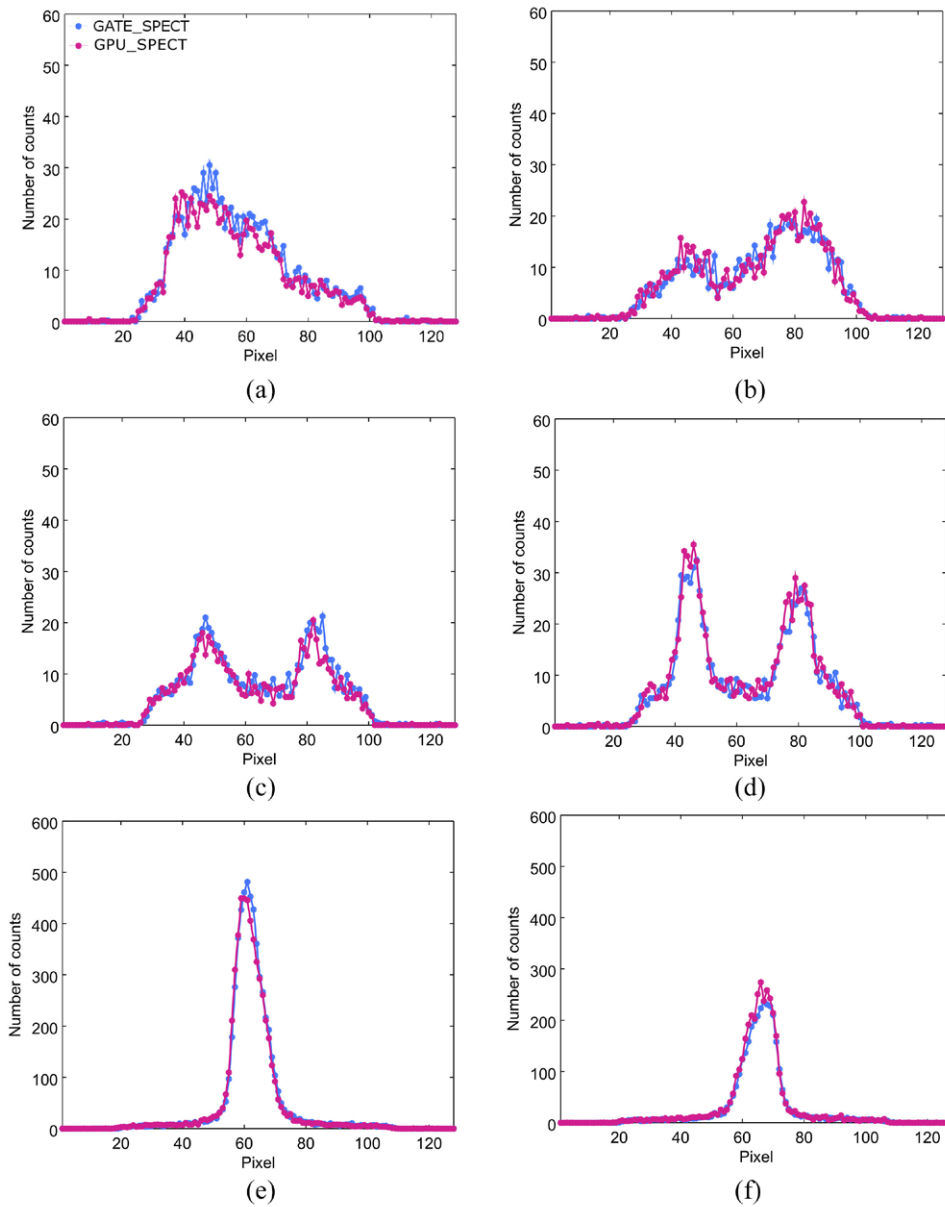


**Figure 9.** Line profiles plotted through different organs of the XCAT-WB planar simulations (shown in figure 8), (a) liver + spleen (anterior view), (b) liver + spleen (posterior view), (c) kidneys (anterior view), (d) kidneys (posterior view), (e) bladder (anterior view), (f) bladder (posterior view).

is based on the well-known Geant4 libraries, which include validated physics models. The proposed SPECT module was implemented within the previously proposed GGEMS (GPU Geant4-based Monte Carlo simulations) framework (Bert *et al* 2013). In this previous work, the GPU implemented Geant4 physics models were validated against standard Geant4, and the proposed model of a single photon processed by a single thread from its birth to its death

**Table 5.** Mean intensity values from ROI placed in the different organs composing the XCAT model from the GPU\_SPECT and GATE\_SPECT projections.

Avg. (Min–Max)	Liver (300 pixels)	Kidneys (110 pixels)	Spleen (150 pixels)	Body (2000 pixels)	Bladder (90 pixels)
GATE_SPECT	22.9 (11–37)	17.4 (8–27)	17.0 (5–29)	4.6 (0–13)	534.4 (80–955)
GPU_SPECT	20.1 (8–35)	15.7 (7–26)	17.3 (8–34)	4.2 (0–13)	488.1 (68–839)

**Table 6.** Computational efficiency for the ‘step & shoot’ acquisition (5 steps) of the XCAT-WB phantom with GATE\_SPECT and GPU\_SPECT using three different GPU cards.

Steps	Activity (GBq)	GATE_SPECT 1 CPU core (days)	GPU_SPECT GTX 690 (h)	GPU_SPECT GTX 980 (h)	GPU_SPECT GTX 980 ti (h)
<b>1</b>	7.56	17	15	8	6
<b>2</b>	7.58	17	16	9	6
<b>3</b>	7.59	18	17	9	6
<b>4</b>	7.61	17	15	8	6
<b>5</b>	7.62	17	15	8	5
<b>Total</b>	37.96	86	78	42	29
<b>Acceleration</b>	—	—	26	49	71

was assessed as efficient for medical imaging and radiotherapy applications, without however considering the specific case of SPECT imaging. We chose to focus first on the widely used hexagonal hole collimator which exhibits a very complex structure with numerous hexagonal holes since it is the most widely used collimator clinically and its specific structure leads to a highly inefficient photon tracking process and consequently to time-consuming Monte Carlo simulations. The originality of our approach is to define the collimator geometry analytically only once at the beginning and subsequently copy it to the GPU memory to be accessible for each thread when running the code. In addition, the proposed simplified description of the collimator reduced to the coordinates of each hexagonal hole center allows minimization of the amount of memory needed. From those center coordinates, the geometric navigation is performed using a set of analytical equations to derive the local position of the considered photon and compute its next interaction distance by ray tracing techniques. A reduced search area is first derived, which is crucial to avoid scanning the whole collimator grid. Ray-tracing techniques are based on analytical equations which allow an efficient and precise distance computation. However, due to the complex structure of the collimator and its numerous holes, the computation of the next interaction distance with a hole (if the current photon position is inside a septum) relies on several ray tracing computations. More specifically, up to thirteen surrounding holes are being tested if the photon is not in the peripheral area of the collimator. Thus, despite the reduced search area, interaction distance computation may slow down the global computation time. Further work could focus on the optimization of such geometric navigation within the collimator.

The proposed GPU-based simulation implementation leads to the same images being obtained as with the reference code GATE v7 in terms of sensitivity and image quality, and for various radioisotope/collimator combinations. A third strategy, which does not consider septal penetration but immediately kills a particle reaching a septum was also tested. From our experiments with  $^{99m}\text{Tc}$  and  $^{111}\text{In}$  imaging, we found a 5% difference in the projection counts between a full MC simulation and this latter strategy. However, sensitivity values and noise levels derived from the various sources were found similar to full MC simulations. On the other



hand, by neglecting septal penetration, the number of tracking steps is minimal, leading to even larger gains in computational efficiency. Indeed, an acceleration factor of 66 was found for cylindrical phantom simulations using this latter strategy when compared with the same simulation using GATE. By comparison the full MC simulation on GPU yielded an acceleration of 22. Although these results suggest that a simple ray tracing approach on GPU appears very efficient for the simulation of  $^{99m}\text{Tc}$  and  $^{111}\text{In}$  imaging it should not be used with  $^{131}\text{I}$  imaging—for which a higher number of diffused photons results in substantial differences in the projection counts both in terms of magnitude and also in terms of their spatial distribution.

For full MC simulations using the proposed GPU SPECT module, the acceleration factors were dependent on the type of collimator used and the radioisotope of interest. From the cylindrical phantom simulations, the measured differences in the execution time are mainly due to photon transport differences inside the collimator, with photons spending more time inside a more complex structured collimator. Moreover, the main difference between  $^{99m}\text{Tc}$ ,  $^{131}\text{I}$  and  $^{111}\text{In}$  imaging is the number of steps performed in the collimator. 364 keV photons of  $^{131}\text{I}$  are very penetrating and are able to cross 1.8 mm thick septa, and as such many interaction distance computations may be necessary inside the collimator for a 364 keV photon before reaching the detector. The resulting acceleration factors are between two and three orders of magnitude when comparing with the execution time obtained on CPU. The full efficiency brought by the GPU strategy was assessed using a voxelized source as this is a common source of interest and associated with increased computations depending on the size of the voxels considered. In this study, we chose to simulate whole-body planar acquisitions from an anthropomorphic model, which may take several months when running on standard CPU simulations. A computing cluster is a common solution to reduce the global simulation time by splitting the total number of emissions and running several simulations in parallel, as used in Garcia *et al* (2015). On a single GPU card, the computation time was reduced by up to a factor of 71, which in a multi-GPU environment would allow to realise a full voxelised SPECT MC simulation of an anthropomorphic phantom with no approximations in a few hours. Indeed the proposed implementation framework is totally transposable to parallelisation in a multi-GPU set-up since each photon is handled by a single thread in an independent fashion. Under these conditions the MC simulation of SPECT images becomes accessible to the wider community for times of execution compatible with clinical practice, for example within the context of radioimmunotherapy dosimetry studies. The GGEMS simulation platform integrating the developments described in this work is intended to be publicly released. In addition, parts of the proposed GPU implementation compatible with GATE will be also integrated in future GATE releases.

## 5. Conclusion

The generation of large image datasets is currently limited by the low computational efficiency of CPU-based Monte Carlo simulation codes in the context of SPECT imaging. The main objective of our work was to evaluate the interest in using GPU cards in the context of SPECT imaging Monte Carlo simulations. We proposed an original GPU-based SPECT simulation implementation based on the Geant4 libraries and a previously proposed generic GPU framework for MC simulations. The accuracy of the proposed implementation was validated against the reference code GATE for different combinations of radioisotopes and collimators. Acceleration factors of between two and three orders of magnitude were obtained from simple cylindrical phantom simulations for the various radioisotope/collimator combinations. In the case of more clinically realistic simulations composed of an anthropomorphic phantom,

whole-body planar images were simulated in one day on a single GPU card in comparison to three months on a single CPU. Further work will focus on the modeling of other collimator geometries such as pinhole and multi-pinhole based systems, which are most frequently encountered in preclinical imaging set-ups.

## References

- Agnostinelli S *et al* 2003 Geant4—a simulation toolkit *Nucl. Instrum. Methods Phys. Res.* **506** 250–303
- Allison J *et al* 2006 Geant4 developments and applications *IEEE Trans. Nucl. Sci.* **53** 270–8
- Assié K, Gardin I, Véra P and Buvat I 2005 Validation of the Monte Carlo simulator GATE for indium-111 imaging *Phys. Med. Biol.* **50** 3113–25
- Autret D, Bitar A, Ferrer L, Lisbona A and Bardiès M 2005 Monte Carlo modeling of gamma cameras for I-131 imaging in targeted radiotherapy *Cancer Biother. Radiopharm.* **20** 77–84
- Bert J, Perez-Ponce H, Bitar Z E, Jan S, Boursier Y, Vintache D, Bonissent A, Morel C, Brasse D and Visvikis D 2013 Geant4-based Monte Carlo simulations on GPU for medical applications *Phys. Med. Biol.* **58** 5593–611
- Brolin G, Gleisner K S and Ljungberg M 2013 Dynamic ( $^{99m}\text{Tc}$ -MAG3 renography: images for quality control obtained by combining pharmacokinetic modelling, an anthropomorphic computer phantom and Monte Carlo simulated scintillation camera imaging *Phys. Med. Biol.* **58** 3145–61
- Crespo C *et al* 2008 Quantification of dopaminergic neurotransmission SPECT studies with  $^{123}\text{I}$ -labelled radioligands. A comparison between different imaging systems and data acquisition protocols using Monte Carlo simulation *Eur. J. Nucl. Med. Mol. Imaging* **35** 1334–42
- De Beenhouwer J, Staelens S, Vandenberghe S and Lemahieu I 2008 Acceleration of GATE SPECT simulations *Med. Phys.* **35** 1476–85
- Descourt P, Carlier T, Du Y, Song X, Buvat I, Frey E C, Bardiès M, Tsui B M W and Visvikis D 2010 Implementation of angular response function modeling in SPECT simulations with GATE *Phys. Med. Biol.* **55** 253–66
- Dewaraja Y K, Ljungberg M and Koral K F 2000 Characterization of scatter and penetration using Monte Carlo simulation in  $^{131}\text{I}$  imaging *J. Nucl. Med.* **41** 123–30
- Garcia M P, Villoing D, McKay E, Ferrer L, Cremonesi M, Botta F, Ferrari M and Bardiès M 2015 TestDose: a nuclear medicine software based on Monte-Carlo modelling for generating gamma camera acquisitions and dosimetry *Med. Phys.* **42** 6885
- Harrison R L, Vannoy S D, Haynor D R, Gillispie S B, Kaplan M S and Lewellen T K 1993 Preliminary experience with the photon generator module of a public-domain simulation system for emission tomography *IEEE NSS-MIC Conf. Record* **2** 1154–8
- Holstenson M, Partridge M, Buckley S E and Flux G D 2010 The effect of energy and source location on gamma camera intrinsic and extrinsic spatial resolution: an experimental and Monte Carlo study *Phys. Med. Biol.* **55** 1735–51
- Jan S *et al* 2004 GATE : a simulation toolkit for PET and SPECT *Phys. Med. Biol.* **49** 4543–61
- Kawrakow I, Mainegra-Hing E, Rogers D, Tessier F and Walters B 2010 The EGSnrc code system: Monte Carlo simulation of electron and photon transport *NRCC Report PIRS-701* National Research Council of Canada, Ottawa, Canada
- Lippuner J and Elbakri I A 2011 A GPU implementation of EGSnrc's Monte Carlo photon transport for imaging applications *Phys. Med. Biol.* **56** 7145–62
- Ljungberg M, Larsson A and Johansson L 2005 A new collimator simulation in SIMIND based on the delta-scattering technique *IEEE Trans. Nucl. Sci.* **52** 1370–5
- Ljungberg M and Strand S E 1989 A monte carlo program for the simulation of scintillation camera characteristics *Comput. Methods Programs Biomed.* **29** 257–72
- Segars W P, Sturgeon G, Mendonca S, Grimes J and Tsui B M W 2010 4D XCAT phantom for multimodality imaging research *Med. Phys.* **37** 4902–15
- Song X, Segars W P, Du Y, Tsui B M W and Frey E C 2005 Fast modeling of the collimator-detector response in monte carlo simulation of SPECT imaging using the angular response function *Phys. Med. Biol.* **50** 1791–804
- Staelens S, Strul D, Santin G, Vandenberghe S, Koole M, D'Asseler Y, Lemahieu I and de Walle R V 2003 Monte Carlo simulations of a scintillation camera using GATE: validation and application modelling *Phys. Med. Biol.* **48** 3021–42

## B.4 Application de GGEMS en curiethérapie de la prostate

# GGEMS-Brachy: GPU GEant4-based Monte Carlo simulation for brachytherapy applications

Yannick Lemaréchal<sup>1</sup>, Julien Bert<sup>1</sup>, Claire Falconnet<sup>2</sup>,  
Philippe Després<sup>3,4</sup>, Antoine Valeri<sup>4,5</sup>, Ulrike Schick<sup>1,2</sup>,  
Olivier Pradier<sup>1,2</sup>, Marie-Paule Garcia<sup>1</sup>, Nicolas Boussion<sup>1,2</sup>  
and Dimitris Visvikis<sup>1</sup>

<sup>1</sup> LaTIM, UMR1101, INSERM, CHRU Brest, France

<sup>2</sup> Service de radiothérapie, CHRU Brest, France

<sup>3</sup> Département de radio-oncologie and Centre de recherche du CHU de Québec, Québec QC, Canada

<sup>4</sup> Département de physique, de génie physique et d'optique and Centre de recherche sur le cancer, Université Laval, Québec QC, Canada

<sup>5</sup> Service d'urologie, CHRU Brest, France

E-mail: [yannick.lemarechal@univ-brest.fr](mailto:yannick.lemarechal@univ-brest.fr)

Received 4 March 2015, revised 23 April 2015

Accepted for publication 23 April 2015

Published 10 June 2015



CrossMark

### Abstract

In brachytherapy, plans are routinely calculated using the AAPM TG43 formalism which considers the patient as a simple water object. An accurate modeling of the physical processes considering patient heterogeneity using Monte Carlo simulation (MCS) methods is currently too time-consuming and computationally demanding to be routinely used. In this work we implemented and evaluated an accurate and fast MCS on Graphics Processing Units (GPU) for brachytherapy low dose rate (LDR) applications. A previously proposed Geant4 based MCS framework implemented on GPU (GGEMS) was extended to include a hybrid GPU navigator, allowing navigation within voxelized patient specific images and analytically modeled <sup>125</sup>I seeds used in LDR brachytherapy. In addition, dose scoring based on track length estimator including uncertainty calculations was incorporated. The implemented GGEMS-brachy platform was validated using a comparison with Geant4 simulations and reference datasets. Finally, a comparative dosimetry study based on the current clinical standard (TG43) and the proposed platform was performed on twelve prostate cancer patients undergoing LDR brachytherapy. Considering patient 3D CT volumes of 400 × 250 × 65 voxels and an average of 58 implanted seeds, the mean patient dosimetry study run time for a 2% dose uncertainty was 9.35 s

( $\approx 500$  ms  $10^{-6}$  simulated particles) and 2.5 s when using one and four GPUs, respectively. The performance of the proposed GGEMS-brachy platform allows envisaging the use of Monte Carlo simulation based dosimetry studies in brachytherapy compatible with clinical practice. Although the proposed platform was evaluated for prostate cancer, it is equally applicable to other LDR brachytherapy clinical applications. Future extensions will allow its application in high dose rate brachytherapy applications.

Keywords: Monte Carlo simulation, GPU, Geant4, brachytherapy, intraoperative radiotherapy

(Some figures may appear in colour only in the online journal)

## 1. Introduction

Intra-operative radiotherapy encompasses a number of applications and organ-specific techniques involving the insertion of different types of radioactive sources in close tumor proximity. A key feature of intra-operative radiotherapy is that in principle the irradiation only affects a local area around the inserted radiation sources and hence radiation exposure of healthy tissues further away from these sources is reduced. Amongst these techniques the most widely used clinically is the brachytherapy procedure which consists of inserting sealed radioactive sources inside an organ, either temporarily or permanently depending on the technique and associated treatment protocol used. Within this context the most popular brachytherapy procedure known as Low Dose Rate (LDR) brachytherapy is associated with the permanent insertion of low activity sources in the organ of interest, using low energy radionuclides such as Iodine-125 or Palladium-103. On the other hand, High Dose Rate (HDR) brachytherapy uses a single high activity radioactive source temporarily placed at different positions in the organ of interest through a catheter. Brachytherapy today is mainly used in the treatment of prostate, breast and gynecological cancers. Within the context of early stage prostate cancer, LDR brachytherapy is associated with significantly better urinary and sexual function compared to patients undergoing radical prostatectomy or external beam radiotherapy (Frank *et al* 2007). LDR brachytherapy is a successful treatment regime for early stage primary prostate cancer with reported 10 year disease free survival rates close to 94% (Morris *et al* 2013). High accuracy in the positioning of the seeds is essential in order to avoid areas of tumor under-dosage (cold spot) due to the limited penetration of the low energy radiation. As reported by a recent clinical study (Sasaki *et al* 2014), patients with recurrence following LDR prostate brachytherapy had positive biopsy sites corresponding to the under-dosed areas identified at the initial dose planning. On the other hand it is also essential to ensure the minimum dose to the nearby organs at risk. Finally, an accurate dosimetry is particularly important for focal brachytherapy treatments, where the aim is to irradiate only a small-localized part of the prostate. This approach may allow reducing the toxic effects of treatment while maintaining similar treatment outcomes when compared with whole-gland therapy (Tong *et al* 2013). In addition, focal brachytherapy is a promising strategy to treat local recurrent prostate cancer after primary external beam radiation failure in order to avoid more aggressive treatments (Wallace *et al* 2014).

In brachytherapy, dosimetry plans are routinely calculated based on the American Association of Physicists in Medicine (AAPM) task group (TG) 43 formalism. This formalism considers the patient as an exclusively liquid water object which is associated with numerous approximations such as tissue homogeneity and absence of inter-seed attenuation (Carrier *et al* 2006, Afsharpour *et al* 2008). Rivard *et al* (2009) have pointed out that accepted

clinical dose parameters can be over- or under-estimated by at least 7% and by as much as an order of magnitude in certain situations, when the TG-43 model is used. The recent AAPM Task Group 186 report provides guidance for the use of model-based dose calculation algorithms (MBDCA) that consist of using alternative and more accurate dose calculation models accounting for non-water equivalent media, such as for instance the collapse-cone method, the grid based Boltzmann solver (GBBS) and Monte Carlo (MC) methods (Beaulieu *et al* 2012). Considering the collapse-cone method (Carlsson and Ahnesjö 2000), a superposition of two pre-calculated dose kernel convolutions for each material density are used, one for the primary and another for the secondary particles. The limitation of such an algorithm is the inaccuracies associated with the modeling of the multiple scattering and associated secondary particles (Beaulieu *et al* 2012). VARIAN Medical Systems (Palo Alto, California, US) has developed Acuros™ BV, a treatment planning system that uses an optimization step based on the TG43 formalism with the final dose calculation using a GBBS approach. This system is able to estimate the dose deposition in the patient in a few minutes. Zourari *et al* (2010) validated this approach for HDR brachytherapy with dose values within 3% in comparison to MC estimations. However, this solver is only currently available for HDR and Pulse Dose rate (PDR) brachytherapy.

The most accurate modeling of physical processes considering the presence of patient specific anatomy and associated tissue heterogeneities can be achieved using MC simulation methods (Rassiah-Szegedi *et al* 2007). However, MC methods are also associated with long execution times, which is one of the major issues preventing their use in routine clinical practice. A computationally efficient approach allowing accurate dose calculations within a few seconds is of particular importance in brachytherapy since it can concern an intra-operative environment. In terms of existing Monte Carlo simulation codes dedicated to brachytherapy, Brachydose (Taylor *et al* 2007) is based on the use of EGSnrc (Kawrakow 2000). An alternative approach that may improve computational efficiency consists in using pre-simulated phase-space files for the source simulation where all particle data (position, direction and energy) are stored. A MC-based brachytherapy code based on Geant4 (ALGEBRA, (Afsharpour *et al* 2012)) has used such phase-space files for the source simulation by removing image voxels that contain seeds. Although this code can provide relatively fast dosimetry calculations (2 min considering voxels of  $2^3 \text{ mm}^3$ ) with an uncertainty of 2% inside the prostate, there are approximations associated with the lack of consideration for seed/voxel overlapping geometry issues. In order to account for such interactions the concept of the parallel world introduced by Yegin (2003) for the EGSnrc code may be used. In Brachydose based on EGSnrc, two particle navigators are used in parallel during the same simulation, one for tracking particles through analytical seed geometry and another to handle particle navigation within the voxelized patient images. A similar approach was proposed by Enger *et al* (2012) considering the use of Geant4 in permanent implant brachytherapy simulations, resulting in dose calculations within eight minutes for  $1.33 \times 1.33 \times 2.5 \text{ mm}^3$  voxels. Although the use of parallel worlds allows to accurately account for seed/voxel interactions, such simulations are not computationally efficient considering the fact that several particle navigators are running within the same simulation. Within an intra-operative environment where multiple dosimetry calculations are needed to optimize the number of seeds and their positions, a real time execution with a minimum of associated approximations is essential. One potential solution for efficient MC simulations without the introduction of approximations is distributed calculations using computer clusters, which are clearly incompatible with routine clinical practice. An alternative approach which has been recently gaining ground is the use of powerful architectures such as Graphics Processing Units (GPUs). Some MC simulation codes were recently implemented on GPU (Jia *et al* 2010, Tóth and Magdics 2010, Hissoiny *et al* 2011, Lippuner

and Elbakri 2011, Jahnke *et al* 2012), targeting specific applications such as external beam radiation therapy and/or medical imaging (Bert *et al* 2013). In brachytherapy the use of GPUs has been previously proposed once (GPUMCD, (Hissoiny *et al* 2011)) showing a potential to reduce associated computational times (70 ms on average for a single brachytherapy seed simulation considering only water material and  $10^6$  particles). However, in this work only a single low-energy brachytherapy seed and water material were considered which does not represent a realistic clinical brachytherapy environment (multiple seeds and tissue densities). In addition, an approximation was introduced in the implementation of the physics processes by omitting the modelling of Rayleigh scattering.

The objective of this work is to propose a GPU GEant4-Based Monte Carlo Simulation for brachytherapy applications (GGEMS-brachy). This code is an extension of a framework already developed by Bert *et al* (2013) based on the well-validated Geant4 physics model. The proposed Monte Carlo code considers the modeling of multiple analytical seeds in patient specific CT images, including inter-seed interactions and the placement of seeds independently of voxel locations (e.g. seeds overlapping multiple voxels). This has been achieved by extending the MC simulation framework with the inclusion of a hybrid GPU navigator, allowing the navigation within a voxelized phantom derived from CT imaging including an analytical based structure for accurately modeling the seeds. The proposed approach was finally evaluated on twelve patient datasets by comparison of LDR dosimetry results to the standard TG43 formalism.

## 2. Materials and methods

### 2.1. GPU architecture and global implementation strategy

In this work, all physics processes are based on the Geant4 (Allison *et al* 2006) MC engine within a generic GPU framework that has been recently proposed for MC simulations covering different medical applications (Bert *et al* 2013). The generic GPU framework was conceived around the use of one thread per particle i.e. where one thread handles a given particle from its birth to its death. This basic framework was extended in order to take into consideration different essential components in performing a full MC based simulation for brachytherapy applications (see figure 1). For an efficient implementation, particles are simulated in different stages of processing stacks. A first stage handles the particle source from a generic radioactive seed, including photon physics effects and navigation within the analytical seed geometry, and distributed to seeds placed within a voxelised volume. A second phase concerns the transportation of the emitted particles within the voxelized patient phantom derived from CT images, including an analytical based structure for accurately modeling the radioactive seeds used in treatment. This operation is performed by developing a hybrid voxelized/analytical GPU navigator. Finally, in the last implementation phase the dose scoring is performed based on a track length estimator (TLE) including uncertainty calculations (Williamson 1987). All of these stages are described more in detail in the following sections.

### 2.2. Physics effects

In the generic GPU framework used as the basis of this work, physical effects were extracted from Geant4 and implemented in GPU without introducing any approximations (Bert *et al* 2013). Given the LDR brachytherapy application considered in this work only three of the implemented physics processes were used in the MC simulations, namely the photoelectric and the Compton scattering from the standard model and the Rayleigh scattering from the



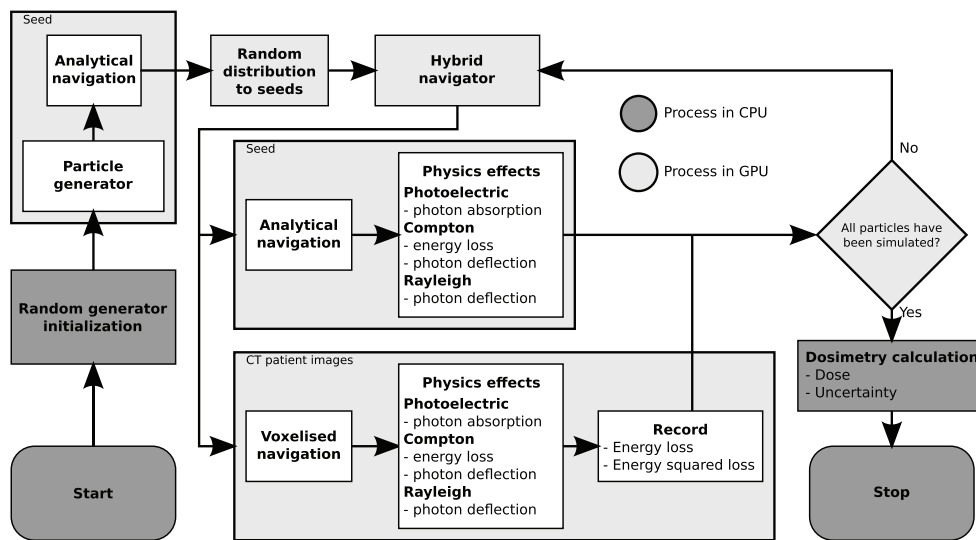


**Figure 1.** Flowchart of the proposed GGEMS-brachy implementation.

Livermore model. The photoelectric cross-sections are obtained by log-log interpolation using a database that stores values in the GPU constant memory for each elementary material and energy bin according to the Geant4 model. In the case of Compton scattering, cross-sections and scattering angles are computed analytically by using the Klein-Nishina formulation, therefore eliminating the need for specific memory allocation. Each interaction distance  $l_\sigma$  (for Compton, Rayleigh and photoelectric interactions) is randomly defined based on their cross-section  $\sigma$  by following:

$$l_\sigma = -\log\left(\frac{\xi}{\sigma}\right) \quad (1)$$

where,  $\xi$  is a random number between 0 and 1. The particle navigator subsequently uses these interaction distances to decide which interaction will occur along a particle path. Concerning the secondary electrons, Chibani and Williamson (2005) have previously shown that the range of secondary electrons from  $^{125}\text{I}$  is smaller than  $3.10^{-4}$  cm in water. Considering that the CT image voxels are  $1 \text{ mm}^3$ , electrons were not tracked during the simulation and their doses were deposited locally within each voxel they were emitted from. Since each of the physics interactions requires access to every material composing the seed and the patient voxelised volume, a database of materials is dynamically built before each simulation considering the CT patient image used. Materials from CT images are derived by transforming Hounsfield units into materials through density conversion given by Schneider *et al* (2000). Material mixtures and their physical properties are built at the beginning of the simulation on CPU using the Geant4 materials library.

### 2.3. Navigation

During a LDR prostate brachytherapy session, 50–70 radioactive seeds are typically placed inside the organ depending on the overall organ volume to be treated with seed strengths from 0.603 U to 0.709 U. It is therefore important to be able to handle multiple seeds including their interactions and their placement within a voxelised volume based on patient specific 3D

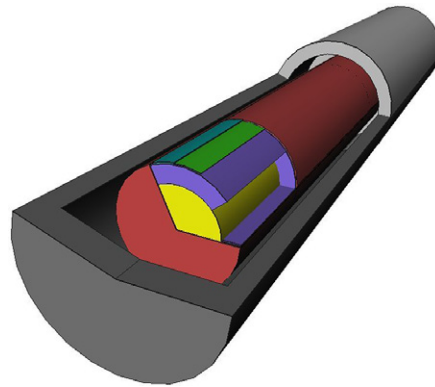


**Figure 2.** STM1251 seed geometry modeled with its different layers. Each layer color in this figure corresponds to a material that composes the seed: Titanium in dark gray, iodine in brown, Copper in blue, Nickel in green, aluminum in light gray and gold core in yellow. The complete STM1251 geometry specifications were described in Kirov and Williamson (2001).

computed tomography (CT) images. In order to facilitate such modeling a hybrid navigator combining within the same simulation framework the analytical modeling of the seeds within the patient CT based voxelised volumes was developed.

**2.3.1. Radioactive source (seed) simulation.** An I-125 seed (STM1251, Bard Medical Division, Covington, GA, USA), commonly used in prostate cancer brachytherapy, was modeled using the geometry and composition described in Kirov and Williamson (2001). Each seed consists of a set of seven successive cylindrical layers composed of titanium, air, iodine, nickel, copper, aluminum and a gold core (see figure 2). The seed has a length of 4.55 mm and a diameter of 0.81 mm, while the gold core is 3.80 mm and 0.18 mm in length and diameter respectively. Finally the radioactive iodine layer has a thickness of 17 nm. In this work only six of the seven seed layers were modeled, since the iodine layer is too thin to concern significant particle physics interactions. The different nested layers are organized similarly to Matryoshka dolls, by defining generic volumes with IDs that follow the rank of the different layers. Considering the particle emission source, photons are randomly placed on the iodine layer with a random direction. Particle energies are sampled from the cumulative density function (CDF) of the I-125 photon spectrum, considering a discretisation into 65 bins. This realistic spectrum was recovered from a complete MCS using Geant4 considering  $10^9$  disintegrations of the I-125 to Te-125. Photons produced by this simulation with energies  $>5$  keV were used to build the final CDF. An analytical navigator handles the particle transport within the different source layers. The first stage of this navigator consists in determining which of the seven volumes composing the seed contains the particle. This is obtained by checking if the current particle is inside each volume, starting from the gold core to the external titanium layer. Subsequently, the identified volume is used to calculate the interaction distances in addition to the layer boundary distance obtained by ray tracing. Given the seed geometry, the intersection point of the ray with a cylinder surface was computed using a ray/cylinder collision algorithm. The final particle step is then obtained by selecting the minimum distance between the interaction distance of each physics effect (photoelectric, Compton and Rayleigh scattering) and the boundary geometry of a seed. Subsequently, the particle is moved to this distance, and if it corresponds to a physics interaction distance the MCS resolves the discrete

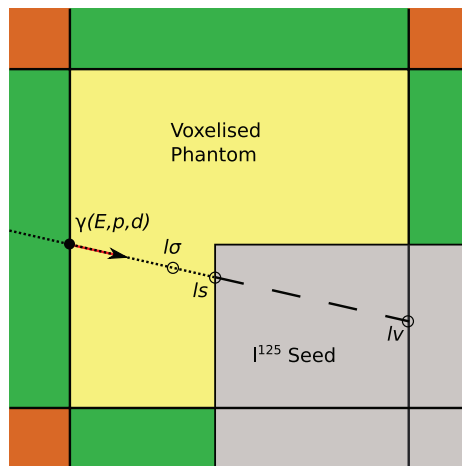


**Figure 3.** Flowchart of the GPU implementation used in the presented hybrid navigator framework.

process by updating the particle state. If the shortest distance corresponds to the boundary geometry the particle does not interact with the medium.

**2.3.2. Hybrid navigator.** In order to closely model clinical conditions, a hybrid navigator was implemented allowing the combination and interactions between the analytically simulated seeds and the voxelised patient specific anatomy based on acquired volumetric CT images. The voxelised navigator tracking is based on a principle similar to the one used in the analytical navigator. Firstly, the photon localization within the voxelized volume is determined allowing the selection of the corresponding material properties. Subsequently, interaction distances for each of the physics effects including photoelectric, Compton and Rayleigh scattering are calculated. Considering boundary geometry distances, two different values can be determined according to the following scenarios. If the voxel contains no seed, only the distance to the next voxel boundary using a simple ray/box collision algorithm (Morton 1966) is calculated. If several seeds are contained in the voxel, the distance to the edge of each seed is used as well. Similarly to the analytical navigator, the minimum distance is chosen, defining if a particle is interacting with the material ( $l_\sigma$ ), entering a seed ( $l_s$ ), or another voxel ( $l_v$ ) as shown in figure 3. If this particle reaches a seed, this automatically activates the analytical seed navigator. The transportation within a seed is performed using the ray tracing method and the analytical navigator as described in the previous section (section 2.3.1) until the particle escapes the source and the voxelized navigation resumes. The proposed hybrid navigator is able to consider several seeds close together within the same voxel as well as considering inter-seed interactions. This is achieved by storing the index of seeds contained in each voxel that can be recovered during the simulation. These index values are pre-calculated before each simulation by using a fast overlap test between seeds and each voxel (Ericson 2004). Seed positions and orientations from a given treatment plan are recovered by reading the configuration file exported by the clinical brachytherapy planning software. These index values are subsequently stored in an efficient manner using compression based on Morton key (Morton 1966). This method allows concatenating and compressing several short binary numbers into a unique integer key value. Considering the specific brachytherapy simulation, only one integer

per voxel is enough to store four different seed indices. This hybrid navigator has the advantage of handling both analytical and voxelized geometries using a single main navigator.

#### 2.4. Dosimetry

The deposited dose and the associated uncertainty are calculated using the energy deposited by each physical effect and the corresponding energy-squared respectively. These values are accumulated within two specific volumes stored on the global memory of the GPU. These volumes can have a different resolution, size and location than the voxelized phantom used in the simulation. The energy cut for the photon navigation was set at 1.11 keV (equivalent to 100  $\mu\text{m}$  in liquid water, corresponding to  $\approx \frac{1}{8}$  of the smaller voxel dimension). This implies that any photons below this energy will be stopped and their energy deposited locally. The final dose (in Grays, Gy) is computed through an integration of the entire seed radioactive life. Two estimators used to compute dose were implemented; namely the analog estimator and the Track Length Estimator (TLE) (Williamson 1987). For the standard approach the dose in each voxel is the sum of the energies deposited divided by the mass of the associated voxel. The TLE method allows a dose estimation using MCS with the same uncertainty but with a lower number of simulated particles. In a classical MCS, photons deposit their energy at a specific point, most of the time randomly along the path between two interactions. In TLE, instead of depositing energy all at once, the energy fluence is computed according to the density of each voxel crossed by the particle, with a value deposited continuously along the particle path using:

$$d(u) = \frac{E_j \cdot l_j \cdot \left(\frac{\mu_{\text{en}}}{\rho}\right)}{V} \quad (2)$$

where,  $d(u)$  is the dose inside the voxel  $u$ ,  $(\mu_{\text{en}}/\rho)$  is the mass energy absorption coefficient,  $l_j$  the length of the particle step and  $E_j$  the energy of the current particle. The dose uncertainty is calculated (Walters *et al* 2002) using density values stored in each phantom voxel:

$$\epsilon(x) = \sqrt{\frac{1}{N-1} \left( \frac{\sum d(x)^2}{N} - \left( \frac{\sum d(x)}{N} \right)^2 \right)} \quad (3)$$

where,  $x$  is a voxel index and  $N$  the number of simulated photons.

#### 2.5. Implementation

Simulation using GPUs requires a specific and efficient data structure. Within this context particle properties are stored as a structure of array (SOA) allowing a coalesced memory access (Jahnke *et al* 2012). The stack of particles is a structure that contains vectors of data, each one containing a different type of information corresponding to each particle (energy, position, direction, state of the particle) equivalent to 39 Bytes of data storage per particle on the global GPU memory. The size of the stack is subsequently adapted according to the size of the GPU global memory. Some of the GPU global memory is also reserved for the simulation data, including physical processes related data, material definition, seed indices on each voxel, dose maps and CT images. The material properties are stored in a database using a SOA format. These values are pre-calculated dynamically before running the simulation using Geant4, and subsequently loaded on the global GPU memory. The parameters associated with

the seeds structure, placement, and orientation as well as the CDF of the I-125 spectrum (see section 2.3.1 above) are stored on the GPU constant memory. The global structure of the GPU simulation is composed of three kernels. A first one is used to initialize the pseudo-random number generator (PRNG) based on the Brent algorithm (Bert *et al* 2013). A second kernel handles the parameterized source seed, including particle emission and navigation through the different layers. Finally, the last kernel concerns the hybrid navigation considering the voxelized phantom and the radioactive seeds. CUDA 5.0 from NVIDIA was used as the programming language. The optimal number of threads per block was determined by following the CUDA occupancy calculator provided by NVIDIA (for example 192 threads/block for a NVIDIA GTX690). The proposed GPU code is also able to run on multiple GPUs by combining CUDA with the Message Parse Interface (MPI). In this context, the total number of particles is evenly split and distributed over the different GPUs for a given MCS. Each GPU runs independently and simultaneously. When all particles are simulated, the energy deposited and corresponding squared value from all GPUs are summed together to the main CPU node. This node handles the computation of the final dose and the associated uncertainty. A desktop computer with an INTEL Core i7 3770 (frequency of 3.4 GHz) and two dual-GPU GTX690 cards (1536 cores operated at a clock frequency of 1.02 GHz) was used for all simulations presented in this paper. Execution times were always compared between a single CPU core and a single GPU.

## 2.6. Validation

**2.6.1. Radioactive source validation.** The modeled  $^{125}\text{I}$  source implemented on GPU was validated by comparing radial dose and anisotropy functions obtained against Brachydose (Taylor and Rogers 2008), which is a reference in brachytherapy dosimetry and well-validated against the TG43 formalism. The radial function corresponds to the dose on the transverse plane of the seed. This dose is normalized by the value measured at a distance of 1 cm from the source, including a geometric correction. Similarly, the anisotropic function is the dose variation along a circle that surrounds the seed. This circle is placed at the seed origin and aligned with the transverse plane of the seed. The dose is then calculated by following this circle, i.e. at a constant distance and for different angles between  $0^\circ$  and  $90^\circ$ . The dose values are normalized according to the final measure at  $90^\circ$ . In order to obtain such a dose function, the  $^{125}\text{I}$  source was centered on a cubic water phantom of  $300 \times 300 \times 300 \text{ mm}^3$  containing voxels of  $1 \text{ mm}^3$ . A total of  $10^9$  photons were simulated and the dose was recorded in every voxel. Finally, the data references for the corresponding source from the Brachydose MCS calculations available on their website<sup>5</sup> (Taylor and Rogers 2008) were used to compare the results obtained from the modeled  $^{125}\text{I}$  source both in terms of radial dose and anisotropic functions.

**2.6.2. Navigation.** The proposed GPU navigation using the hybrid voxelized/analytical object description was validated against Geant4 using the same simulation set-up. The simulated object is a water cube phantom of  $201 \times 201 \times 201 \text{ mm}^3$  with a centrally positioned STM1251 source isotropically emitting photons using the modeled  $^{125}\text{I}$  photon spectrum (see section 2.3.1 above). A 5 mm long slab composed of bone material was placed to the left side of the source, and a slab of 30 mm composed of air to the right side. Every particle escaping a region of interest around the seed was stored into a phase-space file. A first MCS was run using the Geant4 analytical navigator by simulating  $10^8$  photons, including both Compton scattering and photoelectric effects from the standard physics model and Rayleigh scattering from

<sup>5</sup> [www.physics.carleton.ca/clrp/seed\\_database](http://www.physics.carleton.ca/clrp/seed_database).

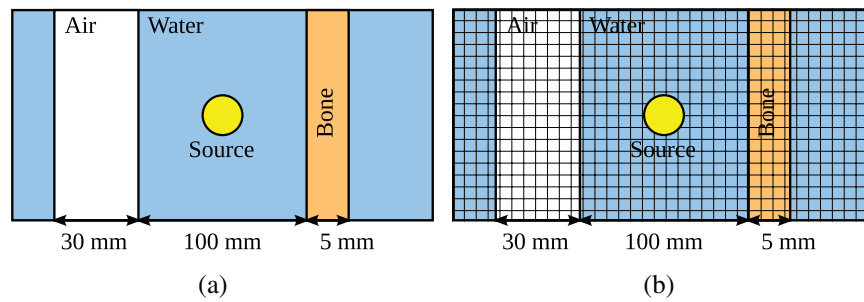


**Figure 4.** Phantoms used for the GPU hybrid navigation implementation based on (a) analytical objects using Geant4 and (b) voxelized and analytical objects using the GGEMS-brachy implementation.

the Livermore physics model. An energy cut of 1.11 keV was set for the photons (equivalent to  $100\ \mu\text{m}$  in liquid water) and no electrons were considered in the physics list. The second MCS run used the hybrid navigation implemented on the GPU (section 2.3.2), considering the same phantom but on a voxelized format ( $1\ \text{mm}^3$  voxels) with the centrally positioned source described as an analytical object. The same number of simulated particles, energy cuts and physics processes used in the Geant4 simulation was considered in this second run. The two set-ups are shown in figure 4.

**2.6.3. Patient study.** An evaluation study was performed on twelve patients undergoing LDR prostate brachytherapy. For each patient the same protocol was used. Patients agreed to the study providing a written consent according to the University of Brest Hospital ethics committee approval and recommendations. For each patient included in the study, a 3D CT scan was performed before the operation and a second one was performed covering the same area one-month after the seeds implantation. The preoperative CT image of  $400 \times 250 \times 65$  voxels with a spacing of  $0.78 \times 0.78 \times 2\ \text{mm}^3$  was used for dose calculations with the GGEMS-brachy platform. The positions, including the orientations, of each implanted seed used for the simulation were manually recovered from the post-operative CT images using the clinical brachytherapy planning software (VariSeed V8.02, Varian Medical systems, Palo Alto, USA). 49–71 seeds were used per patient with an average of 58 seeds. Concerning the MCS, the number of particles was chosen to reach an overall dose uncertainty of 2% within the prostate. A dose map corresponding to the volume and resolution of the CT images used was defined. In order to compare the dose within the prostate and the organs at risks recovered from the TG43 formalism (VariSeed, Varian Medical systems, Palo Alto, USA) and GGEMS-brachy, a physician segmented the prostate, urethra, rectum wall and pubic bone of each patient based on the acquired 3D CT images. Dose volume histograms (DVH) within the delineated organs were subsequently obtained from the TG43 and GGEMS-brachy dosimetry results. The scalability of these results was also evaluated considering up to 4 GPUs (see section 2.5).

To provide further data on the dose calculation and the associated impact of different parameters of the proposed dosimetry platform in comparison to the TG43 formalism, a dedicated study was performed using one of the twelve patient datasets. A total of 59 seeds were used in this patient study where no prostate calcifications were visually present. A first GGEMS-brachy simulation was run considering the same conditions as with the TG43 formalism. The segmented prostate volume of the patient was defined as a homogenous medium of water and the inter-seed navigation was disabled. For this simulation run different configurations were tested and compared. In the first instance the impact of the detailed source description



was investigated using two models of the seed. The first model was the complete geometry description of the STM1251 (section 2.3.1), while the second model was a simplification of the first model by using a single cylinder composed of a homogenous material whose composition was based on the material mixture of the STM1251 source. In the second phase of this study, different prostate tissue compositions were considered, including the definition from ICRU report 46 (ICRU 1992) and CT Hounsfield Units (HU) density conversion from Schneider *et al* (2000). Using the Schneider *et al* (2000) conversion, HUs from 19 to 80 (mean HU within the prostate was 45) are converted to the same soft tissue material.

Finally, in order to evaluate the dose calculations while considering tissue heterogeneity (i.e. the presence of calcifications within the prostate), a simulation with virtual calcifications was performed. Calcifications' properties were defined based on clinical data from Collins-Fekete *et al* (2015) on calcifications within the brachytherapy context. A typical clinical case was set-up using 4 calcifications with a volume of  $0.14 \text{ cm}^3$  each placed inside the prostate within a distance of 10 mm from the prostate center. Concerning the tissue composition, the TG186 recommendation (Beaulieu *et al* 2012) was followed by using the calcification material composition from ICRU report 46.

As a final step in the platform evaluation process, the overall dosimetry simulation for all patients based on GGEMS-brachy was compared with the results obtained using a previously developed brachytherapy dedicated Monte Carlo based dose calculation method, called ALGEBRA (Afsharpour *et al* 2012). This simulation framework uses of phasespace file for the I-125 sources and TLE variance reduction. Voxels that contain the seeds are replaced by water medium and combined with the Geant4 Layer Mass Geometry parallel world (Enger *et al* 2012) in order to perform voxelized/analytical simulations.

### 3. Results

#### 3.1. Radioactive source model validation

The radial dose and anisotropic functions estimated from the GGEMS-brachy simulation for distances up to 10 cm are compared in figure 5 with corresponding Brachydose data references. Both functions recovered from GGEMS-brachy were similar to the Brachydose data references, validating the implemented I-125 source. Deviation averages were 0.82% and 0.46% for radial dose and anisotropic functions respectively.

#### 3.2. Navigation

Both phase space files recovered from the Geant4 and GGEMS-brachy simulations were used to compare the distribution of the particle position along the  $x$ -axis in figure 6. Material slabs are identified in the figure (vertical lines) and show the results for particle interactions with different materials. As figure 6(a) shows Geant4 and GGEMS-brachy lead to the same photon position distributions. A similar agreement can be seen in figure 6(b) considering the distribution of the particle direction cosine along the  $x$ -axis. In addition, similar conclusions in terms of agreement were obtained by comparing particle position and direction for the  $y$ -axis (data not shown). The comparison between Geant4 using a standard analytical navigation and GGEMS-brachy demonstrate that the hybrid navigator does not seem to introduce any errors or biases. Deviation averages were 0.68% and 0.45% for position and direction comparisons respectively.

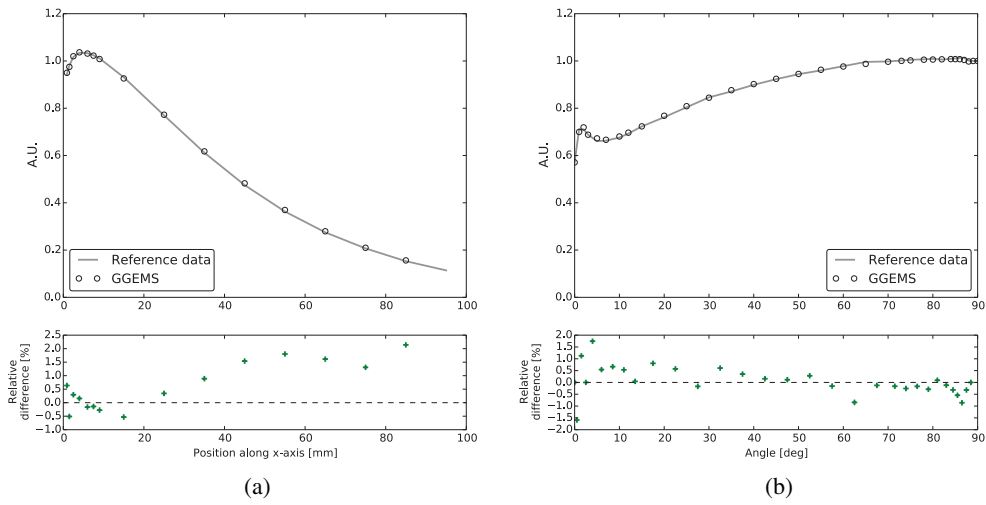


**Figure 5.** Comparison of radial dose (a) and anisotropic ( $r = 5$  cm) (b) function recovered from reference data (Brachydose) and GGEMS-brachy.

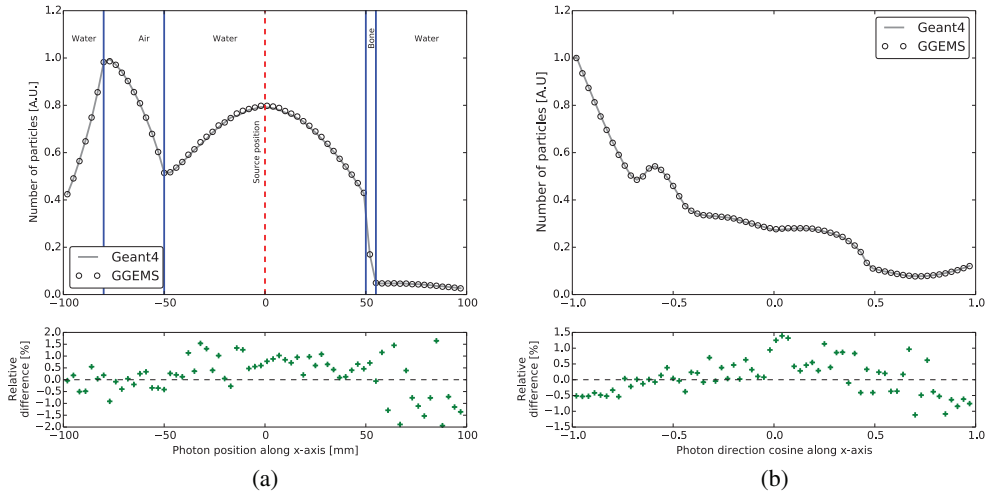


**Figure 6.** Distribution of the photon position (a) and direction cosine (b) along the  $x$ -axis obtained by MCS using Geant4 with analytical geometry and GGEMS-brachy with hybrid (voxelized/analytical) geometry.

**3.3. Patient study**

Isodoses for TG43 and GGEMS-brachy simulations are shown for one patient in figure 7. This figure highlights differences between the two dosimetry protocols. For instance, hot spots in figure 7 show that calcifications and pelvis bones were not taken into consideration by the TG-43 formalism (figure 7(a)) compared to the Monte Carlo simulation (figure 7(b)), leading to a difference on the final local dose distribution. DVH were estimated for all twelve patients. The DVH from a typical patient, corresponding to the mean differences observed between TG43 and GGEMS-brachy for the complete patient cohort, is shown in figure 8. Different dose metrics considering all twelve patients are summarized in table 1. The minimum dose deposited in 90% of

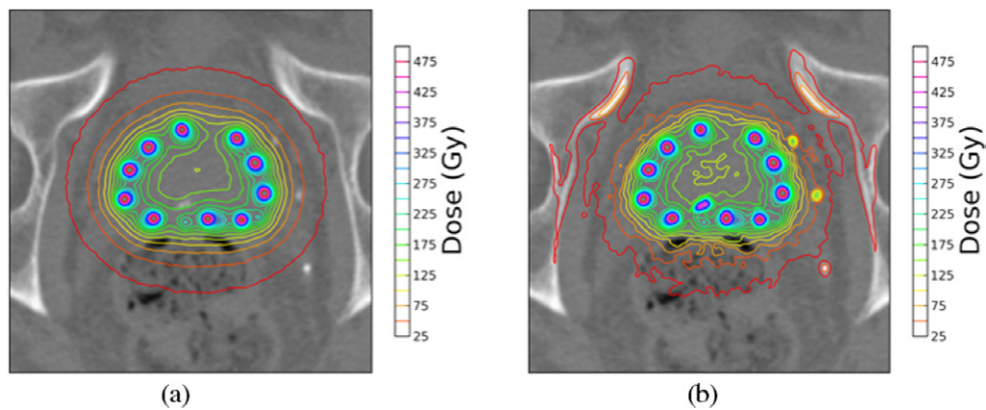


**Figure 7.** Isodoses on the same patient CT image centered on the prostate from simulations using (a) the TG43 formalism and (b) the full MC with GGEMS-brachy.

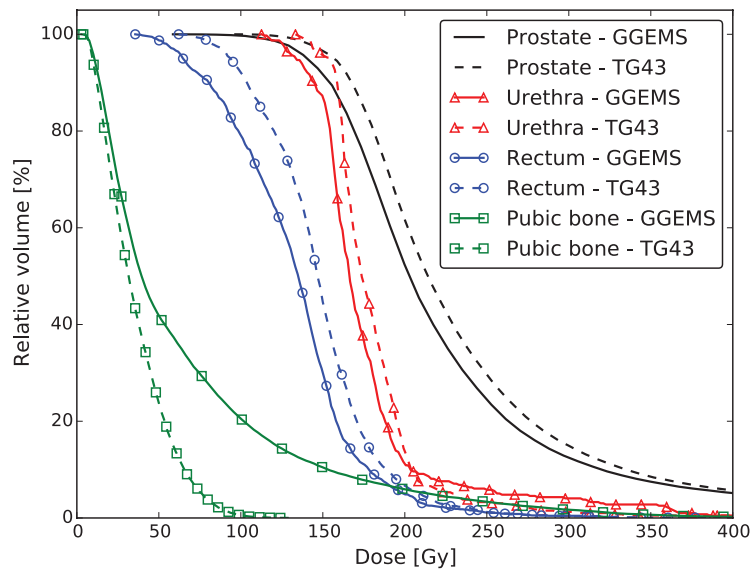


**Figure 8.** Comparison of the dose volume histogram within the prostate and the organs at risk between the TG43 formalism and GGEMS-brachy for one of the patient datasets.

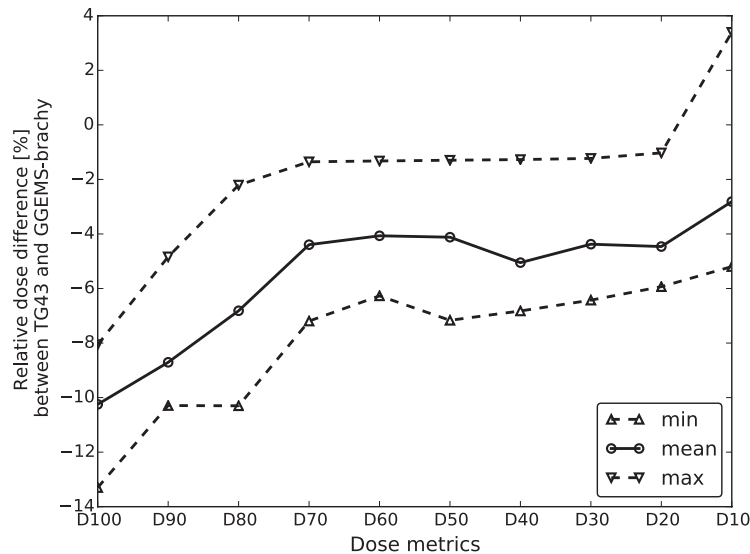
the prostate volume (D90) provides information on the presence of dose cold spot regions within the prostate. The mean D90 relative difference between TG43 and GGEMS-brachy was  $-8.7\%$  (range:  $-4.84\%$ ,  $-10.29\%$ ). These results are in agreement with previous studies: mean  $-6.4\%$  (range:  $-1.8\%$ ,  $-14.1\%$ ) reported in Collins-Fekete *et al* (2015) and a mean difference of  $-7\%$  corresponding to the results of Carrier *et al* (2006). Similarly to all these studies, dose within the prostate region is overestimated using the TG43 formalism relative to the MCS which can in turn lead to potential local recurrences (Crehange *et al* 2013, Sasaki *et al* 2014).

Concerning the organs at risk (OAR), the metrics D10 on the urethra volume provides information on dose hot spots. The mean D10 relative difference between TG43 and GGEMS-brachy was  $-2.00\%$  (range:  $-0.21\%$ ,  $-5.87\%$ ). Similarly, the dose in  $2\text{ cm}^3$  (D2cc) of the rectum

**Table 1.** Mean relative difference of dose metrics within the prostate volume and organs at risks between TG43 and MC for all twelve patients considered in this study.

Organ	Average (%)	Min (%)	Max (%)
Prostate D90	- 8.71	- 10.29	- 4.84
Urethra D10	- 2.00	- 5.87	- 0.21
Rectum wall D2cc	- 13.45	- 20.64	- 8.48
Pubic bone D10	58.28	55.10	62.59

*Note:* Min and Max values represent the extremes considering all twelve patients included in the study.

**Figure 9.** Dose Metrics' comparison between GGEMS-brachy and the TG43 formalism.

wall, also related to dose hot spots within this region, showed a mean difference of  $-13.45\%$  (range:  $-8.48\%$ ,  $-20.64\%$ ) between the TG43 and MCS dosimetry results. While comparing dose hot spots using the D10 within the pubic bone, the mean relative difference was  $58.28\%$  (range:  $55.10\%$ ,  $62.59\%$ ). The D10 value for the GGEMS-brachy simulation was 125 Gy, representing 86% of the dose prescription (145 Gy), revealing an excessive radiation exposure of the pelvic bones. As TG43 formalism considers tissue composition as liquid water, high-density tissues like bones are not taken into account. Bones surrounding the prostate gland should be considered in clinical treatment planning and may require further clinical investigations to evaluate the impact in terms of toxicity and late effects of LDR radiation therapy.

The variability of these dose metrics depends on each patient considering their anatomy (prostate volume, calcifications) and overall treatment planning (number of seeds and their position). The mean relative dose differences for D100 to D10 were calculated within the prostate volume for all patients considered in this study. In addition minimum and maximum values representing the extremes from the different patients were estimated and represented in figure 9. For D100 to D10 the overall average difference was 5% between TG43 and GGEMS-brachy. The relative dose difference was higher for the metrics D100, D90 and D80, revealing the under-dosage of the TG43 formalism. For the others metrics (D70 to D20), the difference

**Table 2.** GGEMS-brachy simulation for one patient using different configurations.

	D90 (Gy)	Relative dose difference (%) compared to the reference
<b>Reference simulation<sup>a</sup></b>	164.99	
<b>Different prostate tissue compositions based on</b>		
ICRU report 46	161.88	− 1.88
soft tissue (density conversion)	163.75	− 0.75
water and calcifications (ICRU report 46)	170.67	3.44
<b>Inter-seed interaction</b>		
with the simplified seed model	156.89	− 4.91
with the complete seed model	159.71	− 3.20

<sup>a</sup> equivalent to the TG43 formalism (prostate with water material and no inter-seed interaction modeling).

was stable around  $-5\%$ . Concerning the D10, representing dose hot spots, the difference was the lowest with  $-3\%$  (up to a maximum of  $+3\%$ ). This describes in some cases the presence of dose hot spots due to calcifications within the prostate volume.

In order to identify and understand the origins of the measured dose differences within the prostate volume between GGEMS-brachy and the TG43 formalism several simulations with different parameters were considered using one of the patient datasets as previously outlined in section 2.6.3. For each simulation D90 within the prostate was calculated and the results are summarized in table 2. An initial dose reference was established for the GGEMS-brachy simulation by considering the prostate volume composed of water and without inter-seed interactions, leading to the same D90 obtained with the TG43 formalism. The definition of the prostate tissue using the ICRU report 46 value and the HU based density conversion using Schneider *et al* (2000) led to a small D90 decrease of  $-1.88\%$  and  $-0.75\%$  respectively. Given these results, the conversion of the CT HUs within the prostate volume into the same soft tissue material based on Schneider *et al* (2000) compared to the ICRU report 46 material (recommended by TG186) led to D90 differences of  $<1.12\%$ . On the other hand, the inclusion of calcifications based on their composition proposed by the ICRU report 46 (also recommended by TG186) led to a D90 increase of  $+3.44\%$ , which is in agreement with previous literature of a mean D90 increase of  $3.88\%$  (Collins-Fekete *et al* 2015).

The second main parameter of the simulation that may impact dosimetry is the inter-seed interaction that was also investigated in this study. While using the complete seed geometry (accurately modeling all seed layers) the D90 decreased by  $-3.2\%$ . By comparison the simplified seed model (a single cylinder composed of a homogeneous mixture derived from all real seed materials) led to D90 differences of  $1.8\%$  relative to the complete seed model simulation. At the same time there was no overall impact in simulation times since the navigation within seeds is not computationally demanding on GPU. Given these results it is clearly better for an accurate dosimetry to consider the complete seed model.

Finally, the twelve patient datasets were used to perform two simulations, one using GGEMS-brachy and the second using ALGEBRA. DVHs from the prostate of a typical patient for both simulations were calculated and plotted in figure 10 showing a good agreement between GGEMS-brachy and ALGEBRA. The overall mean relative discrepancy considering all patients was about  $1.7\%$ . Considering dose values  $<250$  Gy the mean discrepancy

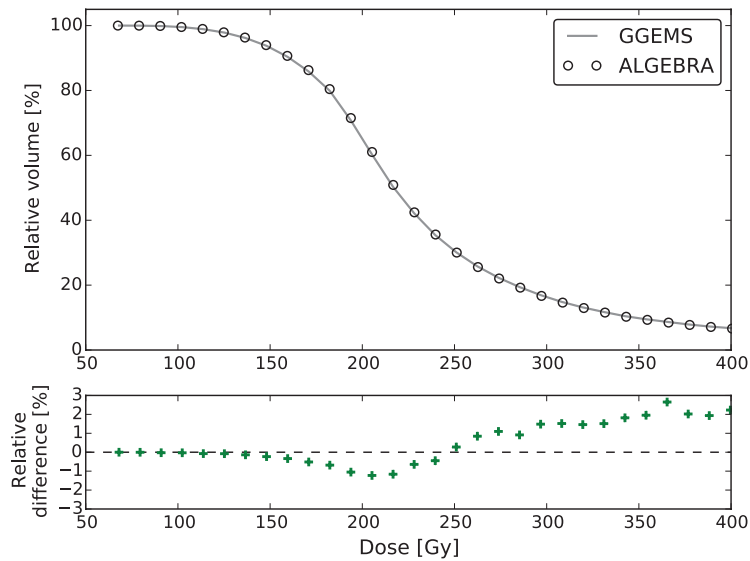


**Figure 10.** DVH within the prostate of a typical patient obtained by GGEMS-brachy and ALGEBRA.

**Table 3.** Simulation time for the GGEMS-brachy MC simulation.

Number of GPUs	Simulation time (s)	Communication time (s)
1	9.35	0.03
2	4.79	0.07
4	2.47	0.09

was 0.41%. For doses  $>250$  Gy, corresponding to dose hot spots located at the periphery of the seeds, the relative discrepancy increased. This can be explained by water material voxels that contain the seeds in ALGEBRA. In addition, these high dose values are associated with relatively small volumes, which in combination with the low MC statistics will systematically increase the relative differences observed between the two codes.

In terms of computational efficiency, a summary of the mean total run time for the dose calculations using the GGEMS-brachy for the twelve patient datasets considering a dose uncertainty of 2% is given in table 3. A mean run time for the complete simulation of 9.35 s and 2.5 s when using one and four GPUs respectively was recorded. As expected, the system scales linearly as the number of particles used per GPU is divided by the number of GPUs used. The communication times which include the memory transfer between the GPUs and CPUs and the dose merging operation once the simulation is completed are also shown in table 3. A copy of the dose map to the CPU and dose calculations are performed regularly by a unique processor to obtain the dose uncertainty in the prostate and allow stopping the simulation when the desired uncertainty is reached. This calculation takes about 30 ms (depending mainly on the dose map size and prostate volume) and the mean uncertainty is divided by the square root of the number of GPUs working in parallel. Final copy and merging operations are performed at the end of the simulation, minimizing their impact on the overall simulation time. As no communications occur between GPUs during



the simulation, the overall calculation time decreases nearly linearly according to the number of GPUs used.

#### 4. Discussion

The AAPM TG-43 formalism, which is the current state of the art in clinical usage, assumes that the patient is homogeneously composed of liquid water. As mentioned in the most recently published AAPM TG-186 report (Beaulieu *et al* 2012), the TG43 formalism is limited. The most accurate and personalized dosimetry can only be performed through Monte Carlo simulations and GBBS algorithms. However, as the TG-186 report points out this solution is currently incompatible in terms of computational burden with a clinical use, especially considering the intra-operative context of some forms of brachytherapy.

In order to decrease Monte Carlo simulation execution times, variance reduction techniques may be employed. In the case of the Acuros<sup>TM</sup> solution, in order to reduce execution times the GBBS solver is only used in the final dose calculation phase. Intra-operative brachytherapy puts constraints on the execution times that can be associated with any dose calculation code to be proposed in this context. Solutions proposed in the literature are mostly associated with different degrees of approximations including modified physics effects and are not sufficiently fast for intra-operative dosimetry. An alternative approach presented in this work concerns an acceleration of Monte Carlo simulations based on the use of alternative hardware architectures such as GPUs. Amongst current Monte Carlo GPU implementations concerning external beam radiotherapy (Jia *et al* 2010, Hissoiny *et al* 2011, Jahnke *et al* 2012) or imaging (Lippuner and Elbakri 2011), only one code was dedicated to brachytherapy and proposed by Hissoiny *et al* (2011). This code, bGPUMCD is an extension of the GPUMCD code for LDR brachytherapy. The associated study was only focused on the use of a single seed considering only Compton scattering and a simplified version of the photoelectric physics process.

The development of GGEMS-brachy presented in this work was based on a GPU implementation framework using Geant4 physics libraries previously proposed for imaging and radiotherapy applications (Bert *et al* 2013). A realistic brachytherapy radioactive source geometry was implemented on GPU allowing simulated inter-seed interaction, removing the need for the use of phase space files and/or approximations associated with handling seed/voxels overlapping. The modeled source was validated considering both the resulting radial dose and anisotropic functions. These modeled virtual seeds are integrated within the voxelized CT image of a patient using a dedicated hybrid navigator developed as part of this work. The proposed hybrid navigator accounts for the interface between seeds and patient CT image voxels with high accuracy. Finally a track length estimator approach for dosimetry calculations was implemented to allow similar dose percentage uncertainties with a smaller number of simulated photons, hence further enhancing the computational efficiency of the proposed platform.

As shown in this study, using GGEMS-brachy for a complete brachytherapy plan (numerous seeds and associated positions) takes a few seconds without any associated approximations. This performance was achieved using a standard computer and associated GPU configuration, which could allow this application to become the basis of a real-time intra-operative dosimetry system. The potential interest of the developed application was assessed on twelve prostate cancer patients undergoing LDR brachytherapy treatment by comparing the GGEMS-brachy and standard TG43 dose calculations and associated dose distributions. Both isodoses and dose histograms revealed variable magnitude differences when comparing prostate dose distributions derived from TG43 and GGEMS-brachy. Average relative differences of  $-8.71\%$

(range:  $-4.84\%$ ,  $-10.29\%$ ) were registered for the D90. These differences can be accounted for by a combination of factors including accurate seed modeling and positioning, the presence of calcifications and their composition, and to a lesser extent on the choice of prostate tissue composition. Further evaluation based on dose metrics revealed that mean differences were stable at  $-5\%$  between D70 to D20 while for the D10, representing dose hot spots, the mean difference was  $-3\%$ . In agreement with literature (Carrier *et al* 2006, Collins-Fekete *et al* 2015), we measured that prostate tissue composition can lead to smaller dose differences (maximum difference of  $-1.88\%$  between the prostate composed of water and the composition proposed by TG186 based on the ICRU report 46) compared to the presence of calcifications (mean differences of  $-3.44\%$ ). Finally as shown in the present study accurately accounting for interseed interactions, seed modeling and voxel/seed placement can improve dose estimation by 3–5%.

In LDR brachytherapy, a high precision in the positioning of the seeds is essential in order to avoid areas of tumor under-dosage (cold spots) due to the limited penetration of the low-energy radiation, while at the same time ensuring the minimum dose in the organs at risk. As reported by a recent clinical study (Crehange *et al* 2013, Sasaki *et al* 2014), patients with biopsy-proven local recurrence had poorer implantation quality with under-dosed areas corresponding to the positive biopsy sites. There is therefore increasing evidence of a strong relationship between local recurrence and dose cold spots. In this context, GGEMS-brachy needs to be integrated with a treatment planning system (TPS). Such a system based on the proposed GPU MCS application will allow the determination of the most appropriate source placement and characteristics (seed activities) given the overall dose prescription. The development of a hybrid approach, where the analytical optimization will be constrained and optimized by the accurate MCS corresponds to the next step in the development of such an intra-operative treatment planning system for brachytherapy applications. Finally, although the current paper was focused on LDR brachytherapy and prostate cancer the developed MCS based dosimetry framework is equally applicable to other LDR brachytherapy clinical applications (for example in gynecological cancers). In addition, in the current GGEMS-brachy application we only considered the physics processes associated with LDR brachytherapy although the original GGEMS framework, which includes electrons' physics processes and tracking on GPU, would allow the implementation of an HDR application. However, it will be clearly necessary to model the sources used for HDR and evaluate the performance of the overall simulation and associated dosimetry in terms of accuracy and speed of execution.

## 5. Conclusions

A GPU MC simulation tool based on Geant4 and dedicated to brachytherapy applications was developed. The application uses a hybrid navigator which consists of a combination of analytically described objects and voxelised patient CT images. Our evaluation shows certain dose differences compared to the simplistic TG43 formalism in LDR brachytherapy for prostate cancer patients. In addition, the proposed MC simulation framework and GPU implementation lead to very fast execution times compatible with clinical practice. Further work will focus on integrating the proposed GGEMS-brachy application within an intra-operative treatment planning system for brachytherapy applications and using the proposed dosimetry platform to demonstrate the potential interest of such simulations in clinical routine by considering a larger number of patient studies. Finally, the application of the proposed platform in HDR treatments will be explored in the future.

## Acknowledgments

This work was partly supported by the French ANR within the Investissements d'Avenir program (Labex CAMI) under reference ANR-11-LABX-0004 (Integrated project CAPRI) and through t-GATE project (ANR-14-CE23-0008).

## References

- Afsharpour H, D'Amours M, Coté Benoit, Carrier J-F, Verhaegen F and Beaulieu L 2008 A Monte Carlo study on the effect of seed design on the interseed attenuation in permanent prostate implants *Phys. Med. Biol.* **57** 3273–80
- Afsharpour H, Landry G, D'Amours M, Enger S, Reniers B, Poon E, Carrier J-F, Verhaegen F and Beaulieu L 2012 Algebra: algorithm for the heterogeneous dosimetry based on GEANT4 for Brachytherapy *Phys. Med. Biol.* **57** 3273–80
- Allison J *et al* 2006 Geant4 developments and applications *IEEE Trans. Nucl. Sci.* **53** 270–8
- Beaulieu L, Carlsson Tedgren A, Carrier J-F, Davis S D, Mourtada F, Rivard M J, Thomson R M, Verhaegen F, Wareing T A and Williamson J F 2012 Report of the task group 186 on model-based dose calculation methods in brachytherapy beyond the TG-43 formalism: current status and recommendations for clinical implementation *Med. Phys.* **39** 6208–36
- Bert J, Perez-Ponce H, El Bitar Z, Jan S, Boursier Y, Vintache D, Bonissent A, Morel C, Brasse D and Visvikis D 2013 Geant4-based Monte Carlo simulations on GPU for medical applications *Phys. Med. Biol.* **58** 5593–611
- Carrier J-F, Beaulieu L, Therriault-Proulx F and Roy R 2006 Impact of interseed attenuation and tissue composition for permanent prostate implants *Med. Phys.* **33** 595–9
- Carlsson A K and Ahnesjö A 2000 Point kernels and superposition methods for scatter dose calculations in brachytherapy *Phys. Med. Biol.* **45** 357–82
- Chibani O and Williamson J F 2005 MCPI: a sub-minute Monte Carlo dose calculation engine for prostate implants *Med. Phys.* **32** 3688–98
- Collins-Fekete C-A, Plamondon M, Martin A-G, Vigneault E, Verhaegen F and Beaulieu L 2015 Calcifications in low-dose rate prostate seed brachytherapy treatment: post-planning dosimetry and predictive factors *Radiother. Oncol.* **114** 339–44
- Crehange G, Krishnamurthy D, Cunha J A, Pickett B, Kurhanewicz J, Hsu I C, Gottschalk A R, Shinohara K, Roach M III and Pouliot J 2013 Cold spot mapping inferred from MRI at time of failure predicts biopsy-proven local failure after permanent seed brachytherapy in prostate cancer patients: implications for focal salvage brachytherapy *Radiother. Oncol.* **109** 246–50
- Enger S A, Landry G, D'Amours M, Verhaegen F, Beaulieu L, Asai M and Perl J 2012 Layered mass geometry: a novel technique to overlay seeds and applicators onto patient geometry in Geant4 brachytherapy simulations *Med. Phys.* **57** 6269–77
- Ericson C 2004 *Real-Time Collision Detection The Morgan Kaufmann Series in Interactive 3D Technology* (Amsterdam: Elsevier)
- Frank S J, Pister L L, Davis J, Lee A K, Basset R and Kuban D A 2007 An assessment of quality of life following radical prostatectomy, high dose external beam radiation therapy and brachytherapy iodine implantation as monotherapies for localized prostate cancer *J. Urol.* **177** 2151–6
- Hissoiny S, Ozell B, Bouchard H and Desprs P 2011 GPUMCD: a new GPU-oriented Monte Carlo dose calculation platform *Med. Phys.* **38** 754–64
- Hissoiny S, Ozell B and Desprs P 2011 Validation of GPUMCD for low-energy brachytherapy seed dosimetry *Med. Phys.* **38** 4101–7
- International Commission on Radiation Units and Measurements 1992 *Photon, Electron, Proton and Neutron Interaction Data for Body Tissues* (Bethesda, MD: ICRU)
- Jahnke L, Fleckenstein J, Wenz F and Hesser J 2012 GMC: a GPU implementation of a Monte Carlo dose calculation based on Geant4 *Phys. Med. Biol.* **57** 1217–29
- Jia X, GU X, Sempau J, Choi D, Majumdar A and Jiang S B 2010 Development of a GPU-based Monte Carlo dose calculation code for coupled electron–photon transport *Phys. Med. Biol.* **55** 3077–86
- Kawrakow I 2000 Accurate condensed history Monte Carlo simulation of electron transport. I. EGSnrc, the new EGS4 version *Med. Phys.* **27** 485–98

- Kirov A S and Williamson J F 2001 Monte Carlo-aided dosimetry of the source tech medical model STM1251 I-125 interstitial brachytherapy source *Med. Phys.* **28** 764–72
- Lippuner J and Elbakri I A 2011 A GPU implementation of EGSnrc's Monte Carlo photon transport for imaging applications *Phys. Med. Biol.* **56** 7145–62
- Morris W J, Keyes M, Spadinger I, Kwan W, Liu M, McKenzie M, Pai H, Pickles T and Tyldesley S 2013 Population-based 10 year oncologic outcomes after low-dose-rate brachytherapy for low-risk and intermediate-risk prostate cancer *Cancer* **119** 1537–46
- Morton G M 1966 *A computer Oriented Geodetic Data Base and a New Technique in File Sequencing* (Ottawa: International Business Machines Company)
- Rassiah-Szegedi P, Fuss M, Sheikh-Bagheri D, Szegedi M, Stathakis S, Lancaster J, Papanikolaou N and Salter B 2007 Dosimetric evaluation of a Monte Carlo IMRT treatment planning system incorporating the mimic *Phys. Med. Biol.* **52** 6931–41
- Rivard M J, Venselaar J L M and Beaulieu L 2009 The evolution of brachytherapy treatment planning *Med. Phys.* **36** 2136–53
- Sasaki H, Kido M, Miki K, Kuruma H, Takahashi H, Aoki M and Egawa S 2014 Salvage partial brachytherapy for prostate cancer recurrence after primary brachytherapy *Int. J. Urol.* **6** 572–9
- Schneider W, Bortfeld T and Schlegel W 2000 Correlation between CT numbers and tissue parameters needed for Monte Carlo simulations of clinical dose distributions *Phys. Med. Biol.* **45** 459–478
- Taylor R E P, Yegin G and Rogers D W O 2007 Benchmarking brachydose: voxel based EGSnrc Monte Carlo calculations of TG-43 dosimetry parameters *Med. Phys.* **34** 445–57
- Taylor R E P and Rogers D W O 2008 An EGSnrc Monte Carlo-calculated database of TG-43 parameters *Med. Phys.* **35** 4228–41
- Tong W Y, Cohen G and Yamada Y 2013 Focal low-dose rate brachytherapy for the treatment of prostate cancer *Cancer Manag. Res.* **5** 315–25
- Tóth B and Magdics M 2010 Monte Carlo radiative transport on the GPU *Fifth Hungarian Conf. on Computer Graphics and Geometry* pp 1–8
- Wallace T J, Torre T, Grob M, Yu J, Avital I, Brcher B L D M, Stojadinovic A and Man Y G 2014 Current approaches, challenges and future directions for monitoring treatment response in prostate cancer *J. Cancer* **1** 3–24
- Walters B R B, Kawrakow O and Rogers D W O 2002 History by history statistical estimators in the BEAM code system *Med. Phys.* **29** 2745–52
- Williamson J F 1987 Monte Carlo evaluation of kerma at a point for photon transport problems *Med. Phys.* **14** 567–76
- Yegin G 2003 A new approach to geometry modeling of Monte Carlo particle transport: an application to EGS *Nucl. Instrum. Methods Phys. Res.* **211** 331–8
- Zourari K, Pantelis E, Moutsatsos A, Petrokokkinos L, Karaiskos P, Sakelliou L, Georgiou E and Papagiannis P 2010 Dosimetric accuracy of a deterministic radiation transport based  $^{192}\text{Ir}$  brachytherapy treatment planning system. Part 1: single sources and bounded homogeneous geometries *Med. Phys.* **37** 649–61

## B.5 Géométrie hybride en simulation Monte-Carlo

# New hybrid voxelized/analytical primitive in Monte Carlo simulations for medical applications

Julien Bert, Yannick Lemaréchal and Dimitris Visvikis

INSERM UMR1101, LaTIM, CHRU Brest, Brest, France

E-mail: [julien.bert@univ-brest.fr](mailto:julien.bert@univ-brest.fr)

Received 24 November 2015, revised 17 February 2016

Accepted for publication 7 March 2016

Published 1 April 2016



CrossMark

### Abstract

Monte Carlo simulations (MCS) applied in particle physics play a key role in medical imaging and particle therapy. In such simulations, particles are transported through voxelized phantoms derived from predominantly patient CT images. However, such voxelized object representation limits the incorporation of fine elements, such as artificial implants from CAD modeling or anatomical and functional details extracted from other imaging modalities. In this work we propose a new hYbrid Voxelized/ANalytical primitive (YVAN) that combines both voxelized and analytical object descriptions within the same MCS, without the need to simultaneously run two parallel simulations, which is the current gold standard methodology. Given that YVAN is simply a new primitive object, it does not require any modifications on the underlying MC navigation code. The new proposed primitive was assessed through a first simple MCS. Results from the YVAN primitive were compared against an MCS using a pure analytical geometry and the layer mass geometry concept. A perfect agreement was found between these simulations, leading to the conclusion that the new hybrid primitive is able to accurately and efficiently handle phantoms defined by a mixture of voxelized and analytical objects. In addition, two application-based evaluation studies in coronary angiography and intra-operative radiotherapy showed that the use of YVAN was 6.5% and 12.2% faster than the layered mass geometry method, respectively, without any associated loss of accuracy. However, the simplification advantages and differences in computational time improvements obtained with YVAN depend on the relative proportion of the analytical and voxelized structures used in the simulation as well as the size and number of triangles used in the description of the analytical object meshes.

Keywords: Monte Carlo simulation, hybrid geometry, voxelized phantom, analytical phantom, medical applications

(Some figures may appear in colour only in the online journal)

## 1. Introduction

Monte Carlo simulations (MCS) are random sampling methods used in many different domains to simulate and solve physical and mathematical problems. MCS applied in particle physics play a key role in medical imaging and particle therapy. In such simulations particles are transported through voxelized phantoms derived from patient anatomical computed tomography (CT) images or based on anthropomorphic numerical models. Each voxel within such a phantom may represent different media allowing the simulation of tissue heterogeneity. For this kind of phantom, particle navigation is simple to implement and subsequently optimize considering that it is performed within a regular grid of voxels (Hubert-Tremblay *et al* 2006, Arce *et al* 2008, Schumann *et al* 2012). However, such a representation is also associated with limitations for certain medical applications. Finite voxel sizes do not allow the incorporation of fine details within the patient CT image-derived voxelized phantoms, such as, for example, artificial implants that can be obtained from computer-assisted design (CAD) modeling (screws, hip replacements, brachytherapy seeds, etc) or anatomical details derived from other imaging modalities, such as, for example, magnetic resonance imaging (MRI) of the arteries, spinal cord, atheroma, etc. A potential solution consists of using smaller voxels to model complex objects, however, which dramatically increases computational run times and data volumes to be handled by the simulation. Alternatively, instead of converting analytical CAD-defined objects into voxels it has been previously proposed to segment and convert patient CT images into mesh-based analytical phantoms (Said *et al* 2008, Young *et al* 2008). In this case, complex objects can be incorporated within a patient's image-derived anatomy. An analytical geometry description is subsequently used to migrate particles within hierarchical volumes composing the complete phantom. One major drawback of this approach is the assumption that each phantom volume is composed of a homogenous medium leading to significant approximations since heterogeneity cannot be modeled. Another approach is the use of a parallel world concept first introduced by Yegin (2003) as part of the electron gamma shower (EGS) code (Nelson *et al* 1985, Kawrakow and Rogers 2000). The basic concept is the use of overlapping worlds containing the geometry of different scenes. This concept was also subsequently implemented in Geant4 (Apostolakis *et al* 2008) for scoring dose within analytical volume applications. In this case only the main world contains physical material properties and is concerned by particle interactions. Subsequently, Enger *et al* (2012) extended this concept with the layered mass geometry (LMG) where each of the two worlds contains material properties, providing an appropriate solution to the combined voxelized/analytical simulation issue. On the other hand, within LMG each parallel world requires its own navigator and geometry, with the particle stepping driven by the smaller step associated with one of these navigators. In addition, running several navigators within the same simulation may hamper computational efficiency. Finally, the implementation within a dedicated MCS of such a navigation mechanism may require significant changes on the MCS code itself.

In this work, we propose an alternative solution that consists of combining both voxelized and analytical phantoms within the same MCS by defining a new hybrid geometric primitive. This new proposed 3D primitive facilitates the use of heterogeneous voxelized phantoms including overlapping complex analytical objects. In addition, only one navigator is required



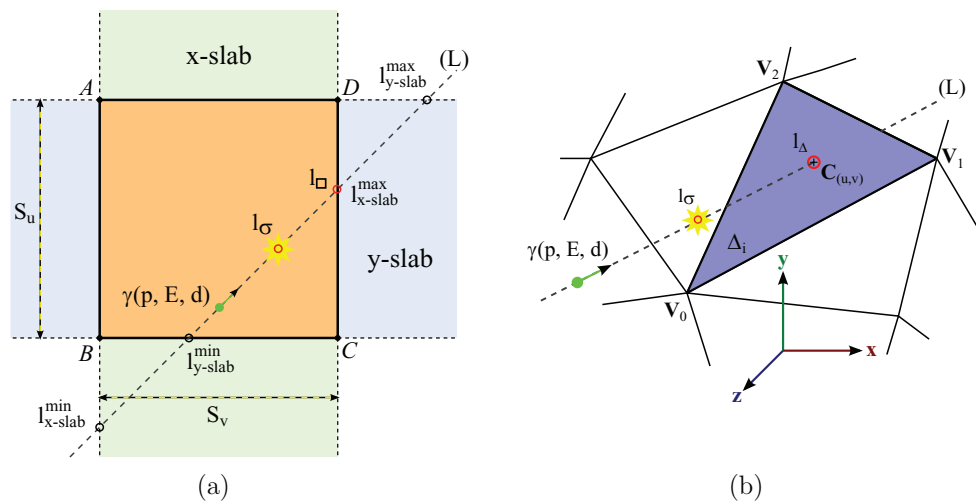


**Figure 1.** Basic scheme of the particle navigator through (a) an analytical box representing a voxel (2D case) and (b) an analytical mesh phantom composed of triangles (3D case).

during the simulation and its implementation within any MCS platform is simple given that it does not require any changes in the navigation mechanism.

## 2. Materials and methods

### 2.1. Particle navigation

In MCS, a particle navigator handles particle tracking within a given environment. Its main role is determining the next position of the particle based on geometrical information and physical process interactions. Let us consider the 2D case with a box ( $ABCD$ ) in figure 1(a), and a photon  $\gamma$  defined by its position  $\mathbf{p}$ , energy  $E$  and direction  $\mathbf{d}$ . According to the particle state and medium properties of the current primitive geometry, the next interaction distances  $l_\sigma$  along the particle path  $L$  are determined based on the physics process provided by the Monte Carlo code. Subsequently, the next volume boundary distance  $l_\square$  along the path  $L$  is considered. If the value of  $l_\sigma$  is smaller than  $l_\square$ , the particle moves to the distance  $l_\sigma$  and the MCS resolves the discrete process. If  $l_\sigma$  is larger, the particle moves to the next voxel boundary without interacting with the medium. These steps are repeated until all particles are either absorbed or escape from the phantom. Therefore, in order to add a new geometric primitive within an MCS, the particle navigator requires only two main elements. The first one is the medium of the object while the particle is spatially located within the primitive, while the second element is the distance between the particle and the primitive boundary obtained by ray tracing.

### 2.2. Voxelized phantom

Since the particle navigator requires geometric information from each primitive contained in the geometry, every primitive type (sphere, box, etc) has to be described using ray-tracing functions considering the different primitives' geometrical specificities. The proposed hybrid primitive allows the combination of both voxelized and analytical geometries. The geometrical properties of the voxelized phantom used in the hybrid primitive are defined using only

two functions, one to determine the voxel index that contains the particle and another one that determines the next distance voxel boundary.

Let us consider the same 2D case as in figure 1(a), but this time the square  $ABCD$  represents a voxel. For computational efficiency purposes, a voxelized geometry in MCS is considered as a parameterized geometry. Within this context a single analytical box representing the voxel is used in the simulation. The voxel position (box vertices) is updated according to the voxel index that contains the particle using its position  $\mathbf{p}$  and the voxel size ( $S_u, S_v$ ). Subsequently using this information the navigator determines the medium crossed by the particle and the associated interaction distances along the particle path  $L$ .

In order to determine the distance to the voxel boundary along the path  $L$ , required by the navigator, an efficient ray/box intersection algorithm (Smits 2002) was implemented. This method considers the particle as a ray defined by a parametric equation  $\mathbf{R} = \mathbf{p} + l\mathbf{d}$ , where  $l$  is the distance between the particle along the path  $L$  and the voxel considered as an axis-aligned bounding box (AABB). The intersection point between the ray and the AABB is determined by considering each intersection of the ray with the slabs that compose the AABB. A slab is defined as the surface between a pair of parallel planes or lines, for example in figure 1(a) the 2D AABB is composed of two slabs ( $x$ -slab and  $y$ -slab). Every distance between the ray and the minimum and maximum boundary slabs is calculated using their respective plane equations. For example, the distance to the  $x$ -slab lower boundary is obtained by solving  $l_{x\text{-slab}}^{\min} = (\delta_{x\text{-slab}}^{\min} - p_x)/d_x$ , where  $\delta_{x\text{-slab}}^{\min}$  corresponds to the minimum position of the plane along the  $x$  axis. The final intersection distance  $l_{\square}$  with the voxel  $ABCD$  is given by the minimum positive value between  $l_{x\text{-slab}}^{\min}, l_{x\text{-slab}}^{\max}, l_{y\text{-slab}}^{\min}, l_{y\text{-slab}}^{\max}$  (see figure 1(a)). In the 3D case a third slab is considered along the  $z$ -axis.

### 2.3. Analytical phantom

The analytical environment can be composed of different geometry primitives such as spheres, torus, boxes, etc. In order to allow the handling of complex analytical geometries, we use a triangular-based mesh as the main primitive (see figure 1(b)). As previously shown in Badal *et al* (2009) and Said *et al* (2008) a mesh is able to represent any kind of object, ranging from simple ones (boxes, spheres, etc) to complex objects obtained using CAD and medical image segmentation. Similarly to the voxelized geometry, the analytical one requires the same two main ray-tracing functions to determine the volume where the particle is located and the distance volume boundary.

The volume containing the particle is identified by keeping in memory the history of the last object ID that the particle crosses. On the other hand, the mesh boundary distance  $l_{\Delta}$  (see figure 1(b)) requires more calculations compared to a simple voxel since a ray-tracing approach is needed between the particle path and every triangle  $\Delta_i$  that composes the primitive. An efficient algorithm of ray/triangle intersection (Moller and Trumbore 1997) was implemented for this operation, where similarly to the ray/AABB algorithm used for the voxelized phantom the particle is considered as a parametric ray. If the ray intersects the plane defined by the triangle  $\Delta_{\mathbf{V}_0\mathbf{V}_1\mathbf{V}_2}$  (see figure 1(b)), the intersection point  $\mathbf{C}_{(u,v)}$  belongs to the surface area of the triangle with barycentric coordinates  $(u, v)$ . The intersection is obtained by first translating the triangle position to the origin based on  $\mathbf{V}_0$ , with the vertex  $\mathbf{V}_1$  and  $\mathbf{V}_2$  becoming  $\mathbf{V}'_1 = (\mathbf{V}_1 - \mathbf{V}_0)$  and  $\mathbf{V}'_2 = (\mathbf{V}_2 - \mathbf{V}_0)$ , respectively, and the particle position  $\mathbf{p}$  is translated into  $\mathbf{p}' = \mathbf{p} - \mathbf{V}_0$ . The distance of the intersection point  $l_{\Delta}$  between the particle and the triangle, including its position  $(u, v)$  on the surface, can be written as follows:

$$\begin{pmatrix} l_{\Delta} \\ u \\ v \end{pmatrix} = \frac{1}{(\mathbf{d} \times \mathbf{V}'_2) \cdot \mathbf{V}'_1} \begin{pmatrix} (\mathbf{p}' \times \mathbf{V}'_1) \cdot \mathbf{V}'_2 \\ (\mathbf{d} \times \mathbf{V}'_2) \cdot \mathbf{p}' \\ (\mathbf{p}' \times \mathbf{V}'_1) \cdot \mathbf{d} \end{pmatrix} \quad (1)$$

Firstly, the denominator  $(\mathbf{d} \times \mathbf{V}'_2) \cdot \mathbf{V}'_1$  is calculated, with a value equal to zero indicating that the ray is parallel to the triangle and not intersecting it. If the value is non-zero, the next test consists of computing  $u$  and checking the collision condition  $0 < u < 1$ . If true, the same verification is performed on  $v$  which must validate the condition  $0 < v < 1$ . Finally, if all tests are positive, meaning that the ray intersects the triangle, the distance  $l_{\Delta}$  is computed. In case of a tetrahedral mesh, this ray/triangle procedure is repeated for every triangle  $\Delta_i$  that composes the mesh. For a non-convex mesh the same ray may possibly intersect several triangles, in which case the closest triangle is chosen.

#### 2.4. Hybrid voxelized/analytical primitive

In this work we propose a new hYbrid Voxelized/ANalytical primitive (YVAN) able to combine both phantom types within the same MCS. This method requires only one navigator and one main world for the whole MCS, optimizing computational times. We assume that analytical objects have a lower hierarchical level than a voxelized phantom, since in medical applications analytical objects will be almost exclusively used to describe structures integrated within a patient's voxelized image. Starting from this assumption, instead of simply combining analytical and voxelized geometries, the proposed method takes advantage of both geometry types to define a new primitive. This is achieved by using the bounding volume hierarchy (BVH) concept (Haverkort 2004), defined as a volume that encloses a set of primitives describing the voxelized phantom. A BVH structure is the most common spatial data structure used for real-time rendering and organizing a scene containing different objects in a hierarchical tree structure, consisting of root, internal nodes and leaves. The voxelized phantom is used to sample and decompose the geometry scene of the simulation, with BVH nodes defined as voxels containing leaves. Each leaf can describe any primitive or part of a primitive. Leaves are defined as triangles related to a mesh, as demonstrated in figure 2(a) where two triangles ( $\Delta_1, \Delta_2$ ) overlap with the voxel ( $ABCD$ ).

The BVH tree is built at the beginning of the simulation. For each node a list of triangles that overlap the corresponding voxel needs to be determined. Considering the large number of voxels and triangles concerned, a computationally efficient algorithm of box/triangle overlapping (Akenine-Moller 2001) was implemented (see figure 2(b)). Firstly, the voxel (considered as an AABB, see section 2.2) and the triangle  $\Delta_i$  are moved so that the voxel is centered on the origin of the world's simulation. The new triangle vertices are then defined as  $\mathbf{u}_i = \mathbf{V}_i - \mathbf{C}$  ( $i \in 0, 1, 2$ ). The intersection point between a voxel and a triangle is determined based on the separating axis theorem, which determines the overlapping between two convex objects by using their projections on different separating axes. For an AABB/triangle overlapping, 13 axis tests are necessary. Based on the frame of the voxel (see figure 2(b),  $\mathbf{e}_0 = (1, 0, 0)^T$ ,  $\mathbf{e}_1 = (0, 1, 0)^T$ ,  $\mathbf{e}_2 = (0, 0, 1)^T$ ), the first 3 axis tests are performed against the minimal AABB that includes the triangle  $\Delta_{\mathbf{u}_0\mathbf{u}_1\mathbf{u}_2}$ . The next step uses a fast plane/AABB overlap test using the normal  $\mathbf{n}$  of  $\Delta_{\mathbf{u}_0\mathbf{u}_1\mathbf{u}_2}$  to determine whether the triangle plane crosses the voxel or not. Finally, nine tests are performed for checking every separating axis of the voxel against the ones of the triangle. This is achieved by calculating the cross product between voxel frame vectors  $\mathbf{e}_i$  and the edge triangle vectors  $\mathbf{f}_j$  for every axis  $i, j \in 0, 1, 2$ , where the edge triangle vectors are  $\mathbf{f}_0 = \mathbf{u}_1 - \mathbf{u}_0$ ,  $\mathbf{f}_1 = \mathbf{u}_2 - \mathbf{u}_1$  and  $\mathbf{f}_2 = \mathbf{u}_0 - \mathbf{u}_2$  (see figure 2(b)).

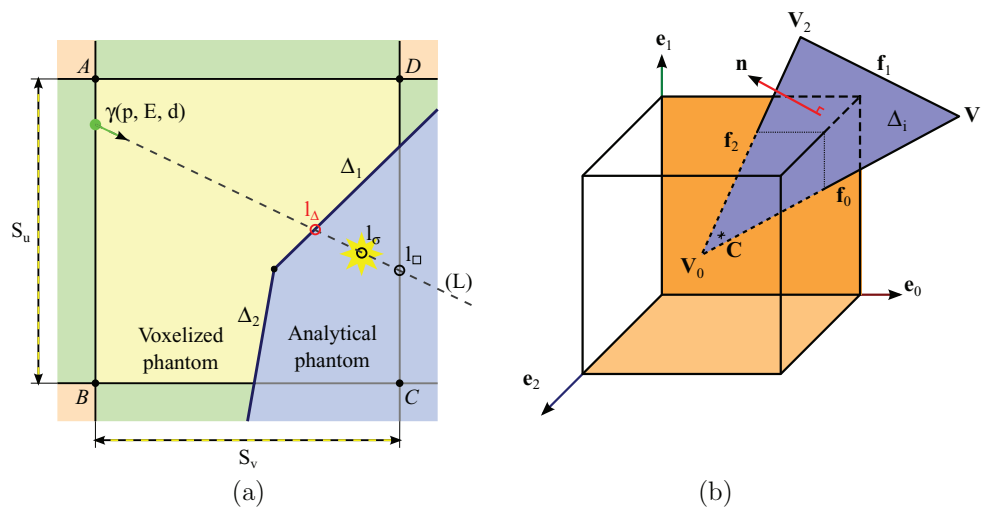


**Figure 2.** Basic scheme of (a) the proposed hybrid voxelized/analytical primitive and (b) the efficient voxel/triangle overlap test in 3D.

The algorithm terminates as soon as a separation between the box and the triangle is found over each axis test. On the other hand, if all tests pass, the triangle overlaps the box. The final BVH tree is constructed by listing triangles that overlap each voxel, and BVH structure data is compressed by removing empty voxels. During the simulation the particles virtually navigate through the BVH tree deciding which kind of geometry (analytical or voxelized) should be used according to each location. If a node does not contain anything, meaning there is no triangle within that voxel, the YVAN primitive will use the voxelized geometry previously presented to transport the particle. On the other hand, if there are triangles, the YVAN primitive will determine the closest volume boundary distance by considering the voxel ( $ABCD$ ) and the associated triangles ( $\Delta_1, \Delta_2$ ) along the particle path as illustrated in figure 2(a). The minimum distance between  $I_\square$  and  $I_\Delta$  is chosen and defines if the particle is entering a mesh or another voxel, respectively.

YVAN can be considered as a polymorphic geometry, with the navigator seeing different kinds of primitives (a mesh or a voxelized volume) depending on the situation. In the case represented in figure 2(a) the particle is entering the mesh through the triangle  $\Delta_1$ . This will automatically activate the mesh within YVAN until the particle escapes this volume and re-enters the voxelized phantom. During this mesh navigation YVAN will return only geometrical information related to the mesh without considering the voxelized volume.

With YVAN, only one navigator runs at a time within the same world improving overall simulation computational efficiency. In addition, given that the navigator considers one object (mesh or voxel) at a time, the number of particle steps is optimal since within the analytical geometry the particle is not overstepped by virtually following every boundary voxel.

## 2.5. Layered mass geometry

The layered mass geometry concept has been implemented in numerous MCS codes and can be considered as the current gold standard methodology enabling combined voxelized/analytical navigation issues. Since it has been used in this work for comparison purposes with the new proposed YVAN primitive, the main concept of the LMG is presented in this section.

The main idea behind this methodology is the use of different layers of geometry in the same simulation, which is equivalent to having parallel worlds. The first approach to the superposition of multiple geometries for MCS was introduced by Yegin (2003) and implemented in EGS (Nelson *et al* 1985, Kawrakow and Rogers 2000). The LMG is a similar solution developed for Geant4 by Apostolakis *et al* (2008) and Enger *et al* (2012). Each parallel world or layer is associated with an independent navigator, which computes the different boundary distances considering only the geometry contained in its own layer. The mass used on each navigator is chosen according to the hierarchy of each layer.

The LMG allows the use of different geometry types (voxelized and analytical) in the same MCS. However, each navigator independently computes the boundary distances of objects contained on the associated layer. The particle is stepped considering the nearest object boundary determined on every layer, which substantially increases the number of steps between two interaction points relative to a single world navigation. In addition, in the case of two layers overlapping analytical and voxelized primitives, the particle step will start from the voxel boundary due to its high sampling geometry. This, in turn, will also increase simulation complexity and therefore lead to longer computational times, particularly in cases where one considers the combination of a large analytical phantom within a voxelized one. Finally, the LMG requires decomposing complex geometries and careful organization in several layers which leads to added complexity.

## 2.6. Implementation

The proposed YVAN primitive was evaluated using homemade software written in C++ for a single-core CPU application (see figure 3). A photon navigator was implemented following the standard approach described in section 2.1. Two other navigators specifically for handling a combination of voxelized and analytical objects were implemented within the same software. The first one was the new primitive YVAN proposed in this work using the overall concept outlined in section 2.4 and based on voxelized and analytical phantom ray-tracing calculations described in sections 2.2 and 2.3, respectively. In order to compare and assess YVAN against LMG, the latter method was also implemented based on the original concept proposed by Enger *et al* (2012) and Yegin (2003) and detailed in section 2.5.

Regarding the physics effects included, the implemented code directly used the Geant4 (Allison *et al* 2006) toolkit as a third-party library as shown in figure 3. The corresponding Geant4 C++ classes are directly called by the implemented software to handle the definition of materials, the computation of cross-sections and the resolution of the discrete processes for the Monte Carlo simulations. Only photon particle processes were considered as detailed in the evaluation section (section 2.7). The developed software included also functions to open mesh raw data exported from Blender™ (Blender Foundation, Amsterdam, Netherlands) and medical images in MetaImage format (MHD). Geometry visualization was handled by the Visualization Toolkit (VTK, Kitware Inc, New York, USA). Finally, the proposed software was validated by comparing results against the GATE MCS platform (Jan *et al* 2011), based on the Geant4 simulation engine.

## 2.7. Evaluation study

**2.7.1. Validation.** Firstly, the proposed YVAN primitive was evaluated considering a simple phantom. The primary aim in the first part of this validation was to assess the developed software including the new YVAN primitive against a full equivalent GATE simulation. The simulation set-up was based on a water phantom of  $200 \times 100 \times 100 \text{ mm}^3$  with a centrally

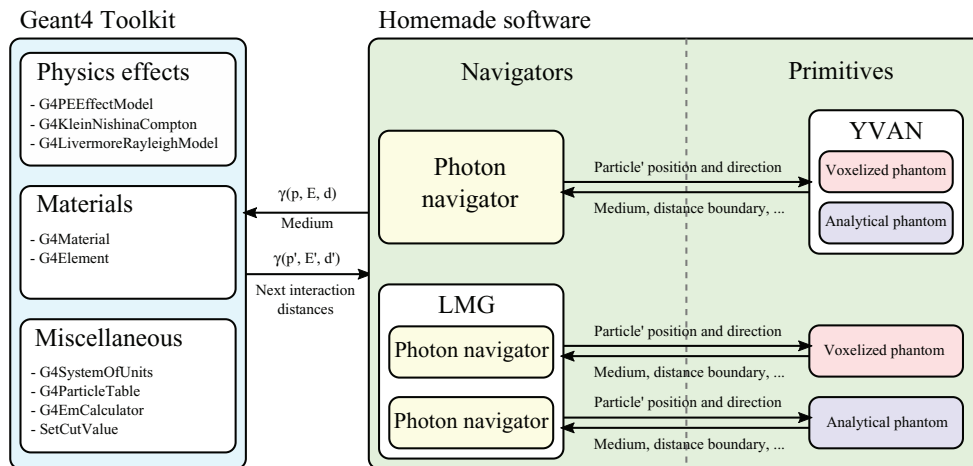


**Figure 3.** Diagram of the developed simulation software showing the overall structure and interactions with the Geant4 toolkit.

positioned point source isotropically emitting photons with an energy of 50 keV. As shown in figure 4(a), a 10 mm thick slab composed of bone material was placed near the right side of the source (at 50 mm from the phantom center) and a 45 mm radius sphere composed of air to the left side at 50 mm (center-to-center). A first GATE simulation was run by generating  $100 \times 10^6$  photons considering Compton scattering and photoelectric effects from the standard model and Rayleigh scattering using the Livermore model provided in Geant4. This GATE simulation used the Geant4 regular navigator dedicated to tracking within analytical environments, with the simulation designed accordingly by using only analytical objects to define the sphere, water box and slab as described in figure 4(a).

A second simulation was carried out to assess the performance of the proposed hybrid YVAN primitive. A voxelized water box phantom including the bone slab with  $1 \text{ mm}^3$  voxels was used for this simulation, where a mesh-based sphere described as an analytical object was included within the voxelized phantom as shown in figure 4(b). This sphere was modeled by a mesh using the open-source software Blender<sup>TM</sup> (Blender Foundation, Amsterdam, Netherlands). Three different modeling precision levels were considered for the sphere, using 224, 960, and 16 128 triangles for the mesh description. Each of the three models was run as a separate simulation in order to estimate the impact of the mesh sampling for the shape definition on the MCS results. Both the new hybrid voxelized/analytical geometry and the LMG navigation were used for each simulation. In order to compare simulations between them, every particle escaping the water phantom was killed and stored in a phase-space file, and overall simulation running times were recorded. Based on each phase-space file, the distribution of the photon positions was estimated for each of the simulations considered. The relative dispersion values between two distributions were estimated by calculating their differences divided by the magnitude of the reference distribution.

**2.72. Imaging application.** A first application-based evaluation study of the proposed hybrid primitive was in the field of medical imaging, and more specifically in the field of coronary angiography simulation using fluoroscopy which may be a typical application requiring the combination of a voxelized phantom derived from a thoracic patient CT and a mesh phantom segmented from a coronary patient MRI (see figure 5(a)). A voxelized phantom was derived



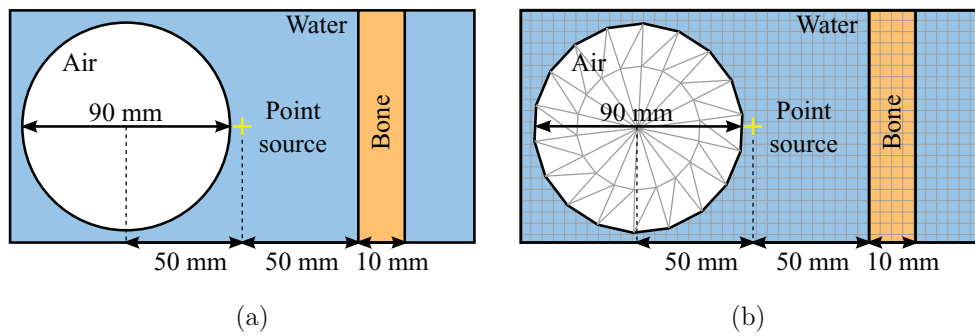


**Figure 4.** Simulation setup for evaluations considering (a) analytical objects and (b) voxelized and mesh objects.

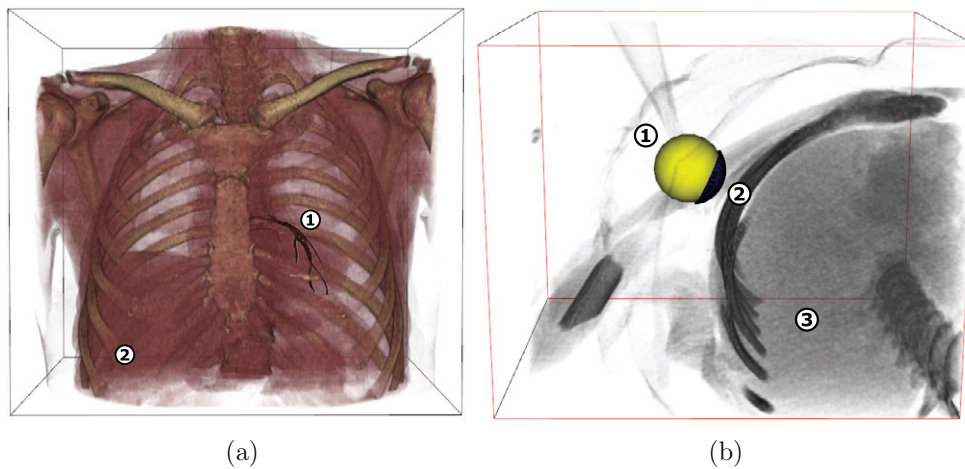


**Figure 5.** Images of the two clinical examples used in the evaluation of the proposed YVAN primitive. (a) Angiography application with (1) the mesh describing the coronaries within (2) a thoracic voxelized phantom; (b) intra-operative radiotherapy phantom showing the (1) source applicator, (2) analytical protective shield and (3) thoracic voxelized phantom.

from a thoracic patient CT by transforming Hounsfield units into materials through a density conversion given by Schneider *et al* (2000). The final voxelized part of the phantom consisted of 42 materials and  $241 \times 164 \times 288$  voxels of  $1.27 \times 2.0 \times 1.27$  mm<sup>3</sup>. Concerning the mesh part of the phantom, a left coronary model segmented from the MRI of a male heart was used and provided by Gu *et al* (2011). This tetrahedral mesh phantom was composed of 9012 triangles. Two different materials were considered for the coronary in order to simulate the presence of a contrast-enhancing agent. More specifically, blood material and a mixture of blood and 20% of iodine was used for the simulation with and without the presence of a contrast agent. A realistic x-ray spectrum was generated using the TASMIP model (Boone and Seibert 1997) considering a classic tube voltage used in angiography of 40 kVp and a 1.2 mm aluminium filter. A cone beam source with a rectangular shape of  $1.3 \times 1.3$  mm<sup>2</sup> emitting particles from an 8° aperture was considered. Finally, a flat panel detector was simulated with a field of view of  $300 \times 300$  mm<sup>2</sup> and a pixel size of  $1 \times 1$  mm<sup>2</sup>. Every particle interacting with the panel was detected without considering any tracking within the detector. The voxelized

phantom was centered over the detector, with a distance of 1.2 m between the x-ray source and the detector. The left coronary model was approximately positioned using the location of the heart in the voxelized CT phantom as shown in figure 5(a).

A first MCS was performed with the developed software considering only the voxelized part of the phantom without accounting for the mesh coronary. Subsequently, several independent simulations were performed considering both the voxelized and analytical phantom parts using the LMG method and the proposed YVAN primitive with and without the use of a contrast agent. For the simulations using the YVAN primitive a BVH tree was pre-calculated before the simulation considering the same resolution as the voxelized phantom (11 382 912 voxels over 9012 triangles). Similarly, and for a fair comparison in terms of both complexity and precision, for LMG based simulations, a regular BVH structure on the coronary mesh was pre-calculated with the same resolution used by YVAN. 2D projection images were recovered for each simulation considering a total of  $2 \times 10^9$  photons emitted from the x-ray source. Final transmission angiography images were obtained by calculating  $-\log(I/I_0)$ , where  $I$  is the 2D projection of the patient recovered from the MCS and  $I_0$  the normalized 2D projection estimated from MCS without the presence of the patient phantom. Finally, all simulations were run using 60 CPU cores on a computer cluster over 15 nodes equipped with Intel Core i7 processors (frequency of 3.4 GHz). For each simulation the total run time was recorded.

**2.7.3. Radiotherapy dosimetry application.** The second medical application-based evaluation study was on intra-operative radiotherapy (IORT) dosimetry using the IntraBeam<sup>TM</sup> (Carl Zeiss, Meditec) system. IORT consists of delivering a single radiation dose targeting the tumor bed just after the tumor removal (Calvo *et al* 2006a, 2006b). Such low-energy applications ( $<1$  MeV) require only photon tracking, since the mean free path for secondary electrons is smaller than a voxel leading to a valid approximation that electrons deposit the whole dose locally (Chibani and Williamson 2005). In practice, a shield is empirically positioned towards any organs at risk (for example the heart in the case of usage during breast surgery) in order to minimise the associated dose (figure 5(b)). The dosimetric impact of this shield can only be resolved through a Monte Carlo simulation that combines a patient voxelized CT and a mesh phantom modeling the shield. Similarly to the imaging application of the previous section, a voxelized phantom was derived from a breast cancer patient's CT images acquired during the intervention. The final voxelized phantom consisted of 42 materials and  $251 \times 201 \times 201$  voxels of  $0.96 \times 0.96 \times 2$  mm<sup>3</sup>. The shield is a cupula with a radius of 40 mm and depth of 20 mm, which is equivalent to a hollow sphere with a solid angle of 120°. The shield was modeled with Blender<sup>TM</sup> as a tetrahedral mesh composed of 2080 triangles. The shield is made of tungsten-coated silicon, which is equivalent to a lead thickness of 50  $\mu$ m. A spherical source of 40 mm isotropically emitting photons on its surface was used to simulate the source applicator of the IntraBeam<sup>TM</sup> (Bouzid *et al* 2015). The real spectrum provided by the system, which is equivalent to a Gaussian energy distribution centered to 27 keV with a standard deviation of 8.5 keV, was used for the source description. Considering the MCS, photoelectric effect and Compton scattering from the standard model and Rayleigh from the Livermore model provided by Geant4 were used. For each simulation a total of  $10^9$  photons were simulated to reconstruct dose maps with dimensions and resolution equivalent to the voxelized phantom. For each of the two methods considered (YVAN and LMG) two simulations were performed with and without the shield in place. For simulations using the LMG and YVAN methods a BVH structure was pre-calculated on the shield the same as the CT image resolution (10 140 651 voxels over 2080 triangles). The same hardware configuration as with the image application in the previous section was used.

### 3. Results

#### 3.1. YVAN validation

From the recorded phase-space file obtained by both simulations using the LMG method and the YVAN primitive with the mesh composed of 16 128 triangles, the photon position along the  $x$ -axis was compared in figure 6(a). The relative error between both plots is also shown in figure 6(a). The dispersion of the photon positions seems to increase between 60 mm and 100 mm along the  $x$ -axis. This is explained by the high attenuation of the bone slab which largely decreases the number of detected particles in this region, which in turn increases the statistical uncertainty and hence the calculated relative dispersion values. The overall absolute mean error between LMG and YVAN simulation results was  $0.28\% \pm 0.31\%$ , a very good agreement showing that the proposed hybrid primitive seems equivalent in terms of simulation to the LMG concept results. In addition, results provided by a purely analytical simulation also showed a good agreement with the hybrid one considering both voxelized and analytical objects. This result also suggests that the YVAN primitive properly transports particles through the mixed geometry described environment within the same MCS.

The impact of the mesh sampling was evaluated by considering the sphere primitive composed of different numbers of triangles. As a reference, a similar MCS considering the complete primitive as an analytical geometry was performed using GATE. From the recovered phase-space files for all of these simulations, photon positions along the  $x$ -axis were compared (see figure 6(b)). As expected, the approximate shape definition associated with a crude sampling of the sphere (224 triangles) led to the largest discrepancy between the two simulations, one considering the meshed and the other the analytical sphere description. In this case the overall absolute relative difference was  $2.8\% \pm 2.2\%$ . By improving the shape definition using a mesh with more triangles, the YVAN and GATE simulations were closer with an overall absolute relative error of  $1.18\% \pm 0.98\%$ . A good compromise between the number of triangles and overall shape definition was a sphere with 960 triangles, leading to an overall difference of  $1.63\% \pm 1.02\%$ .

Run times and the average number of steps recorded for every particle during the tracking are listed in table 1. The run time per  $10^6$  simulated photons using the YVAN object increases only marginally with the number of triangles in the mesh; 57.5 s and 60.1 s for a sphere of 224 and 16 k triangles, respectively. A larger corresponding run time increase was seen for the LMG simulation with 128 s and 146 s for a sphere of 224 and 16 k triangles, respectively. The globally slower simulation times with the LMG navigation (a factor of 2.3 in average) are due to the LMG operational concept, where the particle steps within the meshed objects are constrained by the voxel boundaries. Consequently, the average number of steps recorded during the particles' tracking is almost identical for the different number of triangles used in the mesh structure (125.4, 125.5, 125.4 for a mesh with 224, 960 and 16 k triangles, respectively). In contrast, the number of steps for YVAN was 25% smaller than LMG given that YVAN considers only the mesh boundary in this situation. The ratio of the number of steps between LMG and YVAN is directly linked to the proportion of the mesh volume within the voxelized geometry.

On the other hand, using a high sampling shape definition for mesh structures both for YVAN and LMG simulations will impact on the calculation times required to build the associated BVH tree. For each mesh sampling of the sphere the calculation time for the BVH is listed in table 1. Considering a voxelized volume composed of  $2 \times 10^6$  voxels, the calculation run time of the BVH tree was 16 s, 68 s and 1080 s for a mesh of 224, 960 and 16 k triangles, respectively. One has to consider, however, that even with the highest sampling mesh,

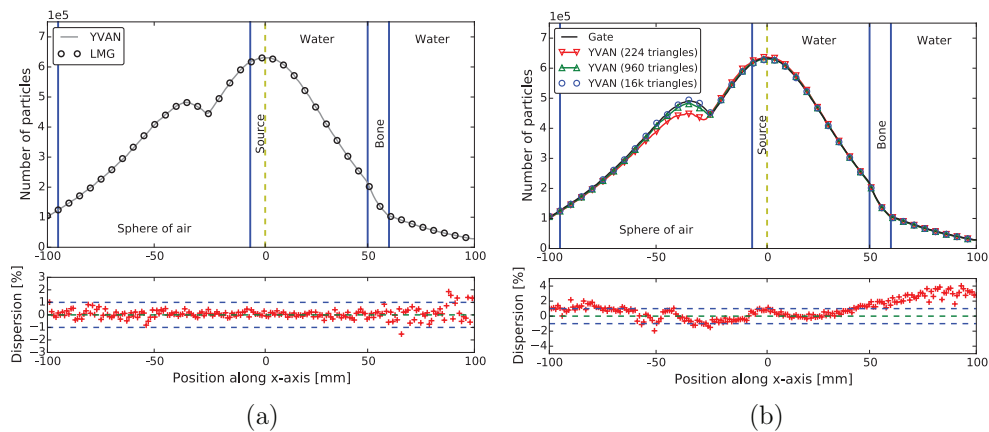


**Figure 6.** Distribution of the photon position along the  $x$ -axis obtained by MCS using (a) LMG simulation and the proposed YVAN primitive (both simulations used a mesh composed of 16 k triangles) and (b) a complete analytical geometry from GATE and the proposed YVAN primitive with different mesh sampling for the sphere (dispersion values were estimated by comparing GATE results with the YVAN simulation using a mesh composed of 16 k triangles). Dashed blue lines on each figure representing dispersion highlight values between the range of  $\pm 1\%$ .

**Table 1.** Simulation performance considering different mesh sampling characteristics for the description of analytical structures within the YVAN and LMG navigators.

	YVAN		LMG		BVH
	Run time (s) / $10^6$ particles	Number of steps	Run time (s) / $10^6$ particles	Number of steps	Calculation time (s)
224	57.5	$96.1 \pm 56.6$	128.7	$125.4 \pm 65.5$	16
960	59.7	$94.1 \pm 56.7$	138.4	$125.5 \pm 65.3$	68
16 128	60.1	$92.9 \pm 56.9$	146.8	$125.4 \pm 65.0$	1080

the 18 min BVH tree calculation time is negligible within the context of the overall simulation computational times (hours or days).

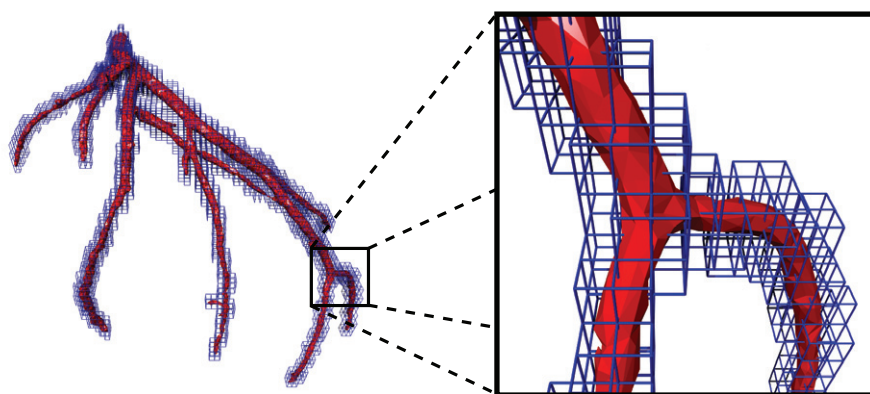
### 3.2. Application-based evaluation

For the angiography and IORT shield simulations, the total run time for building the BVHs was 120 s and 1.7 s, respectively. The factor of 70 difference in the computational time needed for building these BVH structures is due to the fewer triangles of the protective shield mesh relative to the coronary mesh, which, as a result, also overlaps less voxels due to its small size. Some properties of the BVH tree for both mesh structures are listed in table 2, while the final BVH structure for the coronary is displayed in figure 7.

Concerning the angiography simulation, the run time using only the voxelized phantom without the coronary structure mesh was 71 s for one million particles. On the other hand, when using the LMG and YVAN approaches, for the simulation using the combined voxelized and analytical mesh described objects, the run time was 76.1 s and 71.1 s, respectively. The

**Table 2.** Characteristics of the BVHs build for the applications-based simulations.

	Angiography	IORT
BVH calculation		
Number of voxels	11 382 912	10 140 651
Number of triangles	9012	2080
Run time (s)	120	1.7
Number of leaves	2033	1368
Average number of triangles per leaf	12.3	8.1
Data storage size (MB)	66	30
Simulation run time (s/10 <sup>6</sup> particles)		
Voxelized phantom	71.0	67.2
YVAN	71.1	58.1
LMG	76.1	66.2

**Figure 7.** The coronary mesh including the BVH structure for leaves that contain at least one object.

proposed YVAN primitive allows a hybrid voxelized/analytical object simulation with a run time within 0.14% of the one performed with the voxelized phantom alone. The small computational time difference between the two approaches is due to the very small proportion of the coronary mesh volume compared to the whole voxelized phantom.

Transmission angiography images recovered from the MCS using the voxelized phantom only, as well as the LMG navigation and YVAN primitive, are shown in figure 8. Results show that the left coronary modeled by a mesh was well simulated, with the contrast agent within the mesh allowing the identification of each element of the coronary tree within the thoracic voxelized phantom. Profiles through the 2D transmission images obtained using LMG and the proposed YVAN primitive, shown in figure 9, demonstrate close agreement between the two simulations.

Concerning the IORT Monte Carlo simulation, the run time for simulating one million particles with the voxelized phantom alone was 67.2 s. In the case of the LMG and YVAN approaches, simulation run times for one million simulated particles were 66.2 s and 58.1 s, respectively. These values are smaller compared to the voxelized phantom run time since the shield stops a large number of particles substantially reducing the overall simulation time. Similarly to the previous angiography simulation, the use of the YVAN primitive remains the faster method for a simulation using a mixed voxelized/analytical geometry. More specifically, in this case YVAN was faster by 12.2% compared to the corresponding LMG simulation,



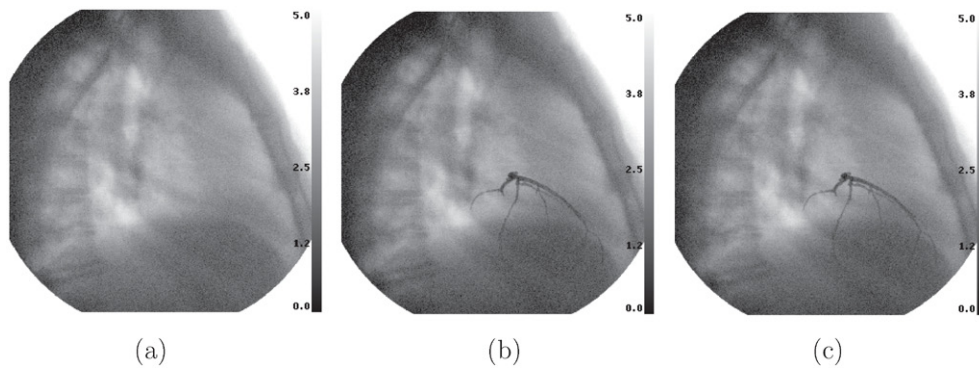


**Figure 8.** Transmission angiography images recovered from MCS using (a) voxelized phantom without mesh object, (b) LMG method and (c) the proposed YVAN primitive.

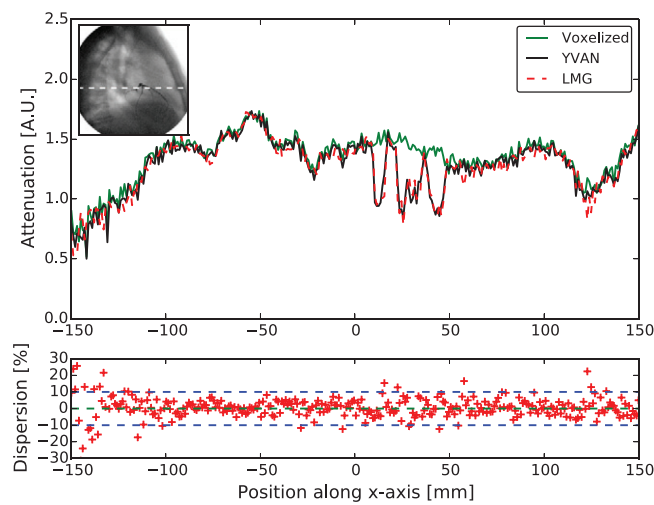


**Figure 9.** Profiles through the 2D transmission images obtained from angiography simulation using only the voxelized phantom, the LMG method and the YVAN primitive. Dispersion values were estimated by comparing LMG results with the YVAN simulation. Dashed blue lines on the figure represent the dispersion highlight values between the range of  $\pm 10\%$ .

which is double the acceleration encountered in the angiography application (6.5%), given the difference in the proportion of the mesh and voxelized volumes in the two applications.

The dose maps recovered from the MCS using the voxelized phantom alone and the YVAN described geometry are shown in figure 10. The first dose map (see figure 10(a)) obtained with the voxelized phantom did not include the protective shield, leading to increased dose deposition at the organs at risk surrounding the treatment source. For instance, a hot spot located at the patient's rib received 75% of the radiation dose prescription and a small liver region received 2.5%. Including the shield in the simulation making use of the YVAN primitive description (see figure 10(b)) led to a dose reduction to 5% and 0.5% of the radiation dose prescription in the rib and the liver, respectively. The results obtained for the IORT application demonstrate the interest of combining hybrid voxelised/analytical object geometries within the field of MCS for therapy applications.



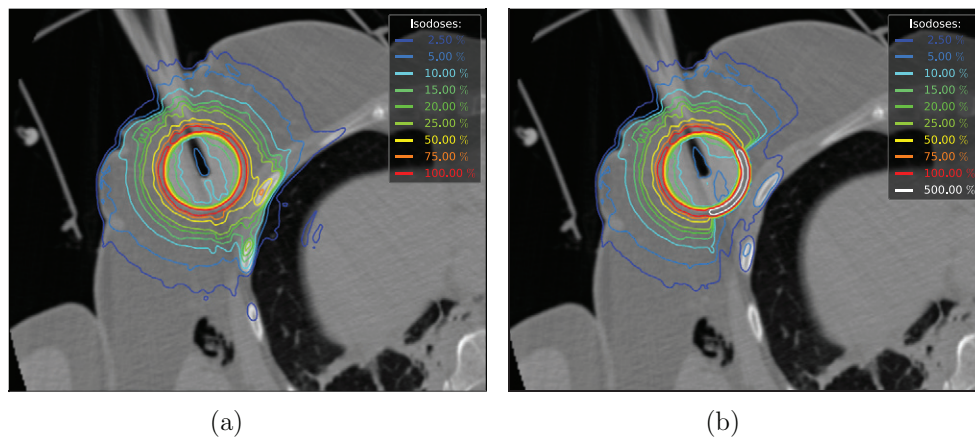


**Figure 10.** Patient CT overlaid with isodose given percentage of the radiation dose prescription obtained from MCS using (a) voxelized phantom without shield and (b) YVAN method including a shield modeled by a tetrahedral mesh.

#### 4. Discussion

Realistic medical imaging and particle therapy simulations using Monte Carlo require a fine and accurate description of the phantom geometry. Such phantom description must combine complementary information provided by multimodality imaging such as, for example, tissue heterogeneity from CT and/or functional imaging (PET and SPECT) and accurate anatomical structure details from MRI and CT images. This is particularly true in the last few years with the expansion of multimodality imaging devices in clinical practice (PET/CT, SPECT/CT), and the recent introduction of PET/MRI. On the other hand, in therapy protocols, simulations need to account for the presence of artificial objects such as radioactive sources and their housing and/or radiation-sensitive nanoparticles, one example being the field of IORT (brachytherapy, IntraBeam<sup>TM</sup>, etc). All of these applications require combining such elements on the same phantom during an MCS, with the overlapping of different type of objects. The previously proposed parallel world or Layer Mass Geometry concept allows in a generic way to overlap any geometry and object description without any associated limitations. However, this concept uses several navigators that run concurrently which inevitably increases computational cost. In addition, the implementation of this method requires a substantial modification of the MC navigation code structure in order to handle the different geometry layers.

The proposed YVAN primitive was developed to incorporate analytical objects inside a voxelized phantom within a simple implementation framework. As such the proposed method does not require any modifications on the MC navigation code, given that YVAN is just a new additional primitive object that can be handled by the main regular navigator of any simulation code allowing an efficient tracking within any given geometry. This new concept of a polymorphic primitive, mixing voxelized with analytical geometries, can also be easily implemented in MC platforms using GPU hardware architectures (Bert *et al* 2013). As an example for the specific case of Geant4, YVAN may be implemented by adding a new Geant4 solid (based on G4VSolid) that itself contains two pre-existing Geant4 solids; namely a voxelized (G4Box) and a mesh (G4TessellatedSolid). In Geant4, each solid must have ray-tracing mandatory functions (DistanceToIn, DistanceToOut, Inside, etc;) in order to perform particle navigation in a given primitive geometry. Therefore, a new YVAN solid will require the definition of these functions to be properly implemented within Geant4. However, instead of

defining ray-tracing functions, the YVAN solid has to call the ray-tracing functions associated to G4Box or the G4TessellatedSolid according to the particle position within the geometry. Since, the ray-tracing functions for these two solids are already implemented on Geant4, only the mechanism that switches between the two primitives will have to be implemented.

Considering example applications in imaging and radiotherapy, the use of YVAN was 6.5% and 12.2% faster than the LMG method, respectively. Differences in the computational time improvements obtained with YVAN were variable based on the relative size and number of triangles used in the description of the analytical objects' meshes. For example, in a case of a large meshed sphere, YVAN was 2.3 times faster than LMG, because the number of steps required for each particle to cross the mesh was different. In LMG, the number of particle steps is driven by the voxel boundaries on the voxelized layer. With YVAN, only the mesh crossed by the particle is considered, hence decreasing the average number of steps required. The YVAN primitive should be therefore most efficient for a simulation that uses large meshes contained on the voxelized phantom.

The use of a complex geometry such as a tetrahedral mesh phantom does not increase the simulation complexity when using the YVAN or LMG methods. The run time for the angiography application simulation using YVAN was equivalent to a simulation using the voxelized phantom only. One major parameter affecting the complexity of YVAN and the results compared to a complete analytical simulation is the sampling of the mesh. A good compromise between object shape definition and number of triangles used in the mesh construction has to be chosen. This number directly depends on the number and size of triangles and voxels. For example, although it is possible to have a complete mesh contained within a single voxel the resulting level of complexity will be very high since for each particle crossing this particular voxel the distance boundary with every triangle composing this mesh will have to be computed.

However, the proposed BVH structure within the YVAN approach is a virtual tree structure which may contain any type of object, including others BVH structures. In order to constrain complexity and incorporate more than one mesh into the voxelized phantom one could construct sub-BVH trees associated with each mesh contained on a given scene. In this case, each mesh is handled by a BVH structure using a virtual uniform grid with a size adapted to each mesh size. Finally, within the proposed implementation a main BVH tree handles the voxelized phantom, where leaves will contain voxels and others overlapped sub-BVH structures. One other main advantage of the proposed BVH structure is the possibility to dynamically update the tree structure. This can be useful for dynamically moving objects, which is usually the case in medical applications while considering physiological patient motion or the displacement of imaging and/or treatment systems. Finally, the BVH tree pre-calculation time necessary to build the data structure for a given geometry, although variable depending on the number of triangles and the size of voxels, is relatively negligible within the context of overall simulation computational times.

The proposed hybrid primitive was evaluated in this work using photon particle tracking. Photons are the simplest particles to simulate since only discrete processes are involved. Despite using only photon simulations to validate and evaluate the YVAN primitive in this work, since YVAN requires only the definition of geometric properties, this new hybrid primitive can be easily used with other particle types, such as electrons or protons. Similarly, YVAN is not limited to the use of meshed phantoms. Any conventional primitive (sphere, box, etc) can be handled by a BVH structure and provide an efficient way to perform voxelized/analytical MCS. Finally, the proposed method is suitable for parallel implementation, especially for the BVH construction, which is built following a voxel-wise approach, which can be parallelized using CPU multi-threading or GPU hardware architectures.

## 5. Conclusions

The aim of this work was to develop a new hybrid primitive capable of combining voxelized and analytical phantoms within the same MCS targeting medical applications. This new hybrid object was assessed through a simple MCS. Results were compared against a MCS using a pure analytical geometry and using the previously proposed layer mass geometry concept. A perfect agreement was found between these simulations, leading to the conclusion that the new proposed hybrid primitive is capable of accurately mixing voxelized and analytical phantoms. Further work will focus on evaluating the use of this new object in different medical applications requiring such hybrid object geometry description in order to further demonstrate the potential impact of this development. Finally, this new concept will be implemented as part of the MC GATE platform to further enhance its utilization.

## Acknowledgments

This work was partly supported by the French ANR within the Investissements d'Avenir program (Labex CAMI) under reference ANR-11-LABX-0004 (Integrated project CAPRI) and through t-GATE project (ANR-14-CE23-0008).

## References

- Akenine-Moller T 2001 Fast 3D triangle-box overlap testing *J. Graph. Tools* **6** 29–33
- Allison J *et al* 2006 Geant4 developments and applications *IEEE Trans. Nucl. Sci.* **53** 270–8
- Apostolakis J, Asai M, Cosmo G, Howard A, Ivanchenko V and Verderi M 2008 Parallel geometries in Geant4: foundation and recent enhancements *IEEE Nucl. Sci. Symp. and Med. Imaging Conf. Rec.* pp 883–6
- Arce P, Apostolakis J and Cosmo G M 2008 A technique for optimised navigation in regular geometry *IEEE Nucl. Sci. Symp. and Med. Imaging Conf. Rec.* pp 857–59
- Badal A, Kyprianou I, Banh D P, Badano A and Sempau J 2009 penMesh—Monte Carlo radiation transport simulation in a triangle mesh geometry *IEEE Trans. Med. Imaging* **28** 1894–901
- Bert J *et al* 2013 Geant4-based Monte Carlo simulations on GPU for medical applications *Phys. Med. Biol.* **58** 5593–611
- Boone J M and Seibert J A 1997 An accurate method for computer-generating tungsten anode x-ray spectra from 30 to 140 kV *Med. Phys.* **24** 1661–71
- Bouzid D, Bert J, Dupre P-F, Benhalouche S, Pradier O, Bousson N and Visvikis D 2015 Monte-Carlo dosimetry for intraoperative radiotherapy using a low energy x-ray source *Acta Oncol.* **54** 1788–95
- Calvo F A, Meirino R M and Orecchia R 2006a Intraoperative radiation therapy: first part: rationale and techniques *Crit. Rev. Oncol./Hematol.* **59** 106–15
- Calvo F A, Meirino R M and Orecchia R 2006b Intraoperative radiation therapy: part 2. Clinical results *Crit. Rev. Oncol./Hematol.* **59** 116–27
- Chibani O and Williamson J F 2005 MCPI: a sub-minute Monte Carlo dose calculation engine for prostate implants *Med. Phys.* **32** 3688–98
- Enger S A, Landry G, D'Amours M, Verhaegen F, Beaulieu L, Asai M and Perl J 2012 Layered mass geometry: a novel technique to overlay seeds and applicators onto patient geometry in Geant4 brachytherapy simulations *Phys. Med. Biol.* **57** 6269–77
- Gu s, Gupta R and Kyprianou I 2011 Computational high-resolution heart phantoms for medical imaging and dosimetry simulations *Phys. Med. Biol.* **56** 5845–64
- Haverkort H J 2004 Results on geometric networks and data structures *PhD Thesis* Utrecht University
- Hubert-Tremblay V, Archambault L, Tubic D, Roy R and Baulieu L 2006 Octree indexing of DICOM images for voxel number reduction and improvement of Monte Carlo simulation computing efficiency *Med. Phys.* **33** 2819–31
- Jan S *et al* 2011 Gate v6: a major enhancement of the Gate simulation platform enabling modelling of CT and radiotherapy *Phys. Med. Biol.* **56** 881–901

- Kawrakow I and Rogers D W O 2000 The EGSnrc code system *Report Pirs-701* National Research Council of Canada
- Moller T and Trumbore B 1997 Fast, minimum storage ray-triangle intersection *J. Graph. Tools* **2** 21–8
- Nelson W R, Hirayama H, and Rogers D W O 1985 *The EGS4 code system SLAC-265* Technical Report, Stanford Linear Accelerator Center
- Said R, Chang J, Young P, Tabor G and Coward S 2008 Image-based meshing of patient-specific data *Int. Conf. on Bioinformatics and Biomedical Engineering* pp 1672–6
- Schumann J, Paganetti H, Shin J, Faddegon B and Perl J 2012 Efficient voxel navigation for proton therapy dose calculation in TOPAS and Geant4 *Phys. Med. Biol.* **57** 3281–93
- Schneider W, Bortfeld T and Schlegel W 2000 Correlation between CT numbers and tissue parameters needed for Monte Carlo simulations of clinical dose distributions *Phys. Med. Biol.* **45** 459–78
- Smits B 2002 Efficient bounding box intersection *Ray Tracing News* **15** (<http://www.realtimerendering.com/resources/RTNews/html/rtnv15n1.html>)
- Yegin G 2003 A new approach to geometry modeling for Monte Carlo particle transport: an application to the EGS code system *Nucl. Instrum. Methods Phys. Res.* **211** 331–8
- Young P G, Beresford-West T B H, Coward S R L, Notarberardino B, Walker B and Abdul-Aziz A 2008 An efficient approach to converting three-dimensional image data into highly accurate computational models *Phil. Trans. R. Soc. A* **366** 3155–73

## B.6 Modélisation et validation du système IntraBeam

*Acta Oncologica*, 2015; Early Online: 1–8

**informa**  
healthcare

### ORIGINAL ARTICLE

## Monte-Carlo dosimetry for intraoperative radiotherapy using a low energy x-ray source

DOUNIA BOUZID<sup>1,2</sup>, JULIEN BERT<sup>1</sup>, PIERRE-FRANCOIS DUPRE<sup>3</sup>,  
SAADIA BENHALOUCHE<sup>1</sup>, OLIVIER PRADIER<sup>1,2</sup>, NICOLAS BOUSSION<sup>1,2</sup> &  
DIMITRIS VISVIKIS<sup>1</sup>

<sup>1</sup>Inserm UMR1101, LaTIM, Brest, France, <sup>2</sup>Department of Radiotherapy, CHRU Brest, France  
and <sup>3</sup>Department of Gynecology and Surgery, CHRU Brest, France

### ABSTRACT

Intraoperative radiotherapy (IORT) is continuously gaining ground in cancer treatment. However, there is currently no planning system associated with these devices, which precludes patient-specific dose delivery optimization. The objective of this study was the development and validation of a Monte Carlo simulation (MCS)-based dosimetry platform using the IntraBeam™ system.

**Methods.** After surgical resection of the tumor this system delivers a single dose fraction at the surface of an applicator irradiating the tumor bed through a 50 kV x-ray beam. The GATE MCS platform was used in this study combining the phase space obtained by modeling the x-ray source and the detailed modeling of the additional parts of the IntraBeam™ system. The model was validated by comparing simulated versus experimental measurements of depth dose curves (DDC) and isotropy. A clinical validation study was also carried out using patient computed tomography images.

**Results.** The mean deviation between measured and simulated DDC was  $2.9\% \pm 4.4\%$  and  $5.9\% \pm 5.7\%$  for the bare needle and the use of applicators, respectively. A good agreement with experimental measurements was also found in terms of dose isotropy with a maximum difference of 2.04% for the 40 mm diameter applicator. A patient study revealed a mean absolute deviation of 0.06 Gy between simulated and thermoluminescent dosimeters (TLD) measured skin doses.

**Conclusion.** This study shows the potential of using the GATE MCS platform to model three-dimensional dose distributions of the IntraBeam™ system for use in IORT.

The aim of partial breast irradiation (PBI) is to reduce the risk of local recurrence in the tumor bed following breast surgery. Within this context different techniques have been described, using interstitial brachytherapy (low or high dose rate), Mammosite (balloon), electron or photon intraoperative radiation therapy (IORT) or external beam radiation therapy (EBRT) [1]. The approach of partial intraoperative breast irradiation with electron or photon beams is particularly attractive since it offers the possibility of a single unified radiosurgical treatment [2]. The surgical lumpectomy is in this case immediately followed by PBI, the whole process requiring approximately 2–3 hours. Therefore this approach reduces overall treatment time and cost associated

with the use of multi-fraction EBRT following breast surgery given the necessary transportation costs and inconvenience. The main difficulty is to obtain accurate and reliable data on the histological resection margins or the presence of an extensive intraductal component, which could imply that the patient would benefit from irradiation of the entire gland [1,2].

Current IORT protocols using the IntraBeam™ system in breast cancer apply a single dose fraction of 20 Gy at the applicator surface to all patients [2]. The current lack of a personalized dose prescription in the case of IORT may be questioned considering European recommendations of individual dose optimization [3]. In addition, the dose distribution delivered to tissues is not known, and therefore cannot

Correspondence: D. Bouzid, Inserm UMR1101, LaTIM, Brest, France; Department of Radiotherapy Centre Hospitalier Régional Universitaire Morvan, 2 avenue Foch, 29609 Brest Cedex, France. Phone: + 33 652576708/+ 33 298018189. E-mail: dounia.bouzid@voila.fr

(Received 11 September 2014; accepted 3 February 2015)

ISSN 0284-186X print/ISSN 1651-226X online © 2015 Informa Healthcare  
DOI: 10.3109/0284186X.2015.1016623

**RIGHTSLINK**  
Copyright Clearance Center



be optimized. Within this context several factors come into play. Firstly, at 50 kV, the dose gradient is so high that any measurements associated with significant uncertainty related to the positioning accuracy of the detector. Second, the low-energy photon spectrum varies rapidly with depth, which makes it difficult to measure since detector response to low energy photons is usually energy dependent. Consequently precise dose calculation and measurements need to take into account the evolution of the spectrum with depth. Finally, at 50 kV (and considering an average energy of  $27.02 \pm 8.80$  keV at the surface of the applicator) water is not exactly a tissue equivalent material. Furthermore, the assumption of considering a patient as a simple water box may not be appropriate in terms of accurate dose calculation, particularly in regions where variable tissue densities and heterogeneities may be present. In order to overcome these limitations, we propose in this work the development of a Monte Carlo (MC) dose calculation platform for the Intrabeam™ system. The proposed development has been carried out using the Geant4 Application for Emission Tomography (GATE) platform [4] to model the x-ray source (XRS) and simulate realistic patient conditions.

The first objective of the present work was the modeling of the Intrabeam™ XRS and validation of the model by comparison of simulated and measured dose distributions in a water phantom. In the second phase of this study the capabilities of the proposed IORT dosimetry platform were evaluated using patient computed tomography (CT) images. In-vivo measurements during patient irradiation were performed using thermoluminescent detectors (TLD) positioned on the skin surface.

## Material and methods

### *Device description*

The mobile miniaturized radiation source of the Intrabeam™ (Supplementary Figure 1, to be found online at <http://informahealthcare.com/doi/abs/10.3109/0284186X.2015.1016623>) produces x-rays by emitting and focusing an electron beam in the electron gun, accelerating the beam with a mean energy of 50 keV and a Gaussian distribution with 5 keV full width at half maximum [5]. The beam then travels down an evacuated tube to strike a thin gold hemispherical target (0.5 μm thick) that lies on the inside end of the tube. The resulting beam consists of x-ray photons coming from the interactions of the electron beam with the gold target filtered by the beryllium layer. Both Bremsstrahlung x-rays and characteristic line radiations are emitted from the tip of the tube with an isotropic photon emis-

sion. Depending on the clinical application, various applicator types can be attached to the XRS. Spherical applicators made of polyetherimide material (15–50 mm) are used to deliver radiation to the tumor bed [6–9].

### *GATE Monte-Carlo simulation*

The GATE MCS platform [4] was used to model the XRS and to perform associated dosimetry calculations on phantom and patient datasets. This modeling was separated into two parts. The first part concerns the XRS, which is invariable and patient independent, while the second part included the patient/phantom description and certain variable device parts such as the applicator. The flexibility of GATE and the versatility of its macro interface allow the modeling of physical and geometrical characteristics of the different components of the XRS, the applicators and the phantom according to manufacturer specifications.

Generated particles were collected in a virtual space called phase space (PHS). The PHS is more precisely developed to store the particles coming from the patient independent part, and is stored to a volume of user defined size, including the characteristics of each particle (type, direction, energy...). In this simulation, the PHS was defined as a hemispherical volume with a diameter of 3.2 mm and a thickness of 1 mm in the z direction. It was used to simulate the fluency of derived photons and their interactions with the media dependent part (applicator/patient). The PHS file was recorded at the surface of the hemispherical bare probe. Once the particle goes outside this surface it is saved in the PHS file without any further scattering. To focus on the Bremsstrahlung interactions we used the standard energy physics list within GATE which takes into account photon paths from 1 keV to 1 TeV. One billion particles were stored in the PHS file (total file volume of 15.2 GB stored as a ROOT file). All MCSs were performed with 109 particles and carried out on a cluster of 200 CPUs (2.74 GHz, 2 GB/CPU).

An energy/dose scoring tool associated with statistical uncertainty implemented within GATE was used to calculate the energy deposition and absorbed dose in a matrix of dose voxels. The voxel size was  $1.75 \times 1.75 \times 1.75$  mm<sup>3</sup>, which corresponds to the 5.3 mm<sup>3</sup> sensitive volume of the ionization chamber (IC) used for the comparative measurements. The dose uncertainty obtained from GATE simulations was evaluated according to several criteria. The actor calculates the deposited energy in MeV (Edep), the absorbed dose D in Gy, the number of hits (a hit occurs each time a primary or secondary particle makes a step in a volume, with or without energy



deposition), and the local statistical uncertainty according to [10]. The squared sum of Edep and D are also provided and can be used to compute the statistical uncertainty when the simulation is split into multiple runs to improve computational efficiency. Equation 1 defines the statistical uncertainty  $\varepsilon_k$  at pixel  $k$ , with  $N$  being the number of primary events,  $d_{kt}$  the deposited energy in pixel  $k$  at primary event  $t$  [10–12].  $S_k$  is an estimate of the standard error of the mean dose in voxel  $k$ .

$$D_k = \sum_t^N d_{kt}$$

$$S_k = \sqrt{\frac{1}{N-1} \left( \frac{\sum_t^n d_{kt}^2}{N} \right) - \left( \frac{\sum_t^n d_{kt}}{N} \right)^2} \quad (1)$$

$$\varepsilon_k = 100 \times \frac{S_k}{D_k}$$

GATE provides both the absolute dose value and the statistical uncertainty associated to this dose.

Using CT images as simulation input requires a method to relate the Hounsfield unit (HU) values of the input image to Geant4 materials. The stoichiometric calibration implemented in GATE is described by Schneider et al. [13] and recommended by the AAPM TG-186 [14]. The procedure is based on a user-defined mass density tolerance parameter and two calibration files describing the piecewise linear correspondence between CT numbers and mass density, and a list of material compositions. The tolerance parameter can be used to tune the number of materials depending on the accuracy required in the simulation. The list of materials generated and the correspondence between materials and HU values are stored and can be used for converting any CT image into materials.

#### Validation on water

Independent verification of depth dose curves (DDCs) and isotropy was carried out using a water phantom specifically designed for low energy XRS. Measurements were carried out at different source-detector distances by integrating the resulting signal for 60 seconds at each position. DDCs were measured using a 5.3 mm<sup>3</sup> soft x-ray PTW IC (34013 type), which is a plane parallel chamber with thin membranes designed for low energy x-rays. The chamber was connected to an UNIDOS™ electrometer measuring electrical charges which are corrected and converted into dose rate. This IC used in this study is the same as the one used by Rivard et al., on the Xoft Axxent XRS [15]. Isotropy was checked by measuring the charge at eight successive incre-

mental (45°) rotations of the radiator with the IC inserted beside the probe (Supplementary Figure 2, to be found online at <http://informahealthcare.com/doi/abs/10.3109/0284186X.2015.1016623>). The deviation of the eight values from their average allowed the calculation of the isotropy that should have a maximum variation of 15% in all directions according to manufacturer specifications.

Using GATE, DDCs and isotropy were simulated under the same conditions as in the experimental set-up and with the same volume as the IC for each slice under the source along the z-axis. For isotropy the angle 0° is chosen arbitrary on GATE and the source is subsequently turning on itself around the z axis by steps of 45°. The maximum difference between measured and simulated results should be < 5% (considering the tolerance of radiotherapy treatment planning systems in general). In this study the maximum difference obtained was 2.04%.

#### Clinical study

In order to evaluate the GATE Intrabeam™ modeling within a clinical context, x-ray CT images of a patient were acquired during IORT after insertion of the applicator into the excision cavity following lumpectomy. Different steps were necessary to specify these dosimetric measurements according to the specifications of measurement methodology from the APPM Update of the AAPM TG43 [16]. Images were acquired with a Somatom Sensation Open CT scanner (SIEMENS Medical, Erlangen, Germany) at 120 kVp with a slice thickness of 2 mm. To ensure sterilization during the transit, a sterilized support to maintain the applicator and a sterile cover close to the surgical site were used.

In vivo dosimetry measurements were performed using seven TLD packs placed equidistant around the incision to quantify the skin dose. Results were compared with GATE by measuring the dose at the same position.

The calibration of TLDs (LiF: Mg, 3 × 3 × 1 mm<sup>3</sup>, TLD700) was done using the proposed methodology by Eaton et al. and the suggestions of Kron et al. [17,18]. Typically, four TLDs were used per packet in order to exclude outliers and reduce the standard deviation of measurements. As TLD measurements provide a relative dosimetry, the dose is determined by comparing the response of a given TLD to the response of a reference dosimeter, which has been irradiated at a point where the dose is precisely known. The unknown dose received by the patient TLDs was calculated using the individual calibration factor of the TLD rods relating their reading to the IC reading which received a known dose. In this study, the reference dosimeter is the IC described in

the section ‘Validation on water’. A scaling factor of 1.004 provided by PTW in order to correct for the PMMA thickness of the inserts was used. The TLDs were handled with tweezers and read out in a manual TLD reader (Harshaw 3500, Thermo Scientific™, OH, USA) with a preheat temperature of 140°C and with a 300°C acquisition temperature. All dosimeters were annealed with a dedicated annealing oven (FIMEL, France) at 400°C for one hour and cooled down to 100°C during two hours. The provided simulated dose values are doses to tissue. A relative conversion factor was obtained by comparing TLD responses in water and TLD responses in real tissue. This was achieved by using TLDs inserted under different thicknesses of pig tissue and comparing the response with TLDs under the same depths of water. A geometrical correction was performed by systematically taking into account the thickness of the TLDs.

#### Absolute dose calibration

As a second validation step an absolute dose comparison was carried out using a different approach. First, a calibration step was necessary due to the low fluency of photons which imply very low doses with GATE. This calibration of the simulated XRS in terms of absolute dose per irradiation time was performed using two distinct steps [19]:

1. Conventional calibration of the beam, by measuring the dose in water  $D_w$  per irradiation time ( $t_{\downarrow trr}$ );  $D_{\downarrow w}/t_{\downarrow trr}$  (Gy/min) at different depths from the surface of the bare probe. Reference measurements were defined as DDCs measured with the IC described above (section ‘Validation study’).
2. GATE simulations of the exact same set-up and associated conditions, using particles from the PHS, in order to obtain  $D_{Gate}$  per simulated particle at the same water depths:  $D_{Gate}/N$ , where  $N$  is the number of simulated particles.

A calibration factor  $F_Q$  depending on the beam quality (50 kV x-ray photons) and the number of particles per irradiation time was subsequently derived using:

$$F_Q = \frac{D_{w/trr}}{D_{Gate/N}} \quad (2)$$

where,  $t_{trr}$  is the irradiation time during an IORT procedure. Following this calibration step and as a second stage of the absolute dose comparison process, the beam simulation in water was replaced by the clinical treatment simulation using patient CT

images. The beam obtained from the PHS was adjusted given the appropriate applicator size. The beam generated during MCSs yields a dose  $D_{Gate}^P$  at the point P corresponding to the skin position where each TLD was placed during treatment. The absolute dose at P,  $D_p$  (in Gy), is given by:

$$D_p = t_{trr} \times F_Q \times D_{Gate}^P \quad (3)$$

A calibration factor of  $F_Q = 1.063 \cdot 10^{14}$  N/min was obtained for the 40 mm applicator diameter.

#### Dosimetric uncertainties analysis

In order to determine the accuracy of the measurements and calculations, uncertainties analysis was performed according to the AAPM TG-138 report and GEC-ESTRO brachytherapy dosimetry uncertainty recommendations [20]. Uncertainties analyses include all dosimetric properties of clinical XRS and all factors that could possibly influence the result of a measurement or calculations. Generic uncertainty assessments have been performed for experimental measurements using IC and TLDs, and MC methods for radiation transport calculations. The uncertainty in TLD measurements has several components, some of which correspond to type A including reproducibility and calibration and some of type B, such as the lack of backscatter and their position on the skin. These uncertainties have been assessed as discussed by the International Atomic Energy Agency in the calibration documentation [20,21]. However, Monte Carlo uncertainties (statistical uncertainties, XRS and Applicator geometry and motions, source energy spectrum) have been calculated using the recommendations of the AAPM TG-43 update and the TG 138 [16,20]. Type A and B components correspond to statistical and systematic uncertainties, respectively. All values provided are for  $1\sigma$ .

#### Results

Figure 1 shows the Monte Carlo simulation on the patient CT volume with the dose deposition and compares the difference in the use of the shielding or not. Figure 2a shows the energy spectrum output of the bare needle in air obtained from the PHS. The mean energy was  $20.64 \pm 10.48$  keV while a peak at the energy of 10 keV was observed which corresponds to the dominating Au-L $\beta$ -fluorescence. Figure 2b shows the energy spectrum for the 40 mm-applicator calculated in GATE using the PHS produced from the bare needle. In this configuration when the applicator is used, the characteristic Au-L-lines are almost suppressed. The shape of the spectrum is globally independent of applicator size. The main difference is the Au-L-lines which are

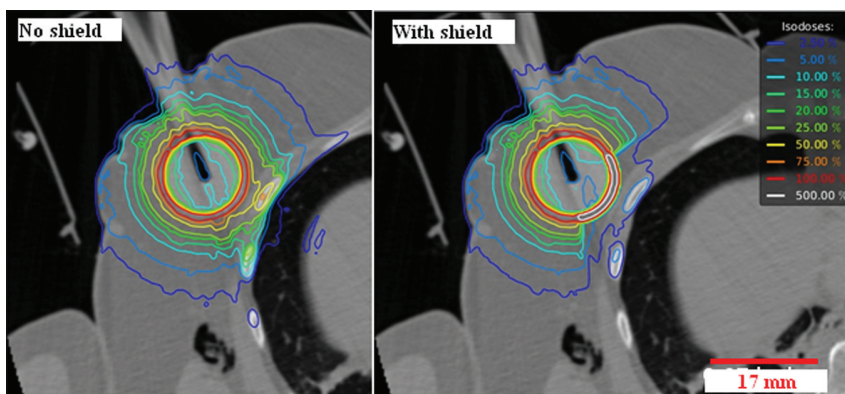


Figure 1. Comparison of the dose distribution of an IORT treatment, respectively without shielding on the left and with shielding placed on the pectoral muscle on the right.

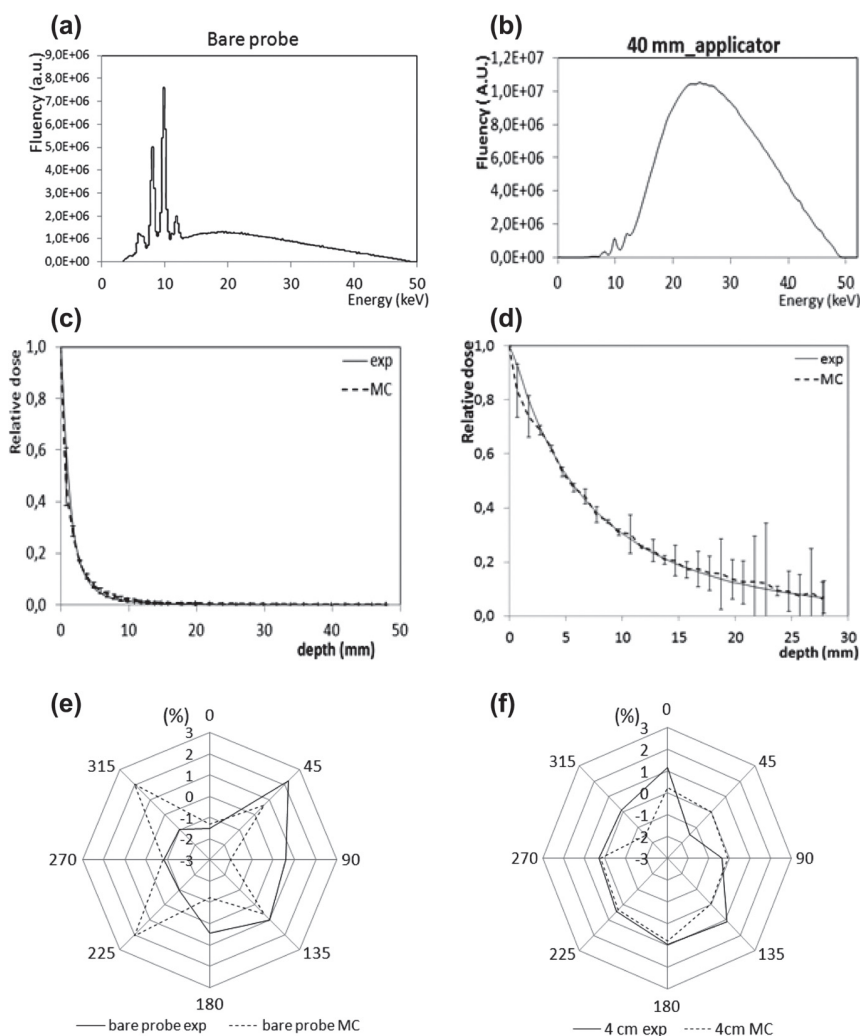


Figure 2. Validation on water: output energy spectrum computed in air (a) for the bare needle source, and (b) for the 40 mm-applicator. Depth dose curves (DDC) for the bare needle(c) and the 40 mm-applicator (d). Relative dose is presented as a function of the depth in water. Experimental measurements have been done using a 5.3 mm<sup>3</sup> soft x-ray PTW IC (34013 type). The error bars represent the relative deviation between calculated and measurement value. Polar plot showing the angular distribution of the dose for the bare probe (e) and the 40 mm-applicator (f). A comparison between MC (dotted lines) and experimental measurements (full lines) is shown.

Acta Oncol Downloaded from informahealthcare.com by 195.83.246.106 on 03/27/15  
For personal use only.

increasingly attenuated with larger applicator sizes. The mean energies obtained were  $26.54 \pm 8.90$  keV,  $26.36 \pm 8.90$  keV,  $27.02 \pm 8.80$  keV,  $27.12 \pm 8.80$  keV, and  $28 \pm 8.80$  keV for applicator diameters increasing in steps of 5 mm from 30 mm to 50 mm. The mean energy for the 30 mm diameter applicator is higher than the 35 mm one due to an additional aluminum filter inserted in order to attenuate the beam.

Measured and MC computed normalized DDC for the 50 kV beam without and with the 40 mm-applicator (Figure 2c and d) show a maximum difference of about 6% for the 40 mm applicator and 2.3% for the bare needle, with a maximum GATE uncertainty of, respectively, 0.2% and 0.04% for the applicator and bare needle (Table 1). The polar plot shows the angular distribution of the dose for the bare probe (e) and the 40 mm-applicator (f), considering both the MCS and experimental measurements. The mean measurement uncertainties with GATE were  $0.25\% \pm 0.14\%$  and  $0.080\% \pm 0.001\%$  for the bare probe and the applicator, respectively. For the bare needle, the maximum deviation from the mean value was 2.04% at  $225^\circ$  and  $315^\circ$  for the GATE simulations, compared to the measured maximum deviation of -0.97%. However, the minimum deviation was -0.61% at  $135^\circ$  for GATE versus -1% for the measurements. For the 40 mm-applicator, the deviation from the mean value was in the range of -1.53%–0.11% and -1.45%–0.14% for the simulations and measurements, respectively. Our results confirm the manufacturer specifications (<15%). Concerning patient study, the comparison has been performed between clinically measured doses using the TLDs and the corresponding MCS results using the patient CT images (Table II). The mean absolute deviation was  $0.06 \pm 0.09$  Gy with a maximum of 0.29 Gy and a minimum of 0 Gy for a distance of 50 mm and 35 mm from the center of the applicator, respectively. The mean statistical uncertainties with GATE simulations were less than 0.8%.

The overall required times for dose calculations in water without and with an applicator was 1.5 hours and 1.75 hours, respectively. For the patient-specific CT-based dosimetry study the computation time was four hours and 46 hours with and without the use of the PHS, respectively, on a single CPU (INTEL Core i7 4770, frequency of 3.4 GHz).

Supplementary Table I (available online at <http://www.informahealthcare.com>) provides a summary of the uncertainties estimation for the current study. Monte Carlo uncertainties were estimated to be approximately 3.4%. This result is in accordance with Rivard et al. who found 2.5% and 5% for the Monte Carlo uncertainties of different radius size for an I-125 seed. Dolan et al. found a MC uncertainty

Table I. GATE uncertainties and relative deviation between measured and simulated results.

Uncertainties	Gate uncertainties (%)		Relative deviation (%)	
	Mean	SD	Mean	SD
Bare needle	0.04	0.03	3.0	4.4
applicator 30 mm	0.22	0.09	5.9	5.5
applicator 35 mm	0.28	0.05	5.6	5.1
applicator 40 mm	0.21	0.10	6.0	5.4
applicator 45 mm	0.22	0.09	5.0	6.1
applicator 50 mm	0.22	0.09	5.9	6.5

of 1.76% for the I-125 seed dosimetry showing good agreement with our value if considering the methodology [16,22]. Based on the evaluation of uncertainties related to TLD measurements in this study the total quoted uncertainty was 16.6%, including lack of backscatter (5%), energy response (8%) and variation in the TLD position on the skin (10%), showing good agreement with previously reported values. The minimum uncertainty according to AAPM TG 61 in the determination of the absorbed dose in water,  $D_w(z)$  (Gy) at a specific location  $z$  was  $\pm 5.3\%$ .

## Discussion

Current use of IORT is based on the prescription and assumed delivery of a fixed dose without considering the potential differences associated with patient-specific anatomy and corresponding tissue characteristics. However, it would be of interest to be able to determine the three-dimensional (3D) dose distribution for each individual patient in order to personalize treatment planning and/or eventually validate the use of a standard prescribed dose. The aim of this study was therefore the development and validation of a MC dosimetry platform for IORT applications based on the use of the Intrabeam™ system. This development was based on the use of the GATE platform. Accurate physical settings were

Table II. TLD measurements and corresponding doses from the patient simulation study using the 40 mm diameter applicator.

Distance skin - applicator (mm)	Dose (Gy)		Relative deviation (%)	Gate uncertainties (%)
	MC	TLD	(%)	(%)
17	0.73	0.64	0.14	0.41
35	1.51	1.51	0.00	0.64
50	0.58	0.90	0.35	0.91
40	0.29	0.29	0.00	0.95
48	0.23	0.23	0.00	0.84
30	0.93	0.87	0.06	0.73
37	0.52	0.49	0.06	0.83



made possible by the development of advanced energy/dose scoring tools and the definition of a PHS allowing a reduction in the overall simulation computational cost.

More specifically, the relative dose distribution measured for the bare source needle indicates a good agreement between measurements and the MCS results. The addition of the applicators obviously results in an alteration of the dose distribution when compared with the bare needle due to their construction characteristics. This change was accurately reproduced by the developed GATE model as shown on the energy spectrum obtained at the surface of the applicator. Finally, although differences between real measured data and GATE measurements were very small close to the tip of the source, they increased with depth because of the very small measured dose magnitudes and the small number of simulated events at those larger distances compared with photon fluency in realistic treatment. Concerning the angular distribution of the XRS emissions around the probe, the simulation results revealed a good conformity with the experimental measurements, confirming the specification of 15% maximal difference provided by the manufacturer. The distribution isotropy was confirmed based on the different circular and concentric isodoses obtained for the bare needle and the 40 mm diameter applicator.

A CT acquisition of a patient was carried out with the applicator in place to obtain the information on source position and the distance between the applicator surface and the skin with sufficient precision for a patient-specific dosimetry validation study. These CT images were used in combination with the GATE XRS model to produce patient-specific 3D dose distribution maps. The results demonstrate a good agreement between TLD measurements and GATE dose results at the same patient skin positions. The patient skin recorded doses ranging from 0.2 Gy to 1.5 Gy are below the threshold for severe skin toxicity ( $< 6$  Gy) and reflect the different tissue thicknesses overlying the applicator. Our single patient dose values are within the range of those recorded by Fogg et al. with a reported maximum average dose of  $2.93 \pm 1.46$  Gy and Eaton et al. [18] with a mean measured skin dose of  $2.9 \pm 1.6$  Gy.

Another significant observation is the doses to normal structures, such as the rib bones, heart and lungs, depending on the depth of the incision and the treated breast side. In order to reduce the dose to such critical structures, the surgeon uses a spherical shielding made of tungsten-impregnated silicone (lead equivalent 0.05 mm) which reduces the doses from 25% to 60% as shown in Figure 1.

To achieve personalized intraoperative dosimetry, several elements are needed including a Monte Carlo

dosimetry platform, patient-specific images and the applicator position. Associating these elements within a “treatment planning system” would allow an inverse dosimetry for patient-specific treatment. In this study we have performed MC calculations of the dose using intraoperative CT imaging, which remains complicated and time consuming to envisage for every patient. For this reason an alternative scenario can be considered based on pre-operative CT images similar to those used for treatment planning in EBRT. These pre-operative CT images can be subsequently used in conjunction with intraoperative x-ray C-arm imaging device to guide the positioning of the applicator in the tumor cavity based on the pre-operative dose planning using the acquired CT images. We are currently studying the clinical feasibility of such an approach using pre-operative CT imaging in particular for breast and spinal metastases applications. Finally, in terms of computational time the current performance of the GATE MCS platform is not compatible with a potential clinical use, even if one considers the use of pre-operative CT imaging and subsequent treatment planning. However, the necessary computational times are expected to be dramatically reduced in the future by using hybrid computing architectures, such as graphical card units (GPUs), including recently proposed implementations for Geant4 based MCSs both in imaging and radiotherapy applications [23–25].

In this study the accuracy of the XRS model was validated, showing good agreement between experimental measurements and simulated results considering a simple water phantom as well as on a single patient study using intraoperative patient CT images that allow accounting for the presence of heterogeneous tissues in the irradiation field. A future study will concentrate on an extended clinical validation of MC-based intraoperative treatment planning and guidance based on pre-operative CT images. Such a future IORT treatment framework based on the proposed dosimetry platform should ensure patient-specific dose optimization and delivery based on accounting for patient-specific tissue heterogeneities and a better precision in applicator placement during IORT treatment.

### Acknowledgments

The authors would like to thank the Carl Zeiss Surgical Group, for helpful information on the applicators' characteristics used in the Intrabeam™ system. This work was funded by a grant (DOSEVAL) from the National Institute of Cancer (INCa) in France. The authors report no conflicts of interest. The authors alone are responsible for the content and writing of the paper.

**Declaration of interest:** The authors report no conflicts of interest. The authors alone are responsible for the content and writing of the paper.

## References

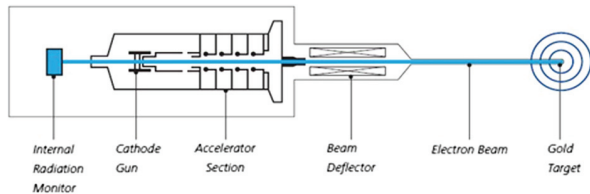
- [1] Hannoun-Lévi JM, Marsiglia H, Garbay JR, Gérard JP. Irradiation partielle du sein: Pourquoi, comment ? *Cancer/ Radiothérapie* 2003;7:200–9.
- [2] Vaidya JS, Tobias JS, Baum M, Wenz F, Kraus-Tiefenbacher U, D'Souza D, et al. TARGeted Intraoperative radiotherapy (TARGIT): An innovative approach to partial-breast irradiation. *Semin Radiat Oncol* 2005;15:84–91.
- [3] Nuis. directive 97/43 euratom du conseil. 1997.
- [4] Jan S, Benoit D, Becheva E, Carlier T, Cassol F, Descourt P, et al. GATE V6: A major enhancement of the GATE simulation platform enabling modelling of CT and radiotherapy. *Phys Med Biol* 2011;56:881–901.
- [5] Clausen S, Schneider F, Jahnke L, Fleckenstein J, Hesser J, Glatting G, et al. A Monte Carlo based source model for dose calculation of endovaginal TARGIT brachytherapy with INTRABEAM and a cylindrical applicator. *Z Med Phys* 2012;22:197–204.
- [6] Yanch JC, Harte KJ. Monte Carlo simulation of a miniature, radiosurgery x-ray tube using the ITS 3.0 coupled electron-photon transport code. *Med Phys* 1996;23:1551–8.
- [7] Beatty J, Biggs PJ, Gall K, Okunieff P, Pardo FS, Harte KJ, et al. A new miniature X-ray device for interstitial radiosurgery: Dosimetry. *Med Phys* 1996;23:53–62.
- [8] Dinsmore M, Harte KJ, Sliski AP, Smith DO, Nomikos PM, Dalterio MJ, et al. A new miniature x-ray source for interstitial radiosurgery: Device description. 1996.
- [9] Ebert MA, Carruthers B. Dosimetric characteristics of a low-kV intra-operative x-ray source: Implications for use in a clinical trial for treatment of low-risk breast cancer. *Med Phys* 2003;30:2424.
- [10] Chetty IJ, Rosu M, Kessler ML, Fraass BA, Haken RKT, Kong FM, et al. Reporting and analyzing statistical uncertainties in Monte Carlo-based treatment planning. *Int J Radiat Oncol Biol Phys* 2006;65:11.
- [11] Chetty I, Curran B, Cygler JE, DeMarco JJ, Ezzell G, Faddegon BA, et al. Report of the AAPM Task Group No. 105: Issues associated with clinical implementation of Monte Carlo-based photon and electron external beam treatment planning. *Med Phys* 2007;34:36.
- [12] Sarrut D, Bardies M, Bousson N, Freud N, Jan S, Letang JM, et al. A review of the use and potential of the GATE Monte Carlo simulation code for radiation therapy and dosimetry applications. *Med Phys* 2014;41:064301.
- [13] Schneider W, Bortfeld T, Sclegel W. Correlation between CT numbers and tissue parameters needed for Monte Carlo simulations of clinical dose distributions. *Phys Med Biol* 2000;45:459–78.
- [14] Beaulieu L, Carlsson Tedgren A, Carrier JF, Davis SD, Mourtada F, Rivard MJ, et al. Report of the Task Group 186 on model-based dose calculation methods in brachytherapy beyond the TG-43 formalism: Current status and recommendations for clinical implementation. *Med Phys* 2012;39:6208–36.
- [15] Rivard MJ, Davis SD, DeWerd LA, Rusch TW, Axelrod S. Calculated and measured brachytherapy dosimetry parameters in water for the Xofigo X-Ray Source: An electronic brachytherapy source. *Med Phys* 2006;33:4020.
- [16] Rivard MJ, Coursey BM, DeWerd LA, Hanson WF, Saiful Huq M, Ibbott GS, et al. Update of AAPM Task Group No. 43 Report: A revised AAPM protocol for brachytherapy dose calculations. *Med Phys* 2004;31:633.
- [17] Kron T, DeWerd L, Mobit P, Muniz J, Pradhham A, Toivonen M, et al. A checklist for reporting of thermoluminescence dosimetry (TLD) measurements. *Phys Med Biol* 1999;44(L15–L17).
- [18] Eaton DJ, Best B, Brew-Graves C, Duck S, Ghaus T, Gonzalez R, et al. In vivo dosimetry for single-fraction targeted intraoperative radiotherapy (TARGIT) for breast cancer. *Int J Radiat Oncol Biol Phys* 2012;82:e819–24. [19]
- [19] Nahum A. Special features of Monte Carlo based treatment planning. *The handbook of radiotherapy physics: Theory and practice*. Ch 28. London: Taylor and Francis; 2007. pp. 615–7.
- [20] DeWerd LA, Ibbott GS, Meigooni AS, Mitch MG, Rivard MJ, Stump KE, et al. A dosimetric uncertainty analysis for photon-emitting brachytherapy sources: Report of AAPM Task Group No. 138 and GEC-ESTRO. *Med Phys* 2011;38:782.
- [21] International Atomic Energy Agency. Absorbed dose determination in external beam radiotherapy based on absorbed dose-to-water standards: An international code practice. Technical Report Series n°398, IAEA: Vienna; 2000.
- [22] Dolan J, Li Z, Williamson JF. Monte Carlo and experimental dosimetry of an [sup 125]I brachytherapy seed. *Med Phys* 2006;33:4675.
- [23] Bert J, Perez-Ponce H, El Bitar Z, Jan S, Boursier Y, Vintache D, et al. Geant4-based Monte Carlo simulations on GPU for medical applications. *Phys Med Biol* 2013;58:5593–611.
- [24] Jia X, Gu X, Sempau J, Choi D, Majumdar A, Jiang SB. Development of a GPU-based Monte Carlo dose calculation code for coupled electron-photon transport. *Phys Med Biol* 2010;55:3077–86.
- [25] Hissoiny S, Ozell B, Bouchard H, Després P. GPUMCD: A new GPU-oriented Monte Carlo dose calculation platform. *Phys Med Biol* 2011;38:754–64.

## Supplementary material available online

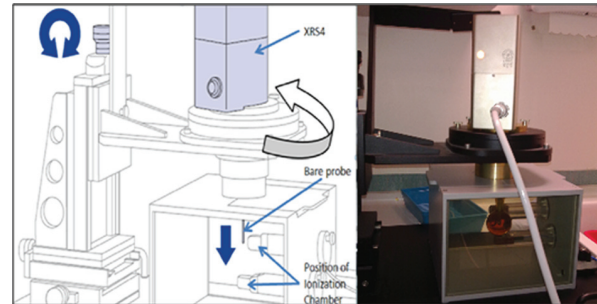
Supplementary Figure 1–2, Supplementary Table I to be found online at <http://informahealthcare.com/doi/abs/10.3109/0284186X.2015.1016623>.



Supplementary material for Bouzid D. et al. Monte-Carlo dosimetry for intraoperative radiotherapy using a low energy x-ray source, Acta Oncologica, 2015, doi: 10.3109/0284186X.2015.1016623



Supplementary Figure 1. X-ray source (courtesy of Zeiss-Meditec, Oberkochen Germany): consisting of a 100 mm long, 3.2 mm diameter tube that is attached to a larger housing, containing an electron gun and associated electronics. The tube is made primarily of molybdenum, except for the final 20 mm made of beryllium acting as a transparent x-ray window. The blue concentric rings represent the isotropic distribution of the dose. The probe is coated with a thin layer of chromium nitride (1  $\mu\text{m}$ ) in order to render the device biocompatible.



Supplementary Figure 2. Water phantom used for the DDC and isotropy measurements (Courtesy of Zeiss-Meditec, Oberkochen, Germany). This phantom consists of a sealed water tank ( $216 \times 217 \times 166 \text{ mm}^3$ ). It allows the accurate positioning of the source tip (or applicator) above or next to ionization chambers that can be inserted in two measuring compartments made of PMMA located on two orthogonal directions (X-Y and Z planes).

Supplementary Table I. Estimation of measurements and calculations uncertainties for the study. Generic uncertainty assessments have been performed for experimental measurements using IC and TLDS, and MC methods for radiation transport calculations. Type A and B correspond to statistical and systematic uncertainties, respectively. All values provide are for  $1\sigma$ .

Category		Typical level (%)	
Ionization chamber (manufacturer's data)			
Calibration factor $N_s$ of the water tank's ionization chamber Unidos electrometer		2.0	
Uncertainty caused by the design tolerance of the IC (20 mm depth in water)		2.0	
Difference in beam quality of the XRS (IC + XRS)		0.6	
Conversion factor for IC into absorbed dose to water		1.5	
Waterproof holder of the IC		0.5	
General errors caused by measurements in water		2.0	
Minimum uncertainty in the determination of absorbed dose to water at 20 mm depth in water according to AAPM TG 61		4.2	
Experimental uncertainties	The determination of water energy dose at different water depth	3.0	
	Minimum uncertainty in the determination of absorbed dose to water of a dose depth curve in water at a specific location z according to AAPM TG 61	5.3	
TLD		Type A	Type B
Repeated measurements		1.5	
Calibration			3.0
Source strength			2.0
Lack of backscatter		5.0	
TLD position on skin			10.0
Quadrature sum		1.6	13.2
Total TLD uncertainties			13.3
MC Statistics		0.5	
MC uncertainties	XRS / Applicator geometry		3.2
	Source energy spectrum		1.0
	Quadrature sum	0.5	3.4
	Total MC uncertainties	3.4	

## B.7 Modélisation des systèmes en radiothérapie externe

444

IEEE TRANSACTIONS ON RADIATION AND PLASMA MEDICAL SCIENCES, VOL. 1, NO. 5, SEPTEMBER 2017

# GATE Monte-Carlo Simulation of an MV-CBCT Flat Panel for Synergistic Imaging and Dosimetric Applications in Radiotherapy

Saadia Benhalouche, Julien Bert, Nicolas Bousson, Awen Autret, Olivier Pradier, and Dimitris Visvikis

**Abstract**—The objective of this paper was to simulate mega-voltage cone beam computed tomography (MV-CBCT) for both imaging and dosimetric purposes, using a portal imaging device modeled on a dedicated Monte-Carlo platform. An X-ray flat panel detector mounted on a Siemens accelerator was modeled with Geant4 application for emission tomography (GATE) according to its geometrical and physical characteristics. This model was validated by simulating 2-D MV images of both a patient and an anthropomorphic phantom and then by reconstructing MV-CBCT volumes. Dose deposited during MV-CBCT procedure was simulated and compared to measurements obtained with dedicated detectors. Portal imaging was also used for simulating inverse reconstruction of dose distributions. The simulated MV-CBCT volumes showed a good agreement with the ground truth which was the computed tomography scans of the patient and the phantom. For dose reconstruction, comparison between GATE calculation and measurements from a matrix of ionization chambers gave between 92% and 96.1% of dose points passing the 3%/3 mm gamma test, depending on the field complexity. As a conclusion, the ability of GATE for concomitant imaging acquisition and dose estimation was demonstrated. This new virtual platform is able to reconstruct imaged volumes and to estimate doses deposited by simple and complex irradiation fields.

**Index Terms**—Monte Carlo (MC) dosimetry, simulations for imaging and therapy, therapy related software developments.

### I. INTRODUCTION

CONTINUOUS improvement in conformal radiotherapy techniques enables to build dose gradients around targets which in turn allow the delivery of higher doses to a tumor volume while sparing surrounding normal tissue and potential organs at risk [1]. Recent radiotherapy techniques involve complex field shaping using multileaf collimators (MLCs) and are increasingly used to treat tumors that in the past might have been considered too close to vital organs for radiation therapy [2].

Manuscript received March 29, 2017; revised May 10, 2017; accepted June 6, 2017. Date of publication June 29, 2017; date of current version August 31, 2017. This work was supported by the French Ministry of Research. (Corresponding author: Nicolas Bousson.)

S. Benhalouche and A. Autret are with INSERM UMR 1101 LaTIM, 29609 Brest, France.

J. Bert, N. Bousson, O. Pradier, and D. Visvikis are with INSERM UMR 1101 LaTIM, 29609 Brest, France, and also with CHRU Brest, 29609 Brest, France (e-mail: nicolas.bousson@chu-brest.fr).

Color versions of one or more of the figures in this paper are available online at <http://ieeexplore.ieee.org>.

Digital Object Identifier 10.1109/TRPMS.2017.2718545

To ensure the proper delivery of the dose prescribed during treatment plan, and to know accurately and precisely the locations of the planning target volume and critical organs, it is essential to reposition the patient before each treatment session. The most common method for patient position verification during fractionated radiation therapy is the use of electronic portal imaging devices (EPIDs). However, since 3-D X-ray computed tomography (CT) provides better spatial information than 2-D EPID images, it is a more desirable method for imaging patients in the treatment position [3], [4].

There are few approaches available to CT imaging in the treatment position. One such approach combines both capabilities of a linear accelerator and a diagnostic CT scanner [5] installed in the same room and using the same gantry. Another approach consists in the use of the megavoltage X-ray source of the linear accelerator and the EPID to acquire projections at different angles around the patient and to reconstruct a 3-D dataset from these projections. This principle is often referred to as megavoltage cone-beam CT (MV-CBCT).

Several Monte-Carlo (MC) codes were used previously for simulations in MV-CBCT imaging. For example, MCNP5 was used to model amorphous silicon (aSi) EPID [2] and to demonstrate the dosimetric potential of such modeling. Monajemi *et al.* [6] used two different codes (EGSnrc and DETECT2000) for the modeling and evaluation of new scintillators as CBCT detectors. However, as stated in a recent review [7], most MC approaches to CBCT modeling intended to simulate kV images only [8]–[10]. For this reason, we will specifically focus on the simulation of MV-CBCT images using the Geant4 application for emission tomography (GATE) platform [11]. This MC simulation tool was initially developed for imaging purposes [12] and has been recently extended to radiotherapy applications [13].

Aside from this simulation point of view, recent papers concerning quality control in radiotherapy addressed the problem of patient-specific quality assurance. Such pretreatment verifications are mandatory for complex intensity modulated radiation therapy (IMRT) but remain very time consuming since each treatment of each patient must be verified. For this reason, automated software-based solutions have been proposed as an efficient alternative to hardware-based ones [14]. In the same perspective a wider use of the EPID has been proposed in [15] for treatment quality control. EPID-based *in vivo* dosimetry is indeed widely investigated at the present moment, either clinically [16] or theoretically [17], [18].

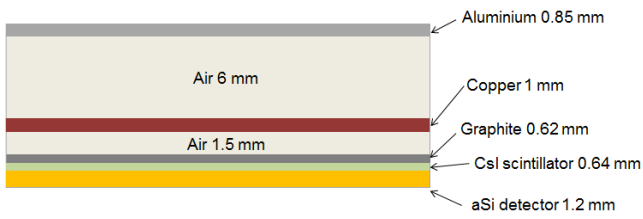


Fig. 1. Schematic of the AG9 EPID model simulated with GATE for MV-CBCT imaging and dose calculation.

Further, relatively little information exists regarding the availability of MC platforms able to model irradiation parts and detector panels for simulating complex treatments and imaging-based applications.

In this context, the purpose of this paper is to model a dual irradiation head and portal imaging setup within a unique MC platform, and to show applications in terms of imaging and delivered dose evaluation. This paper is based on a previous work [19] in which we simulated the whole irradiation head of a Oncor Impression linear accelerator (Siemens, Erlangen, Germany) equipped with a 160 multileaves collimator. This modeling and simulations were done using the GATE platform and a comprehensive dosimetric study was performed to validate the model. A step-and-shoot IMRT plan was also simulated and validated.

This paper is divided into three parts and is organized as follows. First, an accurate modeling of the EPID system, as described by the manufacturer specifications, is added to the initial GATE linac model presented in our previous work. Second, a simulation of MV-CBCT image acquisition and reconstruction is presented. As a last part, the modeled irradiation head/EPID detector couple is used to retrieve the dose delivered to a patient during treatment.

The global objective is to build a synergistic platform modeling the whole linac system and allowing simulating all clinical functionalities. This platform should serve as a basis for a wide range of applications, with the hope that it could be seen as a useful tool for estimating delivered dose.

## II. MATERIAL AND METHODS

### A. Flat Panel Geometry

The X-ray flat panel detector that is mounted on the Oncor accelerator is an AG9 model from Perkin Elmer Optoelectronics (Perkin Elmer Waltham, MA, USA). The system acts like a digital X-ray camera covering a  $41 \times 41 \text{ cm}^2$  area sampled across  $1024 \times 1024$  pixels in total. There is a 0.41 lp/mm spatial resolution, and the system is mounted on a retractable support which deploys in less than 10 s with a positional reproducibility of 1 mm in any direction [1], [20]. The retractable support made of mechanical parts was not included in the present GATE modeling. On the contrary, each component of the flat panel was accurately described in GATE according to available technical data provided by the manufacturer (Fig. 1). The panel consists of a series of layers made of different materials: a 0.85 mm

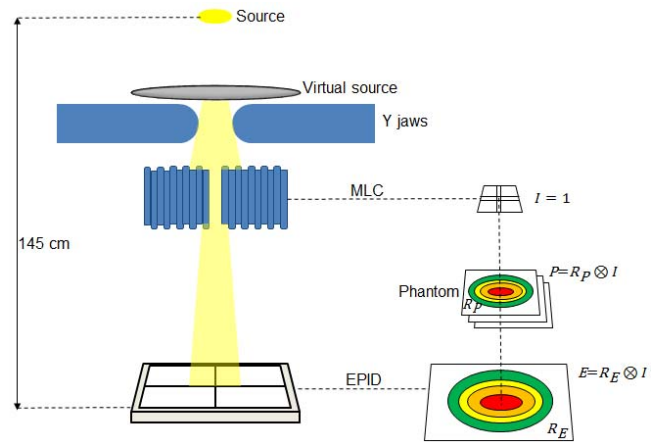


Fig. 2. Digital architecture for simulations. Left: GATE simulation setup. Right: scheme for dose deposition from a beamlet  $I$  at the MLC level, inside a given phantom and inside the EPID plane.

aluminum protection plate, a 6 mm air gap, a 1 mm copper plate, a 1.5 mm air gap, a 0.62 mm graphite plate, a 0.64 mm Kodak Lanex Fine scintillator plate made with cesium iodide (CsI), and a 1.2 mm detectors (pixel elements) made with aSi. Size, geometry and physical characteristics of each material were carefully entered into GATE using a user interface based on macro functions. Once modeled the panel can be irradiated using the high energy photon beam already simulated in GATE as fully described in our previous work [19].

This poly energetic photon beam is generated from a 6 MeV electron beam hitting a tungsten target, and will be referred to from here onward as 6 MV photon beam.

During further MC simulation, the incident photon beam simulated within GATE interacts with the build-up copper plate and the CsI scintillators to convert high energy photons to visible light. Subsequently optical photons will deposit energy within the aSi (only absorption was considered here). The final single projection is recovered by digitizing deposited energy map according to pixels size and converting deposited energy information into luminance pixel value.

### B. Simulation Architecture

As stated above, the Oncor head was simulated with GATE to generate 6 MV photon beams. The radiation source was defined as an electron beam with Gaussian energetic distribution (mean energy 6.7 MeV, standard deviation 0.1 MeV) from which a virtual source was derived. This latter was stored as a phase space (PhS) file and attached to a PhS structure defined as a 20 cm diameter and 1 nm height cylinder, located 7 cm above the jaw banks [19], [21]. The physics constructor was G4EmStandardPhysics\_option3, with a 0.1 mm step limit for  $e^+e^-$  computations.

The flat panel was then simulated and added into GATE with its components and coupled with the linear accelerator thanks to the flexibility of the GATE commands. This digital architecture (Fig. 2) made possible the concomitant rotation of both linear accelerator head and EPID around the isocenter, where

a diffusing element can be centered. Source to EPID (detector input surface) distance was fixed at 145 cm in accordance with the actual system.

### C. MV-CBCT Imaging

The flat panel detector was simulated by superposing multiple layers of size  $41 \times 41 \text{ cm}^2$  in the beam axis (Fig. 1), and fixed at a source-to-interface distance of 145 cm (Fig. 2).

For MV-CBCT images acquisition using the linac+detector setup in GATE, the actor (an actor is a GATE tool attached to a given a structure) "ParticleInVolumeActor" was defined and attached to the scintillator layer inside the EPID. This actor collects and builds a map of the number of particles produced outside the actor volume and interacting within this volume.

An acquisition of 2-D MV projections was simulated over an arc of  $200^\circ$  with  $1^\circ$  increment and a field-size of  $41 \times 41 \text{ cm}^2$ . The CT image set of an RANDO anthropomorphic phantom (The Phantom Laboratory, Salem, NY, USA) and of a head-and-neck patient were used as inputs and automatically converted by GATE into voxelized phantom by transforming Hounsfield Units into materials through density conversion. A  $5 \times 10^8$  particles incident photon beam was generated to simulate each 2-D projection using the modeled flat panel.

### D. Image Reconstruction

A general public utilities (GPU) implementation of the Feldkamp–Davis–Kress (FDK) algorithm [22] was implemented in order to reconstruct a 3-D attenuation volume from the set of 2-D MV projections. The principle of the reconstruction follows three main steps. First, a logarithm function is applied to the projections to get the linear attenuation coefficient (Beer Lambert law) along the lines that connect each pixel of the panel to a virtual X-ray source point located inside the linac head. Projections were also divided by a blank scan for the compensation of nonuniformity. Second, the obtained projections are filtered in the Fourier space with a 1-D ramp filter following the orthogonal direction in regard to the rotation axis of the couple head/flat panel. Finally, these filtered projections are backprojected using a voxel driven approach and the perspective projection matrices given by the positions of the photon source and the positions of the portal imaging for each 2-D projection. The 2-D projections acquired from the RANDO anthropomorphic phantom and from the patient were thus reconstructed to 3-D MV-CBCT images using this GPU-implemented FDK algorithm. Both reconstructed volumes consisted of  $300 \times 300 \times 300 \text{ mm}^3$  voxels of size  $1 \times 1 \times 1 \text{ mm}^3$ .

### E. Dose Delivered to the Patient During MV-CBCT

Dose measurements were made first by using an ionization chamber (IC) in an ordinary cylindrical quality control phantom (Matrix phantom, PTW, Freiburg, Germany) and then by using thermoluminescent dosimeters (TLDs) in the anthropomorphic phantom. Both systems were modeled and simulated in GATE for comparison purposes. For calculating dose maps on a voxelized phantom, Hounsfield Units of the CT scan

were first converted into density maps in order to label each material available. This step allows GATE to recognize and manage the different components of the phantom. As a second step a specific GATE tool referred to as "dose actor" was attached to the voxelized phantom. This dose actor is used to obtain a series of data represented as a 3-D grid after simulation. Typically, stored data in a dose actor are the deposited energy, the deposited dose and the number and location of hits in a given volume.

For the study involving TLDs, square TLDs (LiF: Mg,  $3 \times 3 \times 1 \text{ mm}^3$ , TLD700 from Harshaw, Thermo Scientific, OH, USA) were placed at 17 locations inside the head-and-neck part of the RANDO anthropomorphic phantom. MV-CBCT images were acquired according to the standard clinical protocol delivering 15 monitor units in total. Three identical series of TLD measurements were performed in order to obtain a reliable mean dose value at each location inside the phantom. Furthermore, four TLDs were used per packet placed at each location in order to exclude outliers and to reduce the standard deviation of measurements. TLDs measurements were then compared with doses obtained by GATE simulations.

Calibration of TLDs (LiF: Mg,  $3 \times 3 \times 1 \text{ mm}^3$ , TLD700) was done using the methodology proposed by Eaton and Duck [23] and according to the suggestions of Kron *et al.* [24] for dosimetry measurements. As TLD measurements provide a relative dosimetry, absolute dose is determined by comparing the response of a given TLD to the response of a reference dosimeter (IC) placed inside the cylindrical quality control phantom. This cross calibration process allows to retrieve absolute doses from TLD measurements by relating their readings to the IC readings obtained in perfectly known conditions. In this paper, the reference dosimeter was a Farmer IC with a sensitive volume of  $0.6 \text{ cm}^3$ . The TLDs were handled with tweezers and read out in a manual TLD reader (Harshaw 3500) with a preheat temperature of  $140^\circ \text{C}$  followed by a  $300^\circ \text{C}$  acquisition temperature. Before each measure all TLDs were annealed with a dedicated annealing oven (FIMEL, France) at  $400^\circ \text{C}$  for one hour and cooled down to  $100^\circ \text{C}$  during 2 h.

### F. Dose Reconstruction From IMRT Treatment Plan and Portal Imaging

Complex radiotherapy plans like IMRT must be verified before their actual delivery to the patients. Classically, absolute dose at predetermined points and 2-D relative doses are measured using dedicated detectors inside quality control phantoms. This mandatory step must be done for each patient and for each beam which is very time consuming. Alternative methods have been proposed recently and rely on the use of the EPID for estimating the difference between expected and measured signals, directly at the level of the EPID or after reconstruction.

In this context, the use of MC simulation is of interest for testing and evaluating such methods. As an example, we simulated the noniterative dose reconstruction method based on portal images as described in [17]. This method aims at verifying IMRT delivery before the actual treatment by reconstructing dose from the plan and the EPID.



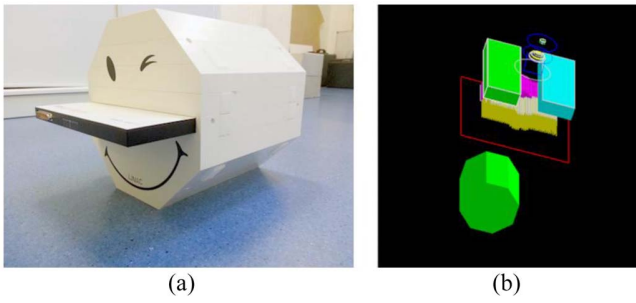


Fig. 3. Octagonal phantom. (a) Octagonal phantom Octavius with the inserted planar detector used for beamlet evaluation. (b) Octavius phantom modeled in GATE for simulations.

The algorithm describes linearly the relationship between pulses (micro-beams or beamlets) defined geometrically at the MLC level, and measured or simulated dosimetrically at the isocenter level and at the EPID level. This relationship can be obtained through measurements but in our case it is quantified by using the MC GATE code.

In IMRT, beams are characterized by multiple segments defined at the level of the MLC which will be referred to as the intensity plane  $I$  (see Fig. 2, right). Oriented according to a given gantry angle, emitted particles undergo interactions and deposit dose along their trajectories for example at the level of the isocenter, where a phantom can be positioned, and at the level of the EPID. This setup is defined as follows: we use a 32 cm high octagonal tissue equivalent phantom (Octavius, PTW) which contains at the isocenter a planar matrix of  $27 \times 27$  ICs (2-D Array seven29, PTW) placed with 1 cm spacing. All this setup, including the EPID, is modeled inside GATE (Fig. 3). The phantom is then irradiated with the 6 MV photon beam previously modeled. Planar dose distributions at the level of the EPID (beamlet-to-EPID response or  $\mathbf{R}_E$ ) and at the level of the phantom (beamlet-to-phantom response or  $\mathbf{R}_P$ ) are calculated with GATE for each beamlet unit on the intensity plane (beamlet of  $2 \times 2$  mm<sup>2</sup>) of the photon beam.

All details can be found in [17] but for sake of clarity we reproduce the main parts of the method in the Appendix of this paper.

#### G. Beamlet Calculation: Generation of Response Functions From GATE

Response functions from the Octavius phantom and from the EPID were precalculated by using GATE simulations. Calculations were performed on a cluster of 100 2.74 GHz CPUs and 2 GB RAM memory under the LINUX operating system. Response calculations were performed with the following parameters:  $2 \times 2$  mm<sup>2</sup> unit size voxels sampled across the MLC field opening ( $6 \times 6$  cm<sup>2</sup>) and corresponding to a surface covering the entire phantom at the level of detectors;  $1 \times 1 \times 1$  mm<sup>3</sup> voxels for covering of the  $32 \times 32$  cm<sup>2</sup> surface at the level of the said phantom; and  $1.8 \times 1.8 \times 1$  mm<sup>3</sup> for voxels covering the  $40.96 \times 40.96$  cm<sup>2</sup> area of the EPID.

This led to a matrix of size  $100 \times 100$  for  $\mathbf{P}$  (cumulative dose at the phantom level) and  $\mathbf{E}$  (cumulative dose at the EPID

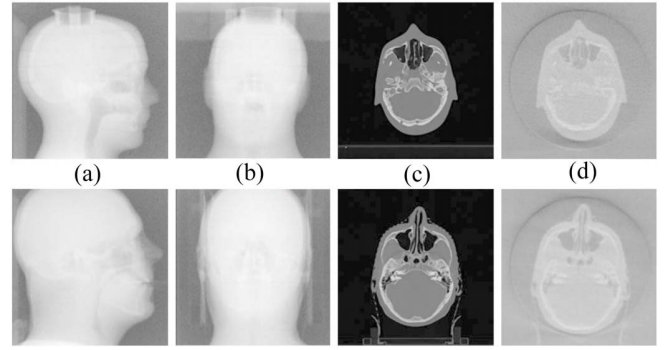


Fig. 4. Real and simulated images. (a) and (b) 2-D projections, respectively, at 0° and 90° from the simulated CBCT, (c) actual CT slice, and (d) corresponding slice from the simulated MV-CBCT. Top: RANDO anthropomorphic phantom and bottom: patient.

level) with  $1 \times 1$  mm<sup>2</sup> and  $1.8 \times 1.8$  mm<sup>2</sup> resolution, respectively. From this matrix configuration and from (2) and (3), we obtained matrices  $\mathbf{R}_P$  and  $\mathbf{R}_E$  with size  $10\,000 \times 81$  (see the Appendix). Lastly, calculation of the inverse matrix  $\mathbf{R}_E^{-1}$  was performed by means of the *linalg.inv* pseudo inverse function available in the *numpy* library of the Python v2.7 software.

### III. RESULTS

#### A. MV-CBCT Imaging

Twelve hours of calculation were mandatory to simulate one 2-D projection using a single CPU. These computations were, however, performed on a cluster of 100 CPUs (2.74 GHz, 2 GB RAM, LINUX operating system) in order to reduce the calculation time. The set of 201 MV 2-D images simulated for both phantom and patient CT with the GATE LINAC+flat panel setup were reconstructed with the FDK algorithm dedicated to cone beam images reconstruction by using an NVIDIA GTX580 GPU. Approximate run time was 1.5 s for one reconstructed volume.

MV-CBCT volumes reconstructed from simulated 2-D EPID images were compared with the ground truth given by the original CT images for both phantom and patient. The resulting projections were filtered by applying a  $\sigma = 0.5$  pixel Gaussian filter and reconstructed images showed good qualitative agreement with real CTs from both phantom and patient (Fig. 4).

A semi-quantitative study was performed for comparing simulated MV-CBCT images with real ones. For this purpose, simulated and actual volumes were spatially co-registered and profiles were traced at an arbitrary location on comparable slices (see Fig. 5 for an example from the RANDO images). Results are given on Fig. 6 and one can see that profiles are very comparable in particular in areas, where intensity gradients are significant. Contrast due to heterogeneities (soft tissues versus bones) is equally noticeable in both cases. However, the simulation process introduces a background noise  $<5\%$  when compared with actual images. This is probably due to 3-D reconstruction algorithm that is not the same between simulation and real images.

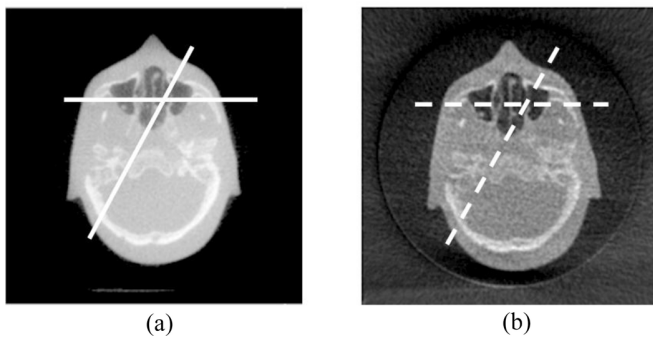


Fig. 5. Phantom study. (a) Real MV-CBCT slice of the RANDO anthropomorphic phantom used as ground truth for comparison study. (b) Co-registered MV-CBCT slice of the same phantom obtained with GATE imaging simulation and reconstruction. White lines correspond to profiles used for semi-quantitative analysis.

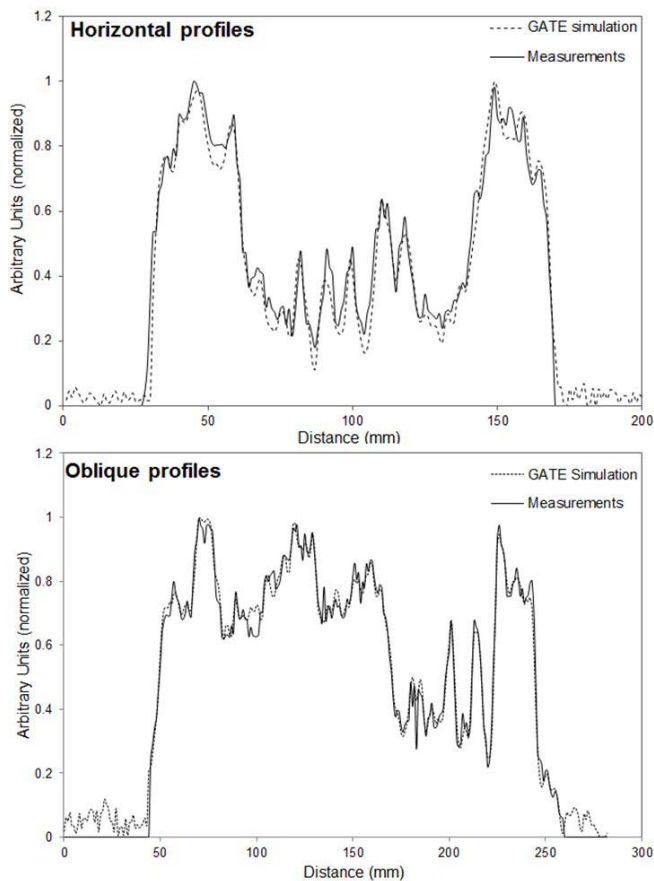


Fig. 6. MV-CBCT intensity profiles obtained for the RANDO anthropomorphic phantom. Solid and dashed lines refer to real and simulated images, respectively, (see Fig. 5). Top: horizontal profile. Bottom: oblique profile. Profiles are normalized according to the maximum value.

### B. Doses From MV-CBCT

1) *Cylindrical Matrix Phantom*: Dose deposited by MV-CBCT over an arc of  $201^\circ$  in a cylindrical matrix phantom was calculated with GATE for 3 protocols (8, 15, 60 MU) and then compared to measurements with a dedicated IC. For simulations, an MU calibration was performed as explained in

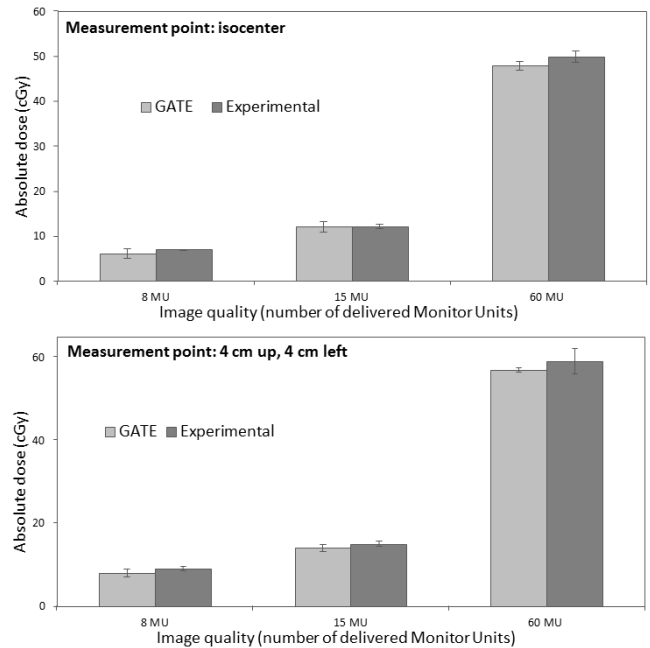


Fig. 7. Histograms of GATE versus measured deposited doses inside the cylindrical phantom for 8, 15, and 60 MU image qualities. Top, bottom: at the isocenter point and at 4 cm up, 4 cm left from the isocenter point, respectively. Error bars are relative to repeated measures and simulations.

our previous article [19]. Results are reported for two verification points: isocenter on the one hand and 4 cm up, 4 cm left from isocenter on the other hand (Fig. 7). The maximum difference was observed at the isocenter point when performing the 8 MU protocol, with doses equal to 6.82 cGy and  $5.73 \text{ cGy} \pm 1.31 \text{ cGy}$  for measurement and simulation, respectively. The mean GATE statistical uncertainties for dose values were  $0.94 \text{ cGy} \pm 0.28 \text{ cGy}$  and  $0.67 \text{ cGy} \pm 0.20 \text{ cGy}$ , respectively, for the isocenter and the second dose point.

2) *RANDO Anthropomorphic Phantom*: A CT scan of the RANDO anthropomorphic phantom was performed using a Siemens SOMATOM Sensation scanner and used as an input data for GATE imaging using the simulated EPID. The 17 TLDs positions located in the head-and-neck area were identified in the GATE output dose volume and calculated as  $1 \times 1 \times 1 \text{ mm}^3$  dose voxels, or dosels [25]. Dose points corresponding to experimental measurements were located in the final dose volume as a mean dose over  $3 \times 3 \times 1 \text{ mm}^3$  dosels to fit the size of TLDs. Comparison between TLD measurements and GATE simulation are reported in Fig. 8.

The mean relative error obtained for GATE doses compared to measurements was  $7.38\% \pm 1.91\%$  while the mean GATE statistical uncertainties for dose values was  $0.95 \text{ cGy} \pm 0.38 \text{ cGy}$ .

### C. Dose Reconstruction From Portal Imaging Device

Dose reconstruction was carried out by matrix inversion according to (4) and by using simulated response functions and deposited portal doses. This solution involved matrices of size  $10000 \times 81$  for response functions  $\underline{\underline{R}}_p$  and  $\underline{\underline{R}}_e$ .



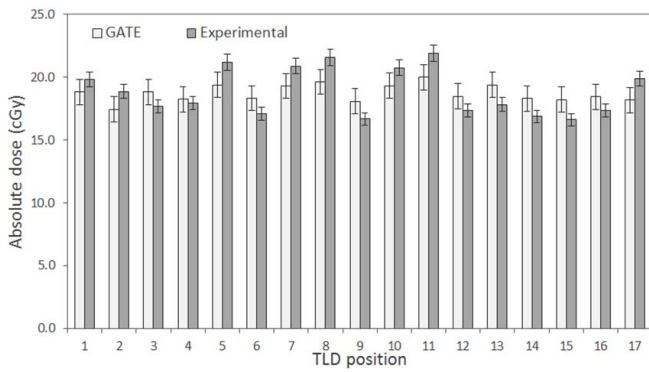


Fig. 8. Comparison of doses obtained with GATE computation and TLD measures inside the head-and-neck area of the RANDO anthropomorphic phantom.

The top of Fig. 9 compares 2-D array IC matrix measurements with reconstructed dose profiles for an open field of size  $4 \times 4 \text{ cm}^2$ . The reconstructed dose agreed well with the measured dose. This result was confirmed by applying the 2-D gamma index test, which gave for the measurements versus GATE comparison, 96.1% of dose points passing the 3% dose difference (DD) and 3 mm distance-to-agreement [26] criteria. Another example is given for a  $3 \times 5 \text{ cm}^2$  asymmetrical field, this time with 93.8% of dose points passing the same criteria as above.

After this validation with regular field shapes, the reconstruction method was applied to a more complex IMRT field as shown on the bottom of Fig. 9. In this case 92% of the evaluated dose points satisfied the 3%-3 mm gamma-index test.

#### IV. DISCUSSION

In a recent review, a list of the GATE platform applicability for radiation therapy and dosimetry applications was provided [11]. In particular, a series of potential applications in radiotherapy was presented and discussed. In this context, one of the objectives of the present study was to give a complementary example of what can be done with such a simulation platform. More precisely the main objective was to model a portal imaging device in GATE and to integrate it in a previously modeled linac [19] in order to simulate MV-CBCT images acquisitions. As a second step, a technique for evaluating the dose deposited inside the target during a treatment delivery and using the portal imager [17] was comprehensively simulated. An example for a complex IMRT treatment was given in order to get knowledge of the 2-D IMRT dose actually delivered at the isocenter of a given volume.

The system was also able to generate MV-CBCT images for a patient and an anthropomorphic phantom by using the same synergistic platform simulated in GATE. Two approaches were used to validate MV-CBCT images. As a first approach, the resulting volumes were compared with actual CT scans which were considered as ground truth images. As a second approach, simulated MV-CBCT of the anthropomorphic phantom was compared with the real MV-CBCT in order to get

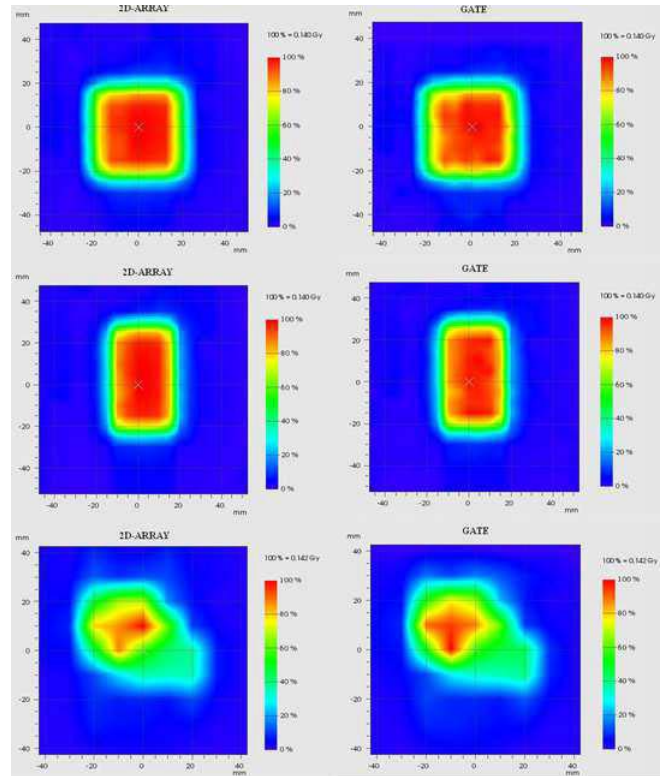


Fig. 9. Comparison between experimental and simulated dose maps for three different fields. Measured experimental maps, on the left, are obtained using a matrix of ICs inserted inside the Octavius phantom. Simulated maps, on the right, are reconstructed from simulated portal images of the phantom irradiated in the same conditions. Top:  $4 \times 4 \text{ cm}^2$  open field. Middle:  $3 \times 5 \text{ cm}^2$  open field. Bottom: step-and-shoot IMRT field.

a semi-quantitative evaluation. Good adequacy was observed in terms of geometry and dimensions (Fig. 5), while contrast due to tissue heterogeneities was also found to be comparable (Fig. 6). Obviously images are not exactly similar because reconstruction algorithm of the manufacturer was not available and we had to implement our own method of MV-CBCT reconstruction, which may not be optimal. Most discrepancies between the two kinds of images certainly come from this algorithmic difference. However, it is important to underline that the objective of the present study was first to prove that an LINAC+EPID system can be modeled using GATE, and second to give an illustration of potential applications of such a simulation system. Considering the dosimetric aspect of the study, comparison between measurements and GATE calculations gave relatively acceptable results with a mean error less than 7% for homogeneous medium, and less than 8% for heterogeneous medium when using the 15 MU image acquisition protocol (this protocol was used to enhance contrast and be able to distinguish soft tissue contrast in head and neck region [27]). Here again, more satisfactory results could reasonably be expected from the use of the same reconstruction methods as the manufacturer. Nevertheless, these results demonstrate that the high energy photon beam simulated from the modeled linear accelerator on the one hand, and the simulated EPID on the other hand can be used for simulating MV-CBCT imaging and its applications using GATE.

An example is given in terms of dose reconstruction by using a noniterative method and EPID images [17]. GATE calculations of response functions and beamlets in a phantom and at the EPID level gave for  $4 \times 4 \text{ cm}^2$  and  $3 \times 5 \text{ cm}^2$  fields, respectively, 96.1% and 93.8% of dose points passing the 3%/3 mm test. As a comparison with real data Yeo *et al.* [17] obtained 99.8% of dose points passing the same criterion for a composite irradiation field of  $4 \times 4 \text{ cm}^2$  and  $6 \times 6 \text{ cm}^2$ .

For a complex IMRT field, our GATE simulations gave 92% of dose points passing the 3%/3 mm criteria while Yeo *et al.* [17] obtained 98.6% for an IMRT subfield.

Here again, the aim was not to validate or even to evaluate the method proposed by Yeo *et al.* [17], but to show that the simulation platform that we have built can be used for a wide range of applications. Dose reconstruction from EPID images is indeed a central domain of interest at the present moment in terms of treatment quality assessment [16]. Such patient-based treatment quality controls are mandatory for IMRT and usually, they are performed by using phantoms and dedicated dosimeters that are very time consuming to install. This can be a limiting factor to the number of patients that a radiotherapy unit can receive. In this context, automated dose reconstruction from EPID images appear valuable in terms of efficiency, and a simulated platform like the one we have described in this paper could be of interest as a validating tool.

## V. CONCLUSION

Comparison with experimental data and measurements show that we have successfully modeled the flat panel detector of the accelerator, demonstrating the ability of GATE for simulating MV-CBCT imaging acquisition and dose estimation. The reconstruction algorithm used for cone beam CT images and the noniterative method for dose reconstruction were able to restore the imaged volumes, and to estimate the dose deposited by simple and complex irradiation fields.

The simulation capability of the whole treatment and imaging parts of a linear accelerator within GATE opens the way to a wide range of applications. As an example, this platform could be used for investigating adaptive radiotherapy by using its ability to compute dose directly and to evaluate the influence of patient movements thanks to EPID-based dose reconstruction.

## APPENDIX

We assume that  $\underline{E}$  is the cumulative dose contributed from all beamlets at a single point on the EPID,  $\underline{P}$  is the cumulative dose on the phantom,  $\underline{R}_e$  is the response function from the beamlet on the EPID and  $\underline{R}_p$  is the response function from the beamlet on the phantom.

In a matrix formulation one can obtain

$$\underline{E} = \underline{R}_e \underline{I} \quad (1)$$

where  $\underline{E}$  is the vector of  $E$ ,  $\underline{I}$  is the vector of  $I$ , and  $\underline{R}_e$  is the matrix of  $R_e$

$$\underline{P} = \underline{R}_p \underline{I} \quad (2)$$

where  $\underline{P}$  is the vector for  $P$ , and  $\underline{R}_p$  in the matrix of  $R_p$ .

By matrix inversion the intensity vector is obtained as

$$\underline{I} = \underline{R}_e^{-1} \underline{E} \quad (3)$$

By plugging (3) into (2),  $\underline{P}$  can easily be solved

$$\underline{P} = \underline{R}_p \cdot \underline{R}_e^{-1} \cdot \underline{E} \quad (4)$$

Using our setup for GATE beamlet calculations, we can precalculate  $\underline{R}_e$  and  $\underline{R}_p$  and calculate the  $\underline{E}$  ( $\underline{E}^{\text{calculated}}$ ) and then (4) gives the deposited dose  $\underline{P}$  ( $\underline{P}^{\text{reconstructed}}$ ) through reconstruction

$$\underline{P}^{\text{reconstructed}} = \underline{R}_p \cdot \underline{R}_e^{-1} \underline{E}^{\text{calculated}} \quad (5)$$

For each segment, the calculated dose response  $\underline{R}_p$  within the Octavius phantom can be scaled by the reconstructed beamlet intensity  $\underline{R}_e^{-1} \underline{E}$  to reconstruct  $\underline{P}$ . By using (5),  $\underline{P}$  can be calculated without calculating  $\underline{I}$ .

## REFERENCES

- [1] H. S. Abou-Elenein *et al.*, "Megavoltage cone beam computed tomography: Commissioning and evaluation of patient dose," *J. Med. Phys.*, vol. 36, no. 4, pp. 205–212, Oct. 2011.
- [2] B. Juste *et al.*, "MCNP5 Monte Carlo simulation of amorphous silicon EPID dosimetry from MLC radiation therapy treatment beams," in *Proc. Conf. IEEE Eng. Med. Biol. Soc.*, San Diego, CA, USA, 2012, pp. 5786–5789.
- [3] R. G. Simpson, C. T. Chen, E. A. Grubbs, and W. Swindell, "A 4-MV CT scanner for radiation therapy: The prototype system," *Med. Phys.*, vol. 9, no. 4, pp. 574–579, Jul./Aug. 1982.
- [4] W. Swindell, R. G. Simpson, J. R. Oleson, C. T. Chen, and E. A. Grubbs, "Computed tomography with a linear accelerator with radiotherapy applications," *Med. Phys.*, vol. 10, no. 4, pp. 416–420, Jul./Aug. 1983.
- [5] K. Kuriyama *et al.*, "A new irradiation unit constructed of self-moving gantry-CT and linac," *Int. J. Radiat Oncol Biol. Phys.*, vol. 55, no. 2, pp. 428–435, Feb. 2003.
- [6] T. T. Monajemi, S. Steciw, B. G. Fallone, and S. Rathee, "Modeling scintillator-photodiodes as detectors for megavoltage CT," *Med. Phys.*, vol. 31, no. 5, pp. 1225–1234, May 2004.
- [7] P. Alaei and E. Spezi, "Imaging dose from cone beam computed tomography in radiation therapy," *Phys. Med.*, vol. 31, no. 7, pp. 647–658, 2015.
- [8] A. Ding, J. Gu, A. V. Trofimov, and X. G. Xu, "Monte Carlo calculation of imaging doses from diagnostic multidetector CT and kilovoltage cone-beam CT as part of prostate cancer treatment plans," *Med. Phys.*, vol. 37, no. 12, pp. 6199–6204, Dec. 2010.
- [9] G. X. Ding and C. W. Coffey, "Radiation dose from kilovoltage cone beam computed tomography in an image-guided radiotherapy procedure," *Int. J. Radiat Oncol Biol. Phys.*, vol. 73, no. 2, pp. 610–617, Feb. 2009.
- [10] B. R. Walters, G. X. Ding, R. Kramer, and I. Kawrakow, "Skeletal dosimetry in cone beam computed tomography," *Med. Phys.*, vol. 36, no. 7, pp. 2915–2922, Jul. 2009.
- [11] D. Sarrut *et al.*, "A review of the use and potential of the GATE Monte Carlo simulation code for radiation therapy and dosimetry applications," *Med. Phys.*, vol. 41, no. 6, Jun. 2014, Art. no. 064301.
- [12] F. Lamare, A. Turzo, Y. Bizais, C. C. Le Rest, and D. Visvikis, "Validation of a Monte Carlo simulation of the Philips Allegro/GEMINI PET systems using GATE," *Phys. Med. Biol.*, vol. 51, no. 4, pp. 943–962, Feb. 2006.
- [13] D. Bouzid *et al.*, "Monte-Carlo dosimetry for intraoperative radiotherapy using a low energy X-ray source," *Acta Oncol.*, vol. 54, no. 10, pp. 1788–1795, Nov. 2015.
- [14] R. A. Siochi, A. Molineu, and C. G. Orton, "Point/counterpoint. Patient-specific QA for IMRT should be performed using software rather than hardware methods," *Med. Phys.*, vol. 40, no. 7, Jul. 2013, Art. no. 070601.

- [15] B. Mijnheer, S. Beddar, J. Izewska, and C. Reft, "In vivo dosimetry in external beam radiotherapy," *Med. Phys.*, vol. 40, no. 7, Jul. 2013, Art. no. 070903.
- [16] A. Fidanzio, L. Azario, F. Greco, S. Cilla, and A. Piermattei, "Routine EPID in-vivo dosimetry in a reference point for conformal radiotherapy treatments," *Phys. Med. Biol.*, vol. 60, no. 8, pp. N141–N150, Mar. 2015.
- [17] I. J. Yeo *et al.*, "Dose reconstruction for intensity-modulated radiation therapy using a non-iterative method and portal dose image," *Phys. Med. Biol.*, vol. 54, no. 17, pp. 5223–5236, Sep. 2009.
- [18] I. J. Yeo, J. W. Jung, B. Y. Yi, and J. O. Kim, "Feasibility study on inverse four-dimensional dose reconstruction using the continuous dose-image of EPID," *Med. Phys.*, vol. 40, no. 5, May 2013, Art. no. 051702.
- [19] S. Benhalouche, D. Visvikis, A. Le Maitre, O. Pradier, and N. Bousson, "Evaluation of clinical IMRT treatment planning using the GATE Monte Carlo simulation platform for absolute and relative dose calculations," *Med. Phys.*, vol. 40, no. 2, Feb. 2013, Art. no. 021711.
- [20] M. Tubiana and F. Eschwège, "Conformal radiotherapy and intensity-modulated radiotherapy—clinical data," *Acta Oncol.*, vol. 39, no. 5, pp. 555–567, 2000.
- [21] L. Grevillot *et al.*, "Simulation of a 6 MV Elekta Precise Linac photon beam using GATE/GEANT4," *Phys. Med. Biol.*, vol. 56, no. 4, pp. 903–918, Feb. 2011.
- [22] L. A. Feldkamp, L. C. Davis, and J. W. Kress, "Practical cone-beam algorithm," *J. Opt. Soc. Amer. A, Opt. Image Sci.*, vol. 1, no. 6, pp. 612–619, 1984.
- [23] D. J. Eaton and S. Duck, "Dosimetry measurements with an intra-operative X-ray device," *Phys. Med. Biol.*, vol. 55, no. 12, pp. N359–N369, Jun. 2010.
- [24] T. Kron *et al.*, "A checklist for reporting of thermoluminescence dosimetry (TLD) measurements," *Phys. Med. Biol.*, vol. 44, no. 10, pp. L15–L17, Oct. 1999.
- [25] D. Sarrut and L. Guigues, "Region-oriented CT image representation for reducing computing time of Monte Carlo simulations," *Med. Phys.*, vol. 35, no. 4, pp. 1452–1463, Apr. 2008.
- [26] D. A. Low, W. B. Harms, S. Mutic, and J. A. Purdy, "A technique for the quantitative evaluation of dose distributions," *Med. Phys.*, vol. 25, no. 5, pp. 656–661, May 1998.
- [27] M. Miften *et al.*, "On the incorporation of daily dose from online megavoltage cone-beam CT in IMRT," in *Proc. 15th Int. Conf. Use Comput. Radiat. Therapy*, Toronto, ON, Canada, 2007, pp. 428–432.

## B.8 Modélisation biomécanique de la prostate

# Modeling the impact of prostate edema on LDR brachytherapy: a Monte Carlo dosimetry study based on a 3D biphasic finite element biomechanical model

K A Mountris<sup>1</sup>, J Bert<sup>1</sup>, J Noailly<sup>2</sup>, A Rodriguez Aguilera<sup>4</sup>,  
A Valeri<sup>5</sup>, O Pradier<sup>1,6</sup>, U Schick<sup>1,6</sup>, E Promayon<sup>3</sup>,  
M A Gonzalez Ballester<sup>2,7</sup>, J Troccaz<sup>3</sup> and D Visvikis<sup>1</sup>

<sup>1</sup> LaTIM, INSERM, UMR 1101, CHRU Brest, Brest, France

<sup>2</sup> Department of Information and Communication Technologies, Universitat Pompeu Fabra, Barcelona, Spain

<sup>3</sup> Université Grenoble Alpes, TIMC-IMAG UMR CNRS 5525, F-38000 Grenoble, France

<sup>4</sup> University of Granada, Granada, Spain

<sup>5</sup> Department of Urology, CHRU Brest, Brest, France

<sup>6</sup> Department of Radiotherapy, CHRU Brest, Brest, France

<sup>7</sup> ICREA, Barcelona, Spain

E-mail: [konstantinos.mountris@gmail.com](mailto:konstantinos.mountris@gmail.com)

Received 4 October 2016, revised 9 December 2016

Accepted for publication 31 January 2017

Published 17 February 2017



CrossMark

### Abstract

Prostate volume changes due to edema occurrence during transperineal permanent brachytherapy should be taken under consideration to ensure optimal dose delivery. Available edema models, based on prostate volume observations, face several limitations. Therefore, patient-specific models need to be developed to accurately account for the impact of edema. In this study we present a biomechanical model developed to reproduce edema resolution patterns documented in the literature. Using the biphasic mixture theory and finite element analysis, the proposed model takes into consideration the mechanical properties of the pubic area tissues in the evolution of prostate edema. The model's computed deformations are incorporated in a Monte Carlo simulation to investigate their effect on post-operative dosimetry. The comparison of Day1 and Day30 dosimetry results demonstrates the capability of the proposed model for patient-specific dosimetry improvements, considering the edema dynamics. The proposed model shows excellent ability to reproduce previously described edema resolution patterns and was validated based on previous findings. According to our results, for a prostate

volume increase of 10–20% the Day30 urethra D10 dose metric is higher by 4.2%–10.5% compared to the Day1 value. The introduction of the edema dynamics in Day30 dosimetry shows a significant global dose overestimation identified on the conventional static Day30 dosimetry. In conclusion, the proposed edema biomechanical model can improve the treatment planning of transperineal permanent brachytherapy accounting for post-implant dose alterations during the planning procedure.

Keywords: prostate brachytherapy, edema dynamics, biomechanical model, Monte Carlo simulation, dynamic dosimetry

(Some figures may appear in colour only in the online journal)

## 1. Introduction

Prostate cancer is the third leading cause of cancer deaths in the male population (Haas *et al* 2008). Trans-rectal ultrasound-guided low-dose rate brachytherapy (LDR) is a widely used low-risk technique for effective prostate cancer treatment. Radioactive seeds of <sup>125</sup>I or <sup>103</sup>Pd are implanted in the prostate gland, guided by trans-rectal ultrasound imaging in order to deliver a homogeneous tumoricidal dose while sparing the healthy surrounding tissues and organs at risk (Davies *et al* 2004). The radioactive seeds are implanted in the prostate using needles inserted in the gland through a rectangular grid mounted on the trans-rectal ultrasound probe. Despite the fact that LDR brachytherapy has been established as a routine operation in the last decades, the Brachytherapy Dose Calculation Formalism used in clinical practice is based on the AAPM TG-43 protocol (Rivard *et al* 2004) and is associated with several limitations. More recent proposals from the AAPM Task Group 186 report provide guidance for the use of alternative and more accurate dose calculation models accounting for non-water equivalent media such as the grid based Boltzmann solver (GBBS) and Monte Carlo (MC) methods (Beaulieu *et al* 2012). However, in all of these dosimetry approaches, a significant factor of error/uncertainty which is not considered, is the prostate tissue damage due to the implantation process resulting in prostate volume changes during and after the operation. These volume changes, associated with the resulting prostate edema, have a significant effect on the actual dose deposition (Waterman *et al* 1998, Leclerc *et al* 2006, Tejwani *et al* 2012, Chira *et al* 2013) to the prostate and the organs at risk (OAR).

The initial body response to biological stress, such as with tissue trauma, is an acute inflammation that involves a cascade of events mediated by a large array of cells and molecules that, under normal circumstances, flow freely in the blood circulatory system. The purpose of these cells and molecules is to locate invading pathogens or damaged tissue, eliminate the offending agents, and restore the body homeostasis (Day *et al* 2006). To maximize the delivery of these mediators in the damaged areas, the capillary permeability increases and blood plasma flows from the vascular network to the interstitial matrix carrying the repairing mediators to their target. This excessive fluid build-up in the interstitial matrix is the main cause of fast occurring edema (Starling 1896), during and after a brachytherapy operation.

Several studies have investigated the influence of edema on post-implant dosimetry (Waterman *et al* 1998, Chen *et al* 2000, Dogan *et al* 2002, Yue *et al* 2006, Sloboda *et al* 2010, Sloboda *et al* 2012, Tejwani *et al* 2012, Chira *et al* 2013). Chira *et al* (2013) have shown that a prostate volume increase of 10% during brachytherapy can lead to an increase in D90 (dose coverage of 90% of the prostate volume) at Day30 of approximately 11.7% in comparison to the D90 measured at Day1. Leclerc *et al* (2006) have shown an overall dose increase of up



to 15 Gy when edema was considered in the dosimetry by means of a weighted dose-volume histogram summation algorithm. Based on the same algorithm Villeneuve *et al* (2008) showed the dose over-estimation in inverse treatment planning systems when treatment planning is done considering pre-implant prostate volumes before the occurrence of edema. In order to improve the post-implant dosimetry, analytical models based on CT and MRI image processing techniques have been developed, considering the edema resolution time course (Waterman *et al* 1998, Leclerc *et al* 2006, Sloboda *et al* 2010, 2012, Tejwani *et al* 2012). The main parameters of these models include the edema magnitude and half-life. In their study, Tejwani *et al* (2012) have shown an exponential resolution pattern for the edema similarly to previously published studies (Waterman *et al* 1998). In contrast, Sloboda *et al* (2010, 2012) reported a near-linear edema resolution time course. In these studies, a large variability on edema magnitude and half-life parameters amongst patients have been reported. The dependence of this dispersion on parameters such as the Gleason score, the needle gestures, the number of implants, the seed activity and the mechanical properties of the tissue has not been extensively investigated. As such the influence of these parameters is still not clear, therefore they have not been considered in the existing analytical edema models (Nath *et al* 2009). Additionally, none of these models account for the intra-operative evolution phase of the edema since the dose deposited during the operation is considered negligible (Dogan *et al* 2002).

The aim of the present study is the improvement of patient-specific edema models, taking into consideration potentially significant parameters that were not considered in previously proposed analytical models. More specifically, we propose a biomechanical computational model based on biphasic mixture theory. The proposed model accounts for the patient-specific geometry of the pubic region and the mechanical properties of the pubic organs of interest. We investigate the impact of the values given to these tissue properties on the edema magnitude, half-life and resolution pattern. The results are compared against clinical findings from relevant studies. These results are finally integrated within a Monte Carlo simulation based dosimetry framework in order to investigate the extent and accuracy of the model's capability to predict relative differences between the estimated deposited dose during treatment planning in Day1 (the day of operation) and that obtained based on Day30 dosimetry findings. The determined relative dose differences in these studies are also compared to related clinical findings.

## 2. Materials and methods

### 2.1. Biomechanical model

The prostate edema and the associated biomechanical response of the pubic region were modeled using the finite element (FE) methodology. Patient specific models were derived from a dataset of pre-operative CT segmented images from 15 patients who underwent LDR brachytherapy within the radiotherapy department of the University Hospital of Brest. Manual segmentation of the prostate and OAR was performed by an experienced clinician. The ISO2MESH toolkit (Fang and Boas 2009) was subsequently employed for the generation of 3D multi-domain tetrahedral mesh representations of the pubic region geometry for each patient. The prostate, bladder, rectum, and the pubic bones were explicitly represented (figure 1).

The software suite FEBio (Maas *et al* 2012) was used for the numerical analysis. Biphasic calculations were performed in order to describe the prostate swelling and its effect on the model geometry, similarly to previous studies on brain edema (Li *et al* 2009) or intervertebral disk swelling (Galbusera *et al* 2011). More specifically the build-in biphasic mathematical models of FEBio suite (<http://febio.org>) were used. The edema was treated as a distributed



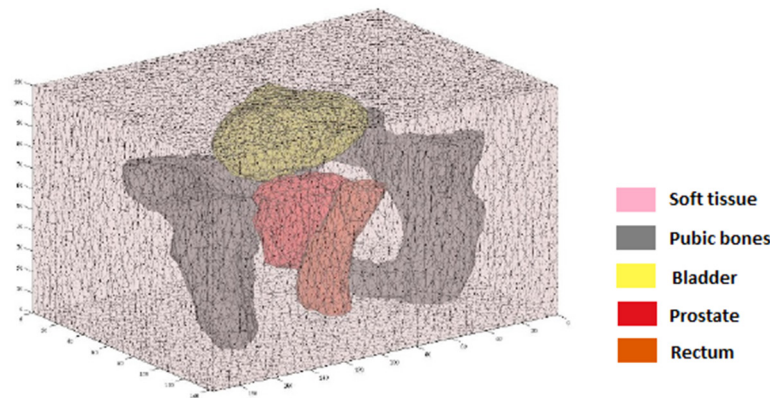


**Figure 1.** Tetrahedral mesh representation of the pubic area. The organs of interest (prostate, bladder, rectum and pubic bones) are discretized within a soft tissue block approximating the surrounding pubic structures.

fluid source within the prostate volume representing inflammation and allowing the simulation of fluid accumulation during the operation day (Day1), i.e. the period during which a maximum edema magnitude is reached according to previously published works (Sloboda *et al* 2010, Tejwani *et al* 2012). After Day1 the edema fluid source was ‘switched off’, and the resolution of the edema as a function of time was controlled exclusively by the mechanical and functional parameters assigned to the prostate and the surrounding tissues. According to the biphasic mixture theory, described in Maas *et al* (2012), a biphasic material is assumed to be a mixture of a porous permeable solid and an interstitial fluid, both intrinsically incompressible. However, this mixture can change volume as interstitial fluid is exchanged with the porous space of the solid. Under quasi-static conditions the conservation of the mass requires that:

$$\text{div}(\mathbf{v}_s + \mathbf{w}) = S_w \quad (1)$$

where,  $\mathbf{v}_s$  is the solid velocity,  $\mathbf{w}$  the fluid flux relative to the solid and  $S_w$  is an external fluid supply term. A simplified version of Starling’s equation (Starling 1896) was used to simulate the external fluid supply term  $S_w$ :

$$S_w = k(p_v - p) \quad (2)$$

where,  $k$  is the filtration coefficient,  $p_v$  the source pressure that simulates inflammation and  $p$  the mixture’s fluid compartment pressure. In the proposed edema model the filtration coefficient  $k$  was assumed equal to 1 (absolute filtration) and the pressure  $p_v$  linearly dependent on time:

$$p_v(t) = \frac{2\Delta}{kt_{\max}^2}t + p \quad (3)$$

The coefficient multiplying time ( $t$ ) in (3) was determined so that the total applied external fluid source is equal to the expected edema magnitude (4):

$$\int_0^{t_{\max}} S_w dt = \Delta \quad (4)$$

where,  $\Delta$  is the edema magnitude (maximum relative prostate volume increase). The edema magnitude is expressed as:

**Table 1.** Material properties used for the modeling of the pubic organs of interest for Test 1.

Domain	Young modulus (MPa)	Poisson ratio	Porosity	Permeability ( $\text{mm}^4 \text{N}^{-1} \text{s}^{-1}$ )
Prostate	0.01–0.1 <sup>a</sup>	0.1–0.45 <sup>a</sup>	0.5	$3.177 \times 10^{-5}$
Bladder and rectum <sup>b</sup>	0.015 MPa	0.49	—	—
Soft tissue	0.001 MPa	0.35	—	—

<sup>a</sup> Prostate drained porous solid phase.

<sup>b</sup> The Young modulus and Poisson ratio of the rectum and the bladder were converted to the  $c_1$ ,  $c_2$  Mooney–Rivlin parameters and bulk modulus.

$$\Delta = \frac{V_{\max} - V_0}{V_0} \quad (5)$$

where,  $V_{\max}$  is the prostate volume associated with maximum edema as measured at Day1 and  $V_0$  is the prostate volume with no edema.

A biomechanical model is described by the assigned materials in the different structures and the corresponding material parameters which are described following. The drained solid skeleton of the prostate model was represented as a neo-Hookean hyperelastic material (Wang *et al* 2016), and the permeability of the saturated biphasic continuum was described through the Holmes–Mow strain-dependent permeability model. The rectum and the bladder were considered as nearly incompressible Mooney–Rivlin materials (Haridas *et al* 2006), and the surrounding continuum (soft tissue in figure 1) was modeled as a compressible neo-Hookean material. Finally, the pubic bones were considered as rigid structures. The mechanical properties assigned to the different structures were derived from previously reported ranges (Hu *et al* 2008, Lee *et al* 2008, Ahn *et al* 2010, Barr *et al* 2012, Li *et al* 2014, Yan *et al* 2012). In the following computational tests only the mechanical properties of the prostate are assumed to be variable for simplicity. The ranges of the mechanical properties used for the prostate and the fixed values used for the other structures as an input to the proposed biomechanical model are summarized in table 1. The output of interest from the proposed model were the prostate volume changes computed for a period of 30 d, for a range of given mechanical parameters (Young Modulus, Poisson ratio) and fluid supply source values.

In order to investigate the relationship between the edema behavior (magnitude, half-life) and the prostate elastic parameters (Young modulus, Poisson's ratio) the model's response was evaluated for a range of Young modulus (0.01–0.1 MPa) and Poisson's ratio (0.1–0.45) values while the other model parameters were maintained constant (Test 1). Additionally, the edema resolution pattern of the model was computed for a mean edema magnitude of  $\Delta = 0.38$  determined in Tejwani *et al* (2012). Extreme values of edema magnitude ( $\Delta = 0.1$ ,  $\Delta = 0.2$ ,  $\Delta = 0.65$ ) were also considered using the material parameters derived from the model assessment experiment varying only the external fluid supply (Test 2). Edema magnitude values greater than  $\Delta = 0.65$  were not considered since they represent clinically unrealistic values and may result in numerical instabilities due to very large deformations. Finally, the edema resolution pattern was computed for the two extreme Young modulus values used in test 1 (i.e. 0.01 and 0.1 MPa) with the other mechanical properties and external fluid supply set as constants. These findings were compared with the resolution pattern computed using the model assessment parameters (Test 3). The patterns computed in tests 2 and 3 were used to investigate the capabilities of the proposed model to determine the impact of the edema magnitude and the edema resolution pattern on post-implant dosimetry. Table 2 summarizes

**Table 2.** Computational scenarios for the investigation of the edema resolution pattern changes.

Variable	Tested values
Edema magnitude— $\Delta^a$	0.1, 0.2, 0.38, 0.65
Young modulus—YM (MPa) <sup>b</sup>	0.001, 0.05, 0.01

<sup>a</sup> The edema magnitude ( $\Delta$ ) represents the percentage prostate volume change in decimal notation (0.1  $\rightarrow$  10%, 0.2  $\rightarrow$  20%, and so on).

<sup>b</sup> The rest elastic parameters were set according to table 1 and  $\Delta$  was set at 0.38 for all cases.

the different scenarios for which the model's edema resolution pattern was computed for. The edema resolution pattern for an edema magnitude of  $\Delta = 0.38$  and the corresponding model assessment parameters are referred for the rest of the manuscript as the mean edema magnitude resolution pattern.

## 2.2. Post-implant dosimetry simulation

For an accurate simulation of the post-implant dosimetry, the GGEMS-Brachy MC framework (Lemaréchal *et al* 2015) was used, considering the inter-seed photon interactions as well as the patient-specific tissue heterogeneities at the voxel level based on patient-specific 3D CT images. This framework developed using CUDA (Kirk 2007) enables an accurate and rapid MC simulation of the dose deposited in voxelized volumes. In GGEMS-Brachy materials from CT images are derived by transforming Hounsfield units into materials through density conversion given by Schneider *et al* (2000). Material mixtures and their physical properties are built using the Geant4 materials library.

In order to integrate the modeled edema dynamics in the dosimetry simulation the computed deformation map obtained using the model's tetrahedral mesh has to be applied on the original voxelized volume (patient's pre-operative CT volume). For this step, the resampling method for interactive deformation of volumetric models previously proposed by Aguilera *et al* (2015) was used. This resampling method was modified to apply the model's deformation map on the initial brachytherapy seeds' positions. The brachytherapy seeds' movement (translation, no rotation) was assumed to depend exclusively on the deformation of the prostate, while any contribution to the prostate deformation from the seeds' geometry and material properties were not taken into consideration. Finally, this resampling approach was implemented using CUDA, allowing the application of the deformation map of a coarse FE mesh consisting of 3200 nodes on a voxelized volume in 23.9 ms.

The impact of the edema model on post-implant dosimetry was investigated by comparing several dose metrics between Day1 and Day30 dosimetry similarly to previous studies (Tejwani *et al* 2012, Chira *et al* 2013). The original pre-implant CT volume of each patient and the seeds' positions, chosen in order to ensure good D90 coverage on the prostate, were used for the Day30 conventional dosimetry. For the Day1 dosimetry simulation the model's deformation during the maximum edema magnitude state was applied both on the initial CT volume and seeds' positions. Additionally, the Day30 'dynamic dosimetry' was calculated considering the dynamic deformation of the CT volume and seeds' positions during the complete edema resolution pattern with a step size of 1 d between each deformation state for the first 30 d after the operation. Day1 dosimetry, Day30 conventional dosimetry and Day30 'dynamic dosimetry' were calculated for all the simulated edema patterns summarized previously in table 2. All the dosimetry calculations were based on  $5 \times 10^8$  emitted particles per simulation with an average dose uncertainty of 2% in the prostate, using a full model of 125I

**Table 3.** Prostate mechanical properties after model assessment<sup>a</sup>.

Domain	Young modulus (MPa)	Poisson's ratio	Porosity	Permeability
Prostate	0.05	0.4	0.5	$3.177 \times 10^{-5}$

<sup>a</sup>These mechanical properties were shown to have the optimal fitting with the reference ground truth measurements of Tejwani *et al* (2012) used in this study

seeds (STM1251, Bard Medical Division, Covington, GA, USA), commonly employed in prostate cancer brachytherapy, and previously modeled in Lemaréchal *et al* (2015) based on the geometry and composition described in Kirov and Williamson (2001). In addition, the use of a previously proposed hybrid navigator (Bert *et al* 2016) allowed to consider several seeds close together within the same voxel as well as considering inter-seed interactions as previously described in Lemaréchal *et al* (2015).

Finally, in order to quantify the observed dose differences and potential impact, the V90 prostate (prostate volume receiving the 90% of 145 Gy), D90 prostate, D10 urethra, D2cc rectum and the D10 pubic bones' dose metrics were computed for all the edema scenarios for Day1 and Day30 (conventional and dynamic) dosimetry.

### 3. Results

#### 3.1. Biomechanical model

The mechanical properties of the proposed biomechanical model used in the computation of the mean edema magnitude resolution pattern, were manually adjusted for all patient datasets to fit the mean edema magnitude values measured in the case-study of Tejwani *et al* (2012) for three control time points (Day1, Day9, and Day30) after the operation (see table 3).

For these selected parameters the model fitted well with the edema magnitude mean values measured at the control time points of the reference study (Tejwani *et al* 2012) considered as ground truth. The computed edema resolution pattern and the calibration values of the edema mean magnitude values at the control time points of the ground truth reference are shown in figure 2.

The dependence of the edema parameters (magnitude, half-life) on the prostate mechanical properties was studied with a series of computational tests, considering a Poisson ratio in the range of 0.1–0.45 and a Young modulus in the range of 0.01 MPa to 0.1 MPa. The relationship of the edema parameters with the mechanical properties of the prostate are shown in figure 3. The proposed biomechanical model led to a higher dependence of the edema parameters on the Young modulus compared to the Poisson ratio. Prostate Young modulus, as measured for example by *in vivo* shear wave elastography (Barr *et al* 2012), have shown high variability amongst cancer patients depending on the overall patient anatomy and tissue constitution (e.g. cancer extent or tissue inflammation). For these reasons only the impact of the prostate stiffness (Young modulus) in the post-treatment dosimetry was investigated, in addition to the impact of the edema magnitude. Figure 4 shows the different computed edema resolution patterns used in the following post-treatment dosimetry simulations.

As shown in figure 4 the prostate stiffness variance affects significantly the overall edema resolution pattern. A very elastic prostate (YM: 0.01 MPa) exhibits a nearly linear edema resolution pattern, while the variation of the edema maximum magnitude with constant mechanical properties doesn't affect the edema resolution pattern.

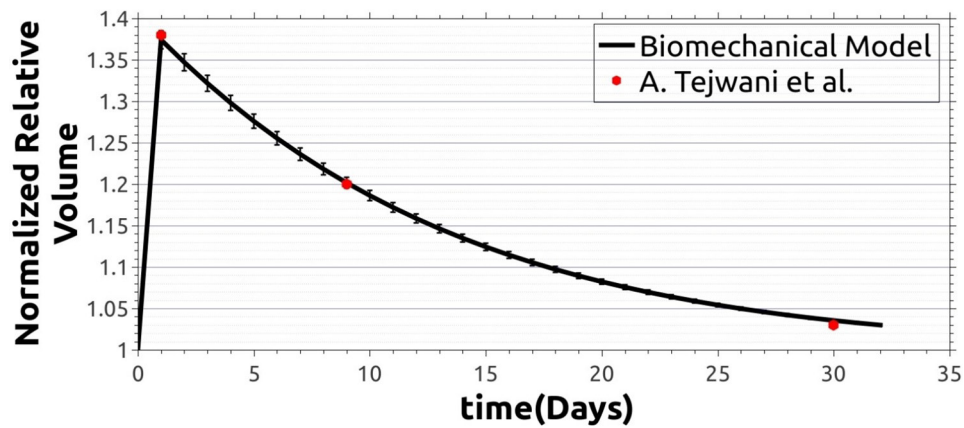


**Figure 2.** The solid continuous curve corresponds to the mean edema resolution pattern calculated for the 15 available patient datasets. The error bars correspond to the standard deviation (SD) considering the 15 patients and the red points correspond to the mean edema magnitude values as measured by Tejwani *et al* (2012).

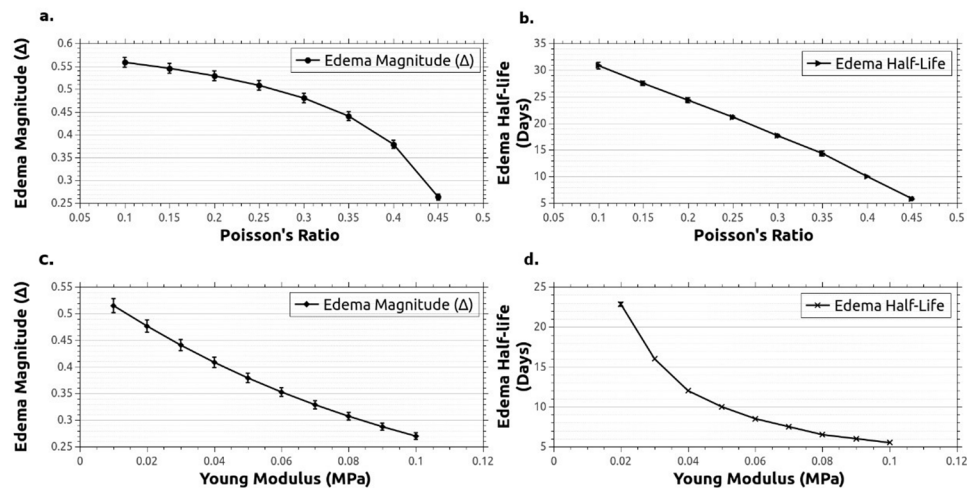


**Figure 3.** Relationship between the edema parameters and the prostate mechanical properties. (a) Edema magnitude dependence on the Poisson's ratio; relationship between (b) the edema half-life and the Poisson's ratio; (c) the edema half-life with the Young modulus; and (d) the edema magnitude with the Young modulus. In all the cases shown above all the other mechanical properties were those defined in table 1. The error bars show the SD amongst the 15 patients' dataset.

### 3.2. Post-implant dosimetry simulation

For all dosimetry simulations, the resampling method for the deformation of volumetric models was applied on the initial CT dataset and seeds' locations. Deformed CT volumes and seeds' locations were generated for each patient and each state of the biomechanical model to take into account the prostate volume changes during the first 30 d after the operation. Figures 5 and 6 show the application of the deformation on a typical patient CT volume and the corresponding seeds displacements respectively.



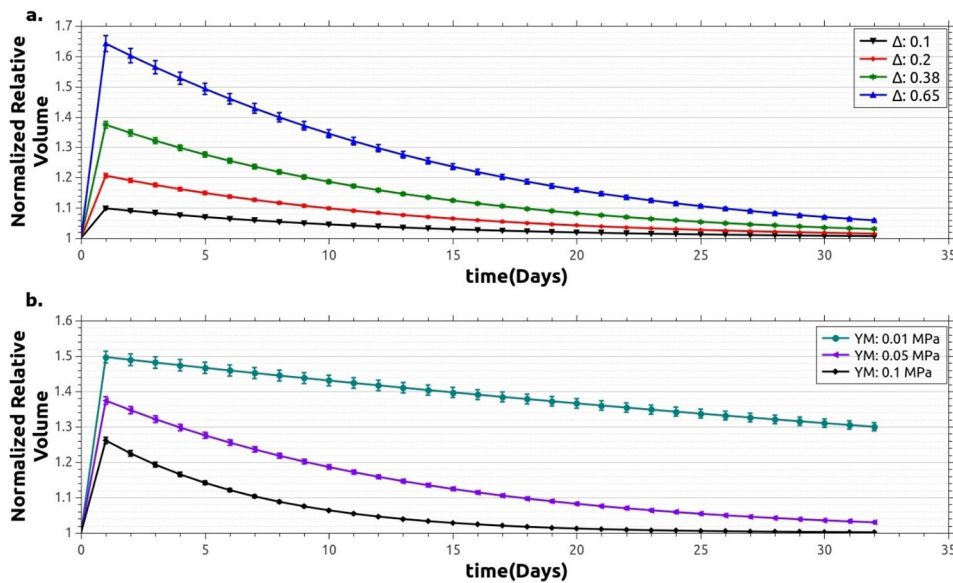


**Figure 4.** In figure (a) the edema resolution patterns for 4 different edema magnitudes at Day1 and Young modulus 0.05 MPa are shown. Figure (b) shows the edema resolution patterns for the three considered Young Modulus scenarios with edema magnitude 0.38. The error bars in both plots show the SD amongst the fifteen patient datasets.

The comparison of Day1 and Day30 dosimetry simulations for the different computed edema resolution patterns highlights the overall underestimation of the actual dose deposited if Day1 dosimetry is performed without considering the edema resolution mechanism, in accordance with previous studies (Tejwani *et al* 2012, Chira *et al* 2013). All the patient datasets used in our study showed an increase in the dose differences between the Day1 and Day30 dosimetry which was proportional to the increase of the maximum edema magnitude ( $\Delta$ ) while the mechanical properties were considered constant. In contrast, taking into consideration the variation of the prostate stiffness, the dosimetric difference between Day1 and Day30 dosimetry was smaller for a highly elastic prostate (YM of 0.01 MPa) compared to a stiffer prostate (YM of 0.1 MPa) due to the nearly linear edema resolution pattern shown in the former scenario and the associated large edema half-life. Additionally, the comparison between the conventional and the dynamic Day30 dosimetry revealed an overestimation of the hot spots measured by the urethra D10 metric in the former case. The relative differences of the dose metrics for all the computed edema resolution patterns are shown in tables 4 and 5.

The deposited dose difference to the prostate ranges between 6.21% and 35.87% considering the edema dynamics (see table 4, column 3) for 0.1 and 0.65 edema magnitude values respectively. Likewise, significant dose differences were measured in the urethra ranging between 4.20% and 31.18%. In addition, dose differences are shown to depend on the prostate stiffness. The lower dose difference between Day1 and Day30 dosimetry was measured for a prostate Young Modulus of 0.01 MPa and was 10.17% and 7.56% for the prostate and the urethra respectively, taking into consideration the edema dynamics. The higher dose difference of 19.21% and 18.85%, for the prostate and the urethra respectively, was measured for a Young Modulus of 0.1 MPa (see table 5, column 3).

In all the tested scenarios the application of the edema biomechanical model led to an overall increase in the D90 coverage of the prostate and an increase in the dose deposited in the



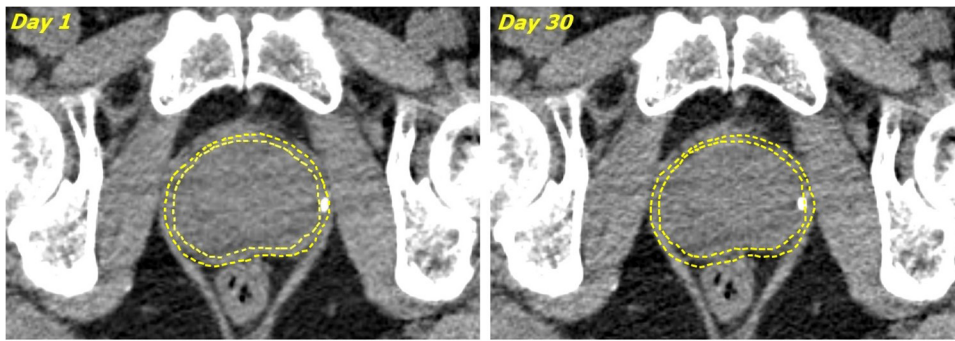


**Figure 5.** CT slices of the pubic region at Day1 (maximum deformation applied) and Day30. The inner and outer dashed-lines represent the Day30 and Day1 prostate contours respectively.

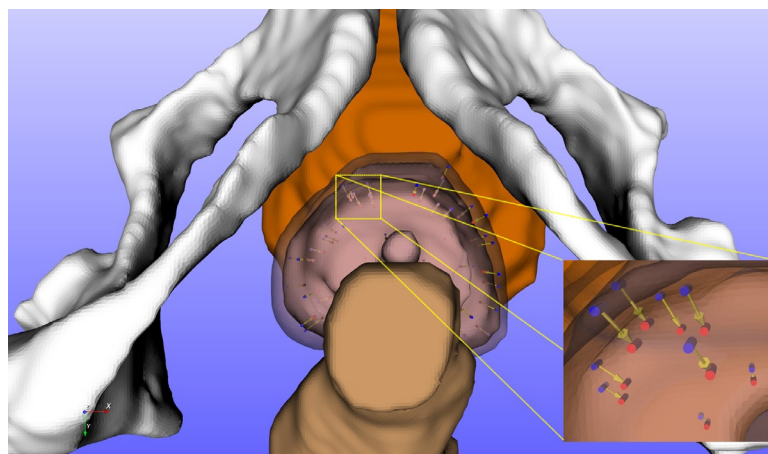


**Figure 6.** A super-imposed 3D representation of the pubic organs of interest. The prostate deformation and seeds' displacements between Day1 and Day30 is shown. The zoomed inset shows the displacement of the seeds from their position at Day1 (blue) to their final position at Day30 (red).

central region of the prostate, where the urethra is located, due to the resolution of the edema and the induced displacements of the brachytherapy seeds. These findings are displayed for the case of an average edema magnitude of  $\Delta = 0.38$  in terms of DVH and isodoses' distribution for a representative patient in figures 7 and 8 respectively.

#### 4. Discussion

Edema is an important error-inducing factor during dosimetric estimations. Big dosimetric diversions can occur depending on the edema magnitude and half-life. Previously developed mathematical models aim at correcting the dosimetric measurements applying global correction factors (Tejwani *et al* 2012). These correction factors are based on mean edema magnitude and half-life values. The big diversion of edema characteristics amongst patients is not considered in these models and therefore their application is limited.

**Table 4.** Mean relative changes for the dose metrics of interest for the 15 patients' dataset between Day1 and the conventional and/or dynamic Day30 dosimetry for the different computed edema magnitude scenarios.

Edema magnitude scenarios	Dose metric	Day30 dynamic relative change (%) $\pm$ (SD)	Day30 conventional relative change (%) $\pm$ (SD)
$\Delta$ : 0.1	Prostate V90	7.7 $\pm$ (3.7)	8.9 $\pm$ (4.6)
	Prostate D90	6.2 $\pm$ (1.1)	5.9 $\pm$ (1.4)
	Urethra D10	4.2 $\pm$ (1.5)	4.9 $\pm$ (1.5)
	Rectum D2cc	-1.0 $\pm$ (0.7)	-0.6 $\pm$ (0.8)
	P. Bones D10	-1.3 $\pm$ (0.3)	-1.2 $\pm$ (0.4)
$\Delta$ : 0.2	Prostate V90	19.0 $\pm$ (3.4)	21.9 $\pm$ (4.7)
	Prostate D90	13.6 $\pm$ (1.5)	13.4 $\pm$ (4.1)
	Urethra D10	10.5 $\pm$ (3.4)	12.2 $\pm$ (4.2)
	Rectum D2cc	4.1 $\pm$ (1.5)	4.4 $\pm$ (3.8)
	P. Bones D10	-2.7 $\pm$ (0.3)	-2.9 $\pm$ (0.8)
$\Delta$ : 0.38	Prostate V90	44.8 $\pm$ (6.0)	50.5 $\pm$ (6.1)
	Prostate D90	22.0 $\pm$ (1.9)	22.2 $\pm$ (2.6)
	Urethra D10	19.2 $\pm$ (2.1)	21.8 $\pm$ (2.1)
	Rectum D2cc	9.3 $\pm$ (2.5)	9.4 $\pm$ (3.1)
	P. Bones D10	-4.4 $\pm$ (0.4)	-4.8 $\pm$ (0.6)
$\Delta$ : 0.65	Prostate V90	80.1 $\pm$ (18.4)	96.7 $\pm$ (20.9)
	Prostate D90	35.9 $\pm$ (5.0)	37.3 $\pm$ (6.6)
	Urethra D10	31.2 $\pm$ (1.9)	36.3 $\pm$ (5.6)
	Rectum D2cc	20.4 $\pm$ (2.9)	20.0 $\pm$ (4.1)
	P. Bones D10	-6.2 $\pm$ (0.6)	-7.0 $\pm$ (1.1)

The proposed biomechanical model in this study was able to successfully simulate the exponential edema resolution pattern reported in previous studies (Waterman *et al* 1998, Tejwani *et al* 2012). For the mean edema resolution pattern ( $\Delta = 0.38$ ), a maximum uncertainty of 1.3%, between the reported values in Tejwani *et al* (2012) at the control points (Day 1, Day 9 and Day 30) and the simulated values using the presented biomechanical model, was measured for the used dataset of 15 patients. The prostate volume changes were associated with an excessive fluid build-up, due to the occurring inflammation and the tissue mechanical properties, considering the biphasic constitution of the prostate. In contrast, with the currently available mathematical models, proposed to date, we have shown that the edema resolution pattern is sensitive to patient-specific variable mechanical properties. The contrast between the linear edema resolution pattern described by Sloboda *et al* (2010) and the exponential resolution pattern shown in previous studies can be associated with the possible prostate stiffness variance in the patient population samples used in these studies. As it was shown by our proposed model, a stiff prostate demonstrates exponential resolution pattern while with a 'softer' prostate the resolution pattern may become linear. The dose differences presented in this study for different prostate Young Modulus values (see table 5) can be attributed to such edema resolution pattern differences. Therefore our study suggests that it is essential to have an *a priori* knowledge of the elastic properties of the prostate in order to estimate the patient specific edema resolution pattern. Ultrasound elastography (Barr *et al* 2012) is an appealing modality for the *in vivo* acquisition of the prostate elastic parameters. Our study suggests that its incorporation in the brachytherapy procedure could be beneficial for the prediction and optimization of the treatment's outcome. Additionally, in order to accurately predict the

**Table 5.** Mean relative changes for the dose metrics of interest for the 15 patients' dataset between Day1 and conventional/dynamic Day30 dosimetry for the different computed prostate young modulus (stiffness) scenarios considered.

Stiffness (Young modulus) scenarios	Dose metric	Day30 dynamic relative Change (%) $\pm$ (SD)	Day30 conventional relative change (%) $\pm$ (SD)
YM: 0.01	Prostate V90	20.8 $\pm$ (5.5)	26.1 $\pm$ (6.4)
	Prostate D90	10.2 $\pm$ (1.7)	10.4 $\pm$ (2.1)
	Urethra D10	7.6 $\pm$ (1.4)	9.3 $\pm$ (1.6)
	Rectum D2cc	6.2 $\pm$ (1.0)	6.3 $\pm$ (1.4)
	P. Bones D10	-1.8 $\pm$ (0.3)	-2.2 $\pm$ (0.5)
YM: 0.05	Prostate V90	44.8 $\pm$ (6.0)	50.5 $\pm$ (6.1)
	Prostate D90	22.0 $\pm$ (1.9)	22.2 $\pm$ (2.6)
	Urethra D10	19.2 $\pm$ (2.1)	21.8 $\pm$ (2.1)
	Rectum D2cc	9.3 $\pm$ (2.5)	9.4 $\pm$ (3.1)
	P. Bones D10	-4.4 $\pm$ (0.4)	-4.8 $\pm$ (0.6)
YM: 0.1	Prostate V90	31.4 $\pm$ (3.5)	34.3 $\pm$ (4.7)
	Prostate D90	19.2 $\pm$ (0.6)	19.0 $\pm$ (0.5)
	Urethra D10	18.9 $\pm$ (6.2)	20.6 $\pm$ (6.1)
	Rectum D2cc	4.2 $\pm$ (2.5)	4.3 $\pm$ (2.8)
	P. Bones D10	-4.2 $\pm$ (0.3)	-4.2 $\pm$ (0.4)

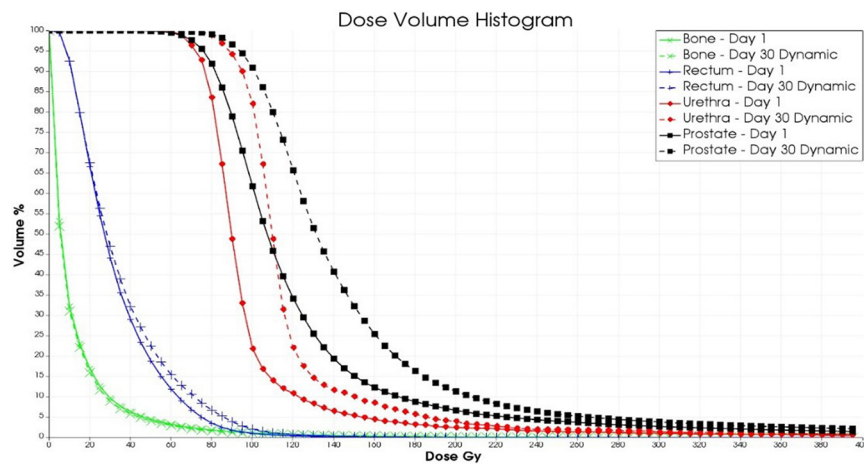


**Figure 7.** DVH representation of the dose deposited in the case of  $\Delta = 0.38$  for a representative patient. The dose deposited in the prostate and the OAR is increased when the edema resolution mechanism is considered due to the prostate contraction and the relative displacements of the seeds.

extent of the edema, further research on the brachytherapy procedure related inflammation is required. In our study a simple linear model of the external fluid pressure due to inflammation was sufficient to simulate the desired edema extent. However, a fully predictive patient-specific biomechanical model may be also possible by incorporating a more realistic inflammation mechanism in our presented model.

Furthermore, this model highlighted the divergence in post-operative dosimetry depending on the edema magnitude and resolution pattern (related edema half-life). The 11.7%

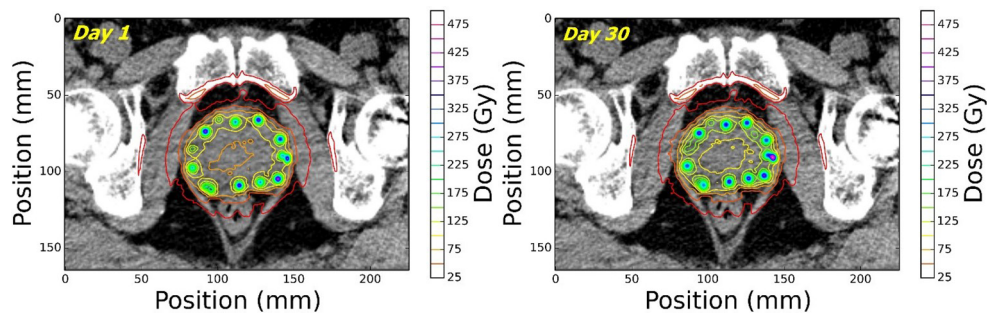


**Figure 8.** Lower dose deposition is recorded in the central area of the prostate, where the urethra is located, in Day1 dosimetry (a) shown by the central isodose (orange—75 Gy) compared to the dynamic Day30 dosimetry (b) where higher dose is shown by the central isodose (yellow—100 Gy).

increase in the prostate D90 reported by Chira *et al* (2013) is within the range predicted by the proposed model, with a D90 increase between 6.2% and 13.6% for an edema magnitude of between 10% and 20% ( $\Delta = 0.1$ –0.2). This has to be considered within the context of a 2% uncertainty in the prostate of our Monte Carlo based dosimetric calculations in combination with the ultrasound resolution induced error in prostate volume extraction, in addition to the lack of prostate volume measurements after the operation in the study of Chira *et al* (2013). In addition, given that there is no evidence that the edema occurs only during the operation, it is also possible that the edema magnitude considered in this study was underestimated.

Relatively to other parameters that may influence dosimetric accuracy in LDR brachytherapy, the prostate D90 increase of between 6.2% and 13.6% as a result of modeling the edema effects is larger than the average of 8.7% and 3.5% differences previously reported between the AAPM Task Group 43 (TG43)/Monte Carlo based dosimetry calculations and the use of accurate prostate calcifications material definition, respectively (Lemarechal *et al* 2015). Within the same comparative context, a more significant impact in the dose to OAR can be seen by accounting for the edema effects, such as the urethra D10 dose increase of approximately 20% relative to 2% differences between the use of the TG43 and MC based dosimetry calculations.

The divergence of the Day30 increase in dose metrics between the different edema scenarios shows that a global correction factor of the Day1 dosimetry as proposed by Tejwani *et al* (2012) cannot be considered as an accurate prediction of the actual dose delivered in the prostate and the OAR. While Day30 dosimetry can evaluate the quality of the brachytherapy procedure, assuming that the edema has resolved by then, it cannot account for the dynamic volume changes and corresponding seed displacements between Day1 and Day30. The dynamic dosimetry algorithm proposed by Leclerc *et al* (2006) has shown average dose differences of 20 Gy in prostate D90 between Day1 and Day30 dosimetry. Similarly, our study shows that dynamic monitoring of volume changes and seeds' displacements lead to an increase in the prostate D90 of 22% but also in the urethra dose hot spots, as described by the urethra D10 of 19.2%, for an average edema magnitude ( $\Delta = 0.38$ ) between Day1 and dynamic Day30 dosimetry. The higher difference between dynamic Day30 and conventional Day30 dosimetry observed, was 5.12% for the case of the higher edema magnitude scenario considered ( $\Delta = 0.65$ ). This has to be considered only as an indication of the potential differences given the small number of patients considered in this study. A bigger population will be clearly necessary to establish the range of expected dosimetric differences and further validate our findings.

A limitation of the proposed mesh based deformable model is the lack of multi-resolution capabilities without an associated increase in the overall computational times. For example, in the case of large edema magnitude scenarios, the quality of the geometry discretization (tetrahedral mesh) using low quality tetrahedra can lead to higher inaccuracies in regions undergoing large deformations. If one was to use finer tetrahedra throughout the prostate volume, to account more accurately for such large deformations the overall computational times would become prohibitive for clinical use. However, a multi-resolution model would facilitate an accurate modeling of interactions and movement of fine structures, such as seeds and calcifications, within the overall prostate volume. Alternative modeling approaches such as the smoothed finite element method (Liu *et al* 2007) or mesh-free methods (Horton *et al* 2010) could possibly be used to avoid these limitations. Such models can also be used in other locally relevant phenomena such as the interactions between prostate tissue and the needles used to insert the radioactive seeds for navigation purposes.

## 5. Conclusions and future work

The first contribution of the presented study is the development of a biomechanical model capable of incorporating patient-specific mechanical properties in the prostate edema resolution pattern computation. The second contribution is the application of the computed deformation map given by the model's mesh topology determined using the original patient CT volume. To our knowledge, this is the first time a dynamic Monte Carlo simulation on deformable voxelized datasets for prostate LDR brachytherapy has been performed. This allowed us to consider the dynamic changes of the patient's anatomy and the seed locations in the dose distribution calculations, a first step towards a truly dynamic dosimetry in LDR prostate brachytherapy.

In the future and in order to improve the proposed biomechanical model we plan to incorporate localized edema effects considering the seeds' activity contribution in the extent of the edema (Tejwani *et al* 2012), replacing the currently used global edema assumptions. In addition, a more accurate inflammation mechanism will be developed aiming towards a predictive model, which will be subsequently introduced within a novel brachytherapy treatment planning framework, incorporating the use of ultrasound based elastography, able to predict the dynamic dose distribution in the prostate and OAR considering the edema dynamics and patient specific prostate tissue properties.

## Acknowledgments

This work was partly supported by the French Brittany Region and by the French ANR within the Investissements d'Avenir program (Labex CAMI) under reference ANR-11-LABX-0004 (Integrated project CAPRI) and through FOCUS project (ANR-16-CE19-0011).

## References

- Aguilera A R, Salas A L, Perandr s D M and Otaduy M A 2015 A parallel resampling method for interactive deformation of volumetric models *Comput. Graph.* **53** 147–55
- Ahn B M, Kim J, Ian L, Rha K H and Kim H J 2010 Mechanical property characterization of prostate cancer using a minimally motorized indenter in an *ex vivo* indentation experiment *Urology* **76** 1007–11



- Barr R G, Memo R and Schaub C R 2012 Shear wave ultrasound elastography of the prostate: initial results *Ultrasound* **28** 13–20
- Beaulieu L *et al* 2012 Report of the task group 186 on modelbased dose calculation methods in brachytherapy beyond the tg-43 formalism: current status and recommendations for clinical implementation *Med. Phys.* **39** 6208–36
- Bert J, Lemaréchal Y and Visvikis D 2016 New hybrid voxelized/analytical primitive in Monte Carlo simulations for medical applications *Phys. Med. Biol.* **61** 3347
- Chen Z, Yue N, Wang X, Roberts K B, Peschel R and Nath R 2000 Dosimetric effects of edema in permanent prostate seed implants: a rigorous solution *Int. J. Radiat. Oncol. Biol. Phys.* **47** 1405–19
- Chira C, Delouya G, Larrivière S, Carrier J F and Tausky D 2013 Prostate volume changes during permanent seed brachytherapy: an analysis of intra-operative variations, predictive factors and clinical implication *Radiat. Oncol.* **8** 177
- Davies B L, Harris S J and Dibble E 2004 Brachytherapy—an example of a urological minimally invasive robotic procedure *Int. J. Med. Robot. Comput. Assist. Surg.* **1** 88–96
- Day J, Rubin J, Vodovotz Y, Chow C C, Reynolds A and Clermont G 2006 A reduced mathematical model of the acute inflammatory response II. Capturing scenarios of repeated endotoxin administration *J. Theor. Biol.* **242** 237–56
- Dogan N, Mohideen N, Glasgow G P, Keys K and Flanigan R C 2002 Effect of prostatic edema on CT-based postimplant dosimetry *Int. J. Radiat. Oncol. Biol. Phys.* **53** 483–9
- Fang Q and Boas D A 2009 Tetrahedral mesh generation from volumetric binary and grayscale images *IEEE Int. Symp. Biomedical Imaging: From Nano to Macro ISBI'09* pp 1142–5
- Galbusera F, Schmidt H, Noailly J, Malandrino A, Lacroix D, Wilke H J and Shirazi-Adl A 2011 Comparison of four methods to simulate swelling in poroelastic finite element models of intervertebral discs *J. Mech. Behav. Biomed. Mater.* **4** 1234–41
- Haas G P, Delongchamps N, Brawley O W, Wang C Y and de la Roza G 2008 The worldwide epidemiology of prostate cancer: perspectives from autopsy studies *Can. J. Urol.* **15** 3866
- Haridas B *et al* 2006 PelvicSim—a computational-experimental system for biomechanical evaluation of female pelvic floor organ disorders and associated minimally invasive interventions *Stud. Health Technol. Inf.* **119** 182–7
- Horton A *et al* 2010 A meshless total Lagrangian explicit dynamics algorithm for surgical simulation *Int. J. Numer. Methods Biomed. Eng.* **26** 977–98
- Hu Y, Morgan D, Ahmed H U, Pendsé D, Sahu M, Allen C and Barratt D 2008 Modelling prostate gland motion for image-guided interventions *Biomedical Simulation* (Berlin: Springer) pp 79–88
- Kirk D 2007 NVIDIA CUDA software and GPU parallel computing architecture *ISMM* vol 7
- Kirov A S and Williamson J F 2001 Monte Carlo-aided dosimetry of the Source Tech Medical Model STM1251 I-125 interstitial brachytherapy source *Med. Phys.* **28** 764–72
- Leclerc G *et al* 2006 Prostatic edema in I125 permanent prostate implants: dynamical dosimetry taking volume changes into account *Med. Phys.* **33** 574–83
- Lee H P, Lin M C and Foskey M 2008 Physically-based validation of deformable medical image registration *Medical Image Computing and Computer-Assisted Intervention-MICCAI 2008* (Berlin: Springer) pp 830–8
- Lemaréchal Y, Bert J, Falconnet C, Després P, Valeri A, Schick U and Visvikis D 2015 GGEMS-Brachy: GPU GEant4-based Monte Carlo simulation for brachytherapy applications *Phys. Med. Biol.* **60** 4987
- Li C, Guan G, Zhang F, Song S, Wang R K, Huang Z and Nabi G 2014 Quantitative elasticity measurement of urinary bladder wall using laser-induced surface acoustic waves *Biomed. Opt. Express* **5** 4313–28
- Li X G, von Holst H, Ho J and Kleiven S 2009 3D finite element modeling of brain edema: initial studies on intracranial pressure using comsol multiphysics *Excerpt from the Proc. of the COMSOL Conf.*
- Liu G R *et al* 2007 Theoretical aspects of the smoothed finite element method (SFEM) *Int. J. Numer. Methods Eng.* **71** 902–30
- Maas S A, Ellis B J, Ateshian G A and Weiss J A 2012 FEBio: finite elements for biomechanics *J. Biomech. Eng.* **134** 011005
- Nath R *et al* 2009 AAPM recommendations on dose prescription and reporting methods for permanent interstitial brachytherapy for prostate cancer: report of task group 137 *Med. Phys.* **36** 5310–22
- Rivard M J, Coursey B M, DeWerd L A, Hanson W F, Huq M S, Ibbott G S and Williamson J F 2004 Update of AAPM task group no. 43 report: a revised AAPM protocol for brachytherapy dose calculations *Med. Phys.* **31** 633–74



- Schneider W, Bortfeld T and Schlegel W 2000 Correlation between CT numbers and tissue parameters needed for Monte Carlo simulations of clinical dose distributions *Phys. Med. Biol.* **45** 459
- Sloboda R S, Usmani N, Monajemi T T and Liu D M 2012 Impact of edema and seed movement on the dosimetry of prostate seed implants *J. Med. Phys./Assoc. Med. Phys. India* **37** 81
- Sloboda R S, Usmani N, Pedersen J, Murtha A, Pervez N and Yee D 2010 Time course of prostatic edema post permanent seed implant determined by magnetic resonance imaging *Brachytherapy* **9** 354–61
- Starling E H 1896 On the absorption of fluids from the connective tissue spaces *J. Physiol.* **19** 312–26
- Tejwani A, Bieniek E, Puckett L, Lavaf A, Guirguis A, Bennish A and Ashamalla H 2012 Clinical Investigations: case series analysis of post-brachytherapy prostate edema and its relevance to post-implant dosimetry. Post-implant prostate edema and dosimetry *J. Contemp. Brachyther.* **4** 75
- Villeneuve M *et al* 2008 Relationship between isotope half-life and prostatic edema for optimal prostate dose coverage in permanent seed implants *Med. Phys.* **35** 1970–7
- Wang Y *et al* 2016 Patient-specific deformation modelling via elastography: application to image-guided prostate interventions *Sci. Rep.* **6** 27386
- Waterman F M, Yue N, Corn B W and Dicker A P 1998 Edema associated with I-125 or Pd-103 prostate brachytherapy and its impact on post-implant dosimetry: an analysis based on serial CT acquisition *Int. J. Radiat. Oncol. Biol. Phys.* **41** 1069–77
- Yan Z *et al* 2012 Modulus reconstruction from prostate ultrasound images using finite element modeling *SPIE Medical Imaging* (International Society for Optics and Photonics)
- Yue N, Mori J, Nath R, Heron D E and Huq M S 2006 External beam radiotherapy boosts to reduce the impact caused by edema in prostate permanent seed implants *Phys. Med. Biol.* **51** 2267

## B.9 Recalage en imagerie multimodale pour la radiothérapie

### Fully automatic deformable registration of pretreatment MRI/CT for image-guided prostate radiotherapy planning

Iyas Hamdan<sup>a)</sup> and Julien Bert  
*LaTIM, INSERM, UMR 1101, CHRU Morvan, Brest, France*  
*Institut de Recherche Technologique b<>com, Cesson-Sévigné, France*

Catherine Cheze Le Rest  
*LaTIM, INSERM, UMR 1101, CHRU Morvan, Brest, France*  
*Department of Nuclear Medicine, CHU Milétrie, Poitiers, France*

Jean Pierre Tasu  
*Department of Radiology, CHU Milétrie, Poitiers, France*

Nicolas Bousson  
*LaTIM, INSERM, UMR 1101, CHRU Morvan, Brest, France*  
*Department of Radiotherapy, CHRU Morvan, Brest, France*

Antoine Valeri  
*Department of Urology, CHRU Morvan, Brest, France*

Guillaume Dardenne and Dimitris Visvikis  
*LaTIM, INSERM, UMR 1101, CHRU Morvan, Brest, France*  
*Institut de Recherche Technologique b<>com, Cesson-Sévigné, France*

(Received 20 October 2016; revised 4 October 2017; accepted for publication 7 October 2017; published 6 November 2017)

**Purpose:** In prostate radiotherapy, dose distribution may be calculated on CT images, while the MRI can be used to enhance soft tissue visualization. Therefore, a registration between MR and CT images could improve the overall treatment planning process, by improving visualization with a demonstrated interobserver delineation variability when segmenting the prostate, which in turn can lead to a more precise planning. This registration must compensate for prostate deformations caused by changes in size and form between the acquisitions of both modalities.

**Methods:** We present a fully automatic MRI/CT nonrigid registration method for prostate radiotherapy treatment planning. The proposed registration methodology is a two-step registration process involving both a rigid and a nonrigid registration step. The registration is constrained to volumes of interest in order to improve robustness and computational efficiency. The method is based on the maximization of the mutual information in combination with a deformation field parameterized by cubic B-Splines.

**Results:** The proposed method was validated on eight clinical patient datasets. Quantitative evaluation, using Hausdorff distance between prostate volumes in both images, indicated that the overall registration errors is  $1.6 \pm 0.2$  mm, with a maximum error of less than 2.3 mm, for all patient datasets considered in this study.

**Conclusions:** The proposed approach provides a promising solution for an effective and accurate prostate radiotherapy treatment planning since it satisfies the desired clinical accuracy. © 2017 American Association of Physicists in Medicine [<https://doi.org/10.1002/mp.12629>]

Key words: multimodal imaging, mutual information, nonrigid registration, prostate radiotherapy

#### 1. INTRODUCTION

Medical images are a vital component of clinical applications; not only for diagnosis but also for treatment planning, delivery, and evaluation. Radiotherapy, a treatment involving the use of ionizing radiation on tumors, can be considered today as an image-guided intervention whose evolution has been clearly linked to imaging. Current trends in prostate radiotherapy involve the delivery of an increasingly conformational dose to the prostate or tumor foci while limiting the dose to the surrounding healthy organs. As such, image

guidance is essential in the treatment planning step for improving the overall dose optimization process. Radiotherapy can be divided into two main categories; external beam radiation therapy (EBRT) and internal radiotherapy, also called brachytherapy. Prostate brachytherapy consists in placing radioactive sources within the prostate. In early-stage prostate cancer, patients undergoing low dose rate brachytherapy, using permanently implanted radioactive sources (such as Iodine-125), have generally better urinary continence and sexual functions compared to other radiotherapy techniques.<sup>1</sup>

Computed Tomography (CT) images can be used in the treatment planning phase in order to calculate dose distribution, based on tissue electron density values. A dose distribution that considers soft tissue heterogeneities, based for example on the use of Monte Carlo simulations, can significantly reduce dosimetry errors.<sup>2</sup> On the other hand, and considering that the CT is not well suited for soft tissue visualization, it is well accepted that Magnetic Resonance Imaging (MRI), with the associated superior soft tissue contrast, can be an advantage in the pelvic region compared to CT.<sup>3,4</sup> As a result, the use of MRI for target delineation in prostate cancer EBRT has been shown to change the delineation of the clinical target volume in up to 20% of the patient cases, compared to CT only based planning.<sup>5</sup> In addition, MR has shown a significant decrease in interobserver delineation variation, particularly at the prostatic apex.<sup>6</sup> Although not yet proven, one would therefore expect that MRI could potentially improve radiotherapy treatment planning and delivery, with reduced associated toxicity, by providing a better delineation of the prostate location as well as the organs at risk. To make use of both MR and CT modalities, for target delineation and dosimetry calculation respectively, it is essential that these images are accurately aligned.

MR and CT images cannot be acquired simultaneously, and in most cases are acquired within a few days or weeks interval. In addition, patient positioning in the MR and CT imaging systems may be different. Therefore, there would be some differences in prostate location and size as a result of temporal evolution deformations, different bladder and rectum fillings as well as patient motion.<sup>7</sup> As such, a nonrigid registration is necessary.

A number of MRI/CT registration techniques dedicated to prostate radiotherapy have been described in the literature. Some of them use pelvic bones and/or implanted fiducial markers as landmarks for rigid registration.<sup>8–10</sup> Out of these three methods, the one proposed by Servois *et al.*<sup>9</sup> had the best performance with a maximum registration error of 2.2 mm. A comparison between two rigid registration methods; namely a landmark-based approach using fiducial gold markers inserted in the prostate and a surface-based method using the iterative closest point (ICP) algorithm was performed by Huisman *et al.*<sup>11</sup> However, manual identification of the markers and manual prostate delineation was required for the first and second method respectively. Although the ICP algorithm gave significantly better results than the other method, registration errors of >2 mm were observed in 14% of the cases, including errors of >5 mm in some of the cases. Another comparison study between two rigid registration methods for prostate radiotherapy was carried out by Korsager *et al.*<sup>12</sup> Both methods needed manual interaction; the first method required identification of landmarks while the other required a bounding box manually defined around the prostate. Vidakovic *et al.*<sup>13</sup> exploited the presence of seeds and needle tracks to perform a rigid registration using the mutual information for postimplant dosimetry in prostate brachytherapy. Their method was limited by time requirements and uncertainties associated with the

identification of needles and seeds. The root mean square (RMS) value following their rigid registration method was of  $2.1 \pm 0.7$  mm. Others made use of planning MRI to facilitate the alignment of diagnostic MRI with the planning CT allowing the mapping of the tumor location from the diagnostic MRI onto the planning CT where a targeted dose plan may be generated.<sup>14</sup> The prostate needed to be manually delineated on the diagnostic MRI at first. Moreover, manually identified landmarks were used in aligning the planning MRI with the CT. Recently, Zhong *et al.*<sup>15</sup> presented a nonrigid registration methodology for MRI-guided prostate radiotherapy where a finite element method (FEM) was used to improve the performance of B-Spline registration. Once more, the presented methodology required a manual delineation of the prostate and the surrounding organs. Moreover, their registration errors were as big as 4.7 mm.

Therefore, most methods dedicated to prostate radiotherapy are limited to rigid transformations only, suffer from the use of implanted markers or require a manual step including prostate segmentation or identification of landmarks. Such step is both time-consuming and subjects to intra- and interobserver variability inaccuracies depending on the experience of the user.

The objective of this work is the development of a fully automatic MRI/CT nonrigid registration method for prostate radiotherapy treatment planning. The proposed methodology does not require any manual segmentation, landmark selection, or markers to be inserted in the prostate. The registration is done in two steps; a rigid registration is used to initialize a second nonrigid registration step. In order to improve the robustness and the computational efficiency of the approach, the registration is constrained to volumes of interest (VOIs). The described methodology is validated on eight clinical patient datasets using both qualitative and quantitative evaluation criteria.

## 2. MATERIALS AND METHODS

The proposed algorithm is a two-step process involving both a rigid and nonrigid registration phase. Each registration is constrained to a different VOI, which is determined automatically by detecting the prostate location.

### 2.A. VOIs determination

The prostate is situated in the pelvic cavity, behind the lower part of the pubic symphysis, which lies at the same level as the two tips (right and left) of the greater trochanter of the femurs (see Fig. 1). Consequently, by detecting these two points we can determine the location of the pubic symphysis and, therefore, the prostate.

To improve the visualization of bone and other higher attenuation structures (for example contrast-enhanced structures) in CT, we use a maximum intensity projection (MIP) in the coronal axis direction. An automatic thresholding, using Otsu's method,<sup>16</sup> is subsequently applied on the MIP image illustrated in Fig. 1. The thresholded image is shown

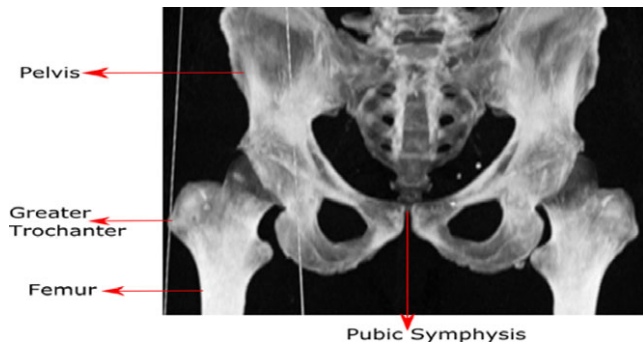


FIG. 1. Pelvis bones. [Color figure can be viewed at [wileyonlinelibrary.com](http://wileyonlinelibrary.com)]

in Fig. 2(a). Finally, an opening morphological transformation is applied to remove any remaining artifacts (scanning bed structures, etc.), as shown in Fig. 2(b).

This final binary image is subsequently used for the detection of the tip of the greater trochanter, considering that it represents the furthest point from the central vertical axis of the image. The axial slice corresponding to the line connecting the two tips is extracted from the CT volume [illustrated in Fig. 3(a)] and then thresholded in order to identify different bony structures in the image (from +700 HU to +3000 HU for cancellous and dense bone respectively). The resulting binary image is shown in Fig. 3(b).

Regions of interest (ROIs) are automatically defined on this binary image, on a slice to slice basis, resulting in a VOI that can be used for the registration. The rigid registration is constrained to a volume around the pelvic structures (pelvic VOI) assuming that the pelvis does not deform between the two acquisitions and, therefore, fulfills a rigid-body

hypothesis. As for the nonrigid registration, it is restricted to a VOI around the prostate only (prostate VOI) in order to account for local deformations in that region.

A connected-component labeling algorithm<sup>17</sup> is applied on the binary image in order to retrieve contours for detecting and identifying different connected regions (labels). The surface of each label is calculated and the two femurs, identified by having the biggest surfaces, are automatically excluded from the pelvic ROI [see Fig. 4(a)]. Finally, the distance between each label pair and the central vertical axis is calculated, allowing the identification and exclusion of the ischium by being further from this axis than the pubic symphysis. The prostate ROI is shown in Fig. 4(b).

## 2.B. Registration

An intensity-based registration is used in this work. A similarity criterion referred to as mutual information (MI)<sup>18</sup> is used to measure the statistical dependence or the information redundancy by measuring the distance between probability densities of corresponding voxels in the two images to be aligned. The main components of the proposed registration method are described in the following paragraphs.

A first registration step is applied to globally align the two images, while the nonrigid registration step that follows is used to determine the local deformations of the prostate. Consequently, the rigid registration helps initializing the nonrigid registration step with a solution that is close to the optimal one, improving both robustness and computation time as well as reducing the probability of local minima for the nonrigid registration. The initial rigid registration, constrained on the pelvic VOI, is based on an affine model (rigid plus scaling and shearing) while the nonrigid registration, restricted to the

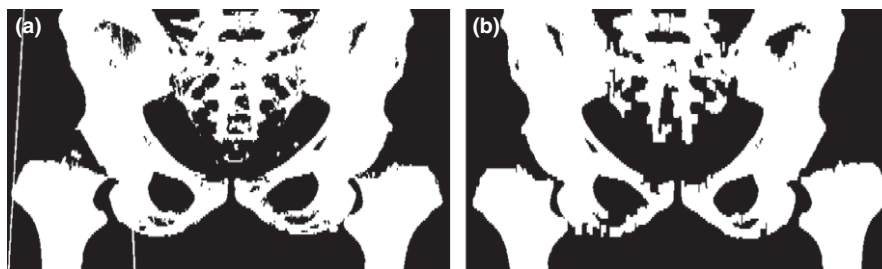


FIG. 2. MIP, (a) after thresholding, (b) after opening operation.

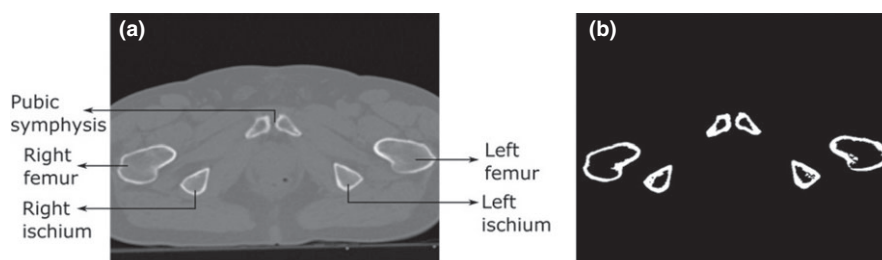


FIG. 3. CT slice used for determining ROIs, (a) original image, (b) thresholded image.

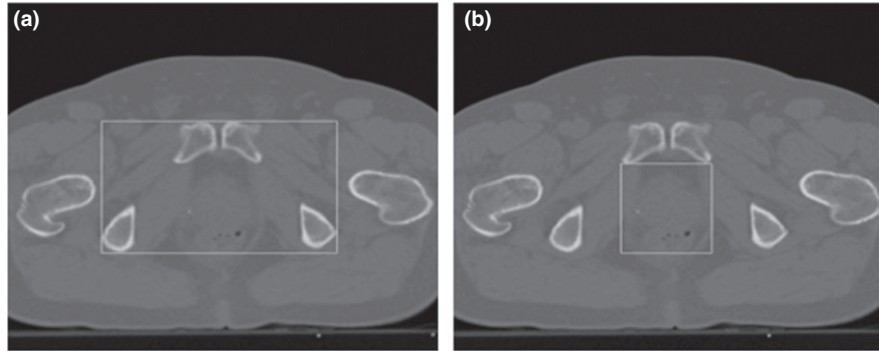


FIG. 4. Determination of ROIs, (a) pelvic ROI, (b) prostate ROI.

prostate VOI, is based on cubic B-Spline functions<sup>19</sup> in order to detect the deformation field between the two images (the MRI and the registered CT). The CT image was deformed, instead of the MRI, to avoid affecting the quality of the MR image (resampling, interpolation, etc.) which would be used for prostate delineation.

The transformation that maximizes the MI between the MR and CT images is determined iteratively using a regular step gradient descent optimizer.<sup>20</sup> This optimizer is an improved form of the original gradient descent optimizer that avoids taking too large steps. At each iteration, the optimizer takes a step in the direction of the derivative, and whenever the optimizer determines that the direction of the derivative changes, the step length is reduced by a factor set by the user. Both initial and minimum step lengths are also defined by the user. The minimum step length controls the accuracy by defining when convergence has been achieved. The approach can be formulated as a minimization problem:

$$\hat{\phi} = \arg \min_{\phi} (-MI(\phi; I_f, I_m)) \quad (1)$$

where,  $\phi$  represents the parameters' vector of B-Spline coefficients. To register the two images, the optimal set of parameters is determined for the transformation  $T(\phi) = [T_x, T_y, T_z]$  such that  $I_m(T(X, \phi))$  is in correspondence with  $I_f$ . The parameters  $\phi$  of the transformation  $T$  are the coordinates of the control points  $\phi_{i,j,k}$ . The optimal set of parameters is determined iteratively using the optimization strategy as follows:

$$\phi_{k+1} = \phi_k + a_k d_k \quad (2)$$

where,  $d_k$  is the search direction, and  $a_k$  is a factor controlling the step size.

### 3. EVALUATION STUDY

#### 3.A. Clinical patient datasets

The proposed method was validated using eight sets of clinical anonymized patient data undergoing LDR brachytherapy for early-stage prostate cancer. For each patient, MR (T1-weighted) and CT pelvic images were pre-operatively acquired (MR and CT images were acquired for the diagnosis and treatment planning respectively). These

images were acquired in different facilities, and using different acquisition systems.

### 3.B. Evaluation metrics

#### 3.B.1. Visual assessment

For all datasets, an expert radiologist segmented the prostate on both modalities before the registration as well as the registered CT after each step of the registration process. The expert was asked to segment the prostate only on the slices where the prostate boundaries on both modalities can be clearly detected without any difficulties. A visual assessment of prostate volumes' overlap was then considered to evaluate both the rigid and the nonrigid registration steps.

#### 3.B.2. Quantitative analysis

The aim of this evaluation is to compare prostate segmented volumes from both MR and CT images after the registration. These volumes are obtained following this workflow:

1. The prostate volume was manually segmented, by the same expert, on both CT and MR images before the registration. Voxels' value within the segmented prostate volume is 1, and 0 otherwise.
2. CT and MR images were registered using the proposed methodology.
3. The transformation that aligns the CT and the MRI was applied on the prostate segmented volume on the CT image, using inverse mapping interpolation (voxels in the registered image were mapped back onto the fixed image in order to avoid holes and overlaps), resulting in the registered prostate volume (prostate volume on the registered CT).
4. Finally, the registered prostate volume was compared to the prostate segmented volume on the MR image.

The evaluation was done using different criteria. At first, the two prostate volumes were used to determine the oriented bounding boxes that enclose the prostate in the MR and deformed CT images. The bounding box was defined as the box with the smallest measure within which all voxels of the



prostate volume can fit. The characteristics (size, center, orientation, etc.) of the two bounding boxes were subsequently compared.

In order to determine the degree of prostate volumes' overlap, the Hausdorff distance ( $d_H$ ) measure was used.  $d_H$  measures the degree of mismatch between two point sets (the position of the center of each voxel in the prostate segmented volumes) by measuring the maximum distance of one point set to the closest point in the second set. Let  $A$  and  $B$  be the two point sets, the Hausdorff distance  $d_H$  is given by:

$$d_H(A, B) = \max\{d_h(A, B), d_h(B, A)\} \quad (3)$$

where:

$$d_h(A, B) = \max_{a \in A} \left\{ \min_{b \in B} \{d(a, b)\} \right\} \quad (4)$$

and  $d(a, b)$  is the distance between the points  $a$  and  $b$ .

In the rest of the paper, we will refer to distances between 2D images (slices) by  $2D\_d_H$ , whereas  $3D\_d_H$  represents the distance between two 3D image volumes.

Finally, the Dice similarity coefficient (DSC) was also used to compute the degree of prostate volumes' overlap between the two images (the prostate segmented volume on the MRI and the prostate registered volume on the deformed CT). DSC can be used to measure how similar two images are, in terms of the number of common voxels. It ranges between 0 (no overlap) and 1 (complete volume overlap). For two given images  $A$  and  $B$ , DSC is calculated as follows:

$$DSC = \frac{2|A \cap B|}{|A| + |B|} \quad (5)$$

where, the operator  $| \cdot |$  represents the size of a set, and  $\cap$  represents the intersection of two sets.

### 3.B.3. Reproducibility and robustness analysis

The evaluation criteria proposed above are used on the registered images after the manual segmentation step. Therefore, errors may originate from either the registration method itself or from the manual segmentation step.

In order to evaluate the segmentation errors, two expert radiologists were asked to segment the whole volume of the prostate twice for all patient datasets. Each expert was blinded to the segmentations performed by the other expert as well as to his first segmentation, when repeating the task for the second time. Experts were asked to segment the prostate on MR and CT images before the image registration process. A week later, both experts were asked to perform the segmentation process for the second time. The experts' segmentations on the CT image were transformed to the deformed CT, using the transformation resulting from the registration process between CT and MR images. Firstly, for all patient datasets,  $3D\_d_H$  was calculated between prostate volumes in both images (prostate segmented volume on the MRI and prostate registered volume on the CT) for each of the two segmentations done by both experts. Subsequently, the reproducibility of the segmentation was studied by

comparing the mismatches from the two segmentations performed by each expert separately (intraobserver variability) and to each other (interobserver variability).

Concerning the registration errors, the robustness of the proposed approach was studied. The robustness study consisted in evaluating the performance of the method in the presence of perturbations, such as for example changes in initialization. Therefore, the initialization of the method was modified (by translating and/or rotating the CT volume before the registration, deformations of up to  $\pm 50$  mm and  $\pm 30^\circ$  were considered) and the registration results were tracked in order to determine the magnitude of perturbations that can be tolerated in terms of the overall registration accuracy.

## 4. RESULTS

Considering overall computational efficiency, the proposed two-step registration method was completed on an average of 2.5 min, on an Intel<sup>®</sup> Core<sup>™</sup> i7-3840QM CPU @ 2.80 GHz processor.

### 4.A. Visual assessment

Figure 5 shows a checkerboard between MR and CT images of one of the patient datasets before [Fig. 5(a)] and after [Fig. 5(b)] the nonrigid registration. A checkerboard between images of the patient dataset with the largest prostate deformations between the two modalities, due to different fillings of the rectum, is illustrated in Fig. 6.

In all cases, the results were visually acceptable and no significant residual misalignment could be observed. The prostate contours following the nonrigid registration were continuous between MR and CT images for all datasets, indicating that the proposed nonrigid registration approach was able to align the images from the two modalities in a prostate imaging context.

### 4.B. Quantitative analysis

Prostate segmented volumes were used to automatically determine a bounding box around the prostate in the MR and the deformed CT images, following the nonrigid registration step, for all datasets. Figure 7 illustrates a bounding box on a CT image of one of the patient datasets, where the centroid represents the  $[x, y, z]$  coordinates of the bounding box center (O) in terms of voxels, the orientation ( $\alpha$ ) is calculated around the central vertical axis, and the size represents the number of voxels contained in the bounding box along the three axes  $x$ ,  $y$ , and  $z$ .

The comparison between the characteristics of these bounding boxes in MR and deformed CT images gave good results, both in terms of voxel size and overall volume, with differences of less than a single voxel and 2% respectively. As for the orientation (here calculated relative to the coronal axis only), bounding boxes had the same orientation with a difference of less than 0.4 radian for all datasets.



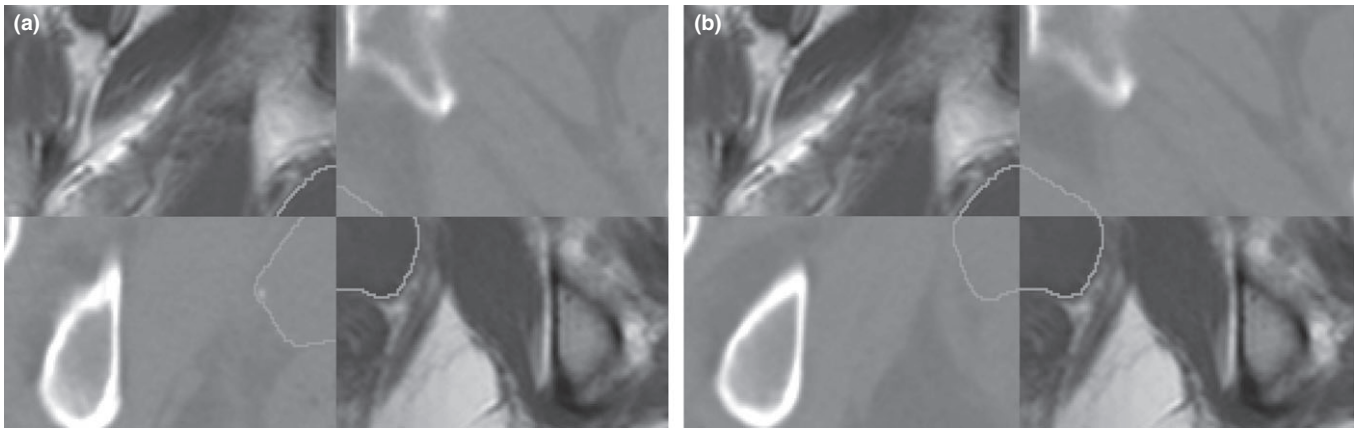


FIG. 5. Checkerboard showing prostate contours on MR and CT images (a) after rigid registration only, (b) after nonrigid registration.

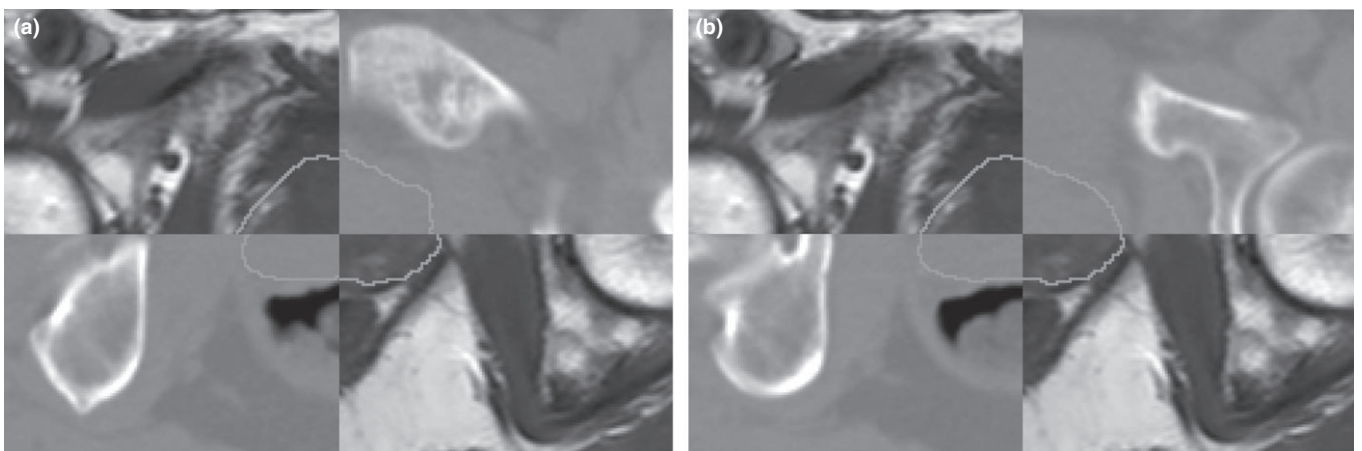


FIG. 6. Checkerboard showing prostate contours on MR and CT images (a) after rigid registration only, (b) after nonrigid registration.

Mismatches between prostate segmented volumes in MR and deformed CT images were calculated for all patient datasets, using  $2D_{d_H}$ . Figure 8 illustrates these mismatches in the form of box plots (box and whisker diagram).

As illustrated in this figure, the median value of the mismatch between prostate segmented volumes in the MR and the deformed CT images was between 1.3 and 1.9 mm. As for the maximum mismatch, it was always less than 2.3 mm for all eight patient datasets.

The Dice similarity coefficient was finally calculated for all datasets in order to assess volume overlap between

prostate segmented volumes in both modalities. DSC was between 0.89 and 0.93 for all patient datasets.

#### 4.C. Reproducibility and robustness analysis

Figure 9 shows one of the segmentations performed by the two experts on CT and MR images, of one of the patient datasets, before the registration.

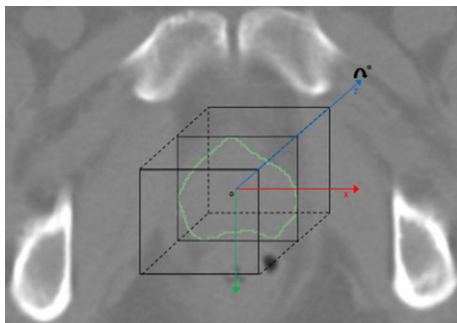


FIG. 7. Bounding box around the prostate on CT. [Color figure can be viewed at wileyonlinelibrary.com]

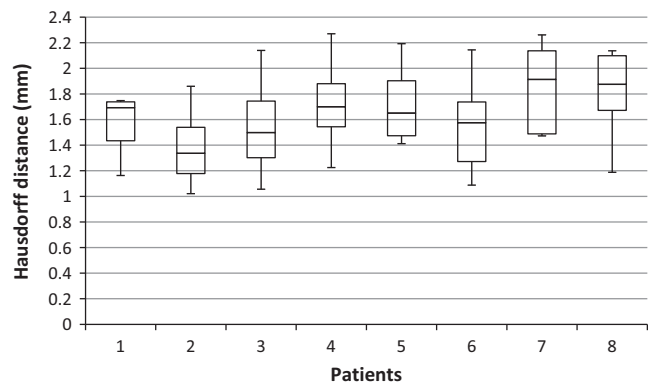


FIG. 8. Box plots representing the 2D Hausdorff distances between prostate segmented volumes in MR and deformed CT images.

As illustrated in Fig. 9, errors were more likely to occur while segmenting the prostate on CT images, especially in the regions of the base and the apex of the prostate. The dimensions of the segmented prostate volumes performed by the two experts in CT and MR images are shown in Table I.

Mismatches between prostate volumes after the registration (the segmented volume from the MRI and the registered one from the deformed CT) were calculated for all patient datasets, using  $3D_{dH}$ . Mismatches in each of the segmentations performed by the two experts are illustrated in Fig. 10 in the form of box plots.

For each segmentation, the median value of the mismatch between prostate volumes in all datasets was calculated. For the first expert, the median mismatch value was 3.1 mm and 4.6 mm for both segmentations. For the second expert, these values were bigger, where median mismatch values for the two segmentations were 5.2 mm and 5.8 mm respectively. Repeating the same task by the two experts revealed intraobserver variability of  $1.5 \pm 0.8$  mm and  $1.7 \pm 0.6$  mm for the first and the second expert respectively. As for the reproducibility of the task, interobserver variability values of  $2.2 \pm 1.3$  mm and  $1.9 \pm 1.3$  mm were measured considering the two repeated segmentations from the two experts respectively.

In terms of robustness, the resulting mismatch between prostate volumes in MR and CT images was always less than 2.3 mm for all patient datasets, irrespective of the magnitude of deformations.

## 5. DISCUSSION

In this study, a novel registration methodology was proposed in the context of prostate radiotherapy. The purpose was to accurately align MR and CT images of the pelvis in order to improve the overall process of treatment planning. Generally, manual segmentation of the prostate or visual identification of landmarks is required in such a registration process. This step can be time-consuming and is associated to reduced reproducibility and robustness which in turn may lead to errors in the registration process and, subsequently, to a nonoptimal dose estimation. The objective of this work was

TABLE I. Dimensions of the segmented prostate.

	Volume (cc)	Size (mm) [length, width, depth]
First expert		
MRI	34.4	[44.3, 36.9, 35.7]
CT	42.2	[49.2, 38.1, 38]
Second expert		
MRI	40.7	[45.1, 36.7, 41.7]
CT	49.9	[51.1, 39.5, 42]

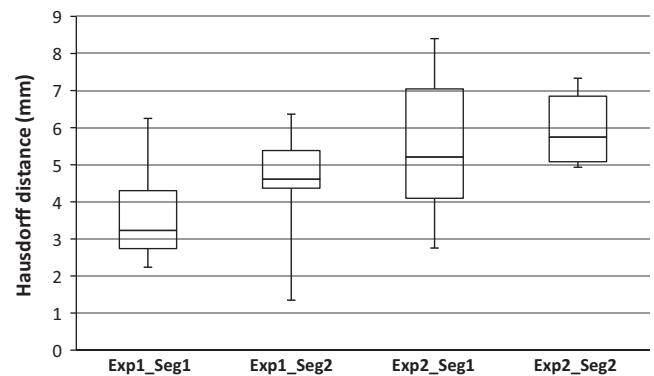


FIG. 10. Box plots representing the 3D Hausdorff distances between prostate segmented volumes in MRI and deformed CT. Exp1 and Exp2 represent the first and the second expert respectively. Seg1 and Seg2 represent the two segmentations.

to propose a fully automatic registration method that can compensate for any prostate deformations and, therefore, ensure an accurate MR/CT image matching.

The proposed registration method was validated on eight clinical patient datasets using both qualitative and quantitative criteria. Considering the absence of ground truth in the clinical datasets, the assessment was based on an expert manual segmentation approach. Each step of this evaluation process was assessed in order to provide relevant associated errors. First of all, a visual inspection of the prostate boundaries' overlap indicated the accuracy of this method where the contours' overlap on both modalities was visually verified and no residual misalignment was found. Quantitative

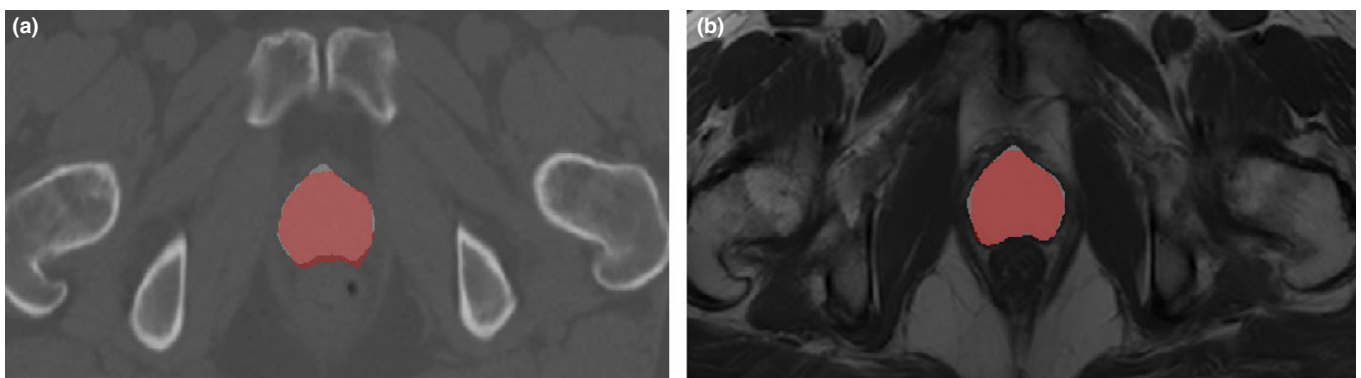


FIG. 9. Prostate volumes segmented by the first (white) and the second (red) expert on (a) CT and (b) MRI before the registration. [Color figure can be viewed at [wileyonlinelibrary.com](http://wileyonlinelibrary.com)]

criteria, such as the bounding box, the Hausdorff distance and the dice similarity coefficient, confirmed the accuracy of the proposed method with a maximum mismatch between prostate volumes in MR and CT images of  $1.6 \pm 0.2$  mm and a dice similarity coefficient of  $>0.89$  for all patient datasets considered. In addition, the inaccuracies caused by the registration method were within the limits of the uncertainties associated with the manual prostate delineation process.

Subsequently, the robustness of the proposed method was also evaluated. The registration was performed following CT volume translations and/or rotations of  $\pm 50$  mm and  $\pm 30^\circ$  respectively, with associated maximum mismatch between prostate volumes in MR and CT images systematically  $<2.3$  mm. Finally, in terms of reproducibility, two experts were asked to delineate the whole prostate volume on MR and CT images twice and for all patient datasets before the registration. Then, the segmentation determined on the CT image was transformed to the deformed CT, using the transformation which aligns the two images. Inter- and intraobserver variability values were subsequently measured in order to determine the errors associated with the segmentation step. Considering the intraobserver variability, a mismatch of  $1.5 \pm 0.8$  mm and  $1.7 \pm 0.6$  mm was observed between both segmentations for the first and the second expert respectively. As for the interobserver variability, the mean mismatch values were  $2.2 \pm 1.3$  mm and  $1.9 \pm 1.3$  mm for the two repeated segmentations performed by the two experts respectively. Overall, there was a trend toward bigger interobserver variability on the CT images since they are characterized by low soft tissue contrast which makes it difficult to detect the prostate boundaries or its interfaces with the surrounding organs, namely the rectum and the bladder. A study by Sannazzari *et al.*<sup>4</sup> on prostate volume and localization in MR and CT images showed that a mean volume overestimation of 34% is observed on CT compared with MRI. This was due to a significant difference along the anterior-posterior and superior-inferior direction where the mean prostate volume was 5 mm larger on CT compared to MRI.

Given that such mismatches can occur while delineating the prostate, the manual segmentation approach is not an objective method for the evaluation of registration related mismatches. On the other hand, the measured errors for the proposed methodology were within the manual segmentation uncertainties.

Considering the current status in the field, most of the previously proposed approaches have worse or at best equivalent performance to that of our proposed approach. In addition, all previously proposed techniques require manual delineation of the prostate, identification of landmarks or markers to be inserted in the prostate and/or some of them being exclusively based on rigid registration only.

Considering that the registration uncertainty has a significant impact on the calculated dose in prostate radiotherapy, the aim of this work, as previously stated, is to propose an accurate registration method that can improve the treatment planning. Su *et al.*<sup>21</sup> studied the dependence of dosimetry calculations on the registration uncertainty. They found that the deviation

in D90 (the minimum dose delivered to 90% of the prostate volume) is less than 5% for registration errors of less than 2 mm. Given that the mean value of the residual mismatch using our proposed registration approach was below 2 mm for all patient datasets considered, ( $1.6 \pm 0.2$  mm) one can conclude that the proposed methodology can limit dosimetry errors associated with image registration residual mismatches to  $<5\%$ . Despite such encouraging results, more patient studies, particularly in the context of prospectively acquired datasets using standardized acquisition protocols, are necessary in order to validate the results of the present study and further assess its reliability before integrating it in a clinical workflow.

Another limitation of the current study is the lack of evaluation of the local intraprostate registration accuracy. In this work, quantitative criteria were used to evaluate the prostate boundaries overlap between both images whereas the overlap of the internal structures was not addressed. Local registration accuracy can be studied using markers inserted in the prostate (for example, implanted markers or a urinary catheter). Unfortunately, the datasets included in the present study did not contain any such features to allow a local registration accuracy assessment. On the other hand, it should be noted that the evaluation of the internal structures' overlap is a challenging task since the presence of implanted markers may introduce some bias to the registration procedure, especially in the case of soft tissues where a nonrigid registration is necessary. A further limitation of the evaluation protocol used in this study is the potential impact of the intra- and interobserver variability in the prostate segmentation task. The prostate segmentation was performed on the original images before the registration, then propagated using the resulting transformations, and subsequently differences between prostate segmented volumes were used to assess the registration accuracy. As such, errors may originate from either the registration method itself or from the manual segmentation step. However, the differences found in the segmented volumes were within the intra- and interobserver variability measures. Finally, in prostate radiotherapy, the prostate is not the only organ of interest, but organs at risk such as the rectum, bladder, and urethra are of much interest too. Following our proposed MRI/CT realignment methodology, one would expect that these organs at risk will be also accurately registered, and this seems to be the case in all of the eight patient datasets used in this study by visual assessment. However, in order to quantitatively measure the exact impact of the proposed method on these organs, a study including the segmentation of these structures needs to be conducted and evaluated on several datasets.

Although this work was dedicated to prostate radiotherapy treatment planning with the acquisition of pretreatment MR and CT images, the proposed registration framework has potential benefits for a variety of image-guided radiation therapy (IGRT) applications, such as treatment delivery precision and dose deposited assessment. For example, in the case of brachytherapy, focal treatment protocols start to emerge and in this case MR images can play a major role in identifying within the prostate volume the tumor foci to be treated. In this type of focal treatment protocols, the ability to accurately



monitor the delivered dose to the planned volumes is essential. Such an approach will require the development of additional registration methods between not only MR and CT but also between MR and US, given that US is the per-operative imaging modality of choice for brachytherapy. In the case of MRI-guided EBRT, adaptive planning using a combined MRI-linear accelerator approach can allow for a real-time treatment delivery guidance. Nevertheless, dose calculations remain the main challenge here since, unlike CT, image intensity in MRI is not directly related to electron density. Therefore, an accurate MR/CT image registration would facilitate the mapping of electron densities to MRI for dose calculations as well as allowing for real-time dose delivery verification.

## 6. CONCLUSIONS AND FUTURE WORK

We presented a nonrigid registration method between 3D preoperative MR and CT images dedicated to prostate radiotherapy treatment planning. This method is fully automatic where no manual segmentation or visual identification of landmarks is required. Our proposed method is based on the maximization of the mutual information in combination with a deformation field parameterized by cubic B-Splines. The proposed method was evaluated on clinical patient datasets demonstrating registration-related residual mismatches of  $1.6 \pm 0.2$  mm.

Future work will involve further evaluation of the proposed approach on a larger number of clinical datasets, including an assessment of intraprostate local registration accuracy as well as the associated precision in the realignment of organs at risk relevant to prostate radiotherapy. This work will also consider the performance of the proposed registration algorithm with datasets containing seeds such as the case in post LDR dose evaluation assessment. Finally, future methodological developments will focus on developing a method for registering the intraoperative US with the preoperative MRI in order to improve structure visualization during the prostate brachytherapy intervention itself, which would subsequently allow guiding the clinician in accurately placing the radioactive sources in their pretreatment planned positions. As such, the method proposed in this study could be combined with the US/MRI registration, so that an integrated solution can be proposed for image-guided prostate brachytherapy procedures.

## CONFLICTS OF INTEREST

The authors have no relevant conflicts of interest to disclose.

<sup>a)</sup>Author to whom correspondence should be addressed. Electronic mail: iyas.hamdan@gmail.com; Telephone: +33(0)2.98.01.81.30.

## REFERENCES

1. Frank SJ, Pisters LL, Davis J, Lee AK, Bassett R, Kuban DA. An assessment of quality of life following radical prostatectomy, high dose

- external beam radiation therapy and brachytherapy iodine implantation as monotherapies for localized prostate cancer. *J Urol.* 2007;177:2151–2156.
2. Lemaréchal Y, Bert J, Falconnet C, et al. GGEMS-Brachy: GPU GEant4-based Monte Carlo simulation for brachytherapy applications. *Phys Med Biol.* 2015;60:4987–5006.
3. Khoo VS, Padhani AR, Tanner SF, Finnigan DJ, Leach MO, Dearnaley DP. Comparison of MRI with CT for the radiotherapy planning of prostate cancer: a feasibility study. *Br J Radiol.* 1999;72:590–597.
4. Sannazzari GL, Ragona R, Ruo Redda MG, Giglioli FR, Isolato G, Guarneri A. CT-MRI image fusion for delineation of volumes in three-dimensional conformal radiation therapy in the treatment of localized prostate cancer. *Br J Radiol.* 2002;75:603–607.
5. Chang JH, Lim Joon D, Nguyen BT, et al. MRI scans significantly change target coverage decisions in radical radiotherapy for prostate cancer. *J Med Imaging Radiat Oncol.* 2014;58:237–243.
6. Villeirs GM, Van Vaerenbergh K, Vakaet L, et al. Interobserver delineation variation using CT versus combined CT + MRI in intensity-modulated radiotherapy for prostate cancer. *Strahlenther Onkol.* 2005;181:424–430.
7. van Herk M, Bruce A, Kroes AP, Shouman T, Touw A, Lebesque JV. Quantification of organ motion during conformal radiotherapy of the prostate by three dimensional image registration. *Int J Radiat Oncol Biol Phys.* 1995;33:1311–1320.
8. Parker CC, Damyanovich A, Haycocks T, Haider M, Bayley A, Catton CN. Magnetic resonance imaging in the radiation treatment planning of localized prostate cancer using intra-prostatic fiducial markers for computed tomography co-registration. *Radiother Oncol.* 2003;66:217–224.
9. Servois V, Chauveinc L, El Khoury C, et al. Comparaison de deux méthodes de recalage d'images de scanographie et d'IRM en curi-thérapie prostatique. Intérêt pour l'évaluation thérapeutique. *Cancer/ Radithérapie.* 2003;7:9–16.
10. van Dalen JA, Huisman HJ, Welmers A, Barentsz JO. Semi-automatic image registration of MRI to CT data of the prostate using gold markers as fiducials. *Biomed Image Regist.* 2003;2717:311–320.
11. Huisman HJ, Futterer JJ, van Lin EN, et al. Prostate cancer: precision of integrating functional MR imaging with radiation therapy treatment by using fiducial gold markers. *Radiology.* 2005;236:311–317.
12. Korsager AS, Carl J, Riis Ostergaard L. Comparison of manual and automatic MR-CT registration for radiotherapy of prostate cancer. *J Appl Clin Med Phys.* 2016;17:294–303.
13. Vidakovic S, Jans HS, Alexander A, Sloboda RS. Post-implant computed tomography-magnetic resonance prostate image registration using feature line parallelization and normalized mutual information. *J Appl Clin Med Phys.* 2006;8:21–32.
14. Chappelow J, Both S, Viswanath S, et al. Computer-assisted targeted therapy (CATT) for prostate radiotherapy planning by fusion of CT and MRI. *SPIE Med Imaging.* 2010;7625:76252C.
15. Zhong H, Wen N, Gordon JJ, Elshaikh MA, Movsas B, Chetty IJ. An adaptive MR-CT registration method for MRI-guided prostate cancer radiotherapy. *Phys Med Biol.* 2015;60:2837–2851.
16. Otsu N. A threshold selection method from gray-level histograms. *IEEE Trans Syst, Man, Cybern.* 1979;9:62–66.
17. Suzuki S, Abe K. Topological structural analysis of digitized binary images by border following. *Comput Vis, Graph, Image Process.* 1985;30:32–46.
18. Mattes D, Haynor DR, Vesselle H, Lewellin TK, Eubank W. Nonrigid multimodality image registration. *Proc SPIE Med Imaging.* 2001;4322:1609–1620.
19. Rueckert D, Sonoda LI, Hayes C, Hill DLG, Leach MO, Hawkes DJ. Nonrigid registration using free-form deformations: application to breast MR images. *IEEE Trans Med Imaging.* 1999;18:712–721.
20. van der Bom IMJ, Klein S, Staring M, Homan R, Bartels LW, Pluim JPW. Evaluation of optimization methods for intensity-based 2D-3D registration in x-ray guided interventions. *SPIE Med Imaging.* 2011;7962:796223.
21. Su Y, Davis BJ, Furutani KM, Herman MG, Robb RA. Dosimetry accuracy as a function of seed localization uncertainty in permanent prostate brachytherapy: increased seed number correlates with less variability in prostate dosimetry. *Phys Med Biol.* 2007;52:3105–3119.

